

Atomic Mixtures in Radiofrequency Dressed Potentials



Elliot Bentine

University College

University of Oxford

A thesis submitted for the degree of

Doctor of Philosophy

Hilary Term, 2018

For my Grandparents

Acknowledgements

I would like to first extend my thanks to my supervisor, Chris Foot, for guiding me through my doctorate. Throughout this work he has been patient and receptive to ideas, always present and ever willing to discuss new physics.

The experimental apparatus used in this thesis is complex, and has required a number of people to keep it running smoothly - in this I have been fortunate to share the company of some very talented people. Tiffany Harte first introduced me to the experiment, and it has been my great pleasure to work with her for much of this doctorate. I can only hope that her dedicated work ethic and thoughtful approach have rubbed off on me. Ed Owen often reminded me of the need to enjoy my work, and I fondly remember laughing in the lab with him. Ben Yuen has provided useful criticism and meticulous feedback. I am grateful for the efforts of Kathrin Luksch, Adam Barker and Shinichi Sunami, who are now the bright future of this apparatus; they have each brought dedication, a fresh perspective and vigor. I am certain the experiment is safe in their hands.

Leo Xu, Sean Ravenhall and Rowan Moore have all been terrific company, and I have enjoyed sharing the basement with them. A special mention also goes to Dimitris Trypogeorgos, who first supervised my Masters project and in doing so introduced me to the Foot group.

A large number of support staff in the Clarendon make our experimental work possible. I would particularly like to thank Mat Newport, John Denton and Simon Moulder from the mechanical workshop, Dan Franks and Alan Francis from stores, and Roy Jelfs. Graham Quelch has also offered invaluable technical assistance.

Outside of the Physics Department, I would like to thank the various friends who have kept me going over these years. My old housemates Matthias and Michaela are especially worthy of mention, for the many times they listened to my ranting when the experiment would not behave. Pobiega and Raid have been good company during many evenings. My parents, Richard and Rebecca, and my brother Harry have been extremely supportive throughout this work. Last, but by no means least, I would like to thank Emma for her patience and support during these years.

Atomic Mixtures in Radiofrequency Dressed Potentials

Elliot Bentine

University College
University of Oxford

*A thesis submitted for the degree of
Doctor of Philosophy*

Hilary Term, 2018

We have developed experimental techniques to confine two species of ultracold atoms in trapping potentials that are independently controlled by applied radiofrequency (rf) fields. Elementary species-selective manipulations are demonstrated for the isotopes ^{85}Rb and ^{87}Rb , such as changing the relative positions of the species. More detailed manipulations are possible, such as creating a double-well potential for one species that is overlapped with a single harmonic well of the other.

We observed that both isotopes have long lifetimes in the rf-dressed potentials when separate; this is well known for ^{87}Rb which has very favourable collision properties, but the stability of ^{85}Rb in rf-dressed potentials had not previously been demonstrated. A large rate of inelastic inter-species collisions was observed when the clouds were brought together, and our results identify this as being due to two-body collisions between ^{85}Rb and ^{87}Rb . We explain the origin of these losses using a qualitative model. Our experimental data is compared to computations of the inelastic loss rate coefficients that have been carried out using coupled-channel calculations by theoretical chemists at Durham University.

We have created double-well potentials for ultracold atoms by dressing with three rfs, as reported in our published work. Since this first demonstration we have eliminated sources of noise from the experimental apparatus using a systematic method, enabling a quantum degenerate gas of ^{87}Rb to be loaded into a double-well potential with $6.7\ \mu\text{m}$ separation between the wells. This is an order of magnitude improvement over our previously published work, and this separation is confirmed by matter-wave interference observed between atoms released from the two wells. In the near future, this apparatus will be able to split a quantum degenerate, two-dimensional gas, as has been performed for one-dimensional gases elsewhere. Moreover, many technical improvements have been implemented, allowing large amounts of data to be measured under highly reproducible conditions.

Contents

1	Introduction	13
2	Theory of rf-dressed potentials	16
2.1	Atoms in a magnetic field	17
2.1.1	The magnetic moment	17
2.1.2	An atom in an external field	18
2.2	The dressed-atom picture	20
2.2.1	An approximate solution	22
2.3	The semi-classical picture	24
2.3.1	The rf interaction in the semi-classical picture	25
2.3.2	The rotating-wave approximation	26
2.3.2.1	The effective field in the rotating frame	28
2.3.3	The Bloch-Siegert shift	29
2.3.4	Floquet theory	29
2.4	Radiofrequency-dressed potentials to confine atoms	31
2.4.1	Non-adiabatic loss	32
2.5	The shell trap	33
2.5.1	Rotation of the static field	34
2.5.1.1	The coupling strength	35
2.5.2	Trap frequencies and the character of confinement	37

2.6	Multiple rf dressing	39
2.7	Radiofrequency spectroscopy	40
2.7.1	Resonant frequency and linewidth	42
2.7.2	The effect of gravitational sag	43
2.8	Conclusion	44
3	The experimental apparatus	45
3.1	The experimental sequence	46
3.1.1	The magneto-optical trap (MOT)	47
3.1.2	Transporting the cloud of cold atoms	48
3.1.3	Magnetic quadrupole trap	50
3.1.4	The time-orbiting potential (TOP) trap	51
3.1.5	Sympathetic cooling	54
3.1.6	Radiofrequency-dressed potentials	56
3.1.7	The time-averaged adiabatic potential (TAAP) trap	56
3.1.8	Shell trap	59
3.2	The laser system	62
3.2.1	The reference laser	63
3.2.2	Microwave offset locks	65
3.2.2.1	The repumping laser offset lock	68
3.2.2.2	The cooling laser offset lock	68
3.2.3	Generating light for simultaneous dual-species operation	70
3.3	Static and radiofrequency magnetic fields	73
3.3.1	MOT coils	73
3.3.2	High current Coils	73
3.3.3	The AC coil array	74
3.3.4	Dressing rf fields and the rf signal chain	75
3.4	Imaging systems	80

3.5	The experimental control system	82
3.5.1	The previous control system	82
3.5.2	The new control system	83
3.5.3	Safety interlocks	85
3.6	Remote monitoring	87
3.7	Conclusion	89
4	Multiple-radiofrequency dressed double-well potential	91
4.1	A 3-rf dressed double-well potential	92
4.1.1	Verifying the calculated rf-dressed eigenstates	94
4.2	RF noise and atom loss	98
4.2.1	Eliminating spurious noise	99
4.2.2	Intermodulation products	102
4.3	A double-well potential with 6.7 μm separation	103
4.3.1	Loading atoms into the double-well potential	103
4.3.2	Distinguishing the wells	104
4.3.3	Balancing the potential	109
4.4	Matter-wave interference	112
4.5	Conclusion and Outlook	113
4.5.1	Improving the quality of the fringes	115
4.5.2	Stability of the double-well potential	116
4.5.3	Towards quantum tunnelling	118
5	Species-Selective rf-dressed potentials	120
5.1	Introduction	120
5.2	The sign of the Landé g_{F} -Factor	122
5.3	The magnitude of the Landé g_{F} -factor	123
5.3.1	The Species-Selective TAAP (SSTAAP)	126

5.3.1.1	Controlling the overlap	127
5.3.1.2	Loading the trap	129
5.3.1.3	Further control using the rf field	132
5.4	Multiple radiofrequencies	135
5.4.1	Mixtures of hyperfine states	135
5.4.2	Mixtures of isotopes or atomic species	137
5.4.2.1	Manipulations	139
5.4.2.2	Loading	142
5.4.2.3	Extension to additional frequencies	142
5.5	Conclusions	144
6	Inelastic Collisions in rf-dressed potentials	146
6.1	^{85}Rb and ^{87}Rb in the TOP: a benchmark	148
6.2	Interspecies inelastic loss in the 2RF trap	152
6.3	Inelastic loss in rf-dressed ^{85}Rb - ^{85}Rb	154
6.3.1	Determining rate coefficients	154
6.4	Inelastic loss in rf-dressed ^{85}Rb - ^{87}Rb mixtures	161
6.4.1	Identifying the inter-species loss mechanism	161
6.4.1.1	Determining the dominant loss mechanism	163
6.4.2	An intuitive model for the two-body loss	170
6.4.3	Measuring the two-body inelastic rate constant $k_2^{85,87}$	175
6.4.3.1	Discussion of results	177
6.4.4	Comparison to a coupled channel model	180
6.5	Conclusions and Outlook	182
7	Conclusions	184
7.1	Future experiments	185
7.1.1	2D gases	185

7.1.2	Quantum-tunnelling	185
7.1.3	Combining time-averaging techniques with multiple-rf dressing	186
7.1.4	Experiments with mixtures	187

Bibliography		189
---------------------	--	------------

List of Figures

2.1	The dressed-atom basis	21
2.2	Atom-photon interactions	22
2.3	Eigenstates in the rotating wave approximation	24
2.4	B_{eff} in the rotating frame	29
2.5	The coupling strength	36
2.6	A multiple-rf double-well potential	39
2.7	The model used for rf spectroscopy	42
3.1	The experimental apparatus	46
3.2	The TOP trap	52
3.3	Sympathetic cooling in the TOP	55
3.4	The TAAP trap	57
3.5	Determining the phase required to produce a circularly-polarised rf-dressing field	61
3.6	Functional block diagram of the optical layout	64
3.7	Principles of a digital phase-frequency detector	66
3.8	Error signals produced by the two offset lock units	68
3.9	Dual species light by slave modulation	72
3.10	Illustration of the AC coil array	75
3.11	Sporadic phase jumps in the DDS output	77
3.12	The horizontal imaging system	79

3.13	The sequence inspector	86
4.1	A 3-rf dressed double-well potential	92
4.2	Verifying the calculated rf-dressed eigenstates	97
4.3	Rabi spectroscopy	100
4.4	Splitting protocol	105
4.5	Artefacts in time-of-flight images	106
4.6	rf spectroscopy in the double-well potential	110
4.7	Manipulating the double-well potential	111
4.8	Signature of matter-wave interferometry	114
4.9	Stability of the MRF double-well potential	117
4.10	Predicted tunnelling rates in the multiple rf double-well potential	119
5.1	Manipulating species of different sign (g_F) with a single rf	124
5.2	Isotopes in a single-rf shell trap	125
5.3	Isotope-selective manipulations using a single rf in the SSTAAP	128
5.4	Loading the SSTAAP trap	130
5.5	Projection into dressed states	133
5.6	Multiple rf for two hyperfine states	136
5.7	A scheme for confining two species with different $ g_F $ in overlapped shell traps	138
5.8	Manipulating ^{85}Rb and ^{87}Rb using the rf polarisation	140
5.9	Raising and lowering ^{85}Rb and ^{87}Rb	140
5.10	MRF ^{87}Rb single well and ^{85}Rb double well	143
6.1	Searching for inelastic loss in the TOP	151
6.2	Inelastic loss in the 2RF TAAP	153
6.3	Inelastic loss of ^{85}Rb in the TAAP	156
6.4	Benchmark for the lifetime of ^{85}Rb alone in the SSTAAP	164

6.5	Identifying the loss mechanism	169
6.6	Loss of ^{85}Rb at different densities n_{87}^{max}	171
6.7	Precession of the rotating frames	173
6.8	Expected behaviour of $k_2^{85,87}$ versus B_0	174
6.9	Change in two-body rate constant with static field	178
6.10	Distribution of overlap by magnetic field magnitude	180
6.11	Comparison to coupled channels for 350 mG series	181
7.1	A time-averaged ring with multiple dressing frequencies	186

Chapter 1

Introduction

Quantum-degenerate atomic gases at nanokelvin temperatures have generated an enormous research field that has expanded rapidly since the pioneering experiments that created Bose-Einstein condensates of rubidium [1] and sodium [2] in 1995. The field has diversified to achieve quantum degeneracy for fermionic isotopes [3], rare-earth metals with large magnetic dipole moments [4, 5], and ultracold molecules [6, 7]. The work in this thesis uses atoms of the two stable isotopes of rubidium to develop sophisticated ways of manipulating and controlling the atoms. The isotope ^{87}Rb has atomic properties that make it extremely suitable for this work, in particular an inelastic collision cross-section which is much smaller than for other atoms including the other isotope used here, ^{85}Rb . We employ a variant of magnetic trapping techniques in which the potential is modified by the application of a strong radiofrequency field. This has been developed in Oxford and elsewhere using ^{87}Rb , and this thesis reports the first experiments for ^{85}Rb and mixtures of both isotopes in such potentials.

Quantum simulation experiments that use mixtures of atomic species are well suited to study the behaviour of impurities coupled to larger quantum systems. They achieve a high degree of control over the individual constituents and their interactions, provide atomically pure systems, and can directly observe the dynamics of pro-

cesses analogous to those occurring in solid-state devices. Experiments have observed non-equilibrium dynamics [8, 9], polaronic phenomena [10, 11] and the disruption and localisation of phases by scattered impurities [12], while control over individual impurities has led to the successful doping of cold gases with single atoms [13, 14] or observation of spin impurities propagating in lattices [15]. Impurities provide a means to non-destructively probe the larger systems with which they interact. For instance, an impurity tunnelling in a double-well potential can be used to measure excitations of a larger bath within which it is immersed [16].

Such schemes require the ability to manipulate the ultracold gas in a species-selective way. When the electronic structure of the trapped species differ this can be performed using optical dipole force potentials, but there are many combinations of species for which this technique cannot be used. The stable isotopes of rubidium, ^{85}Rb and ^{87}Rb , are one such example, and alternative methods must be used to manipulate these species independently.

The solution is to employ a magnetic method of trapping, and thus discriminate between these optically similar species by exploiting the difference in their magnetic dipole moments. Radiofrequency-dressed potentials confine atoms through a combination of static and radiofrequency magnetic fields [17, 18]. The resulting potentials are smooth and free from corrugations which arise in optical dipole force traps, and have extremely low heating rates due to negligible spontaneous emission [19]. The coupling between the atom's magnetic moment and the dressing field is vectorial, allowing manipulations of the potential to be made using the polarisation of the rf field [20].

A recurring theme of this thesis is developing new experimental techniques to further enhance rf-dressed potentials, allowing these advantages to be harnessed for a wider range of experiments. We describe how using multi-frequency radiation increases the flexibility of this technique, and demonstrate a double-well potential formed by

dressing atoms with three radiofrequencies [21, 22]. New techniques are implemented to manipulate mixtures of ^{85}Rb and ^{87}Rb , and the observation of inelastic loss provides an improved understanding of collisions in rf-dressed potentials.

The structure of this thesis is as follows. We begin in Chapter 2 by reviewing the theory of neutral atoms interacting with a radiation field, and the formation of rf-dressed potentials in which atoms can be trapped. This is followed in Chapter 3 by a description of the existing ^{87}Rb apparatus used for the experimental work in this thesis, and we describe a number of updates made to achieve stable, autonomous operation and the simultaneous laser-cooling and confinement of ^{85}Rb . Our multiple rf implementation is introduced in Chapter 4, and we describe the preliminary demonstration of a double-well potential and subsequent further work to achieve a well separation that is small enough to observe matterwave interference after time-of-flight expansion. In Chapter 5, we consider the species-selectivity of rf-dressed potentials, devising and implementing schemes to independently manipulate the two isotopes ^{85}Rb and ^{87}Rb . We observed a high rate of inelastic collisional loss for this mixture and investigated these processes in detail, as described in Chapter 6. We conclude with an outlook for future experiments in Chapter 7.

Chapter 2

Theory of rf-dressed potentials

This chapter examines the theoretical foundations of rf-dressed potentials. We start by describing the interaction of an atom's magnetic dipole moment with an external magnetic field, which is central to all methods of magnetic confinement. We calculate the energy level structure when an oscillating magnetic rf field is applied, providing perspectives from both the dressed-atom and semi-classical models and considering details beyond the rotating wave approximation. Having established the theory of dressed states, it is applied to inhomogeneous static fields to explain how rf-dressed potentials confine atoms. The combination of a static quadrupole field and rf-dressing field is central to this apparatus, and we investigate the resulting 'shell' trap in detail. The theory is extended to a multiple rf field, and we examine the double-well potential that is produced when three frequencies are applied. Finally, we conclude with a discussion of rf spectroscopy, which is used to characterise rf-dressed potentials throughout this thesis.

2.1 Atoms in a magnetic field

The magnetic moment $\vec{\mu}$ of an atom interacts with an externally applied magnetic field \vec{B} . The Hamiltonian of this system is

$$\mathcal{H} = -\vec{\mu} \cdot \vec{B} \quad (2.1)$$

This interaction is at the heart of all methods of magnetic confinement.

2.1.1 The magnetic moment

The atom's total magnetic moment comes from those of the nucleus and constituent electrons. The electronic magnetic moment can in turn be separated into that due to the total electronic orbital magnetic moment $\vec{\mu}_L$ and the total electronic spin magnetic moment $\vec{\mu}_S$, defined by

$$\vec{\mu}_L = -g_L \frac{\mu_B}{\hbar} \vec{L}, \quad \vec{\mu}_S = -g_S \frac{\mu_B}{\hbar} \vec{S} \quad (2.2)$$

The g-factors g_L and g_S are constants of proportionality that relate these quantities to the orbital and spin angular momentum, respectively \vec{L} and \vec{S} with magnitudes $\hbar\sqrt{L(L+1)}$ and $\hbar\sqrt{S(S+1)}$. A strong spin-orbit interaction couples these magnetic moments via an interaction proportional to $\vec{S} \cdot \vec{L}$, and the eigenstates have well-defined electronic angular momentum \vec{J} and electronic magnetic moment μ_J . Experiments with ultracold atomic vapors typically trap alkali atoms in their ground electronic state¹, for which the total orbital angular momentum $L = 0$ and the total spin angular momentum $S = 1/2$; thus, $\vec{J} = \vec{S}$ and $\mu_J = \mu_S$.

Likewise, the nuclear magnetic moment μ_I is proportional to the nuclear angular momentum \vec{I} . An interaction couples the nuclear and electronic magnetic moments,

¹with a notable exception of Rydberg atom experiments

with an energy thus proportional to $\vec{I} \cdot \vec{J}$. The eigenstates have well-defined total angular momentum \vec{F} , of magnitude $\hbar\sqrt{F(F+1)}$, and these hyperfine levels are labelled by the quantum number F . In the vector model, this is represented by the vectors \vec{I} and \vec{J} precessing around their conserved total angular momentum [23]. The total magnetic moment of the atom is

$$\vec{\mu} = -g_F \frac{\mu_B}{\hbar} \vec{F} \quad (2.3)$$

where g_F is the Landé g-factor [23]. Under the application of an external field this remains the case, provided the field is sufficiently weak that both nuclear and electronic magnetic moments interact more strongly with each other than with the external field².

2.1.2 An atom in an external field

We now consider the application of a static, external field $\vec{B}_0 = B_0 \vec{e}_B$, which is aligned parallel to \vec{e}_B (*ie* $B_0 > 0$). The energy of the atom is determined by the alignment of the magnetic moment $\vec{\mu}$ with respect to the external field \vec{B}_0 . The eigenstates of the Hamiltonian defined in eqn. (2.1) are the Zeeman states $|m_F\rangle$, labelled by the projection of their total angular momentum \vec{F} onto the quantisation axis, \vec{e}_B . For weak field strengths³ the corresponding eigenenergies are $E_m = m_F g_F \mu_B B_0$.

For states with $m_F g_F > 0$ the magnetic dipole moment is aligned in opposition to the external field, and the energy is reduced for lower magnitudes of B_0 . These so-called ‘low-field seeking’ states are attracted to regions of weaker magnetic field, and by engineering a field minimum in free space it is possible to confine atoms in

²This is the Zeeman regime. In the Paschen-Back regime, under the influence of stronger external fields, the magnetic moments $\vec{\mu}_J$ and $\vec{\mu}_I$ instead precess individually around \vec{B} rather than their total, and F is no longer a good quantum number [23].

³We work in the low-field limit where only the linear Zeeman terms are important, and henceforth neglect the quadratic and higher-order terms.

these states using static fields. One such example is the spherical quadrupole field,

$$\vec{B}_0 = B' (x\vec{e}_x + y\vec{e}_y - 2z\vec{e}_z) \quad (2.4)$$

with quadrupole gradient B' , which corrals atoms around the field node at the origin, and is easily produced using two coils in an anti-Helmholtz configuration. The potential energy in this field is

$$U(x, y, z) = m_F g_F \mu_B B' \sqrt{x^2 + y^2 + 4z^2} \quad (2.5)$$

For typical laboratory conditions, macroscopic coils produce gradients B' in the range of 100s of G cm^{-1} , while trapping volumes are millimeter-scale. As $m_F g_F \sim 1$, the potential depth is approximately a millikelvin, sufficiently deep to confine laser cooled atoms⁴.

Our apparatus uses a combination of static and oscillating magnetic fields to confine atoms in so-called ‘rf-dressed’ potentials⁵, where an oscillating magnetic field is combined with an inhomogeneous static field to produce confinement [17]. Before examining this method of confinement we will first solve the Hamiltonian of a stationary atom interacting with static and oscillating magnetic fields. Two approaches are used. In the first instance the dressed-atom formalism is employed, which helps emphasise the role of the interaction between the rf field and atom. Second, we invoke a semi-classical picture that provides an intuitive vector model of the rf-dressing process. It may seem surprising to present the fully quantised model first, but we do so to provide a clear picture of the atom-photon interaction that is central to rf-dressed potentials.

⁴Note that eqn. (2.5) does not strictly apply at high energies where the quadratic Zeeman effect becomes important.

⁵Also referred to as ‘adiabatic potentials’ in the literature.

2.2 The dressed-atom picture

The dressed-atom picture describes an atom interacting with a strong, quantised radiation field [24]. In this context, strong means that the Rabi frequency is greater than the separation between the energy levels. The rate of spontaneous emission is negligible for rf transitions, and this process is excluded from the derivation presented here⁶. We also neglect the motion of the atom, which otherwise weakly couples the dressed eigenstates and causes loss from the trap [26].

The Hamiltonian for the combined atom-photon system consists of three terms

$$\mathcal{H} = \mathcal{H}_{atom} + \mathcal{H}_{field} + \mathcal{H}_{int} \quad (2.6)$$

The first term corresponds to the energy of the atom in the absence of the rf field, *ie* the energies of the Zeeman substates. Without loss of generality, we align the coordinate system such that \vec{e}_z is along the direction of the static field \vec{B}_0 , such that $\mathcal{H}_{atom} = g_F \mu_B \hat{F}_z B_0 / \hbar$. The operator \hat{F}_z measures the projection of the atom's angular momentum onto the \vec{e}_z axis. The eigenstates of \mathcal{H}_{atom} are the Zeeman states $|m_F\rangle$ with associated eigenenergies $E_m = m_F g_F \mu_B B_0$.

The second term comprises the energy of the quantised rf field in the absence of the atom.

$$\mathcal{H}_{field} = \hbar\omega \left(a^\dagger a + \frac{1}{2} \right) \quad (2.7)$$

where a^\dagger and a are the creation and annihilation operators for rf photons of angular frequency ω . The eigenstates of \mathcal{H}_{field} are Fock states $|N\rangle$ of well-defined photon number N , with corresponding eigenenergies $(N+1/2)\hbar\omega$. As $N \gg 1$ for the 'classical' rf fields used in this work we henceforth disregard the negligible zero point energy of $\hbar\omega/2$.

⁶This is valid because the Rabi frequency is much greater than the linewidth of spontaneous emission [25]. When important, these processes can be incorporated into the model by out-coupling photons from the field into a separate reservoir [24].

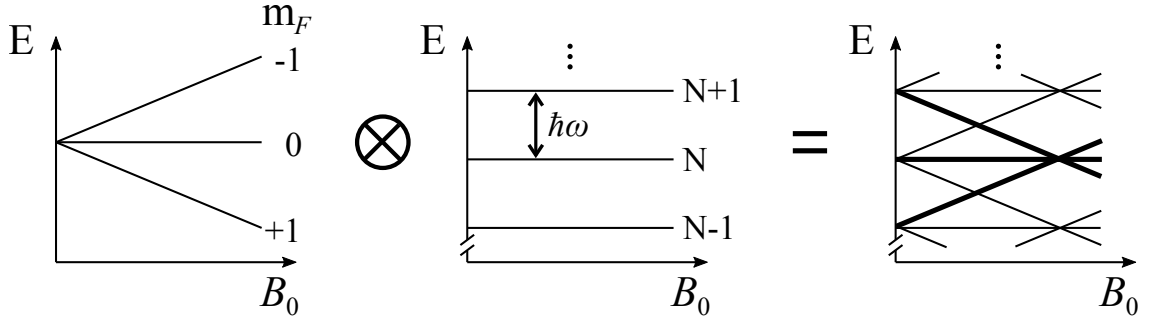


Figure 2.1: **The dressed-atom basis:** Eigenenergies of the Zeeman states and photon Fock states are shown as a function of B_0 ; their tensor product is shown on the right (the uncoupled states). A manifold of the uncoupled states is highlighted in bold. The illustration is for $F = 1$ and $g_F < 0$, as for the lower hyperfine state of ^{87}Rb .

The third term in eqn. (2.6) encompasses the interaction between the atom and radiation field. When $\mathcal{H}_{int} = 0$ (no interaction), the eigenstates of the system are tensor products of the Zeeman states $|m_F\rangle$ and Fock states $|N\rangle$, which we label as the uncoupled states $|N, m_F\rangle$. The eigenenergies are given by

$$(\mathcal{H}_{atom} + \mathcal{H}_{field}) |N, m_F\rangle = (m_F g_F \mu_B B_0 + N \hbar \omega) |N, m_F\rangle \quad (2.8)$$

and illustrated in Fig 2.1 as a function of the static magnetic field amplitude, B_0 . They resemble a ladder, with the repeating motif of the Zeeman energies $E_m = m_F g_F \mu_B B_0$ occurring every $\hbar \omega$ for a different photon number. When the rf field is resonant with the Zeeman splitting (*ie* $\hbar \omega = |g_F \mu_B B_0|$) the energies of the uncoupled states are arranged in manifolds of degenerate states for which the integer $N' = \text{sign}(g_F) m_F + N$ is constant.

The interaction between the magnetic dipole moment and the field permits the exchange of angular momentum and energy between them. For an rf field of arbitrary polarisation, \mathcal{H}_{int} takes the form [27]

$$\mathcal{H}_{int} = \lambda_{\sigma+}(F_+ a + F_- a^\dagger) + \lambda_{\sigma-}(F_+ a^\dagger + F_- a) + \lambda_\pi F_z (a + a^\dagger) \quad (2.9)$$

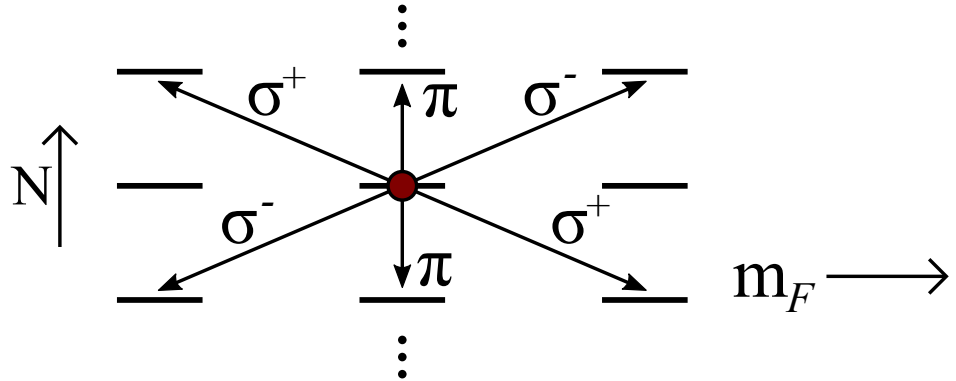


Figure 2.2: **Atom-photon interactions:** Different states (horizontal bars) of $|N, m_F\rangle$ are coupled by different absorption and emission processes, as shown here for one state (marked with a red dot).

where $F_{\pm} = (F_x \pm iF_y)$ are the raising and lowering operators for the atomic angular momentum, and λ_{σ^+} , λ_{σ^-} , λ_{π} are the atom-photon coupling strengths, which depend on the polarisation of the field and the volume of the field modes. We have collected together terms to represent the rf field as a linear combination of circular polarised and π -polarised components about \vec{e}_z . The atom may absorb a photon from the radiation field that causes the projection of its angular momentum along the quantisation axis to be raised (F_+a), lowered (F_-a) or unchanged ($F_z a$). Similarly, the atom's angular momentum can be changed through emission of a photon into the radiation field (a^\dagger terms). These processes are illustrated in Fig 2.2.

The complete dressed-atom Hamiltonian reads:

$$\mathcal{H} = \frac{g_{\text{F}} \mu_{\text{B}}}{\hbar} B_0 \hat{F}_z + \hbar\omega(a^\dagger a + 1/2) + \lambda_{\sigma^+}(F_+ a + F_- a^\dagger) + \lambda_{\sigma^-}(F_+ a^\dagger + F_- a) + \lambda_{\pi} F_z (a + a^\dagger) \quad (2.10)$$

2.2.1 An approximate solution

We seek to determine the eigenstates of eqn. (2.10). As previously noted, in the vicinity of the rf resonance the uncoupled states within each manifold of N' are

nearly degenerate. They are coupled by either the σ^+ or σ^- component of the field, according to whether the sign of g_F is positive or negative. For this example we take the sign to be negative, which is the case for ^{87}Rb in the lower hyperfine state which has $F = 1, g_F = -1/2$. To obtain an approximate solution⁷, we keep only the λ_{σ^-} terms in eqn. (2.9), neglecting all others that couple states well separated in energy. The approximate Hamiltonian is

$$\mathcal{H} = \hbar\omega a^\dagger a + \frac{g_F \mu_B}{\hbar} F_z B_0 + \lambda_{\sigma^-} (F_+ a^\dagger + F_- a) \quad (2.11)$$

In this approximation, N' is a good quantum number as we have neglected the terms that couple states in different manifolds. It follows that each eigenstate will be a superposition of uncoupled states $|N, m_F\rangle$ within the same manifold. Arranging the uncoupled basis states $|N, m_F\rangle$ according to these manifolds and representing eqn. (2.11) in matrix form,

$$\mathcal{H} = \begin{pmatrix} \ddots & & & & & \\ & \hbar N' \omega + \hbar \delta & \frac{\Omega}{\sqrt{2}} & & & \\ & \frac{\Omega}{\sqrt{2}} & \hbar N' \omega & \frac{\Omega}{\sqrt{2}} & & \\ & & \frac{\Omega}{\sqrt{2}} & \hbar N' \omega - \hbar \delta & & \\ & & & & \ddots & \\ & & & & & \ddots \end{pmatrix}, \quad \text{in the basis} \begin{pmatrix} \vdots \\ |N+1, +1\rangle \\ |N, 0\rangle \\ |N-1, -1\rangle \\ \vdots \end{pmatrix} \quad (2.12)$$

where we have introduced the angular detuning $\delta = \omega - |g_F| \mu_B B_0 / \hbar$ and $\Omega = 2\lambda_{\sigma^-} \sqrt{\langle N \rangle}$ with $\langle N \rangle \gg 1$ the average photon number, and we have used that $\sqrt{N+1} \approx \sqrt{N}$ for $N \gg 1$. The 3×3 block-diagonal Hamiltonian is easily diagonalised using standard methods. The eigenvalues of the dressed system are equal

⁷This is equivalent to taking the rotating wave approximation in the semi-classical picture, as we will see later. Clearly the solution is exact for circularly-polarised σ^- rf, for which the λ_{σ^+} and λ_{π} terms are zero.

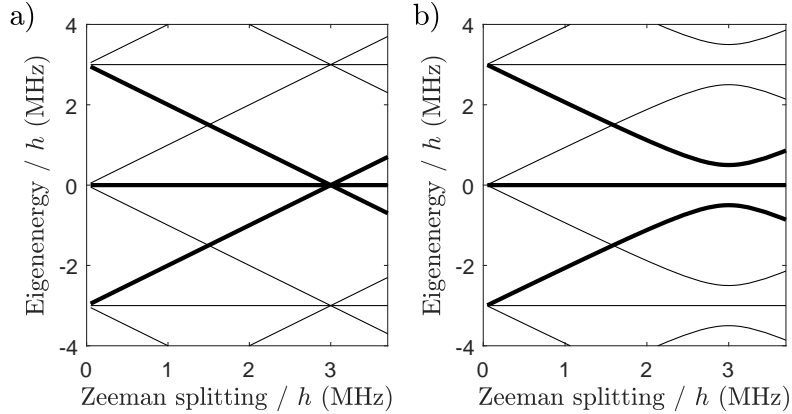


Figure 2.3: **Eigenstates in the rotating wave approximation:** Dressed eigenenergies are plotted as a function of the Zeeman splitting for **a)** no atom-photon coupling and **b)** non-zero coupling. One manifold is emphasised in bold. The rf frequency is $\omega/2\pi = 3$ MHz.

to

$$N'\hbar\omega + \tilde{m}_F\hbar\sqrt{\delta^2 + \Omega^2} \quad (2.13)$$

where \tilde{m}_F labels each dressed eigenstate in the N' manifold $|N', \tilde{m}_F\rangle$, and $\tilde{m}_F \in \mathbb{Z} : -F \leq \tilde{m}_F \leq F$.

These eigenenergies are plotted in Fig 2.3a as a function of detuning. The interaction between the atom and the rf field creates an avoided crossing at the resonance; the eigenenergies of the coupled system are driven apart where the uncoupled states of the manifold previously intersected. States where \tilde{m}_F is positive exhibit a potential minimum at the resonance ($\delta = 0$), providing a mechanism to confine atoms in these dressed states when the detuning varies with position. We return to this point in Sec 2.4.

2.3 The semi-classical picture

An alternate perspective is provided by the semi-classical picture, which considers quantised atomic states interacting with a classical radiation field \vec{B}_{rf} in the presence

of a static magnetic field \vec{B}_0 . Following equation eqn. (2.1) and still neglecting motion of the atom, the Hamiltonian is

$$\mathcal{H} = -\vec{\mu} \cdot (\vec{B}_0 + \vec{B}_{\text{rf}}) \quad (2.14)$$

As before and without loss of generality the coordinate system is aligned such that $\vec{e}_z \parallel \vec{B}_0$.

2.3.1 The rf interaction in the semi-classical picture

The rf field oscillates at an angular frequency ω with the arbitrary polarisation

$$\begin{aligned} \vec{B}_{\text{rf}} = & B_x \cos(\omega t) \vec{e}_x \\ & + B_y \cos(\omega t + \phi_y) \vec{e}_y \\ & + B_z \cos(\omega t + \phi_z) \vec{e}_z \end{aligned} \quad (2.15)$$

The interaction energy between the magnetic moment of the atom, $\vec{\mu}$, and the external field \vec{B}_{rf} is equal to:

$$\mathcal{H}_{\text{int}} = -\vec{\mu} \cdot \vec{B}_{\text{rf}} \quad (2.16)$$

where the magnetic moment $\vec{\mu} = -g_{\text{F}}\mu_{\text{B}}\vec{F}/\hbar$ as before. To evaluate the dot product we represent the vector \vec{F} in terms of angular momentum raising and lowering operators:

$$\vec{F} = \frac{\hat{F}_+ + \hat{F}_-}{2} \vec{e}_x + \frac{\hat{F}_+ - \hat{F}_-}{2i} \vec{e}_y + \hat{F}_z \vec{e}_z \quad (2.17)$$

and thus the interaction is

$$\begin{aligned}
\mathcal{H}_{int} = & \frac{g_F \mu_B}{\hbar} \frac{\hat{F}_+}{2} (B_x \cos(\omega t) - i B_y \cos(\omega t + \phi_y)) \\
& + \frac{g_F \mu_B}{\hbar} \frac{\hat{F}_-}{2} (B_x \cos(\omega t) + i B_y \cos(\omega t + \phi_y)) \\
& + \frac{g_F \mu_B}{\hbar} \hat{F}_z B_z \cos(\omega t + \phi_z)
\end{aligned} \tag{2.18}$$

This resembles the interaction in the dressed-atom picture, eqn. (2.9), with the different σ^+ and σ^- polarisation components now corresponding to rotations of \vec{B}_{rf} around the quantisation axis \vec{e}_z .

2.3.2 The rotating-wave approximation

To solve the Hamiltonian the same approximation is made as in Sec 2.2.1, and for consistency we again take the example of ^{87}Rb in the $F = 1$ hyperfine level. This was previously motivated by only considering terms that couple nearly degenerate states within the same manifold. We first transform into a frame \mathbf{x}' that rotates about \vec{e}_z at the dressing frequency ω , through the transformation

$$U = e^{-\text{sign}(g_F) \hat{F}_z \omega t / \hbar} = \sum_{m_F} e^{-\text{sign}(g_F) m_F \omega t} |m_F\rangle \langle m_F| \tag{2.19}$$

which transforms the Hamiltonian according to⁸

$$\mathcal{H} \rightarrow \mathcal{H}', \quad \mathcal{H}' = \left(U \mathcal{H} U^\dagger - i \hbar U \frac{\partial U^\dagger}{\partial t} \right) \tag{2.20}$$

The oscillating field of eqn. (2.15) appears different in the rotating frame. Terms of B_x and B_y that co-rotate with the frame appear stationary, while counter-rotating terms now rotate at an angular frequency 2ω . The field components parallel to the rotation

⁸To derive this, apply the transformation U to the Time-Dependent Schrödinger Equation (TDSE) and rearrange to produce a new TDSE in the rotating frame.

axis are unaffected by the transformation; those arising from \vec{B}_0 are unchanged, while B_z terms continue to oscillate at a frequency ω . The ‘rotating wave approximation’ is now employed; all terms that oscillate in the rotating frame are neglected, leaving a Hamiltonian that is time-independent. This can be represented as a matrix in the basis of Zeeman states $|m_F = 1, 0, -1\rangle$, in which the raising and lowering operators are defined

$$F_z = \hbar \begin{pmatrix} 1 & & \\ & 0 & \\ & & -1 \end{pmatrix}, \quad F_+ = \begin{pmatrix} 0 & \sqrt{2} & \\ & 0 & \sqrt{2} \\ & & 0 \end{pmatrix}, \quad F_- = \begin{pmatrix} 0 & & \\ \sqrt{2} & 0 & \\ & \sqrt{2} & 0 \end{pmatrix} \quad (2.21)$$

and thus the Hamiltonian under the rotating-wave approximation is

$$\mathcal{H}'_{\text{rwa}} = \begin{pmatrix} -\hbar\delta & \frac{g_F\mu_B}{2\sqrt{2}} (B_x - ie^{-i\phi_y} B_y) & \\ \frac{g_F\mu_B}{2\sqrt{2}} (B_x + ie^{i\phi_y} B_y) & 0 & \frac{g_F\mu_B}{2\sqrt{2}} (B_x - ie^{-i\phi_y} B_y) \\ & \frac{g_F\mu_B}{2\sqrt{2}} (B_x + ie^{i\phi_y} B_y) & \hbar\delta \end{pmatrix} \quad (2.22)$$

where as before $\delta = \omega - |g_F|\mu_B B_0/\hbar$ is the angular detuning from resonance. We make one final frame transformation $\mathbf{x}' \rightarrow \mathbf{x}''$, applying the operator $R = e^{-i\alpha F_z/\hbar}$ to adjust the phase of the rotating frame such that the \vec{e}''_x axis aligns to the horizontal field components defined by B_x and B_y . With phase angle $\alpha = \text{atan}\left(\frac{B_y \cos \phi_y}{B_x - B_y \sin \phi_y}\right)$, the Hamiltonian transforms to

$$\mathcal{H}''_{\text{rwa}} = \hbar \begin{pmatrix} -\delta & \Omega/\sqrt{2} & \\ \Omega/\sqrt{2} & 0 & \Omega/\sqrt{2} \\ & \Omega/\sqrt{2} & \delta \end{pmatrix} = -\hbar\delta F''_z + \hbar\Omega F''_x \quad (2.23)$$

The semi-classical dressed eigenenergies are thus $\tilde{m}_F \hbar \sqrt{\delta^2 + \Omega^2}$, which are consistent with the result from the dressed-atom picture. The angular Rabi frequency, Ω ,

is defined [28]

$$\Omega = \frac{g_F \mu_B}{2\hbar} \sqrt{B_x^2 + B_y^2 - 2B_x B_y \sin(\phi_y)} \quad (2.24)$$

It is often stated that in the rotating wave approximation only components of the magnetic field perpendicular to the static field \vec{B}_0 couple the Zeeman states and are thus responsible for the avoided crossing [20, 28]. This statement is true, but potentially misleading, as it suggests that any perpendicular field will suffice. For our example of ^{87}Rb in the $F = 1$ state, it is clear that the coupling of eqn. (2.24) vanishes when $B_x = B_y$ and $\phi_y = \pi/2$. By analogy to eqn. (2.9), a clearer statement is that a specific circular polarisation about \vec{e}_z is responsible for coupling the states and so producing the avoided crossing. The amplitude of that circular polarisation is related to the components of the field that oscillate perpendicular to the quantisation axis, \vec{e}_z .

2.3.2.1 The effective field in the rotating frame

The Hamiltonian of eqn. (2.23) resembles that of a magnetic dipole in a static magnetic field, eqn. (2.1). The dressed eigenstates $|\tilde{m}_F\rangle$ correspond to Zeeman states of an ‘effective field’ [29], which in the rotating frame \mathbf{x}'' of eqn. (2.23) is equal to $\vec{B}_{\text{eff}} = (\hbar\delta\vec{e}_z'' - \hbar\Omega\vec{e}_x'')/|g_F|\mu_B$.

Viewed from the initial non-rotating frame \mathbf{x} , the effective field precesses around the axis \vec{e}_z with angular frequency ω and tilt angle $\theta = \delta/\Omega$ (see Fig 2.4). When far detuned the effective field aligns (anti)parallel to the static field \vec{B}_0 ; the eigenenergies are only slightly perturbed from their undressed values and the dressed eigenstates are approximately equal to the undressed Zeeman states in the static field⁹. At resonance, \vec{B}_{eff} is perpendicular to \vec{B}_0 , and there is significant admixture of the Zeeman states of \vec{B}_0 to comprise each dressed eigenstate.

⁹Note that for large negative detunings $|\tilde{m}_F\rangle \approx |m_F\rangle$, while for large positive detunings $|\tilde{m}_F\rangle \approx |-m_F\rangle$

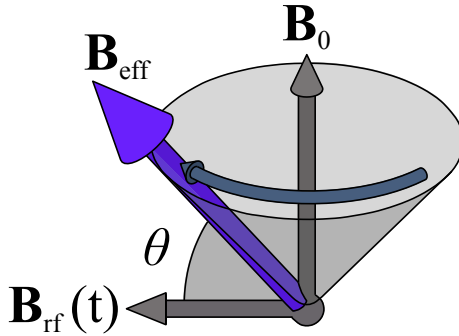


Figure 2.4: B_{eff} in the rotating frame: The effective field \vec{B}_{eff} lies in a plane defined by the static field \vec{B}_0 and the circularly-polarised component of \vec{B}_{rf} to which the rotating frame is aligned. \vec{B}_{eff} precesses around \vec{B}_0 with tilt angle θ .

2.3.3 The Bloch-Siegert shift

In both the semi-classical and dressed-atom description, we applied the rotating wave approximation to neglect counter-rotating terms from the Hamiltonian to find a neat analytical solution for the eigenstates. The effect of these terms is to shift the position of the rf resonance - the ‘Bloch-Siegert’ shift [30] - which can be understood using either a semi-classical model [30, 31] or in the dressed-atom formalism [32]. An intuitive interpretation is that the counter-rotating terms off-resonantly dress the eigenstates in the rotating frame, causing a shift in the eigenenergies.

The Bloch-Siegert shift becomes increasingly important for dressing fields of larger amplitudes [31, 33]. This behaviour is simple to understand from the dressed-atom picture; the terms responsible for the shift couple states in different manifolds and, for greater dressing field amplitudes, the energy separation between these states decreases as the manifold is pushed apart.

2.3.4 Floquet theory

We conclude the discussion of techniques to calculate the dressed eigenstates by briefly introducing Floquet theory [34], which is applicable for calculating the eigenstates of

time-periodic Hamiltonians¹⁰. The technique is well-suited to numerical methods and neglects no terms from the Hamiltonian (unlike in the rotating wave approximation), providing accurate results for fields of arbitrary polarisation. It is also applicable to atoms dressed with more than one frequency component [21, 36]¹¹, and is the primary method by which we calculate the multiple-rf dressed eigenstates. A semi-classical theory is used here.

The Hamiltonian is periodic in time with period $T = 2\pi/\Delta\omega$, with $\mathcal{H}(t) = \mathcal{H}(t + T)$. Floquet's theorem dictates that eigenstates of this Hamiltonian are of the form

$$\mathcal{H} |\Psi(t)\rangle = e^{i\lambda t} |\Phi(t)\rangle \quad (2.25)$$

where $|\Phi(t)\rangle$ has the same time-periodicity as the Hamiltonian, $|\Phi(t)\rangle = |\Phi(t + T)\rangle$.

The operator $\hat{U}(t, t')$ evolves a wavefunction forward in time from $t \rightarrow t'$,

$$\hat{U}(t; t') |\psi(t)\rangle = |\psi(t')\rangle \quad (2.26)$$

Advancing the time of the system by T , an eigenstate of the Hamiltonian behaves as

$$U(0; T) |\Psi(0)\rangle = e^{i\lambda T} |\Psi(0)\rangle \quad (2.27)$$

and thus eigenstates of the Hamiltonian are also eigenstates of the propagator. The characteristic exponents λ can be related to the eigenvalues of the Hamiltonian [34], with dressed eigenenergies $E = \hbar\lambda$. In this way, calculating the dressed eigenenergies of the system becomes a problem of determining the eigenvalues of the operator $U(0; T)$.

We determine $\hat{U}(t; t + T)$ by numerical integration of the Schrödinger equation.

¹⁰It is analogous to the Bloch theorem for Hamiltonians that are periodic in spatial coordinates [35].

¹¹With the caveat that each frequency must be an integer multiple of a common fundamental, and the periodicity of the system must be suitably short to keep the calculation times reasonable.

As the eigenvalues are the same regardless of the basis chosen, we take the basis of Zeeman states $|m_F\rangle$ for convenience, in which all operators of the Hamiltonian (F_-, F_+, F_z) have straightforward matrix representations. Exploiting the identity,

$$\hat{U}(t; t') = \sum_{m_F} \left(\hat{U}(t; t') |m_F\rangle \right) \langle m_F| \quad (2.28)$$

and the bracketed term is determined by integrating the time-dependent Schrödinger equation, taking each Zeeman state $|m_F\rangle$ as an initial state. Once a matrix representation of $\hat{U}(0; T)$ in this basis has been calculated, the eigenvalues $e^{i\lambda T}$ follow from standard matrix techniques. Note that if λ is an eigenvalue of \mathcal{H} , so too is $\lambda + n\hbar\Delta\omega$, $n \in \mathbb{Z}$ [34], and the eigenenergies thus form a ladder with interval determined by the system periodicity.

2.4 Radiofrequency-dressed potentials to confine atoms

We now consider how the resulting energy level structure is harnessed to trap atoms. In the rotating wave approximation the eigenenergies are of the form

$$U(\vec{r}) = \hbar\tilde{m}_F\sqrt{\delta^2(\vec{r}) + \Omega^2(\vec{r})} \quad (2.29)$$

where both the detuning and resonant Rabi frequency now carry a spatial dependence; these result from a change in the magnitude and direction of the static field $\vec{B}_0(\vec{r})$ at different positions in the trap. For states with \tilde{m}_F positive, the dressed energy U is minimum when $\sqrt{\delta^2 + \Omega^2}$ is minimised, creating a potential minimum in space in which to confine atoms. The increase in energy away from this point can result from an increase in $\delta(\vec{r})^2$ with negligible change in Ω (the resonant configuration), or an

increase in both $\delta(\vec{r})^2$ and $\Omega^2(\vec{r})$ (the off-resonant configuration). In the off-resonant case the increase in $\Omega^2(\vec{r})$ does not arise from a change in rf amplitude, which is typically uniform over the trap. Instead, it arises through a change in direction of the static field, which affects the vectorial coupling between the atom and rf-dressing field. This mode of operation is most often exploited in rf dressed-atom chips, where it is possible to change the static field direction over small length scales, and has been used to produce a controllable double-well potential [20] that can coherently split a BEC [37].

The dressed potentials on this apparatus operate in the resonant configuration, with strong confinement resulting from an increase in δ away from the resonance where atoms are trapped. This ‘shell trap’ is detailed below, after a general statement regarding the motion of atoms in rf dressed potentials.

2.4.1 Non-adiabatic loss

We have so far neglected the impact of an atom’s motion on the rf dressed eigenstates. For a trapped atom to remain in the same dressed eigenstate as it traverses the avoided crossing it must adiabatically follow the local eigenstate $|\tilde{m}_F(\vec{r})\rangle$. If it does not, the atom transitions to a different dressed state in which it is no longer confined, leading to non-adiabatic loss¹².

The loss rate can be estimated using the well known Landau-Zener model [38, 39], which gives the probability of a diabatic transition during a transit over the avoided crossing, from a detuning of $-\infty \rightarrow \infty$, as $P_{LZ} = e^{-2\pi\Omega^2/v_{LZ}}$, where the Landau-Zener velocity $v_{LZ} = \partial\delta/\partial t$ [18]. The loss rate decreases with increasing rf amplitude and decreasing quadrupole gradient, which can be understood as follows. Larger rf amplitudes broaden the avoided crossing with respect to δ , decreasing the rate of

¹²Hyperfine states with $F > 1$ have more than one trapped state for which $\tilde{m}_F > 0$, and so non-adiabatic transitions can also occur to other trapped states. However, atoms performing multiple non-adiabatic transitions will still eventually reach an untrapped state and be lost from the trap.

change of the dressed eigenenergies during the transit and thus the loss rate. The quadrupole gradient converts the velocity of an atom in real space to the Landau-Zener velocity, and a weaker gradient decreases v_{LZ} . Larger rf amplitudes and weak gradients also reduce the harmonic trap frequency, and thus the number of transits over the avoided crossing per second. For most of this work the adiabatic loss rate is negligible compared to inelastic loss or that due to rf noise (see Sec 4.2.1), but it is an important consideration for future experiments (see outlook, Chapter 4).

The Landau-Zener model is only a rough approximation; atoms do not oscillate from $\delta = \pm\infty$ with constant v_{LZ} , and instead remain trapped within the harmonic region of the crossing. A more thorough treatment of adiabaticity formulates the effect of atomic motion in terms of a gauge potential that couples the dressed eigenstates [40]. Furthermore, the trajectory may be non-classical, such as in a Bose-condensate, and in this case a more detailed quantum mechanical model is required [41], as was recently applied to dressed states [42].

2.5 The shell trap

Our apparatus uses a ‘shell trap’ formed by combining an rf-dressing field with a static spherical quadrupole field. We define the rf-dressing field

$$\begin{aligned}\vec{B}_{\text{rf}} = & B_x \cos(\omega t) \vec{e}_x \\ & + B_y \cos(\omega t + \phi_y) \vec{e}_y \\ & + B_z \cos(\omega t + \phi_z) \vec{e}_z\end{aligned}\tag{2.30}$$

which is the same as eqn. (2.15) but now with \vec{e}_x , \vec{e}_y , \vec{e}_z the laboratory coordinate system (which is not generally aligned with the quantisation axis). The static quadrupole

field is defined

$$\vec{B}_0(x, y, z) = B'(x\vec{e}_x + y\vec{e}_y - 2z\vec{e}_z) \quad (2.31)$$

where the quadrupole gradient is B' and \vec{e}_z is an axis of cylindrical symmetry. The Zeeman splitting varies as a function of position, and the resonance condition $|g_F\mu_B\vec{B}_0| = \hbar\omega$ is fulfilled for points on an isomagnetic surface we refer to as the ‘resonant spheroid’, defined as

$$r_0 = \frac{\hbar\omega}{|g_F\mu_B\vec{B}_0|} = \sqrt{x^2 + y^2 + 4z^2} \quad (2.32)$$

Atoms are trapped on the surface of this spheroid, typically congregating near the bottom under the influence of gravity. Both the angular detuning $\delta(\vec{r}) = g_F\mu_B|B_0(\vec{r})| - \hbar\omega$ and the Rabi frequency $\Omega(\vec{r})$ have a spatial dependence. The first arises from the variation in Zeeman splitting with position in the quadrupole field, while the spatial dependence of $\Omega(\vec{r})$ arises from the rotation of the static field with position.

2.5.1 Rotation of the static field

Although the rf-dressing field is uniform, the direction of the static quadrupole field $\vec{B}_0(\vec{r})$ varies with position \vec{r} in the trap. Combined with the vectorial coupling of the magnetic dipole moment, this rotation of $\vec{B}_0(r)$ causes the atom-photon coupling to vary with position.

To calculate the interaction term of the semi-classical Hamiltonian at a particular point in space (x, y, z) , it is first necessary to represent the laboratory rf field of eqn. (2.30) in a coordinate system aligned to the quantisation axis. We follow the method of Heathcote [43], and specify such a coordinate system \mathbf{x}' with $\vec{e}_{z'} \parallel \vec{B}_0$. The basis vectors of \mathbf{x}' are uniquely defined by the relations $\vec{e}_{x'} = \vec{e}_{z'} \times \vec{e}_z$ and $\vec{e}_{y'} = \vec{e}_{x'} \times \vec{e}_{z'}$, as is the transformation $S : \mathbf{x} \rightarrow \mathbf{x}'$ that maps a vector from \mathbf{x} to \mathbf{x}' . In the rotated

Polarisation	Constraints
Circular	$B_y = B_x = B, B_z = 0, \phi_y = \pi/2$
Linear	$B_x = B, B_z = B_y = 0$

Table 2.1: Definitions of specific laboratory-frame rf field polarisations.

coordinate system \mathbf{x}' , the transformed rf field $\vec{B}'_{\text{rf}} = S\vec{B}_{\text{rf}}$ is:

$$\vec{B}'_{\text{rf}} = \begin{bmatrix} \cos(\gamma) \cos(\theta) & \sin(\gamma) & \cos(\gamma) \sin(\theta) \\ \cos(\theta) \sin(\gamma) & -\cos(\gamma) & \sin(\gamma) \sin(\theta) \\ \sin(\theta) & 0 & -\cos(\theta) \end{bmatrix} \begin{bmatrix} B_x \sin(\omega t) \\ B_y \sin(\omega t + \phi_y) \\ B_z \sin(\omega t + \phi_z) \end{bmatrix} \quad (2.33)$$

which is used to calculate the interaction in the semi-classical picture $g_F\mu_B$ at an arbitrary position \vec{r} , as eqn. (2.18) is valid for the rf field in the transformed frame \mathbf{x}' . The angles θ, γ are defined [43]

$$\cos \theta = \frac{2z}{\sqrt{x^2 + y^2 + z^2}} \quad \cos \gamma = \frac{x}{\sqrt{x^2 + y^2}} \quad (2.34)$$

2.5.1.1 The coupling strength

As a result of this rotation, the atom-photon coupling strength (quantified via the resonant angular Rabi frequency, Ω) varies over the surface of the resonant spheroid. Nodes are located where $\Omega(\vec{r}) \rightarrow 0$, corresponding to a vanishing avoided crossing at which adiabatic following cannot be sustained, leading to atom loss.

A general expression for $\Omega(\vec{r})$ can be derived by combining eqn. (2.24) with the components of \vec{B}'_{rf} [43]. Two important examples are shown in Fig 2.5, which correspond to the circularly-polarised and linearly-polarised laboratory fields defined in Table 2.1. For the handedness of circularly-polarised rf used here the angular Rabi

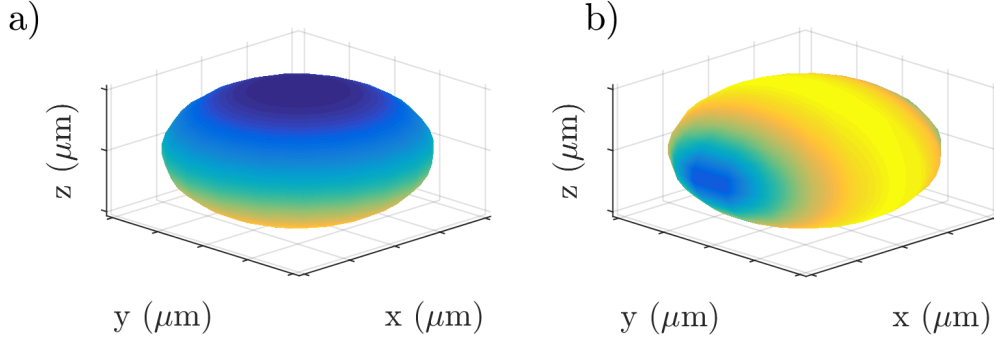


Figure 2.5: **The coupling strength:** The variation in coupling strength over the surface of the resonant spheroid is plotted for **a)** circular and **b)** linear polarisations of the rf field. Dark blue colors indicate weaker coupling.

frequency at resonance obeys [28, 19]

$$\Omega(\vec{r}) = \frac{g_F \mu_B B}{2\hbar} \left(1 - \frac{2z}{\sqrt{x^2 + y^2 + 4z^2}} \right) \quad (2.35)$$

with a maximum of $\Omega_0 = g_F \mu_B B / \hbar$ at the bottom of the resonant spheroid, and a node of coupling strength at the top where the quantisation axis is inverted. When using linear polarisation, the coupling strength is [28, 19]

$$\Omega(\vec{r}) = \frac{g_F \mu_B B}{2\hbar} \left(\frac{y^2 + z^2}{\sqrt{x^2 + y^2 + 4z^2}} \right) \quad (2.36)$$

with maxima of $\Omega_0 = g_F \mu_B B / 2\hbar$ at locations in the (y, z) plane where $\vec{B}_{\text{rf}} \perp \vec{B}_0$, and nodes along \vec{e}_x where $\vec{B}_{\text{rf}} \parallel \vec{B}_0$.

On resonance, the energy of the dressed state $U \propto \Omega(\vec{r})$, and a variation in coupling strength over the surface of the resonant spheroid exerts a ‘coupling force’ on the trapped atoms, directed from regions of strong coupling towards the nodes. This attraction is typically undesired due to the non-adiabatic loss occurring at the nodes, and in our trap it is fortunately overwhelmed by the gravitational force. The force is greater for stronger rf amplitudes and quadrupole field gradients, which both increase the gradient of $\Omega(\vec{r})$ over the surface of the shell trap. It can be controlled

through the polarisation of the rf field, providing a way to manipulate atoms in the trap; for example, by varying the polarisation of the dressing field to sweep the node of coupling strength in a circle (and thus rotate the direction of the coupling force) to stir the atoms [44].

2.5.2 Trap frequencies and the character of confinement

Under typical operation, atoms congregate at the bottom of the shell under the influence of gravity. Atoms trapped on the lower portion of the resonant spheroid experience a highly anisotropic confinement that is characterised by strong trap frequencies in the vertical direction (100s of Hz) and weak trap frequencies in the horizontal plane (~ 10 Hz). At the bottom of the shell, the vertical confinement arises from the large energy cost associated with an increased detuning $\delta(\vec{r})$ from resonance. The radial confinement comes from interplay between gravitational potential energy, which pulls atoms to the bottom of the shell, and the variation in coupling strength around the surface of the spheroid. These different mechanisms of confinement give the shell trap its extremely anisotropic character.

Analytic expressions for both harmonic trap frequencies are found from a power series expansion about the potential minimum, closely following Merloti *et. al.* [19]. For the circularly-polarised rf field of Table 2.1 the system is cylindrically symmetric, and the minimum is located on the z -axis at

$$z_{\min} = -R = -\frac{r_0}{2} \left(1 + \frac{\epsilon}{\sqrt{1-\epsilon^2}} \frac{\Omega_0}{\omega} \right) \approx -\frac{r_0}{2} \quad (2.37)$$

where $\Omega_0/2\pi = |g_F|\mu_B B/h$ is the Rabi frequency at the bottom of the shell, and the ratio $\epsilon = Mg/2g_F\mu_B B' \tilde{m}_F$ compares the force of gravity to that exerted by the quadrupole field. The approximation holds when $\epsilon \ll 1$ which is true of typical operation. Expanding the potential about this minimum, and evaluating the curvature

$c_i = \frac{\partial^2 U}{\partial i^2} |_{(0,0,z_{\min})} = m\omega_i^2$ gives [19]

$$\omega_r = \sqrt{\frac{g}{4R}} \left(1 - \frac{\tilde{m}_F \hbar \Omega_0}{2MgR} \sqrt{1 - \epsilon^2} \right)^{1/2} \approx \sqrt{\frac{g}{2r_0}} \left(1 - \frac{\tilde{m}_F \hbar \Omega_0}{Mg r_0} \right)^{1/2} \quad (2.38)$$

$$\omega_z = 2|g_F| \mu_B B' \sqrt{\frac{\tilde{m}_F}{M\hbar\Omega_0}} (1 - \epsilon^2)^{3/4} \approx 2|g_F| \mu_B B' \sqrt{\frac{\tilde{m}_F}{M\hbar\Omega_0}} \quad (2.39)$$

The vertical trap frequency is increased for larger quadrupole gradients, which compress the avoided crossing with respect to z , and lower rf amplitudes, which reduce the width of the avoided crossing in δ . Both increase the curvature c_z , resulting in tighter confinement. The radial confinement arises from the aforementioned interplay between gravitational potential energy and coupling force. For a sufficiently low rf field amplitude and high quadrupole gradient, the vertical trap frequencies exceed kHz while the radial trap frequencies are tens of Hz, allowing the realisation of a 2D degenerate Bose gas with chemical potential $\mu < \hbar\omega_z$ [19].

For a linear polarisation, $\omega_x \neq \omega_y$. Instead,

$$\omega_y = \sqrt{\frac{g}{4R}} \text{ and } \omega_x, \omega_y \text{ as before, with } B \rightarrow B/2 \quad (2.40)$$

The confinement in ω_x does not change, despite a change in the coupling strength $\Omega(\vec{r})$. Nodes now exist at $\pm R\vec{e}_x$ where $\vec{B}_0 \parallel \vec{B}_{\text{rf}}$, and the maximum value $\Omega_0 = g_F \mu_B / 2\hbar$. Although Ω_0 decreases to half the value for a circular polarised field of the same magnitude B , the node is located only half the distance around the spheroid, thus the coupling force $F_c = -\tilde{m}_F \hbar \partial_x \Omega(r)$ in this direction is unaltered. The force vanishes along \vec{e}_y , as the Rabi frequency is constant for all points in the plane $x = 0$ for which $\vec{B}_{\text{rf}} \perp \vec{B}_0$. Thus, confinement along \vec{e}_y is determined only by the gravitational potential energy.

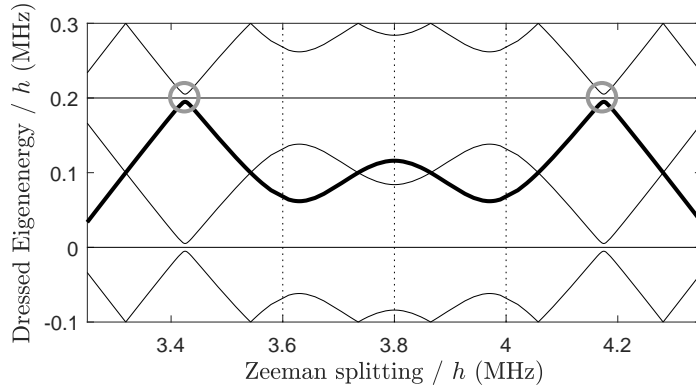


Figure 2.6: **A multiple-rf double-well potential:** A linear-polarised dressing field with three frequency components $\omega_i = 3.6, 3.8, 4.0$ MHz irradiates a ^{87}Rb atom in the $|F=1\rangle$ state. The rf resonances are indicated by vertical dotted lines. The eigenenergies are plotted as a function of the Zeeman splitting $g_F\mu_B B_0$, with a double-well eigenstate indicated by the bold line. Grey circles highlight avoided crossings from higher-order interactions (see text).

2.6 Multiple rf dressing

Dressing with multiple frequency components provides increased control over the dressed state eigenenergies. Each applied frequency is resonant with a different Zeeman splitting, thus multiple avoided crossings can be created and individually controlled with this technique [45]. We calculate eigenenergies using the Floquet method.

A double-well potential results from using three frequency components [21], with angular frequencies $\omega_1, \omega_2, \omega_3$ (see Fig 2.6). These are integer multiples of a common fundamental, $\Delta\omega$, which determines the periodicity of the system and thus the time propagation used for the Floquet calculation. The dressed eigenenergies have a ladder structure, with manifolds that repeat every $\hbar\Delta\omega$. In the dressed-atom picture this periodicity arises because the uncoupled states contain energy $E_{\text{rf}} = \sum_i n_i \hbar\omega_i$ in the radiation field, where $n_i \gg 1$ are the photon numbers in each field mode of angular frequency ω_i . The double-well potential occurs for those eigenstates with energy minima at the resonances with ω_1 and ω_3 . Increasing the amplitude of either frequency component drives the corresponding avoided crossing further apart, and so

increases the energy of the associated potential minimum. The barrier is formed by the dressing frequency ω_2 ; it is pushed lower as the amplitude of this component is increased, and for sufficiently high amplitudes the barrier flattens.

Additional weaker avoided crossings appear in the eigenenergies, occurring at resonances with sum and differences of the applied dressing frequencies. In the dressed-atom picture they arise through higher-order interactions between the atom and dressing field [46]. Their presence limits the depth of the double-well potential, as atoms with sufficient energy to reach these avoided crossings are lost from the trap. In the limit $\Delta\omega \rightarrow 0$ an infinite number of these higher-order processes cause loss throughout the potential.

2.7 Radiofrequency spectroscopy

Radiofrequency spectroscopy is a technique that is frequently used to calibrate magnetic fields, where addressable transitions between energy levels lie in the range of MHz [47]. It provides an accurate means to measure the magnitude of a static field, or the amplitude of an rf-dressing field.

In this method a sample of atoms are held within a magnetic trap and a weak rf probe of angular frequency ω_p is applied. The separation between the trapped and untrapped energy levels of an atom varies as a function of coordinates in the trap. When any of these transitions become resonant with the rf probe, the atom is ejected. After applying the probe, the number of atoms remaining is counted; this loss is measured for different probe frequencies, from which a resonance is observed.

Any method of confinement requires that potential energy change as a function of position. For neutral atoms this variation in potential energy is achieved through a spatial variation of the atom's energy level structure; for example, in a static magnetic field trap it is the spatial dependence of the Zeeman energy $m_F g_F \mu_B B_0(\vec{r})$ that pro-

vides confinement of the low-field seeking states. This structure also determines the separation between eigenenergies of trapped and untrapped states, thus the potential energy and transition frequencies at a point in the trap are related. This provides the foundation for rf spectroscopy; the potential energy determines the density distribution of atoms in the trap, which in turn determines the proportion of atoms resonant with an applied probe.

To discuss some qualitative features of rf spectroscopy we use the following simple model. We start with a pure condensate of chemical potential μ_0 and atom number N . The application of an rf probe at angular frequency ω_p drives atom loss at points in space where ω_p is resonant with any transition to untrapped states. We assume that all atoms with sufficient energy to reach the resonance are efficiently outcoupled from the trap, similar to Easwaran [47], and thus the application of the rf probe truncates the potential to a new depth E_{depth} . We assume the probe is applied for a long duration, allowing a new chemical potential to be established¹³, $\mu' = E_{\text{depth}}$. From the definition of the chemical potential of the Bose-condensed state, it follows that the new atom number N' obeys

$$\frac{N'}{N} \approx \left(\frac{E_{\text{depth}}}{\mu_0} \right)^{5/2} \quad (2.41)$$

It is further assumed that the rf probe is ‘weak’, such that the resonant surface on which loss occurs may be considered infinitely thin and the trapped eigenstate is not deformed by the probe’s application. We also neglect the fact that reducing N will change the condensate fraction, noting that the ‘cut’ may also cool the remaining atoms and that a high condensate fraction is seen on our experiment even for deep cuts. This model is illustrated in Fig 2.7.

We define $U(\vec{r})$ as the potential energy of a trapped atom in the state $|\tilde{m}_F\rangle = |1\rangle$

¹³As noted by Fernholz [48], atoms with sufficient velocity may diabatically transit the resonance, and thus remain trapped. We assume that over long durations the velocities and kinetic energies are randomised by collisions, leading to further loss until an equilibrium situation is reached.

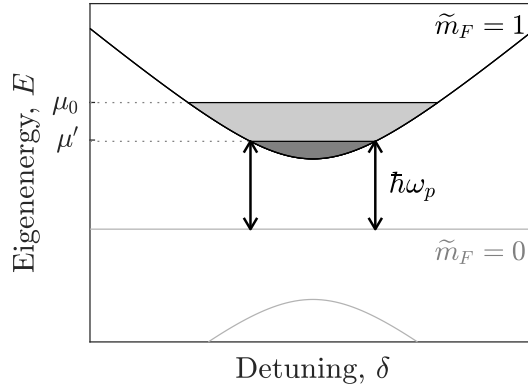


Figure 2.7: **The model used for rf spectroscopy:** Dressed energy levels for $F = 1$, plotted as a function of detuning δ along the z -axis. A condensate is initially trapped in the $\tilde{m}_F = 1$ state, depicted by the light filled region indicating the chemical potential μ_0 . Application of the rf probe at angular frequency ω_p truncates the potential, establishing a new chemical potential μ' (darker shaded region). The other dressed eigenstates $\tilde{m}_F = 0, -1$ are shown (light grey lines) to illustrate the transition.

at the point \vec{r} and $\omega_p = S(\vec{r})/\hbar$ as the corresponding angular frequency of a single-photon transition at this position. For motion along the z -axis of our adiabatic potential shell trap (and for the moment neglecting gravity)

$$S(z) = \hbar\sqrt{\Omega^2 + \delta(z)^2}, \quad \text{with } \delta(z) = 2g_F\mu_B B'z - \hbar\omega \quad (2.42)$$

$$U(z) = S(z) \quad (2.43)$$

where we have taken a transition corresponding to $\tilde{m}_F = 1 \rightarrow \tilde{m}_F' = 0$. Note that $S(z)$ does not go to zero at $\delta = 0$; the value of this local minimum is $S_{\min} = \hbar\Omega$.

2.7.1 Resonant frequency and linewidth

The resonant frequency is that which causes the greatest loss of atoms. For the stated transition in this example, the resonance occurs for $\omega_p = \Omega$, as we now discuss. Under the above assumptions, the final atom number is a minimum $N' = 0$ when the probe is resonant at the bottom of the potential $U(z)$, *ie* $\omega_p = \Omega$, allowing all atoms

to drain from the trap. Even for short probe durations, where some of the above approximations may not hold, the final atom number is a minimum for this probe frequency because the number density at the potential energy minimum is greatest and so a resonance here causes the greatest outcoupling of atoms.

For a BEC in an adiabatic potential, it would be reasonable to assume that the rf-resonance linewidth should be of order μ_0/h . For typical atom numbers and trap frequencies used in our investigation of MRF potentials [21], the chemical potential is of order $h \times 1$ kHz. The full-width half-maximum (FWHM) of the resonance occurs when $N'/N = 1/2$, corresponding to $E_{\text{depth}} = (1/2)^{2/5}\mu_0 \approx 0.75\mu_0$. For $U(z) = S(z)$ this trivially implies that the resonance FWHM corresponds to $0.75\mu_0/\hbar$. However, observed resonances are typically shifted and broadened by gravity, as we now discuss.

2.7.2 The effect of gravitational sag

When gravity is incorporated $U(z) \neq S(z)$. Instead,

$$U(z) = S(z) + mgz \quad (2.44)$$

This causes a shift in the resonant frequency. As the rf-dressed potential is approximately harmonic near the resonance $\delta = 0$, we take $S(z) \approx m\omega_z^2 z^2/2 + \hbar\Omega$. The gravitational sag shifts the minimum of $U(z)$ to a position $z_{\text{min}} = -g/\omega_z^2$, where g is the gravitational acceleration. As a result, the resonance is shifted by $\delta\omega_p = S(z_{\text{min}})/\hbar - \Omega = mg^2/2\omega_z^2\hbar$. For example, in our demonstration of multiple-rf dressed potentials, typical parameters are $\omega = 3$ MHz, $B' = 82$ G cm⁻¹ and $\Omega = 2\pi \times 200$ kHz [21]. The angular trap frequency is $\omega_z = 2\pi \times 290$ Hz, giving a corresponding shift in the resonance of $\delta\omega_p \approx 2\pi \times 3$ kHz.

Gravitational sag also broadens the resonance feature. Near the minimum of $U(z)$ there is a non-zero gradient in $S(z)$ of $\partial_z S(z) \approx mg$. The finite width of the cloud

Δz thus produces a first-order broadening of the resonance feature of approximately $\Delta\omega_p = mg\Delta z/\hbar$. For the previous example, where $\mu_0 = 1$ kHz, the Thomas-Fermi radius of the cloud is $\Delta z = 1.6 \mu\text{m}$; as a result, the resonance is broadened to $\Delta\omega_p = 2\pi \times 3.4$ kHz.

2.8 Conclusion

This chapter has presented an overview of the theory of an atom interacting with a combination of static and oscillating magnetic fields. We examined this situation from both semi-classical and fully-quantised pictures, and detailed specific features of the rf-dressed potentials that result when the static field is a spherical quadrupole field. This provides a theoretical foundation for understanding our experimental work to manipulate atoms in rf-dressed potentials. To conclude, we outlined a qualitative model to understand rf spectroscopy, which is a technique used to characterise these potentials at several points throughout this thesis.

Chapter 3

The experimental apparatus

All experimental work in this thesis was undertaken using the apparatus detailed in this chapter. As with many cold-atom experiments, our apparatus is a two-chamber design (see Fig 3.1). Atoms are collected in a Magneto-Optical Trap (MOT) using laser cooling, then transported to a high-vacuum glass cell where they are confined by a combination of static and oscillating magnetic fields and cooled by evaporation. Our apparatus can produce pure ^{87}Rb condensates, or cold thermal mixtures that also include ^{85}Rb .

This chapter begins with a complete description of the experimental sequence used to produce ultracold atoms (Sec 3.1), with a particular focus on the production of ^{85}Rb - ^{87}Rb mixtures that is new to this thesis. This is followed by a summary of the essential hardware components. These consist of a laser system to produce light for cooling atomic clouds of rubidium (Sec 3.2); coils and associated electronics to generate confining magnetic fields (Sec 3.3); and optical systems to image the atomic clouds (Sec 3.4). We conclude with the design and rewrite of the experimental control program, and the installation of interlocks and monitoring to achieve safe autonomous operation of the experiment.

Various aspects of this machine have been detailed in previous theses. Details of

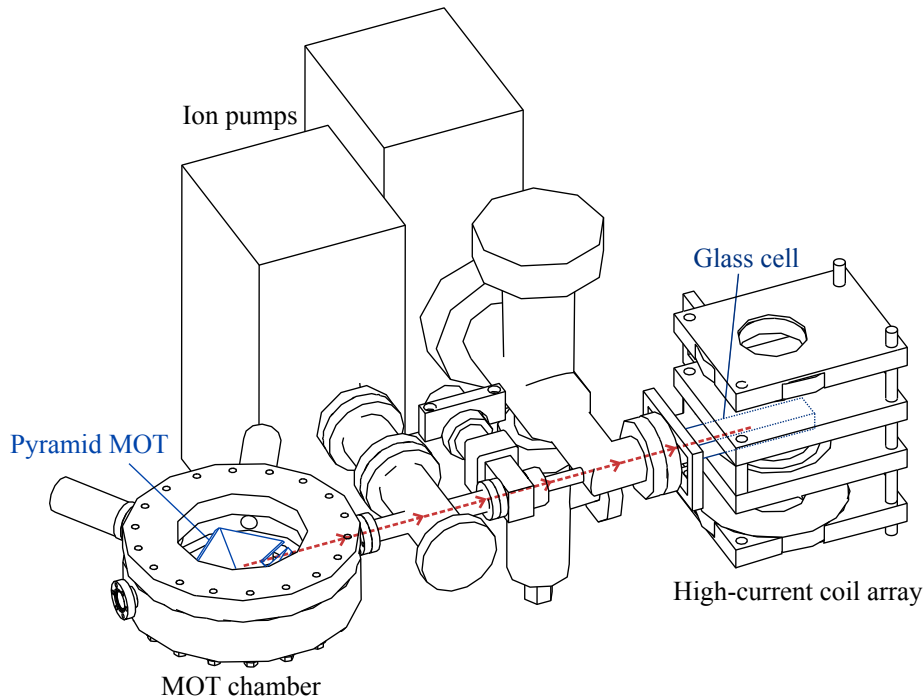


Figure 3.1: **The experimental apparatus:** A laser-cooled cloud of atoms is collected in the MOT, then transported to the glass cell for experimentation along the red, dotted path. The CAD model was originally created by Sheard [49].

the vacuum system, MOT and transport procedure are found in Sheard’s thesis [49]. Explanations of the Time-Orbiting Potential (TOP), Time-Averaged Adiabatic Potential (TAAP) and shell trap are in the theses of Gildemeister [28] and Sherlock [50], and additional details of the laser system are found in Harte’s thesis [22].

3.1 The experimental sequence

The progression of a typical sequence is described in the following sections. First, a cloud of laser-cooled atoms is collected in a MOT. These atoms are loaded into a magnetic trap, and transported to an ultra-high vacuum glass cell for experimentation. Forced rf evaporation cools the cloud, first in the quadrupole trap and subsequently in the TOP. Once the cloud reaches $\sim 1 \mu\text{K}$, it is loaded into rf dressed potentials for further evaporation and experiments. All sequences are written in Matlab using the

new experimental control program¹.

3.1.1 The magneto-optical trap (MOT)

Every experiment starts by collecting a cloud of laser-cooled atoms in the MOT. The design used here is a ‘pyramid’ configuration; a single vertical beam illuminates four mirrors arranged in a V-shaped square-based pyramid from above, and the reflection of light from the mirror surfaces produces the five other beam directions required to laser cool all axes of motion [51]. With only one incident beam, the Pyramid MOT is easy to align and the operation is more robust than a standard 6-beam MOT, but it is not possible to perfectly balance the powers of beams in each direction due to losses at the mirror surfaces. Further, the MOT is centered above one of the mirrors (and thus off-centre to the pyramid itself) to avoid the imperfect coating at the mirror edges. Details of the construction and alignment procedure are found in Sheard’s thesis [49]. Loading is monitored using a CCD camera, which collects light scattered from the fluorescing cloud to enable observation for diagnostic purposes and a calculation of atom number from the total fluorescence [52].

In single species operation the MOT loads 4×10^9 ^{87}Rb atoms in 20 s using light that is 22 MHz red-detuned from the cooling transition at a peak intensity of 10 mW/cm². Resonant repumping light is required to close the laser cooling cycle and prevent atoms from accumulating in states that are dark with respect to the cooling light; the intensities used are typically a few percent of the cooling light intensity. The rubidium pressure required for appreciable loading rates is maintained by running the dispensers at 4.2 A for six and a half minutes at the end of each day.

For dual-species operation cooling and repumping light is produced for both ^{85}Rb and ^{87}Rb . The ^{85}Rb light has significantly lower intensities², and only a small number

¹for future generations of experimentalists, exact specifications of all sequence timings and values are under version control in the ‘enterprisesequences’ git repository.

²It is created by frequency modulating the ^{87}Rb light, see Sec 3.2 for details.

of ^{85}Rb atoms (around 1×10^8) are collected in the MOT as a result. Their fluorescence signal is overwhelmed by that from the larger number of trapped ^{87}Rb atoms. Parameters for the ^{85}Rb MOT are therefore optimised under single-species operation with only ^{85}Rb cooling and repumping light present, by disabling the modulation and changing the offset locks to operate the cooling and repumping lasers on the ^{85}Rb transitions. We find it is necessary to operate at a frequency detuning of 11 MHz, which is smaller than the optimum for ^{87}Rb , and attribute this behaviour to the low intensity of the cooling light, which is approximately 1 mW/cm^2 , hence $I < I_{\text{sat}}$. The power broadening is therefore less than the typical conditions for ^{87}Rb , and the maximum scattering force that slows and captures atoms is enhanced more by a reduced detuning. Furthermore, the smaller number of ^{85}Rb atoms means that the cloud is less optically thick, and rescattering of light is less important.

3.1.2 Transporting the cloud of cold atoms

Very different pressures are required for loading the MOT and subsequent experiments in the glass cell. The first requires pressures of 10^{-9} mbar for acceptable MOT loading speeds, while the second demands an ultra low vacuum of 10^{-11} mbar to prevent background collisions from limiting the lifetime of trapped atoms. This pressure differential is maintained by a ~ 0.5 m low-conductance tube, along which atoms are transported using a combination of mechanical and magnetic methods as discussed previously [49, 50, 28].

The majority of this transit is performed by mechanical transport, using a magnetic trap formed by the MOT quadrupole coils that are mounted on the stage of a *Parker Hannefin 404 XR* transport rail. First, atoms must be loaded from the MOT into this magnetic quadrupole trap, but clouds in the MOT are diffuse due to photon rescattering within the cloud that produces an effective $1/r^2$ repulsion between pairs of atoms. This reduces the phase space density, which must be increased before

loading into the quadrupole trap to avoid heating. To do so, the detuning of the cooling beams is increased by 50 MHz over 50 ms, which decreases the atom-photon scattering cross-section (and thus rescattering rates) to achieve higher densities in a ‘compressed MOT’ (c-MOT) stage. The quadrupole gradient is ramped down to perform a few milliseconds of sub-Doppler cooling, and finally the repumper beam shuttered to allow the cooling light to optically pump atoms into the $|F = 1\rangle$ state over 1.5 ms. After rapidly ramping the quadrupole current from 0 A to 50 A over 1 ms the transport-mounted quadrupole trap is loaded [28].

The optical pumping of ^{87}Rb into the $|F = 1\rangle$ level is not perfect, and a small fraction of atoms remain in the $|F = 2\rangle$ level. Later stages of rf evaporation preferentially remove $|F = 1, m_F = -1\rangle$ atoms (over $|F = 2, m_F = 2\rangle$ atoms) because the applied weak rf field is resonant at a lower potential energy [53]. The sympathetically cooled $F = 2$ population is barely depleted, and towards the end of the evaporation sequence it adds a significant heat load to the evaporation of $F = 1$ atoms, reducing the final atom number in the BEC. To prevent this, these $F = 2$ atoms are removed by illuminating the cloud with cooling light from the imaging probe beam for 60 ms after transporting to the glass cell. This step became necessary after optimisations decreased the total duration of rf evaporation from 2 min to 30 s. Presumably, during the previous longer evaporation ramps the $F = 2$ atoms were lost through inelastic collisions before the critical final stages of evaporation.

The mechanical rail translates the quadrupole trap to ferry atoms along the transport path, and they exit the pyramid MOT through a small notch cut in the mirrors. The motion is performed quickly to minimise atom losses due to collisions with background vapor. To navigate obstacles along the transport path, such as the mirrors or sides of the differential tube, the cloud is laterally steered using a coil mounted to the side of the transport (‘transport push’). The burst of high current in both MOT and transport push coils each sequence causes heating, but given the 1 min sequence

time the duty cycle is low enough that air cooling from an array of fans is sufficient, and the coils equilibrate around 40 °C.

The mechanical transport travels 80% of the full distance to the glass cell, but the vertical imaging system prevents overlaying the transport quadrupole with that of the high current coils at the glass cell. The remainder is completed by magnetic transport, where the high-current Push, Auxiliary and Quadrupole coils are switched to adiabatically transfer the trapped cloud from the transport quadrupole coils to the center of the glass cell [49].

When ^{85}Rb is present, these various stages of transport occur simultaneously to those of ^{87}Rb ; ^{85}Rb atoms are subjected to the same magnetic fields, sweeps of the cooling light detuning and timings that are optimised for the ^{87}Rb cloud. The initial feasibility of these sequences for ^{85}Rb was proven by locking the cooling and repumping ECDLs to the ^{85}Rb transitions without modulation, and transporting a pure ^{85}Rb MOT to the glass cell using the standard sequence devised for ^{87}Rb . The transport is not optimised to reduce heating of the ^{85}Rb atoms, which have a negligible heat capacity compared to the much larger ^{87}Rb clouds that they are in thermal contact with. The extremely efficient sympathetic cooling of ^{85}Rb by ^{87}Rb (see below) means that a high initial ^{85}Rb atom number is not required after transport.

3.1.3 Magnetic quadrupole trap

The transport procedure loads $\sim 10^9$ atoms into the magnetic quadrupole trap at the glass cell at a temperature that is hundreds of μK . The potential energy of an atom in this trap is

$$U_{\text{quad}} = m_F g_F \mu_B |B'| (x\vec{e}_x + y\vec{e}_y - 2z\vec{e}_z) \quad (3.1)$$

where the quadrupole gradient B' is generated by the current flowing through the high-current quadrupole coils. The potential depth is large and thus well-suited to these initial hot clouds. Evaporative cooling using a weak rf field begins in this potential and the quadrupole gradient is increased to the maximum field gradient $B' = 375 \text{ G cm}^{-1}$ to compress the cloud and thus maximise the elastic collision rate. The evaporative rf probe drives loss when the rf field is resonant with the Zeeman splitting, $\hbar\omega = g_F\mu_B|B|$, and is used to remove atoms with much greater energy than the average of the ensemble. It is turned on at a frequency of 120 MHz and swept down to 18 MHz over 12 s, producing $\sim 50 \mu\text{K}$ clouds of 5×10^7 atoms. At lower temperatures the evaporation becomes inefficient due to (Majorana) spin-flip losses that occur near the centre of the quadrupole [2, 41], the rate of which increases for colder clouds. Further evaporation must take place in the TOP trap.

3.1.4 The time-orbiting potential (TOP) trap

The TOP trap is formed by a combination of a static quadrupole field and a bias field that rotates in the horizontal plane³, of the form

$$\vec{B}_{\text{TOP}} = B_{\text{TOP}} [\cos(\omega_{\text{TOP}}t)\vec{e}_x + \sin(\omega_{\text{TOP}}t)\vec{e}_y] \quad (3.2)$$

The rotation rate $\omega_{\text{TOP}}/2\pi = 7 \text{ kHz}$ is less than the Larmor frequency of atoms in the field B_{TOP} , so that the atomic states adiabatically follow the field, but faster than the atomic motion so that atoms experience the time-averaged harmonic potential given by [54]

$$U(x, y, z) = m_F g_F \mu_B \frac{(B')^2}{4B_{\text{TOP}}} (x^2 + y^2 + 8z^2) \quad (3.3)$$

³This type of trap was one of the first used for successful BEC production [1]

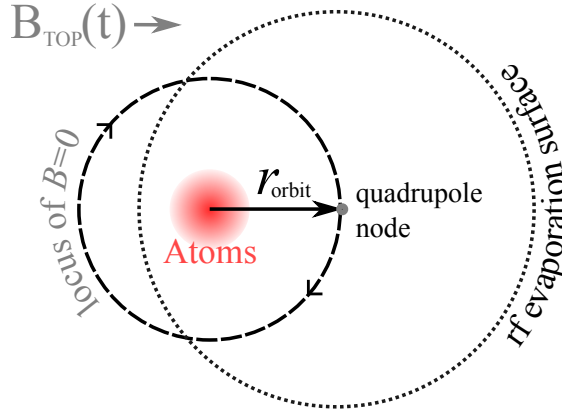


Figure 3.2: **The TOP trap:** A rotating bias field displaces the quadrupole node in an orbit around the cloud of atoms. Loss occurs for atoms that intersect this path, called the ‘circle of death’. Evaporation is performed by applying a weak rf field, which ejects atoms at the resonance (dotted black line, ‘evaporation surface’). The radius of the resonant spheroid evaporation surface decreases as the rf frequency is lowered during the evaporation ramp.

This results in oscillation frequencies of

$$\omega_x^2 = \omega_y^2 = m_F g_F \mu_B \frac{(B')^2}{2mB_{\text{TOP}}}, \quad \omega_z^2 = 8\omega_x^2 \quad (3.4)$$

The rotating bias field displaces the node in the quadrupole field away from the potential minimum, preventing spin-flip losses which would otherwise occur in colder clouds so that evaporation can proceed to BEC at ~ 100 nK temperatures. The node orbits in the horizontal plane at a radius $r_{\text{orbit}} = B_{\text{TOP}}/B'$ (see Fig 3.2). Atoms at positions that lie along this orbit (the so-called ‘circle of death’) are lost through the spin-flip mechanism, imposing a potential depth to the TOP trap of

$$U = (r_{\text{orbit}}, 0, 0) = \frac{1}{4} m_F g_F \mu_B B_{\text{TOP}} \quad (3.5)$$

Before loading the TOP trap from the quadrupole trap, the cloud is first adiabatically decompressed by reducing the quadrupole gradient to 48 G cm^{-1} to improve the

mode-matching between the quadrupole and TOP potentials⁴. The TOP field ramps up to $B_{\text{TOP}} = 17 \text{ G}$ over 0.3 s; this period is kept short to minimise atom loss as the quadrupole node spirals outwards through the cloud. The weak rf field is turned on to resume evaporation, cutting from an initial frequency of 28 MHz to 6.5 MHz over 11 s to produce a BEC of 2×10^5 atoms⁵. As the ramp proceeds the harmonic trap frequencies are tightened to further increase the elastic collision rate by increasing the quadrupole gradient to 262 G cm^{-1} and decreasing B_{TOP} to 7.5 G. The measured heating rate for a BEC in the final trap is 40 nK s^{-1} at 100 nK, and the lifetime is limited by the background vacuum pressure.

For the investigation in Chapter 6 it is important that the anisotropy of the TOP fields is known. When the amplitudes of the TOP field in the \vec{e}_x and \vec{e}_y directions (B_x and B_y) are equal the potential has cylindrical symmetry and the frequencies f_x and f_y are degenerate. The anisotropy in these fields determines the ratio of the trap frequencies along the \vec{e}_x and \vec{e}_y axes, with $B_y/B_x \approx f_x^2/f_y^2$ for small anisotropy, and we therefore determine the imbalance by performing frequency measurements. The vertical imaging system is used to simultaneously observe motion along the \vec{e}_x and \vec{e}_y axes of a BEC that is initially kicked by a short pulse of magnetic field from the Push coil. The amplitude of oscillation is small to reduce the effect of anharmonicity in the trap. The magnitude of the rotating field B_{TOP} can be characterised through rf spectroscopy, because the Zeeman splitting at the potential energy minimum is equal to $E = g_F \mu_B B_{\text{TOP}}$, but even for a BEC in a balanced TOP with $B_x = B_y$ the resonance is broadened by the finite size of the condensate, the quadrupole gradient and gravitational sag (as discussed in Sec 2.7 in the context of rf-dressed potentials).

When using two species, the field magnitude is more precisely determined using the

⁴some heating during loading is unavoidable due to the inherent difference between the initial (linear) and final (harmonic) potential.

⁵Previously, the initial TOP evaporation used the ‘circle of death’ to evaporate hot atoms by adjusting the potential depth as a function of time. However, we found that the spin-flip loss mechanism outcouples atoms too slowly from hotter clouds, and all evaporative loss now proceeds using the faster outcoupling of the rf evaporation.

positions of ^{85}Rb and ^{87}Rb in the Species-Selective TAAP (SSTAAP) scheme.

3.1.5 Sympathetic cooling

During dual-species evaporation, a small number of ^{85}Rb atoms are sympathetically cooled by the surrounding ^{87}Rb thermal cloud. The weak rf field used to evaporate atoms preferentially ejects ^{87}Rb atoms in the state $|F, m_F\rangle = |1, -1\rangle$, with $g_F^{87} = -1/2$, over those of ^{85}Rb $|2, -2\rangle$, with $g_F^{85} = -1/3$; the resonance between the applied rf and the atomic Zeeman splitting occurs at a lower potential energy for ^{87}Rb than for ^{85}Rb , and with both species in good thermal contact it is predominantly ^{87}Rb atoms of higher than average energy that are removed during the rf frequency sweep. Sympathetic cooling between these species has been demonstrated previously [55, 56, 57]. Even for experiments that ultimately use pure ^{85}Rb samples after evaporation, sympathetic cooling provides a means to overcome a zero in the ^{85}Rb - ^{85}Rb s -wave scattering length that occurs for collision energies of 300 μK and otherwise prevents direct evaporation without exploiting a Feshbach resonance [58, 55, 59].

Good thermal contact between the two species is essential for sympathetic cooling. This requires a physical overlap of the two thermal clouds and a reasonable value for the inter-species s -wave scattering length, here $\sim 250 a_0$ [58]. In the TOP trap each species has different harmonic trap frequencies and thus gravitational sag. The clouds cease to overlap when the difference in their sag is comparable to the width of the thermal cloud, which reduces the thermal contact and thus the effectiveness of sympathetic cooling. For our typical TOP trap parameters this occurs in the TOP at a temperature of 300 nK. In addition, the inelastic loss rate must be low, as is the case for these two species in static magnetic fields (see Chapter 6).

An example trajectory of evaporation is shown in Fig 3.3, alongside the ^{87}Rb -only BEC trajectory. Initially the atom numbers of each species obey $N_{87} \gg N_{85}$, and the evaporation of ^{87}Rb proceeds much the same as when the ^{85}Rb is absent.

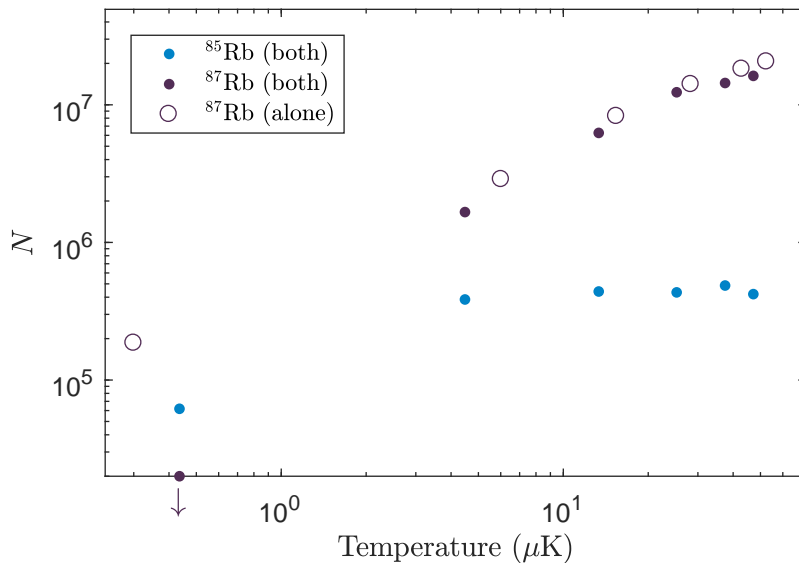


Figure 3.3: **Sympathetic cooling in the TOP:** A comparison of evaporation trajectories for $^{85}\text{Rb} + ^{87}\text{Rb}$ and ^{87}Rb alone. The atom number of both species is plotted as a function of the temperature, which decreases as the evaporation proceeds. The atom number and temperature for each species is measured using resonant absorption imaging, and either only ^{85}Rb or only ^{87}Rb can be observed in a single experimental sequence. For ^{87}Rb alone the same evaporation ramp produces a BEC of 2×10^5 atoms.

Sympathetic cooling is highly efficient in this regime, and almost no ^{85}Rb atoms are lost over an order-of-magnitude change in temperature. As the ^{87}Rb atom number is reduced to that of ^{85}Rb , the heat capacities of the ^{85}Rb and ^{87}Rb thermal clouds become comparable, causing evaporation to become inefficient with respect to loss of ^{87}Rb atoms, *ie* requiring ejection of a greater number of ^{87}Rb atoms for the same fractional decrease in temperature. Ultimately, for a sufficiently large initial number of ^{85}Rb , the ^{87}Rb is completely depleted leaving only a cold ^{85}Rb sample. The final temperature at which this occurs decreases as N_{85} decreases, because of the lower heat load imposed on the ^{87}Rb bath. For extremely low initial numbers of ^{85}Rb , it is possible to cool ^{87}Rb below the BEC transition temperature before this happens [59]. Once the supply of ^{87}Rb is exhausted, the rf field continues to cut into the ^{85}Rb distribution and cause ^{85}Rb atom loss.

3.1.6 Radiofrequency-dressed potentials

Most experimental work in this thesis uses rf-dressed potentials. We detail the following sections for ^{87}Rb atoms only; the implications of having two species are discussed in Chapter 5.

3.1.7 The time-averaged adiabatic potential (TAAP) trap

The TAAP time-averages the rf-dressed shell trap using a low frequency magnetic field [40], here the TOP field rotating in the horizontal plane. The resulting potential resembles a vertical double well⁶, with each well located at the intersection of the resonant spheroid and the rotation axis [61]. Although in principle the potential energies of these wells can be balanced, for all of this work atoms are deliberately loaded into the lower well and we henceforth neglect the upper well. The harmonic trap frequencies, shown in Fig 3.4, are determined by the amplitude of the dressing rf field, the quadrupole gradient and the magnitude of the rotating field B_{TOP} . In the limit $B_{\text{TOP}} \gg \hbar\omega/g_F\mu_B$ they approach the harmonic frequencies of the TOP trap, and when $B_{\text{TOP}} = 0$ they equal those of the shell trap.

The TAAP is used to adiabatically load atoms into rf dressed potentials from the TOP trap, as illustrated in Table 3.1 and discussed in Gildemeister’s thesis [28]. The rf field of angular frequency ω is turned on when $B_{\text{TOP}} > \hbar\omega/g_F\mu_B$, such that the quadrupole node’s radius of orbit is larger than the horizontal semi-axis of the resonant spheroid; thus the resonant spheroid orbits far from the atom cloud. Atoms are projected from the state $|F = 1, m_F = -1\rangle$ in the TOP to the dressed state $|F = 1, \tilde{m}_F = 1\rangle$ with less than 10% atom loss. The similarity of harmonic trap frequencies between the TOP and TAAP at large B_{TOP} prevents heating. Reducing B_{TOP} decreases the radius of orbit, until the resonant spheroid intersects the cloud

⁶Time averaging the rf-dressed potential in different ways achieves different trapping geometries, *eg* a ring trap [60].

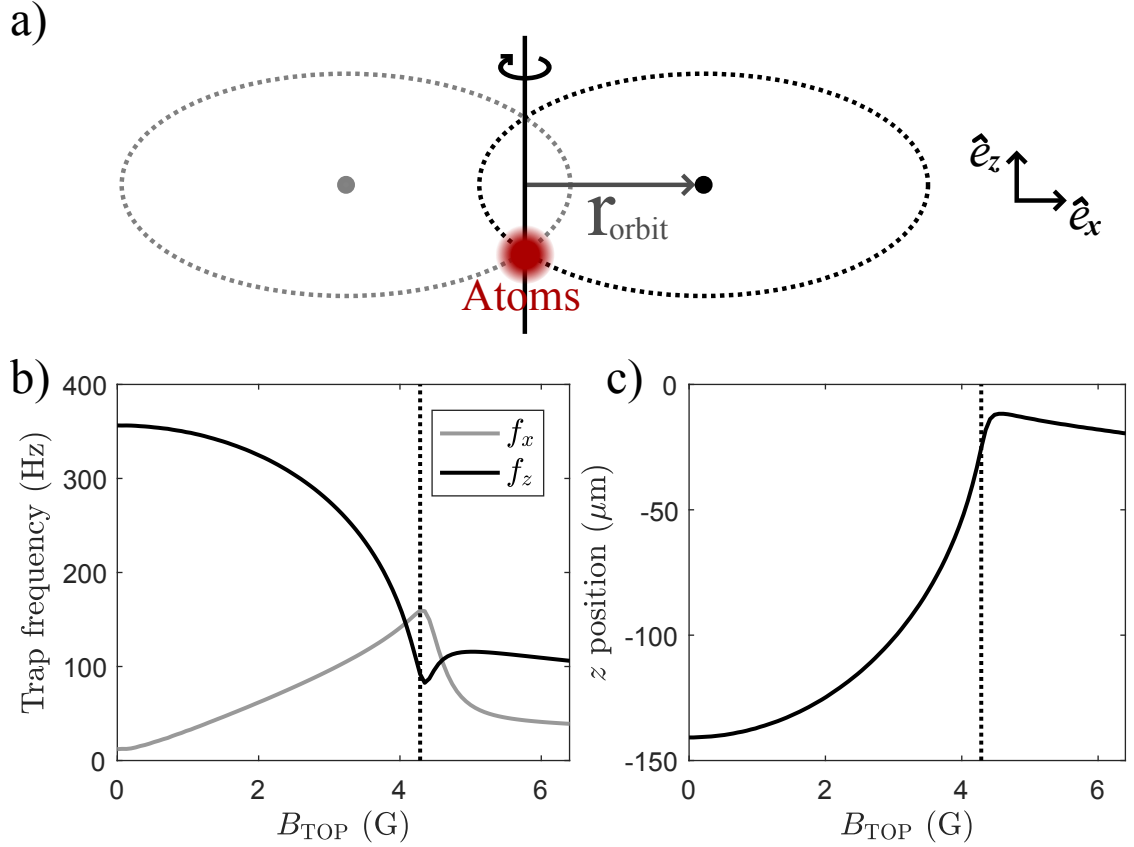


Figure 3.4: **The TAAP trap:** **a)** An illustration of the TAAP. The resonant spheroid (black, dotted) is swept in an orbit of radius r_{orbit} around the vertical axis by the time-averaging TOP field, and atoms are trapped at the lower intersection of the spheroid with the rotation axis. A light grey dotted line shows the spheroid's position after half a rotation of the bias field. **b)** Harmonic trap frequencies in the TAAP and **c)** vertical position of the potential minimum as a function of B_{TOP} . The vertical dotted line marks the resonance $g_F \mu_B B_{\text{TOP}} = \hbar \omega$ where the spheroid touches the vertical axis. The calculations are for a 3 MHz dressing field, of magnitude 0.57 G and quadrupole gradient $B' = 150 \text{ G cm}^{-1}$.

Regime	Schematic	Eigenenergies
TOP		
TAAP, $g_F\mu_B B_{\text{TOP}} > \hbar\omega$		
TAAP, $g_F\mu_B B_{\text{TOP}} = \hbar\omega$		

Table 3.1: **Loading the TAAP:** The **Schematic** column depicts the orbit (dashed) of the quadrupole node (black dot), the position of the atom cloud (red) and the resonance with the dressing rf field (black, dotted). Light grey lines show the node and resonance half a rotation period later. The **Eigenenergies** column depicts atomic eigenenergies as a function of x in solid lines. Atoms are trapped on the eigenstate highlighted with a thick line, and the rotation axis is depicted by a solid vertical line. Other colors and line styles are consistent with the schematic panel. See text for explanation. Quadrupole field gradient is $B' = 100 \text{ G cm}^{-1}$, $\omega = 2\pi \times 3 \text{ MHz}$.

when $g_F \mu_B B_{\text{TOP}} = \hbar \omega$, loading atoms into the TAAP potential minimum.

We typically load atoms into the TAAP at temperatures of 1 μK to 2 μK . Large rf amplitudes $B_{\text{rf}} = 0.57 \text{ G}$ (corresponding to Rabi frequencies of 400 kHz at the bottom of the resonant spheroid) are used to reduce losses from nonadiabatic following of atoms over the avoided crossing. Further evaporation to BEC is performed in the TAAP rather than the shell to exploit the higher geometric mean trap frequency which gives a higher elastic collision rate. As in the TOP trap a weak rf field is applied, driving transitions between dressed states to eject atoms with higher than average energy [47]. This typically uses a sweep from $f = (\omega/2\pi + 1.5 \text{ MHz})$ to $f = (\omega/2\pi + 0.5 \text{ MHz})$ over 2 s, creating a BEC of $\sim 1.5 \times 10^5$ atoms.

The TAAP is always loaded using a dressing field that is circularly polarised about \vec{e}_z to maximise the coupling strength at the bottom of the shell. A node of vanishing coupling strength is located at the top of the resonant spheroid, and thus always far removed from the atoms.

3.1.8 Shell trap

The shell is adiabatically loaded from the TAAP by ramping $B_{\text{TOP}} \rightarrow 0$, confining atoms on the surface of the resonant spheroid. Under the influence of gravity they accumulate at the bottom, and experience a highly anisotropic potential with weak radial confinement (10s of Hz) and strong vertical confinement (100s of Hz). The characteristics of this potential were examined in Sec 2.5.

An accurate calibration of the rf fields is required for the work in this thesis. The dressing field amplitudes produced by each \vec{e}_x and \vec{e}_y coil pair are determined using rf spectroscopy, with each coil pair measured separately to remove cross talk. After loading a shell dressed with circularly-polarised rf the amplitude of one pair is ramped to zero over 200 ms, leaving a BEC confined by a linearly-polarised rf field

that is radiated from the remaining coil pair⁷. During these measurements we also record the amplitude of the voltage induced in a pickup coil, calibrating it for use as a measure of rf amplitude. As there is some ambiguity as to which rf transition was driven during rf spectroscopy, we perform trap frequency measurements to confirm the amplitude of the rf-dressing field.

Producing a circularly-polarised rf field requires the correct phase ϕ_y between \vec{e}_x and \vec{e}_y coils to be known. It is determined by observing the number of atoms remaining in the shell trap after loading and holding for a long duration (typically 20 s), for different phase differences ϕ_y between the x and y dressing rf sources. The number remaining depends on three considerations:

1. The number initially loaded from the TAAP; ellipticity in the rf field reduces the minimum coupling strength around the equator of the resonant spheroid, and thus that experienced by the atoms during a full period of the rotating B_{TOP} field. An imperfect phase decreases the number of atoms loaded due to increased non-adiabatic loss. No atoms are loaded for $\phi_y = 0$ or π , as these linearly polarised fields have a node of coupling strength on the equator.
2. The lifetime of atoms in the shell due to non-adiabatic following, which is maximised for circular polarisation with the coupling strongest at the bottom of the shell.
3. The presence of rf noise, which reduces the lifetime if resonant with transitions to untrapped dressed states. The transition frequencies depend on the Rabi frequency, which is a function of phase ϕ_y but also symmetric about a maximum value $\phi_y = \pi/2$ when the rf-dressing field is circularly polarised.

All of these contributing factors are symmetric about $\phi_y = \pi/2$. The circular polarised phase is identified from this point of symmetry in the measured remaining

⁷The quadrupole gradient is also decreased to keep ω_z constant.

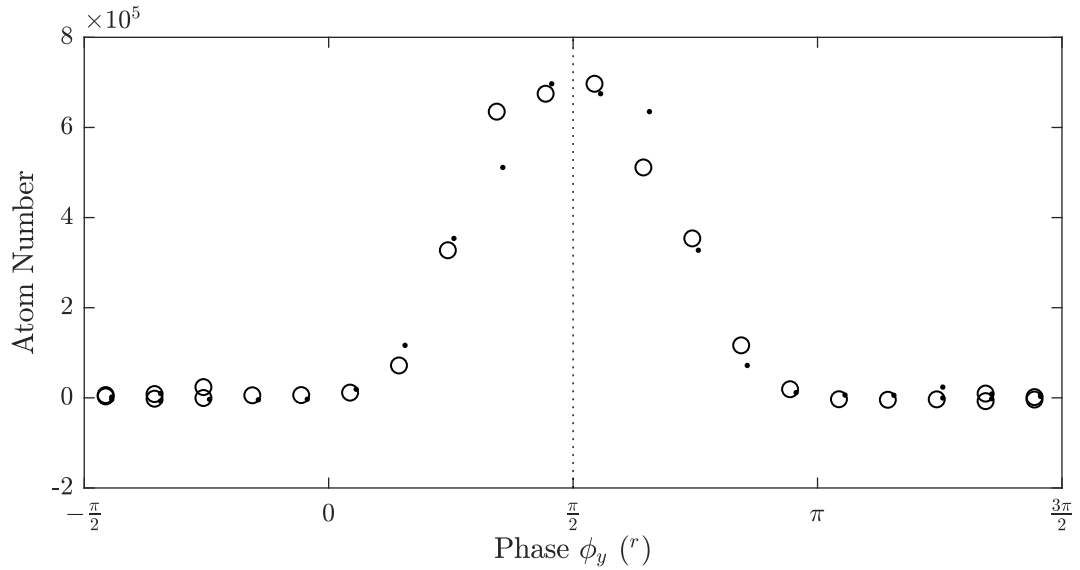


Figure 3.5: **Determining the phase required to produce a circularly-polarised rf-dressing field:** Atom number remaining after loading the shell trap and holding for a duration, as a function of the phase ϕ_y . Both circles and dots are the same data, reflected through the line $\phi_y = \pi/2$ to show the symmetry.

atom number (see Fig 3.5).

Having explained the different stages involved in a typical sequence we now examine the individual systems that comprise the apparatus.

Name	Transition	Detuning from reference (GHz)
^{85}Rb Cooling	$F = 3 \rightarrow F' = 4$	1.126
^{87}Rb Cooling	$F = 2 \rightarrow F' = 3$	0
^{85}Rb Repumper	$F = 2 \rightarrow F' = 3$	4.042
^{87}Rb Repumper	$F = 1 \rightarrow F' = 2$	6.568

Table 3.2: **Required optical frequencies for dual-isotope operation:** Frequency detunings are given relative to the ^{87}Rb cooling transition, and determined from published reference values [52].

3.2 The laser system

A robust laser system is an essential component of a reliable BEC apparatus. Laser light of the correct frequency and sufficient amplitude is essential to collect atoms in the MOT and image the atomic distributions at the end of an experimental sequence.

The following specifications are required of the laser system used for our dual-isotope experiments. First, the production of light at frequencies corresponding to the cooling and repumping transitions for each species (see Table 3.2), with precise control over the detunings and a linewidth much smaller than that of the transitions (6 MHz [52]). For each species, the cooling light must be at, or near, resonance for absorption imaging, red-detuned by 22 MHz (for ^{87}Rb) or 11 MHz (for ^{85}Rb) during the MOT, and swept over 50 MHz to compress the MOT before transport. The amplitude must be sufficient to collect a large number of atoms in the pyramid MOT, typically 400 mW entering the vacuum chamber. To image the final clouds, light pulses must be switched at microsecond timescales. Finally, during dual-species operation light for both species must be produced simultaneously to load both isotopes into a MOT.

The previous iteration of our laser system fulfilled these criteria for single species experiments with ^{87}Rb . Two external-cavity diode lasers (ECDLs) were locked to the cooling and repumping transitions, and the required frequency detunings of the cooling light were achieved by double-passing the light through two AOMs in series, first red-shifting the frequency of the light, then blue-shifting [22]. In general this arrangement performed well, but losses incurred during the double pass required the use of additional injection-locked ‘slave’ lasers, and the range of accessible frequency detunings was limited by the bandwidths of the AOMs to about 60 MHz⁸. It was not possible to scan either ECDL to the ^{85}Rb transitions, nor was it possible to produce light to simultaneously laser cool both isotopes.

⁸Additionally, some change in alignment of the seed beam for the injection-locked lasers was inevitable as the AOM frequency was swept. The laser mode-hop free tuning range required reduced the long-term stability of the apparatus.

A block diagram of the current system is shown in Fig 3.6. One ECDL is locked on resonance with the ^{87}Rb cooling transition to provide a frequency reference (Sec 3.2.1), against which two other ECDLs are offset locked via beat note detection (Sec 3.2.2). The beat note frequencies are tunable over several GHz to provide light resonant with the cooling and repumping transitions of either species and perform frequency sweeps of the light, while the large offset lock error signal and recapture range gives stable operation. When laser cooling of two isotopes is required, the lasers are locked to the ^{87}Rb transitions and light for exciting transitions in ^{85}Rb is produced as sidebands by current modulation of two injection-locked diode lasers (Sec 3.2.3). The combined cooling and repumping light is amplified by a Tapered Amplifier (TA) to provide sufficient intensities for the MOT. Unmodulated ^{85}Rb cooling light for imaging is sourced from the cooling ECDL by changing the frequency of the offset lock.

The layout is modular with each optical breadboard serving a specific role, and linked by optical fibres to decouple each layout. This makes the layout extensible, reconfigurable and the system easier to understand. For example, since concluding the work with ^{85}Rb the injection-locked repumping slave laser was no longer required and has been bypassed to simplify the layout. Future upgrades can be connected quickly or interchanged with minimal downtime.

3.2.1 The reference laser

A *Toptica DL Pro* ECDL is used to provide a stable reference from which all other laser frequencies are offset. It is locked to the ^{87}Rb cooling transition using modulation transfer spectroscopy (MTS), a sub-Doppler spectroscopy technique with the advantages of a large error signal ($\sim 2\text{ V}$ in this work) with a steep gradient and flat background [62]. Furthermore, the signal is dominated by closed transitions which makes it easy to isolate a unique locking point. In contrast, techniques like frequency-modulation spectroscopy give a signal for each allowed transition between hyperfine

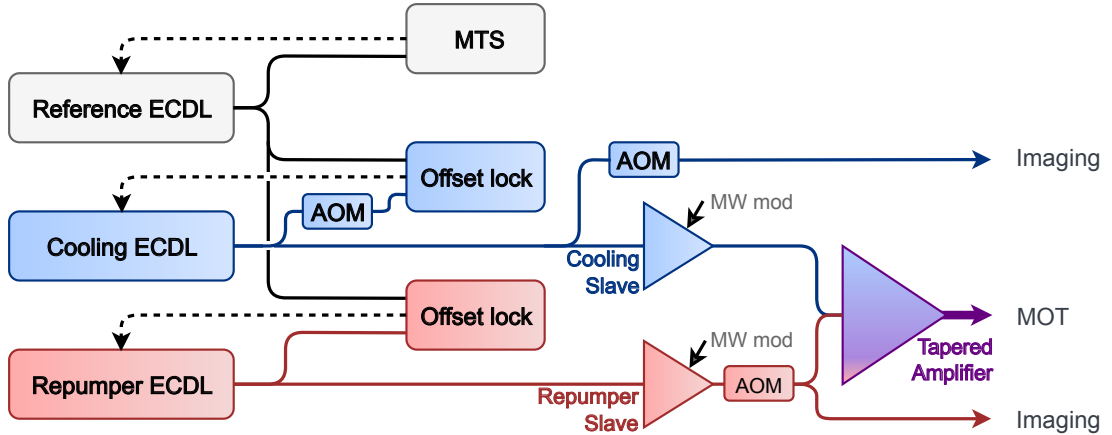


Figure 3.6: **Functional block diagram of the optical layout:** Light propagates from left to right along the solid lines. Dotted lines indicate feedback to stabilise the frequency of an ECDL.

levels, and hence a crowded spectrum. The MTS signal arises from a non-linear interaction of the probe beam and a modulated pump beam that is mediated by atoms in a vapour cell. A four-wave mixing process creates sidebands on the probe, and a photodiode measures the beat note between the probe and sidebands that oscillates at the modulation frequency. The in-phase and quadrature components of the signal provide a measure of absorption and dispersion arising from the optical transitions [63].

In our setup, the pump laser beam is modulated at 10.15 MHz using a *Photonics Technology 1015* EOM. The beat note phase is extracted from the photodiode signal using a home-built lock-in amplification scheme [28]. The error signal is input into a *Toptica Digilock 110* PID module which provides feedback to servo the voltage applied to the ECDL's grating piezoelectric via a *Toptica SC 110* module, stabilising the laser output frequency. The *Digilock* unit is controlled through a computer which enables remote operation and relocking. When locked the laser has a linewidth of 180 kHz, determined from the root mean square of the error signal, which is sufficiently small compared to the 6 MHz linewidth of the relevant transitions.

Light is distributed from the frequency-stabilised ECDL to the two offset lock

units. As the power requirements for the offset locks are low the laser diode is run at a lower current to extend the lifetime.

3.2.2 Microwave offset locks

Two offset locks were constructed to increase the versatility of the laser system for the dual-species work. In addition, this locking technique provides greater stability of the apparatus; the large error signal discourages the lasers from leaving lock, while the large recapture range ensures continued operation even if they do. In future, this arrangement can be used to provide light with a frequency detuning of many GHz for non-destructive imaging methods such as those in refs [64, 65].

An offset lock servos a laser's output frequency to maintain a fixed detuning from a reference laser. When light from both lasers is directed onto the same photodiode, interference causes the light intensity to beat at their frequency difference. In this experiment, the \sim GHz beat note frequencies are detected using high bandwidth photodiodes and measured using digital microwave techniques.

At the heart of each offset lock lies a phase-frequency discriminator (PFD), which compares two oscillating signals and outputs a signal that depends on their frequency difference. A simple illustration of how these detectors work is shown in Fig 3.7. Two signals of frequencies f_A and f_B are input into the PFD, and a rising edge on either signal causes the corresponding charge pump to deliver a pulse of current. One pump charges the output capacitor, while the other discharges it. If $f_A = f_B$ then the signal A causes pulses that load charge onto the capacitor as frequently as B removes it. The phase difference between the signals A and B determines the fraction of time that the charge remains on the output capacitor, and thus the output voltage V_{out} when time-averaged is proportional to the phase difference, θ . If $f_A \neq f_B$ then the capacitor is either more often discharged (when $f_A < f_B$) or more often charged ($f_A > f_B$), and the output voltage rails either positive or negative depending on the

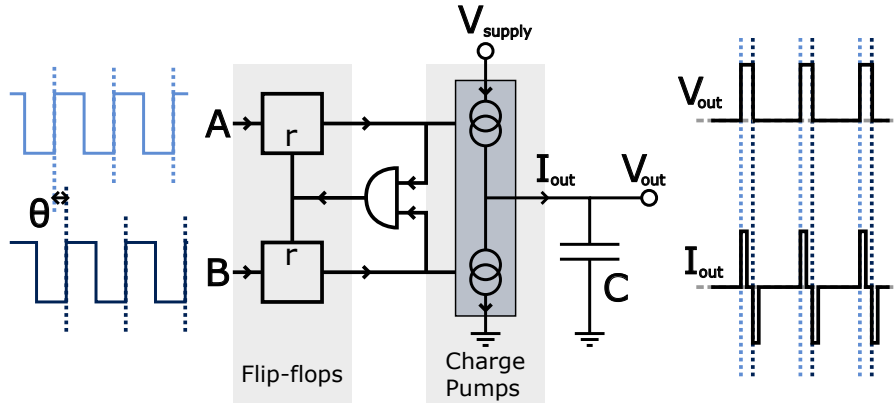


Figure 3.7: **Principles of a digital PFD:** Two signals A and B are incident on the PFD. See text for an explanation. Schematic adapted from reference [66].

sign of $(f_A - f_B)$; thus the device also functions as a frequency comparator.

The bandwidth of a PFD is typically limited to ~ 100 MHz. To work at microwave frequencies the input signal is frequency-divided using a fast digital counter, thus converting GHz input signals into the MHz frequency range. For added flexibility, the division ratio can differ between the two input signals, as is the case here; the beat note frequency is divided by an integer N using a high-speed prescaler and two digital counters [66], while a third counter divides a reference frequency f_{ref} by the integer R . We use $N \gg R$, which allows microwave beat notes to be compared to signals from inexpensive and agile MHz waveform generators.

An overview of the repumping and cooling offset lock components and specifications are given in Table 3.3. Both home-built lock units accept fibre-coupled light from the reference and slave lasers via fibre-to-fibre ports on the front panel, and light is internally combined using a fibre-coupled beam-splitter before illuminating a fibre-coupled photodiode. The use of fibre-coupled optics here is compact, but also practical; there are fewer degrees of freedom, and the fibre ensures both sources are spatially mode-matched onto the photodiode to maximise the detected beat note signal. Both sources must have the same polarisation when illuminating the photodiode to produce interference. The first unit constructed (repumping laser) used a PM

beam-splitter, although we have since observed reliable operation using a cheaper non-PM component for the cooling laser. The higher frequency repumping laser beat note is detected using a ~ 9 GHz bandwidth integrated photodiode (*D2-160*) that outputs an amplified and digitised signal. The cooling light has a lower bandwidth requirement; a Thorlabs *DET025AFC/M* biased Silicon detector is used, which is AC-coupled with a *ZX85-12G-S+* bias tee, and boosted with two *ZX60-3018G-S+* low noise-amplifiers.

The implementation of our feedback loop most closely follows that of Appel [67], though useful information can also be found in references [68, 69]. Beat note frequency division and comparison is performed by a PLL integrated circuit that is mounted in an *EV-ADF411XSD1Z* evaluation board. The on-chip registers that determine the division ratios N and R are programmed using the *SDP-S* USB connector board and the accompanying evaluation board software, and the offset locks are operated with a fixed frequency division ratio N/R . The target beat note frequency is equal to $f_{\text{beat}} = N/R \times f_{\text{ref}}$, and when required we manipulate f_{beat} by changing f_{ref} .

The output from the charge pump of the PLL integrated circuit is filtered and integrated to produce a feedback signal to servo-control the grating piezoelectric and current of the slaved ECDL. We emphasise that the PFD output can only update as fast as the divided reference signal, thus f_{ref}/R provides a ceiling that the bandwidth of the lock cannot exceed⁹. To achieve high bandwidth locking it is therefore preferable to use high reference frequencies and to minimise R . The choice of f_{ref} here is limited by the 20 MHz bandwidth of the waveform generator, and high frequency components of the feedback signal must be attenuated to prevent oscillations about the set point at the PFD output frequency. Upgrading to a higher frequency source would increase the lock bandwidth, but the system is already sufficient to perform the c-MOT sweeps that are the most demanding stage of our sequences. Both locking

⁹In reality the lock bandwidth will be limited to an order of magnitude below this update rate.

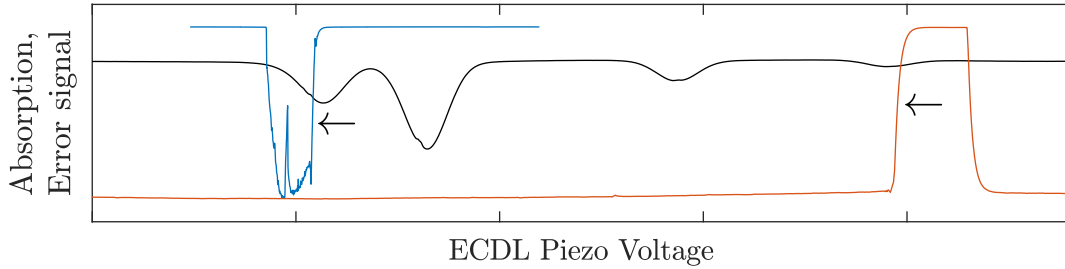


Figure 3.8: **Error signals produced by the two offset lock units:** The cooling is shown in blue and the repumper in red. The piezo voltage is not stated, as it differs between the two ECDLs. The lasers are locked to the edges indicated by the arrows. The left-most edge of the cooling error signal corresponds to a beatnote of the desired frequency, but with light from the ECDL red-detuned with respect to the reference, instead of blue-detuned. Other edges are due to the maximum or minimum bandwidths of the offset locks.

signals are shown in Fig 3.8, and we discuss the specifics of each lock below.

3.2.2.1 The repumping laser offset lock

Light from the repumping ECDL is coupled into an optical fibre and taken directly to the offset lock. A 10 MHz reference frequency is produced by a *Stanford DS345* waveform generator. Light is blue-shifted 92 MHz by a single pass AOM before reaching either the glass cell or the MOT, and thus the beat note is chosen to lock the laser at a frequency detuning of 92 MHz below (red of) the ^{87}Rb repumping transition.

3.2.2.2 The cooling laser offset lock

Several different optical frequencies are required of the cooling ECDL during a typical sequence (see Table 3.4). The *ADF4118* PLL integrated circuit has a minimum bandwidth of 100 MHz, and the detected beat note must remain above this limit at all times. To achieve this, light from the cooling ECDL is first blue-shifted by a single pass through an AOM running at the fixed frequency of $f_0 = 284$ MHz before entering the offset lock. The frequency difference between the cooling ECDL and the reference laser is thus red-detuned from the observed beat note, $f_{\text{cool}} - f_{\text{ref}} = f_{\text{beat}} - f_0$. The

	Cooling	Repumper
Photodiode	<i>DET025AFC/M</i> (Thorlabs)	<i>D2-160</i> (Vescent)
Bandwidth	2 GHz	9.3 GHz
Beam-splitter	<i>FC780-50B-APC</i> (Thorlabs)	custom (Oz Optics)
PLL	<i>ADF4118</i>	<i>ADF4107</i>
Frequency range	0.1 to 3 GHz	1 to 7 GHz
R	1	10
N	64	6476
Reference frequency	1.5 to 19.5 MHz	10 MHz

Table 3.3: **Part numbers for the offset locks:** Part numbers for construction of the cooling and repumping offset locks, and relevant specifications.

	Detuning (MHz)	Beat note frequency (GHz)
MOT		
^{87}Rb Cooling	-22	0.262
^{87}Rb Repumping	0	6.476
cMOT		
^{87}Rb Cooling	-22 to -72	0.262 to 0.212
Imaging		
^{87}Rb Cooling	6	0.100
^{87}Rb Repumping	0	6.476
^{85}Rb Cooling	6	1.226

Table 3.4: **Beat note frequencies used during a typical sequence:** The stated detunings are given with respect to the transition at zero field; after accounting for the Zeeman shift from the imaging bias field the imaging cooling light is resonant with the atomic transition. The ^{85}Rb cooling light for MOT and c-MOT and repumper light for imaging is produced by modulation (see Sec 3.2.3).

lowest frequency beat note required during a sequence is for producing ^{87}Rb probe imaging light, which must pass through a double-pass AOM shutter that blue-shifts the light by 2×95 MHz. For imaging on the cycling σ^+ transition $|F = 2, m_F = 2\rangle \rightarrow |F' = 3, m'_F = 3\rangle$ the imaging light must be 6 MHz blue-detuned from the zero-field transition to account for the Zeeman shift of the ground and excited states in the applied magnetic bias field, thus requiring a beat note frequency of 100 MHz. The frequency reference is generated by an *Agilent 33220A* waveform generator, controlled using an analog voltage output from the experimental control.

3.2.3 Generating light for simultaneous dual-species operation

To simultaneously collect both ^{85}Rb and ^{87}Rb in the MOT, ^{85}Rb cooling and repumping light must also be generated. These optical frequencies could be supplied using another two ECDLs, each locked to a ^{85}Rb transition, but this is an expensive solution that requires a significant amount of extra optics and alignment in addition to two complete laser heads and their associated drive electronics. Alternatively the additional components can be produced using modulation techniques, since all required optical transitions lie within the modest frequency range of 6.6 GHz. Rubidium dual-isotope setups have been demonstrated using EOMs driven with multiple frequencies to produce the required light from a single carrier [70, 71], although the required EOM is expensive.

A cheaper alternative is to modulate the current of a diode laser at microwave frequencies, as has been demonstrated to produce ^{87}Rb repumping light from a carrier at the ^{87}Rb cooling transition [72, 73]. Current modulation is used here to add ^{85}Rb cooling light as a sideband to the ^{87}Rb cooling light, and likewise ^{85}Rb repumper as a sideband to ^{87}Rb repumper, shown in Fig 3.9. The current of an injection-locked ‘slave’ diode (*Panasonic LNC728PS01WW*) is modulated instead of the ECDL itself

to avoid suppression of the sidebands, as the modulation frequency is mismatched to the external cavity's free spectral range [73]. The modulation also produces other sidebands, but these are weak and far detuned from all ^{85}Rb or ^{87}Rb transitions, and do not affect the operation of the MOT (although the power in these other sidebands is effectively wasted).

A *DS Instruments SG6000L* signal generator produces the required microwaves for each slave¹⁰. The output is amplified by a low-noise *Minicircuits* amplifier (cooling *ZX60-P162LN+*; repumper *ZX60-272LN-S+*) and combined with the DC laser current using a bias tee (cooling *ZFBT-6G-FT*; repumper *ZX85-12G-S+*). The DC and ~ 10 mW microwave power is fed to the laser diode via coaxial cable which is cut and soldered directly to the diode pins as in refs [72, 74]. This achieves sufficient modulation strengths, and further impedance matching is not required. The intensity of the sidebands is sensitive to both the temperature and current of the injection-locked laser, which change the free running characteristics of the laser diode and thus the gain of each mode; for very large changes in operating conditions it is even possible for the slave to lase predominantly at the sideband frequency [75], which is undesired here. Maximum sideband amplitudes of about 15% of the carrier are possible, but beyond this the laser becomes unstable and outputs predominantly at the sideband frequency. Depending on the number of ^{85}Rb atoms needed, the sideband is between 5% to 15% amplitude. The slave lasers are enclosed in perspex boxes to improve their temperature stability, and we monitor the sideband amplitude on an optical spectrum analyser (OSA) throughout the day. The long-term stability is also improved by leaving the slave modulation on permanently as mode hops can occur when it is switched on and off. Unmodulated light is still available when required, *eg* for imaging, by taking light from the ECDL instead of the slave output.

¹⁰The requirements of the microwave sources are not particularly high; as the linewidth of the transition is 6 MHz it is extremely unlikely that the phase noise of any commercial synthesiser will pose a limitation. Provided there are no spurious peaks that produce sidebands resonant with other transitions there is little reason to use a more expensive source.

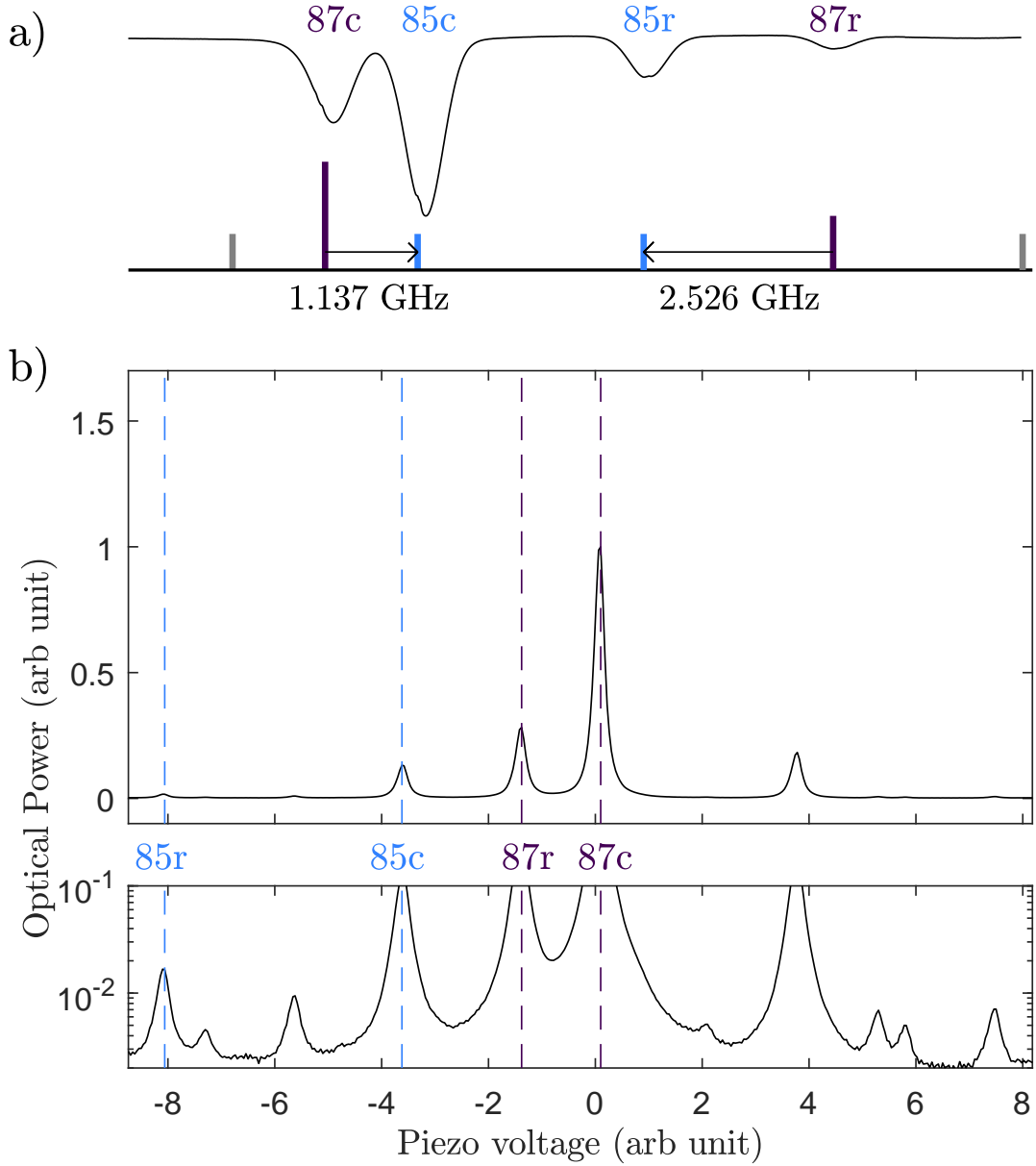


Figure 3.9: **Dual species light by slave modulation:** **a)** Illustration of the required optical frequencies produced from the modulated diode lasers overlaid on a Doppler-broadened Rb spectroscopy signal. The modulation frequencies used are labelled. **b)** Combined light from the modulated cooling and repumping injection-locked slaves as observed on an OSA. The sidebands are separated from their respective carriers by an amount that exceeds the 300 MHz free-spectral range (FSR), and only one FSR is shown. ^{85}Rb and ^{87}Rb cooling (c) and repumping (r) components are labelled. The lower trace is on a logarithmic scale to make weak higher-order sidebands visible. A moving average has been applied to the trace to smooth out high frequency noise. *Note that the relative amplitudes of cooling and repumping light shown here are not representative of the ratio used for the MOT.*

The combined outputs from both slaves seed the TA, which amplifies the multiple optical frequencies to provide light for the MOT. Additional frequency components due to non-linear mixing in the TA are suppressed due to the greater than 1 GHz separation of the components [76]. These intermodulation products are anyway far-detuned from transitions of either species. Previous groups have observed that temperature fluctuations in the gain medium of the TA change the distribution of power between the output modes [70], however our atom numbers are sufficiently stable after transport to suggest this is not a limitation here. Our TA also preserves the relative amplitudes of the seed components even when saturated, as noted previously [76].

3.3 Static and radiofrequency magnetic fields

The section presents a brief overview of the hardware required to produce magnetic fields used for trapping and manipulating ultracold atoms.

3.3.1 MOT coils

The MOT coils that provide the quadrupole fields used for magneto-optical trapping and mechanical transport of atoms to the glass cell are mounted on a *Parker Hannefin 404 XR* transport rail, as described by Sheard [49].

3.3.2 High current Coils

An array of high current coils generate the magnetic fields required for the magnetic transport of atoms to the glass cell and the final quadrupole field that confines them. Their specifications are found in previous theses [49, 28]. The quadrupole gradient at the glass cell with coil current I is

$$\vec{B}_{\text{quad}} = B' (x\vec{e}_x + y\vec{e}_y - 2z\vec{e}_z) \quad (3.6)$$

where $B' = bI$ and $b = 1.17 \text{ G cm}^{-1} \text{ A}^{-1}$.

The current through each coil pair is controlled using a bank of MOSFETs [77] and driven by a high-current *Magnapower SQA-30-330* power supply (later replaced with two series *Delta Electronika SM15-400* to reduce noise, see Sec 4.2.1). The maximum field gradient we can apply is limited by Ohmic heating in the coils, and both coils and MOSFET bank are water cooled to dissipate heat; at 330 A the quadrupole coil equilibrates at about 70 °C. The coolant (*Hexid A40*) is temperature controlled and circulated by a customised *ATC K12* chiller¹¹ at a pressure of 5 bar and temperature of 11 °C.

3.3.3 The AC coil array

The AC coil array is sandwiched between the high current quadrupole coils and surrounds the glass cell, as shown in Fig 3.10. Up-to-date specifications of the current coil array are listed by Harte [22].

The outermost coils produce the 7 kHz rotating bias field used for the TOP trap and TAAP trap [28, 50]. Field components along the \vec{e}_x and \vec{e}_y direction are created using pairs of coils either side of the cell, which are connected in series to ensure an equal current flows through both. The signal is sourced from an *Agilent 33220a* function generator, from which an in-phase and quadrature component is derived. Analog mixers multiply these components with analog voltages from the experimental control, enabling individual adjustment of the \vec{e}_x and \vec{e}_y field magnitudes during the sequence. The signals are amplified by a *Crown XLR5000* audio amplifier and connected to the coil pairs using a transformer to match the impedance. The maximum TOP field amplitudes created during a typical sequence are $\sim 25 \text{ G}$.

The antenna that applies the weak rf fields used to eject atoms during rf evaporation is a few turns of wire. The applied rf frequencies range from 0.4 MHz to 120 MHz.

¹¹maximum flow rate 25 L min⁻¹, 14 kW capacity

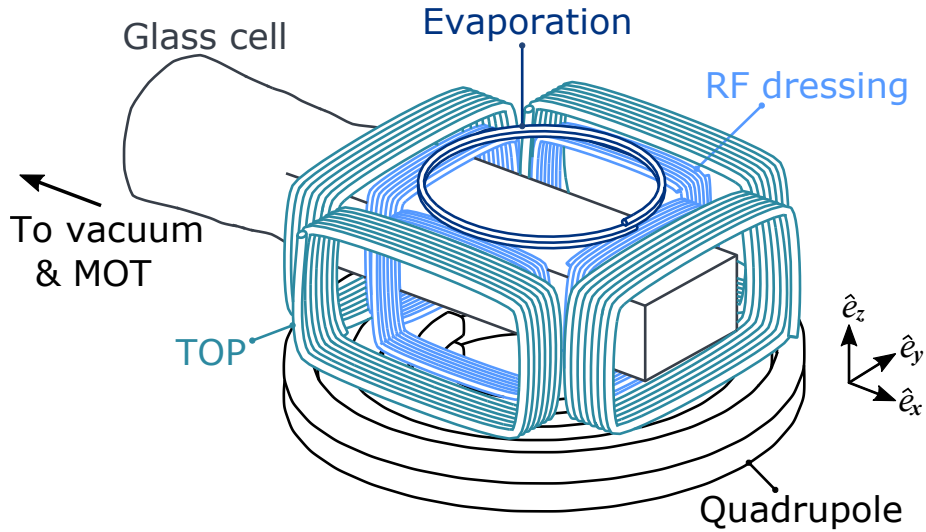


Figure 3.10: **Illustration of the AC coil array:** For clarity only the lower coil of the quadrupole coil pair is shown.

No attempt is made to impedance match the coil; this would be challenging due to the wide frequency range applied, and in any case the power is sufficient after amplification with a 1 W *Minicircuits ZHL1-2WS* amplifier. A DDS unit (described below) produces the rf signal.

3.3.4 Dressing rf fields and the rf signal chain

The innermost coils apply the radiofrequency dressing fields. The rf signals along the \vec{e}_x and \vec{e}_y directions are independently generated, and amplified using *Minicircuits LZY-22+* amplifiers which are powered using a linear power supply (*SOLA HD SLS-24-120T*). The coil pairs in each direction are matched to the $50\ \Omega$ amplifier output using a wide-band impedance match, extensively detailed by Harte [22]. The apparatus achieves dressing rf fields of sufficient amplitudes to load the TAAP without large atom loss ($\sim 0.5\ \text{G}$) over the frequency range 2.5 MHz to 4.5 MHz.

All dressing rf signals are generated by two DDS units constructed by the *Central Electronics Group* at Oxford and described in Gildemeister’s thesis [28]. As part of the work in this thesis the pre-existing DDS control software was rewritten from

scratch. Each unit provides 4 channels of up to 150 MHz and 0.2 V amplitude, and is interfaced to a control computer via a *National Instruments* 32-bit digital output card *PCI-6534*. A unit is comprised of 6 shielded submodules as follows:

- a 60 MHz clock distribution board
- a board that interfaces the high density cable from the control computer to the unit's backplane
- four *Analog Devices AD9854* DDS chips mounted in their evaluation boards.

Each *AD9854* is individually addressable, and configured by writing to registers internal to each DDS chip over the parallel backplane of the unit. Logic internal to the *AD9854*, such as increasing the signal phase or updating the digital-to-analog converter, is driven by a 300 MHz internal clock. These clocks are phase-locked to the external 60 MHz reference clock to phase-lock the output of each channel.

Although these DDS units had been used previously for a number of rf-dressed experiments [61, 60, 44], critical flaws in their design were revealed during this work that required amending.

The first issue prevented triggering the DDS channels in synchronisation, and is understood as follows (see Fig 3.11a). After all channels are configured an 'update' is broadcast, which signals each DDS to operate using the new parameters. The update signal is transmitted from the *PCI-6534* card in the control computer by pulling one digital line of the backplane high. Unfortunately, the existing hardware provided no means to synchronise this update signal with the internal 300 MHz system clock on each DDS chip. A delay in propagating the update signal along the backplane of the unit results in a different phase between signal and clock for each chip. Occasionally, the 'update' may arrive immediately before the rising edge of an internal clock for some (but not all) channels. The chips for which the signal missed the edge must wait

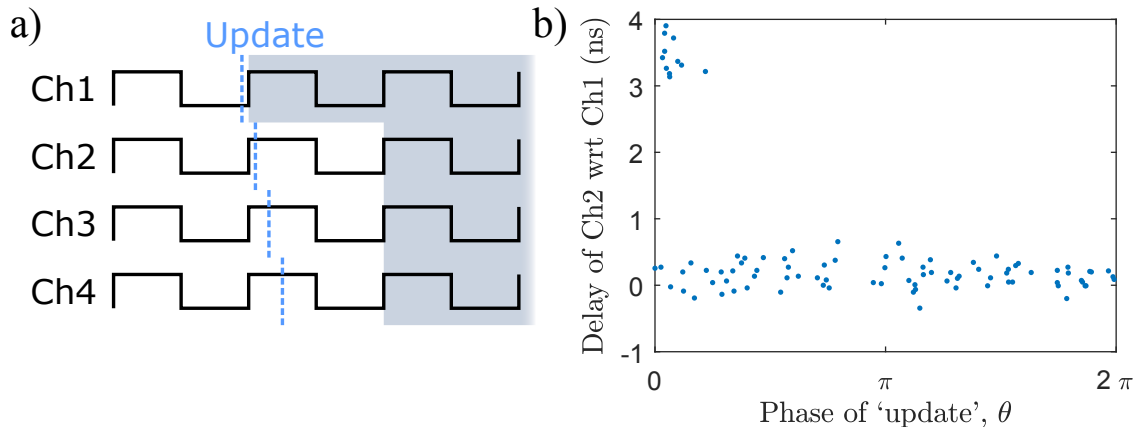


Figure 3.11: **Sporadic phase jumps in the DDS output:** **a)** An illustration of the problem. The update signal has a different relative phase with respect to the 300 MHz internal clock of each DDS channel, exaggerated here for clarity. The figure shows it arriving just before the clock edge on channel 1, but just after for all other channels. This causes a $1/300$ MHz delay before the later channels output. **b)** Measured delay between the output of two DDS channels as a function of the random phase of the ‘update’ signal with respect to the 300 MHz internal clocks. A delay occurs sporadically for small phases, when the ‘update’ is close to the rising edges of each clock. The delay in propagating along the backplane causes the update signal to sometimes arrive before the clock edge of channel 1 and after that of channel 2.

a full clock cycle to respond, producing a sporadic phase delay of ~ 0.1 rad between channels of the DDS.

Fortunately, the 300 MHz system clocks are phase-locked to the 60 MHz reference. The solution was to insert a flip-flop on the digital line used to broadcast the update signal, between the *PCI-6534* and the DDS units, which is triggered by the rising edge of the 60 MHz clock. This fixes the phase of the incoming ‘update’ command with respect to the rising edge of the internal DDS clocks, within a region of Fig 3.11b where the sporadic delay does not occur.

The second issue was spurious frequency peaks on the output of the DDS. This differs from phase noise on the dressing rf source, which predominantly causes heating in the trap through dipolar excitations [78]¹². The DDS was plagued with an exceedingly poor spurious free dynamic range, and the output was littered with large sidebands at

¹²our in-trap heating rate of 30 nK s^{-1} in the TAAP suggests phase noise is not a limitation

Scheme	Connection Diagram
3 rf, double well, linear (see Chapter 4.4)	
2 rf, 2 species, circular (see Sec 5.4.2)	

Table 3.5: **DDS connections:** Configuration used for each of the rf dressing experiments. The polarisation of the dressing rf field is listed as either circular or linear.

100s of kHz separation from the carrier. As discussed in Sec 4.2, severe atom loss from the trap occurred whenever these peaks became resonant with atomic transitions to untrapped dressed states. Ultimately, these peaks were caused by switch-mode power supplies embedded in the unit, and vanished after we exchanged them for a quieter linear power supply. It is likely that they were undetected in earlier experiments because the previous narrowband impedance match attenuated these sidebands and prevented loss.

The multiple-rf waveforms are created by combining the single-frequency outputs of multiple channels using splitters *ZSC-2-2* before amplification. All channels used for the multiple-rf waveform are phase-locked to the same 60 MHz source. Depending on the experiment, different configurations of the DDS connections are used as listed in Table 3.5.

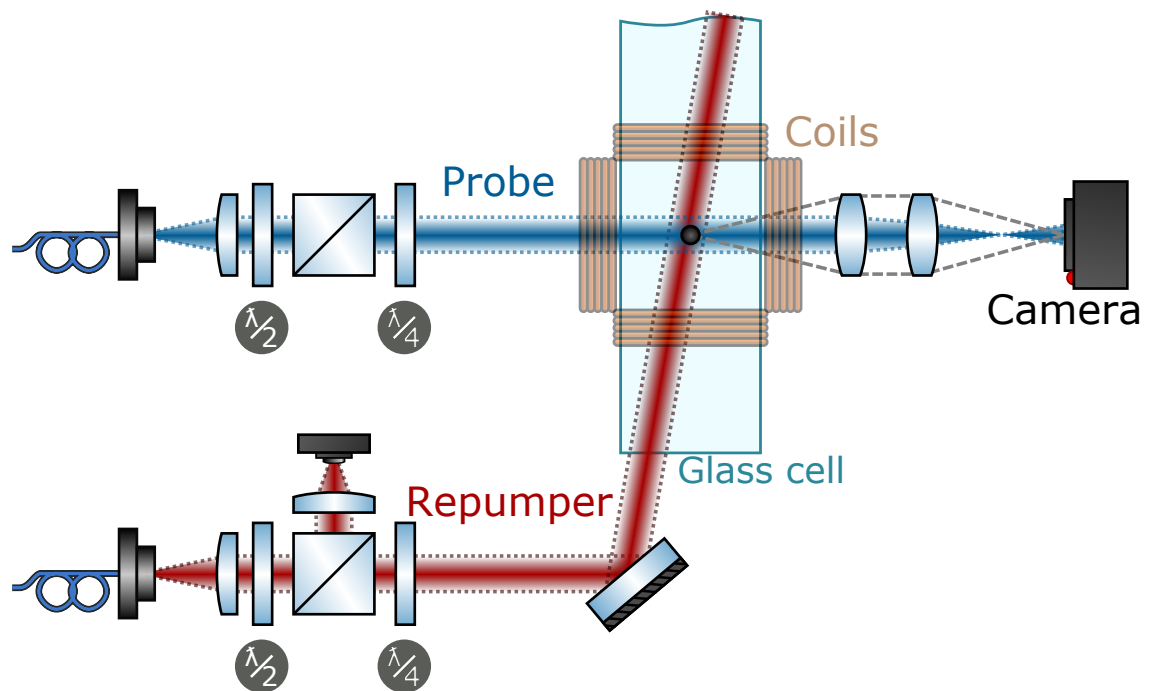


Figure 3.12: **The horizontal imaging system:** Lenses after each bare fibre output collimate the beam after expansion. The probe beam diameter is 6 mm and typical imaging powers are about 1 mW. Polarising beam splitters clean the polarisation. For the cooling light this means that polarisation drifts in the fibre are apparent as intensity fluctuations, rather than as a change in the effective atomic scattering cross section. The $\lambda/4$ waveplates produce circular polarised light. A photodiode monitors drifts in the power of the repumping beam.

3.4 Imaging systems

A number of imaging systems allow us to characterise the cooled cloud, either *in situ* or after ballistic expansion. Almost all of the work in this thesis is undertaken using the horizontal imaging system depicted in Fig 3.12. Two 25 mm doublet lenses of focal length 10 cm image the cloud of atoms onto the CCD at $\times 1$ magnification, with a resolution limited by the CCD pixel size of $6.45\ \mu\text{m}$. It is usable at all stages of our sequences; the wide field-of-view enables imaging of large clouds immediately after transport and also evaporated clouds over a range of different temperatures and time-of-flight durations up to 24 ms.

There is also a high resolution vertical imaging system, which has a magnification of $\times 14$ and is diffraction limited to $1.6\ \mu\text{m}$; the centrepiece is a compound four lens objective of focal length 3.76 cm, which includes correction for aberration from each lens and the 2 mm glass cell to achieve a NA of 0.27 [79]. This imaging system also serves to focus the light from a dipole trap based on a 2-axis acousto-optic deflector, and further details can be found in Harte’s thesis [22]. Pulses of probe light for both systems are switched using AOMs in the double-pass configuration to provide fast shuttering times and a good extinction ratio, and combined with a mechanical shutter to prevent light leakage¹³.

In absorption imaging a probe beam of resonant light is incident on a cloud of atoms, which absorb light and imprint a shadow onto the probe. Imaging the shadow reveals the distribution of atoms along the beam path. Three pictures are taken to compose such an absorption image. The first two, one with atoms and one ‘reference’ image without, are both illuminated by the probe beam and used to measure the optical density of the cloud. The third ‘dark’ image is not illuminated, and accounts for hot pixels and background light illumination of the CCD. The number of atoms is

¹³This also enables the AOM to remain on provided the mechanical shutter is closed, which keeps the AOM running warm.

calculated using the measured attenuation of the probe beam and the known atom-photon absorption cross-section. We use imaging probe beams of intensity less than I_{sat} and neglect the power broadening that is discussed in ref [80].

Accumulated dust on the imaging optics produces interference patterns in the coherent probe beam. These fringes shift as the optics move from acoustic noise, and the pattern differs between the first and second pictures. When the absorption image is composited this produces artefacts that lead to systematic errors in the measured atom number. These artefacts are removed by post-processing the absorption images using principal component analysis [81, 82], in which an eigenbasis of fringe patterns is constructed from multiple reference images (here, 50 to 200) and used to produce a reference image that most closely matches the fringes seen in the picture with atoms. The comparison is made using pixels far from the region of interest (and thus void of atoms), and works well because the long-ranged correlation in the fringe patterns allows an accurate estimate to be made of the (obscured) fringes at the location of the atomic cloud.

Atoms are imaged using light resonant with the cycling cooling transition to give a strong absorption signal and well defined absorption cross-section. As both ^{85}Rb and ^{87}Rb are trapped in the lower hyperfine states, a brief exposure to repumping light is required to transfer the populations to the upper hyperfine states before imaging. For ^{87}Rb , a short 360 μs pulse is sufficient, while ^{85}Rb requires a longer exposure of at least 1 ms to completely repump the cloud using the weaker ^{85}Rb sideband on the repump laser¹⁴. Only one species is imaged at a time; the cooling transitions for ^{85}Rb and ^{87}Rb are separated by 1.1 GHz which greatly exceeds their 6 MHz linewidths.

¹⁴Alternatively the repumping offset lock set point could be changed mid-sequence so that the carrier is resonant with the ^{85}Rb repumping transition, but the current solution has worked well.

3.5 The experimental control system

The control system that drives the apparatus has been rewritten for the work in this thesis, and the new approach is described here. This section is neither a programming guide, nor a reference for the API itself, which already contains extensively documented commands and classes. Instead, it aims to motivate why a rewrite was necessary, to outline the technical details of the new implementation, and to discuss the features and advantages of the new system.

3.5.1 The previous control system

The previous control system is described in Gildemeister’s thesis [28]. Sequences are authored using a *Labview* program resembling a ‘spreadsheet’; time progresses along columns from left to right, updating the digital and analog channels according to the values listed in the rows. The DDS units are controlled through a separate *Labview* program, which resembles a table of the amplitude, phase and frequency at different points in time.

This implementation has a number of shortcomings:

- **Prone to errors:** The entire sequence was defined as a single table, with no ability to composite sequences out of separate files. As about 80% of the instructions are identical between the most basic sequence (transport to glass cell) and the most advanced (multiple rf shells) this encouraged duplication between sequences. For example, if a change was made to the c-MOT parameters this had to be manually added to all sequence files in use. Over time, errors would accumulate, and significant time was lost debugging broken sequences. In addition, the associated DDS ramps for each sequence were stored in separate files, and had to be manually loaded into each control program.
- **Hard to read:** The flat table structure is not particularly human-readable, and

it would take time to understand more complicated sequences. Columns could be given a 7 character label, but more extensive documentation was impossible.

- **Hard to work with:** Often parts of the sequence would overlap, making it hard to change the timings associated with one part without affecting others.
- **No version control:** Sequences were generally dumped in a folder marked ‘old’ and given a date suffix. No tool existed to identify changes between similar sequences.
- **Limited parameter sweeps:** There was only a rudimentary capability to perform sweeps, either over single analog voltages or the duration of a column. Sweeping the parameters of rf ramps output from the DDS was not possible. Significant time and sanity was wasted performing detailed sweeps by manual entry.
- **No history:** There was no historical record of sequences that had run, nor an easy way to associate measurements in a series with corresponding parameter values. Significant effort from the experimentalist was required to manually curate the data. This was also prone to error.

3.5.2 The new control system

The new control system is based on the existing hardware, which is described previously [28]. The hardware instructions are still represented in a table format that specifies the analog and digital values at times during a sequence, but the tables themselves are generated by a *MATLAB* package and configured using a high-level application-programming interface (API) that we call ‘GLaDOS’¹⁵. The associated *Labview* programs that interface the DDS units and experimental control hardware

¹⁵This is a cultural reference, rather than a meaningful acronym.

were rewritten for compatibility with this new approach and to enable remote network operation and batch runs. These upgrades solved many of the previous issues and provided numerous new features. In particular,

- **Easier to use:** GLaDOS provides low-level commands for control over digital and analog channels, but also a number of higher-level commands to *eg* load the MOT or produce a BEC in the TOP trap. Authored sequences are extremely quick to read and interpret, presenting only the relevant information for the sequence's intended purpose. Contrast this to the 'table' approach, where the important information was drowned out among the definitions for every other channel.
- **Reduced operator error rate:** Sequences can be based off existing templates through an inheritance model, which discourages duplication and so reduces errors. For example, fixing an issue in the `Transport` template will also fix this for any sequences derived from it. Individual channels can be plotted as a function of time, and the full sequence inspected using a visual tool (see Fig 3.13).
- **Automatic data curation:** Generated sequence objects are stored in the *HDF5* archival data format and minted with a unique ID that is used to associate output such as absorption images. When a sequence is generated from a template, every parameter is automatically saved as metadata in the file. These can be retrieved when using the accompanying analysis *MATLAB* package to identify trends or the results of parameter sweeps. Sequences and output are stored on the departmental data server.
- **Version control:** Historical changes to sequences and calibrations are recorded in a *git* repository. Past and current sequences can be easily compared, which

helps when locating the cause of recent bugs. Previous sequences can be re-run using more recent calibrations.

- **Improved low-level control:** Analog and digital channels can output arbitrary functions¹⁶. For instance, it is simple to generate a train of pulses on a digital channel, whereas this would require many columns in the previous tabular approach. The frequencies, phases and amplitudes of DDS channels are also controllable. For example, we used this to implement amplitude ramps defined as a cubic spline, which are used to split a BEC in our multiple rf double-well potential.
- **Arbitrary parameter sweeps** Generating batches of sequences in which any parameter changes is as simple as writing a for loop. This greatly enhanced the capabilities of our apparatus to perform sweeps.

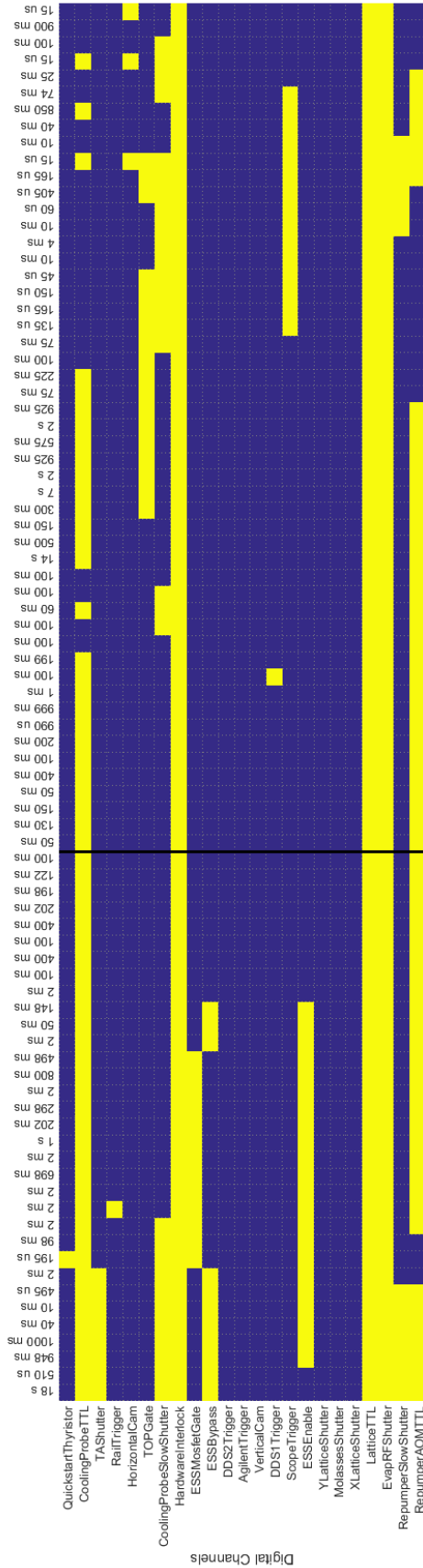
This improved work flow greatly increased our efficiency, and the automatic data curation and arbitrary parameter sweeps were necessary steps towards automatic operation of the experiment. Before the apparatus could run remotely a number of hardware changes were required, which we now discuss.

3.5.3 Safety interlocks

The apparatus uses a number of high power supplies, and relies on water cooling to dissipate kW of heating power generated by the coil array. Even so, at the highest quadrupole coil currents used during a sequence the coils equilibrate at a temperature of 70 °C after only a few seconds of operation; a failure in the cooling system would quickly lead to disaster.

Remote operation requires an interlock to automatically intervene and shutdown the high power supplies. The following system has been designed and implemented,

¹⁶Limited by the on-board memory of the control FPGA and the 15 μ s channel update rate.



t=25.5010005s, v=10

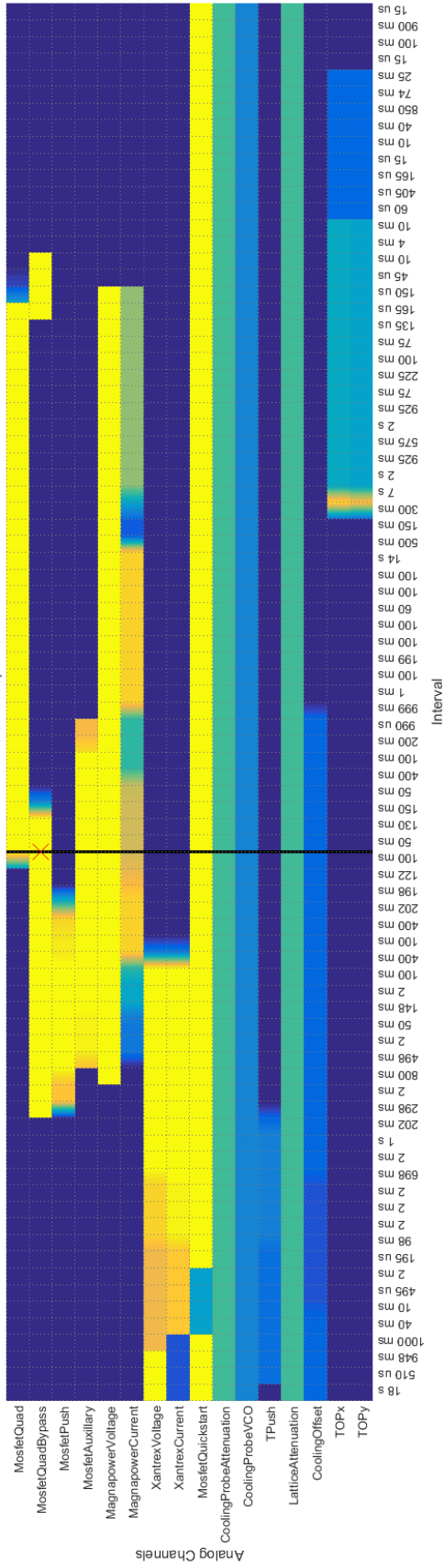


Figure 3.13: The sequence inspector: A *Matlab* tool used to debug timings and values generated by GLaDOS. Physical channels correspond to rows, with time progression from left to right. Key sequence timings are labelled in appropriate units along the bottom. The cursor (black line) is used to measure values and intervals. This particular sequence produces a BEC in the TOP trap.

which consists of a 2-layer ‘software/hardware’ interlock with requirements as listed in Table 3.6. The ‘hardware’ interlock is driven by a *Galil RIO-47100* programmable logic controller¹⁷, which monitors the temperatures of 5 *K-type* thermocouples using a *SCB-48306* signal conditioning board. The hardware interlock trips if any thermocouple goes outside the temperature ranges specified in Table 3.6, and also if any are disconnected. For good thermal contact the thermocouples are bonded to the coils using thermally conductive cement, and the wires mechanically secured with cable ties. A *Gentech FS-01* flow switch monitors the circulation of coolant.

The ‘software’ interlock is a *Labview* program that reads 4 different *K-type* thermocouples connected to the experimental control computer. These values are also logged to the monitoring database, see Sec 3.6. When the software interlock is tripped the experimental control interrupts the currently running sequence and enters a safe state that requires manual intervention. When either interlock is tripped the hardware interlock disables all high current power supplies listed in Table 3.7, and remains in this state (indicated by a red LED) until rebooted via manual intervention.

3.6 Remote monitoring

Good monitoring also assists in the remote operation of our apparatus. Ideally such a system should provide historic data and not just real-time observations, to allow problems to be identified in long, automated batches that run for durations of many hours. It should also be reliable and easy to extend in future, and provide a well-designed user interface to make the data easily accessible.

We use the increasingly popular combination of an *InfluxDB*¹⁸ database combined with *Grafana*¹⁹ to provide an aesthetically pleasing and feature-rich interface. *InfluxDB* is a time-series database that is used to store individual time-stamped mea-

¹⁷These devices have been used by another group to interlock an oven source [68]

¹⁸<https://www.influxdata.com/>

¹⁹<http://www.grafana.com/>

	Measurement	Condition
Hardware		
	Quadrupole coil TC	$8^{\circ}\text{C} < T < 65^{\circ}\text{C}$
	Auxiliary coil TC	$8^{\circ}\text{C} < T < 30^{\circ}\text{C}$
	TOP coil TC	$8^{\circ}\text{C} < T < 30^{\circ}\text{C}$
	TPush coil TC	$9^{\circ}\text{C} < T < 45^{\circ}\text{C}$
	MOT coil TC	$8^{\circ}\text{C} < T < 40^{\circ}\text{C}$
	Flow switch	Coolant flowing
	Software interlock	Not tripped
Software		
	Quadrupole coil TC	$T < 70^{\circ}\text{C}$
	TOP coil TC	$T < 50^{\circ}\text{C}$
	MOT coil TC	$T < 45^{\circ}\text{C}$
	TPush coil TC	$T < 45^{\circ}\text{C}$

Table 3.6: **Interlock Requirements:** These conditions must be satisfied, otherwise the interlock trips to disable the high current power supplies. The software and hardware interlocks read different thermocouples (TCs); the use of two TCs on some coils is intentional to provide added safety. The disparity between some interlock temperatures monitoring the same coil are due to temperature gradients across the coils, which make the TC temperatures sensitive to their placement.

Device	Usage
<i>Crown XLR5000</i>	TOP field audio amplifier
<i>DE SM15-400</i>	High current coil supply
<i>Xantrex XFR 20V-60A</i>	MOT coil supply
<i>Lambda ESS</i>	TPush coil supply

Table 3.7: **Interlocked devices:** The listed devices are disabled when the interlock is tripped. The *Crown XLR5000* does not have an in-built interlock functionality; it is turned off by interlocking the mains supply to the amplifier.

surements of any parameter in the lab. These correspond to physical quantities such as temperatures, voltages, and calculated values such as the atom number in the MOT, but also variables like the current experimental control state. The database provides a number of interfaces over which to submit readings, though the most convenient is to upload data using an HTTP POST request, which is supported by most programming languages. *Grafana* is a dashboard monitoring program that provides a polished and well constructed user interface to extract and plot data from the database. In addition to numerous plotting widgets it also provides support for user alerts if a variable fails a conditional test, *eg* if the MOT atom number drops below a certain value for a specified duration.

A number of parameters are measured and uploaded using various *Labview* programs. To monitor low-level sensors like thermocouples and photodiodes we use cheap *Arduino Mega2560* devices which contain 16×10 -bit analog input channels. Although the on-chip analog-to-digital converter is inaccurate, monitoring is mostly used to observe long-term drifts and as such absolute accuracy is not so important. A home-made *C#* program interfaces with each *Arduino* over a USB serial port, polls the analog channels and uploads the response to *InfluxDB*, with additional support for channel configurations such as names, supersampling to increase resolution, sample rates and conversion functions.

3.7 Conclusion

The essential components of our ultracold atom apparatus have been described, and an overview given of typical operation. Our robust laser system is frequency stabilised using microwave offset lock techniques and uses modulation techniques to provide cooling and repumping light for both rubidium isotopes simultaneously. We detailed upgrades to the control system, monitoring and interlocks that have enabled us to

achieve remote operation of our experiment.

Chapter 4

Multiple-radiofrequency dressed double-well potential

We have implemented a double-well potential for cold atoms by dressing them with multiple frequencies. This novel technique is described with particular attention paid to technical details of the experimental work, especially the reduction of deleterious rf noise that led to significant atom loss in the first iteration of our apparatus. Our first experimental results with this potential have been published in ref [21], and the methods used to calculate and interpret the rf spectroscopy measurements therein are explained in this chapter. This proof-of-principle demonstration produced a double-well potential with a separation that was too large for many purposes, and here we describe the reduction of this separation to $6.7\ \mu\text{m}$ which is sufficiently close to observe matter-wave interference after time-of-flight expansion of a split condensate. To conclude, we discuss the present limitations to our apparatus, propose further improvements and consider the feasibility of applying the double-well potential to tunnelling experiments.

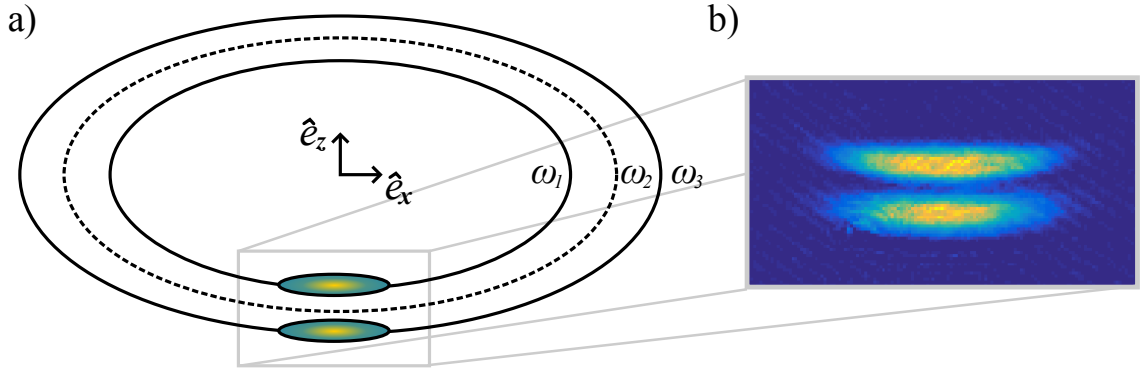


Figure 4.1: **A 3-rf dressed double-well potential:** a) The three frequency components of the dressing field are resonant on three coincident spheroids of different radii. Atoms are trapped at potential minima resonant with ω_1 and ω_3 . They accumulate at the bottom of the spheroids under the influence of gravity (here, yellow slabs). b) An absorption image of thermal atoms in the double-well potential.

4.1 A 3-rf dressed double-well potential

Our double-well potential is formed by combining a static quadrupole field with an rf dressing field of three frequency components, $\omega_i/2\pi$, $i \in [1, 2, 3]$ as described in Sec 2.6. Each rf frequency is resonant with the Zeeman splitting on one of three resonant spheroids, which are concentric (see Fig 4.1). The first and third components, ω_1 and ω_3 , produce avoided crossings that are potential minima for the trapped atoms, while the second frequency ω_2 produces a ‘barrier’ avoided crossing that connects these two concentric shell traps. The relative energy of each well’s potential minimum, and that of the barrier, are controlled through the amplitudes of each dressing rf component, B_i . Increasing B_1 , B_3 raises the potential energy of the well formed at the corresponding resonance, while increasing B_2 lowers the energy of the barrier. This provides a handle with which to modify the potential as a function of time, for example by changing $B_2(t)$ to raise or lower the barrier. It also enables us to compensate for the difference in gravitational potential energy of the two vertically-

displaced wells¹. The ω_i are integer multiples of a common fundamental frequency, $\Delta\omega$. When all $g_F\mu_B B_i \ll \hbar\Delta\omega$, the wells are separated by a distance of approximately $\Delta z = \hbar\Delta\omega/g_F\mu_B B'$, corresponding to the distance between the unshifted resonances for ω_1 and ω_3 . At higher barrier amplitudes the wells are squeezed closer together because of higher order interactions between the atom and the rf field which shift each atomic resonance.

Atoms accumulate at the bottom of the resonant spheroids under the influence of gravity, experiencing weak radial and strong vertical trap frequencies as in the single rf shell trap². The image of thermal atoms in the double-well potential shown in Fig 4.1 is taken from our first demonstration of a multiple rf double-well potential [21], as described in the thesis of T. Harte [22]. The dressing-rf field was comprised of circularly-polarised frequency components at 3 MHz, 3.6 MHz and 4.2 MHz. For the preliminary work, this large frequency separation of 0.6 MHz that spans the full bandwidth of the rf-dressing coils was chosen for three reasons. First, a large frequency separation creates a large spatial separation between the wells, allowing atoms in each well to be clearly resolved in-situ using our low NA horizontal imaging system³. We also used a weak quadrupole gradient of 83 G cm^{-1} to further expand the separation. Second, the depth of the double-well potential is increased for a greater frequency separation as the higher-order avoided crossings that truncate the potential occur at a greater frequency detuning from the resonance. Finally, the dressing rf Rabi frequencies required to lower the barrier are proportional to the frequency separation, and so working with large Rabi frequencies to guarantee that adiabatic loss is negligible requires a large frequency separation. These parameters relaxed the technical criteria required for loading the double-well potential without significant atom loss,

¹This feature is particularly important for splitting a Bose-Einstein condensate, where the energy of the wells must be balanced to within the chemical potential.

²though we stress that the condition for a 2D Bose gas that the chemical potential $\mu \ll \hbar\omega_z$ is not met in any experiments discussed here.

³In Section Sec 4.3.2 we discuss methods to distinguish atoms in each well for a smaller spatial separation that is beyond the resolution of the imaging system.

and reduced the impact of heating on our initial loading procedures.

This work also clearly demonstrated control over the double-well potential using the rf field, with atoms controllably transported between the wells by adiabatically deforming the potential. In principle any combination of rf amplitude, frequency and polarisation can be used to shape the double-well potential, but it is sufficient to only modify the amplitudes. This is convenient, as rf frequency ramps⁴ can cause heating and atom loss in rf dressed potentials [78]. Further discussion of these manipulations is postponed until Sec 4.3.1, in the context of evenly loading a double-well potential characterised by a smaller separation.

Although transporting thermal atoms between the wells demonstrated control over the potential, it did not provide an accurate, quantitative measurement of the dressed eigenenergies for comparison to theory. An alternative method was required for this purpose.

4.1.1 Verifying the calculated rf-dressed eigenstates

To verify our model of multiple-rf-dressed potentials, we performed rf spectroscopy on atoms trapped in the double-well potential (this technique is described in Sec 2.7). A first-order rf transition is driven to eject atoms, with photon energy $\hbar\omega_p = \Delta E_i$ equal to the energy difference between the initial and final dressed eigenstates [47]. The resonance frequency shifts as the double-well potential is deformed through a change in the dressing rf amplitudes, and we measure the transition frequencies over a range of dressing field parameters to confirm our calculations of the dressed eigenstates. A BEC is used to increase the resolution of the measurement (see Sec 2.7).

⁴The implementation of frequency ramps is also complicated by the need to compensate for the variation in radiated power due to the changing impedance of each dressing field coil pair in the \vec{e}_x and \vec{e}_y direction.

A linearly-polarised rf field dresses the atoms,

$$\vec{B}_{\text{rf}} = \sum_i^3 B_i \cos(\omega t + \phi_i) \vec{e}_y \quad (4.1)$$

Starting with a BEC trapped in a shell trap created by a single dressing component of $\omega_1 = 3$ MHz and $B_1 = 534$ mG single rf trap, atoms are loaded into the multiple-rf dressed potential by slowly increasing the amplitude B_3 of the 4.2 MHz component to 709 mG over 150 ms, then that of the 3.6 MHz component B_2 over 300 ms to establish each avoided crossing and form the double-well potential. The atoms remain in the initial well at all times, with the other rf components applied only to distort the dressed energy levels. The weak rf probe was applied for 40 ms, and the remaining atom number measured by absorption imaging after time-of-flight expansion⁵.

The amplitudes and phases of the 3 dressing rf components are extracted from a voltage waveform measured on a calibrated pickup coil prior to the application of the rf probe (see Fig 4.2a). Saturation of the dressing rf amplifiers cause both B_1 and B_3 to decrease by a few percent as the ‘barrier’ rf amplitude B_2 increases, but by using the pickup waveform this effect is incorporated in our calculations. We assume that the pickup coil imparts no relative phase shift between the dressing components, and thus that phases extracted from the pickup waveform are representative of the actual field components. This is realistic given that this single-turn coil has a self-resonant frequency many times greater than the dressing frequencies, and should therefore impart a similar phase shift for each component.

Having determined the dressing rf field, we calculate the dressed eigenenergies modulo $\hbar\Delta\omega$ using the semi-classical Floquet theory described in Sec 2.3.4. The calculation is performed for points along the z -axis near the rf resonances, corresponding to the bottom of the shells where atoms are confined. In the dressed atom picture

⁵to produce reasonable optical depths of order ~ 1 for accurate number determination in absorption imaging

the eigenenergies are arranged in an infinite ladder of periodicity⁶ $\hbar\Delta\omega$. We select one ‘rung’ of this ladder, and identify the dressed state on which atoms are trapped. The potential energy of an atom in this state is equal to the gravitational potential energy plus the dressed eigenenergy. We determine candidate rf transition frequencies at the location of the potential energy minimum, reasoning that the rf probe causes the greatest atom loss when resonant at the greatest atomic density. The transition frequencies are determined from the energy separation between this eigenstate and others on the ladder. This method gives the frequency of a particular candidate rf transition, but it cannot determine which of these transitions are forbidden or allowed. The selection rules for an applied rf probe depend on the photon numbers of each rf field mode in the initial and final eigenstates, which is beyond the capability of our present semi-classical method. They can be determined using a fully-quantized resolvent formalism currently being developed by Dr. Yuen [46].

The calculated transition frequencies are in good agreement with those experimentally observed in the multiple rf potential (see Fig 4.2b), which are extracted from the resonance features by fitting an asymmetric parabola to the dip in atom number [22]. We find good agreement between the expected transition frequency and the observed resonances as the amplitude B_2 is changed from 0 G to 1 G and also when the phase of the second rf component ϕ_2 is changed⁷. We note that any systematic error in the measurement of the relative dressing field phases via the pickup coil would result in clear disagreement for this comparison, supporting our earlier assumption that the pickup coil does not introduce a relative phase shift between dressing rf components.

To conclude, in the first implementation of the multiple rf dressing technique [21], we demonstrated the ability to control and manipulate atoms in a double-well po-

⁶the periodicity arises because each bare state contains energy $E_{\text{rf}} = \sum_i n_i \hbar\omega_i$ in the radiation field, where $n_i \gg 1$ are the photon numbers in each field mode of frequency ω_i .

⁷To understand the importance of the relative phases between the multiple rf components, consider that changing the phase alters the maximum value of the dressing field, and thus the importance of an atom’s nonlinear response. In the resolvent formalism, it can be understood as constructive or destructive interference between different atom-photon transitions [46].

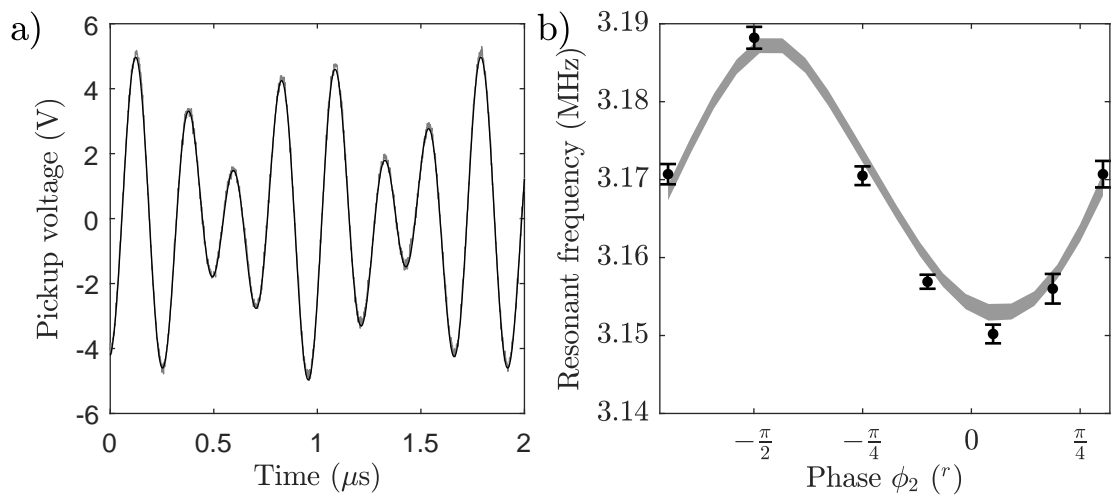


Figure 4.2: **Verifying the calculated rf-dressed eigenstates:** **a)** A three-frequency voltage waveform measured from the pickup coil is shown in light grey. A black line is overlaid, plotted using the extracted amplitude and phase of each component. **b)** Error bars show measured resonant frequencies of rf spectroscopy as a function of the phase ϕ_2 . The grey line shows predicted values calculated from Floquet theory. The width corresponds to the predicted uncertainty in the resonant frequency due to uncertainty in the quadrupole gradient and rf amplitude calibrations. For details of the fitting procedure used to extract the frequency of the rf resonance from data, see the thesis of T. Harte [22].

tential produced by dressing with three frequency components. The wide separation between the wells aided the characterisation of these potentials and reduced the technical requirements, but it was too large for experiments involving interference or tunnelling. Calculations of the rf dressed eigenenergies were confirmed using rf spectroscopy, and in doing so we verified our ability to determine the dressed eigenenergies using only the waveform measured on a pickup coil. These techniques are a crucial diagnostic for smaller well separations, where the technical constraints are more stringent and the imaging resolution is insufficient to observe the individual wells *in situ*.

To achieve a double-well potential with a significantly smaller separation requires a reduction in $\Delta\omega$. This results in a closer spacing of the transition frequencies to untrapped states, and is thus more susceptible to extraneous noise. Before atoms could be loaded into such a potential we first needed to remove deleterious rf noise that was present on the apparatus.

4.2 RF noise and atom loss

Spurious frequency components of rf noise cause atom loss if they become resonant with any atomic transitions to an untrapped state; even weak amplitudes corresponding to Rabi frequencies of Hz are detrimental to atom number for experiments on timescales of seconds, should they become resonant. The transition frequencies change as we manipulate the double-well potential, including during loading of the trap, and a large window of the frequency spectrum must be free of spurious noise to avoid loss. Furthermore, the existence of rf transitions comparable to the Rabi frequency of the applied rf field makes rf-dressed potentials vulnerable to noise from 10s of kHz to MHz. This range is typically densely populated with many different noise sources due to the widespread use of switch-mode power supplies (SMPS).

SMPS are ubiquitous because of their improved power density and efficiency com-

pared to traditional linear power supplies [69]. They operate at switching frequencies of around 100 kHz to resonantly drive the windings of a small transformer, typically with ‘dirty’ square-wave pulses that contain multiple harmonic components [83]. These frequencies are well above the bandwidth of most voltage regulators, and are suppressed by filtering of the output. Unfortunately, the implementation of filter stages in commercial power supplies is often lacklustre, allowing this noise to radiate through the laboratory or contaminate the output or ground.

4.2.1 Eliminating spurious noise

To remove rf noise from our experiment the technique of ‘Rabi spectroscopy’ is used to identify the frequencies responsible for atom loss. This information makes finding the noise source significantly easier⁸. In rf spectroscopy the frequency of an rf probe is varied to determine the (fixed, unknown) Rabi frequency of the dressing field. Conversely, in Rabi spectroscopy we vary the Rabi frequency to characterise an unknown, fixed external field responsible for atom loss. By adjusting the frequencies of atomic transitions in and out of resonance the noise can be identified and distinguished from other losses, such as the non-adiabatic loss that occurs naturally at both low and high rf amplitudes due to non-adiabatic following⁹. Sharp loss features at intermediate dressing rf amplitudes can only be explained by the presence of external noise.

Transitions exist at many different frequencies for an rf dressing field of given frequency and amplitude. For example, one set of allowed transitions [47] occurs for the set of angular frequencies $n\omega \pm m\Omega = S(\Omega)/\hbar$, with n integer, $m \in \frac{1}{2}, 1$, and the transition frequency is $S(\Omega)/h$. As before, loss occurs for any $S(\Omega)/h = f_p$, where

⁸It is even possible to use a portable hand-held spectrum analyser and pickup coil in a ‘mine-sweeper’ configuration to find the electronic unit responsible.

⁹Very high amplitudes also lead to loss due to the vanishing radial confinement, which pushes atoms to the node of coupling strength at the top of the resonant spheroid where non-adiabatic following cannot be maintained.

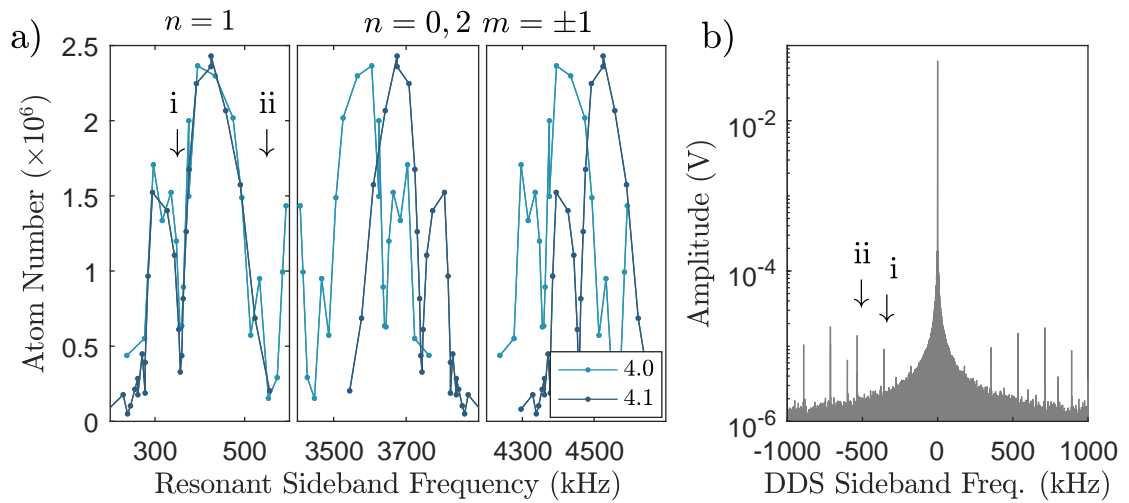


Figure 4.3: **Rabi spectroscopy**: A technique to characterise external rf noise. **a)** The atom number remaining in the shell trap after 8 s of hold duration is plotted against possible dressing rf sideband frequencies that would be resonant with atomic transitions. The amplitude and frequency of the dressing field are varied; here, $\omega = 2\pi \times 4.0, 4.1$ MHz are shown over a range of amplitudes. Loss features for each dressing frequency coincide at *i* and *ii*. **b)** The output spectrum of the dressing rf DDS source. Two sidebands have been identified with the atom loss features *i* and *ii*. These spurious peaks were large enough to be clearly visible on the Fourier transform of an oscilloscope.

f_p is the frequency of the rf noise. Observing atom loss at a given Rabi frequency $\Omega/2\pi$ does not uniquely identify the frequency responsible; a second measurement at a different dressing frequency is required to determine both n and m .

We consider a particularly problematic case in detail. Atom loss arose from a series of sidebands on the dressing rf DDS source, where $f_p = \omega/2\pi + f_s$ and the sideband frequency f_s was fixed. The condition for resonance $S(\Omega) = f_p$ implies that observed loss at known Ω and ω suggests that candidate sideband frequencies at $2\pi f_s(n, m) = |(n - 1)\omega \pm m\Omega|$ are suspect. To observe loss, we held a thermal cloud at a temperature of 1 μ K in a shell trap for 8 s and measured the remaining atom number at different dressing field frequencies and amplitudes. Fig 4.3a shows the result of plotting the atom number versus candidate frequencies $f_s(n, m)$. It is immediately clear that the loss features of 4.0 MHz and 4.1 MHz only overlap at $f_s = 350, 560$ kHz. Upon inspection, these sidebands were clearly visible in the DDS's output spectrum (Fig 4.3b). Even though their amplitudes are almost four orders of magnitude below the carrier, they cause significant loss. The wide-band impedance match used for our multiple-rf dressing does not filter these sidebands. They arose from an embedded 5 V SMPS inside the DDS crate, and vanished (along with the atom loss) once this was replaced with a linear supply.

In general an ‘unclean’ spectrum will not have just one unwanted noise source, but many. This can complicate the interpretation of such spectra, or even entirely obfuscate the picture. However, we were fortunate that each spurious component had a very different amplitude, and so caused very different atom loss rates. Starting at timescales of milliseconds, identifying and cleaning noise, then repeating at longer hold times allows each noise source to be addressed in turn. This technique was frequently used to identify a number of noise sources, most of them due to SMPS. A notable source of rf noise that we could identify but not completely remove arose from the 10 kW Magnapower high current coil supply. This radiated many harmonics

of 37 kHz through the quadrupole coils, creating a field at the atoms. Disassembling the supply showed that this noise arose from an enormous 1 V ripple on a 5 V power rail, sourced from a SMPS internal to the device¹⁰. Our hypothesis is that the large ripple results from component degradation, a likely candidate being capacitors inside the SMPS filter stage of this decades-old device.

For most of the work described in this thesis, we worked around this irremovable noise source. The amplitude of the noise was attenuated by filtering through two ceramic capacitors in Y-configuration between the output terminals and ground, which sufficiently reduced the loss rate to undertake the work here. Atom loss still occurs during ramps of the dressing rf amplitude if transitions pass through resonance with the stronger harmonics of this fixed noise source; a discontinuity was added to our ramps to ‘hop’ over these resonances, with a compromise found between reducing atom loss and the heating that results from the kick. Since the completion of this work, the Magnapower high current supply has been replaced with two Delta Elektronika *SM 15-400* running in parallel, finally removing this noise from the spectrum.

4.2.2 Intermodulation products

The same considerations regarding spurious noise can be extended to intermodulation products, which are additional frequency components that result from non-linear mixing in the rf amplifiers. They occur at angular frequencies

$$\omega_{\text{imp}} = n_1\omega_1 + n_2\omega_2 + n_3\omega_3, \quad n_1, n_2, n_3 \in \mathbb{Z} \quad (4.2)$$

As with spurious noise, these weak field components cause atom loss when resonant with atomic transitions and are unwanted. In producing the double-well potential we choose three dressing frequencies that are integer multiples of a common fundamental,

¹⁰I am grateful to Bob Collins and Miles Wright from Magnapower for providing schematics.

$\Delta\omega$. The intermodulation products then only occur at $\omega_{\text{imp}} = n\Delta\omega, n \in \mathbb{Z}$. As $\hbar\Delta\omega$ is equal to the periodicity of the ladder of dressed eigenenergies, these intermodulation products can only drive transitions to an equivalent eigenstate in another manifold, and no atom loss occurs.

4.3 A double-well potential with 6.7 μm separation

After removing rf noise we were able to successfully load a double-well potential with a smaller well separation. The dressing rf frequency separation was reduced from 0.6 MHz to 0.2 MHz and the quadrupole gradient increased to $B' = 219 \text{ G cm}^{-1}$, giving a separation of 6.7 μm between the wells. The dressing field components at frequencies 3.6 MHz, 3.8 MHz and 4.0 MHz were calibrated using the general procedure outlined in the apparatus section, as were the pickup coils. In this section, we unambiguously prove that the population is split between the wells at this smaller separation, even though the individual wells cannot be resolved *in situ*. By splitting a condensate, we see matter-wave interference with a fringe spacing consistent with the expected well separation.

4.3.1 Loading atoms into the double-well potential

Our procedure follows our previous work at wider separation [21, 22], and the final sequence is shown in Fig 4.4. We start with atoms in a linearly-polarised single frequency shell trap, $\omega_1 = 2\pi \times 3.6 \text{ MHz}$ and $B_1 \approx 500 \text{ mG}$, which forms half of the double-well potential.

- First, we ramp up (from zero) the amplitude B_3 of an additional $\omega_3 = 2\pi \times 4.0 \text{ MHz}$ dressing rf field while reducing the amplitude B_1 , which is performed adiabatically to minimize heating. This second dressing field produces the avoided crossing that constitutes the second potential well, although the eigen-

states corresponding to potential minima at each resonance are not yet connected.

- We apply the $\omega_2 = 2\pi \times 3.8$ MHz field, creating the ‘barrier’ avoided crossing that links the eigenstates of each well to form the double-well potential. Significant atom loss occurs when the amplitude $B_2 = 100$ mG, which appears to arise from resonance with the remaining noise on the quadrupole coil supply. To avoid loss, we turn on the rf field at an amplitude $B_2 = 230$ mG. This is not ideal as the sudden change in the potential kicks the atoms, but the resulting heating is preferable to loss.
- B_2 is increased to lower the barrier, allowing atoms to distribute between the two wells, and after a wait to establish equilibrium we reduce B_2 to raise the barrier and separate the wells.

Typical final values are $B_1, B_2, B_3 = 277, 353, 337$ mG, where $B_1 \neq B_3$ compensates the different gravitational potential energy of each well. The entire process is performed with a shorter duration compared to ramps at larger separations; the trap frequencies are higher due to lower Rabi frequencies and higher quadrupole gradients, and the atoms are transported over a smaller distance, all of which permit adiabaticity on shorter timescales. These faster times reduce the impact of the remaining rf noise on atom number.

4.3.2 Distinguishing the wells

The double-well potential is too small to resolve in-situ using the horizontal imaging system¹¹. Instead, atoms from each well are first separated in time-of-flight, after imparting a different velocity kick to each population during release, before an absorption image is taken on our horizontal imaging system. This permits standard

¹¹it is not possible to use the vertical imaging system as the two wells are displaced along the vertical direction

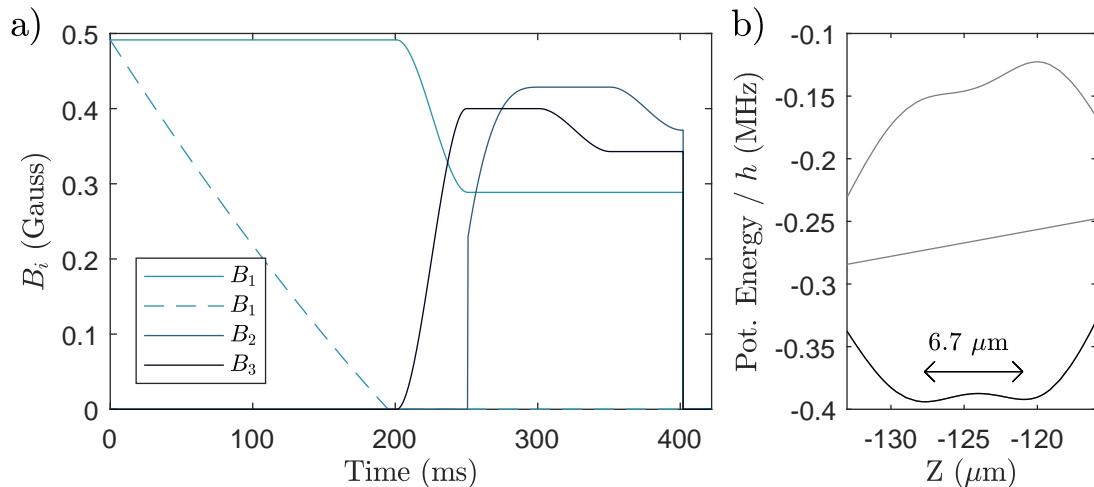


Figure 4.4: **Splitting protocol:** **a)** $B_i(t)$ amplitude ramps used to split a BEC between the double-well potential. The dashed line is the amplitude of the perpendicular coil which is ramped off to provide a linearly polarised dressing field after initially loading the TAAP with circular polarised rf. **b)** The double-well potential immediately before atoms are released.

time-of-flight analysis techniques to determine the characteristics of atoms in each well, such as temperature, subject to the assumption that the kick is evenly distributed across each cloud.

To impart the kick, we ramp down the strength of the quadrupole field quickly to 90% of its original value over 1 ms, then turn off the quadrupole field to release the trap. This quadrupole gradient ramp sweeps the resonant spheroids outwards, faster than the atomic motion can follow, which displaces the atoms from their potential minima and exerts a force equal to the gradient of the potential. The final momentum kick is the integral of this force during the ramp, and although atoms in each well are trapped on the same eigenstate the bounds of this integral differ between the upper and lower wells. The resulting kicks are different enough that the two clouds separate faster than each cloud's thermal expansion at the typical temperatures of $0.5 \mu\text{K}$ used, so that after 5 ms the two clouds are clearly distinguished. Longer time-of-flights reduce the optical depth and thus the signal-to-noise ratio, but only

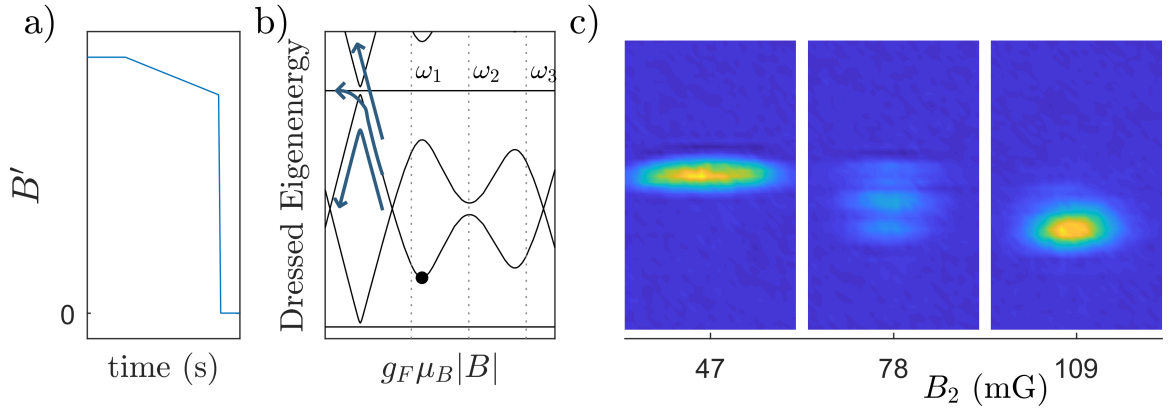


Figure 4.5: **Artefacts in time-of-flight images:** See text for details. **a)** Sketch of the quadrupole field as a function of time, showing slow ramp before a sudden turn off. **b)** The dressed eigenenergies as a function of Zeeman splitting. Atoms (dot) follow the eigenstates as the quadrupole field collapses, and may transition (blue arrows) to other states at the weak crossing near $\omega_1 - \Delta\omega$. **c)** Time-of-flight absorption images of thermal atoms. Crossover between adiabatic and diabatic following at turnoff occurs near 78 mG. Each eigenstate is kicked differently as the field collapses, changing the final position of the cloud.

marginally improve the distinction between the already well separated clouds. We note the kicks are such that the wells swap their vertical order, with the (*in situ* lower) ω_3 well appearing above the ω_1 well in time-of-flight.

Care must be exercised when interpreting the time-of-flight images, and we have observed artefacts that can be particularly confusing (see Fig 4.5). Separate clouds appear after time-of-flight for small amplitudes of B_2 that are insufficient to lower the barrier and thus load both wells, and the population distribution between the clouds is itself a function of B_2 . This artefact is particularly confusing as the observed behavior is similar to that of tipping atoms from one well to the other over a lowered barrier. We attribute the artefact to atoms from the ω_1 well either diabatically or adiabatically passing through the weak avoided crossing near $\hbar(\omega_1 - \Delta\omega) = g_F\mu_B B(r)$ during the fast ramp of the quadrupole field. If B_2 is sufficiently large atoms will adiabatically follow the higher order avoided crossing near $\omega_1 - \Delta\omega$, otherwise flipping to a new eigenstate. These eigenstates exert different forces on the atoms as the quadrupole

field continues to collapse, and under time-of-flight these kicks are transformed into different final positions. Fortunately, the crossover between these adiabatic or diabatic regimes occurs at a relatively low B_2 of around 85 mG for the parameter range discussed here. Above this, the behaviour is predominantly adiabatic and there is no ambiguity. This is sufficiently far removed from the range of interest where B_2 is large enough to flatten the barrier, which occurs for values $B_2 > 340$ mG.

Although it is often useful to separate the clouds after time-of-flight, this is not always desired. Overlap is required for matter-wave interference, which we achieve by turning off the rf field and keeping the quadrupole gradient on during time-of-flight. This projects atoms from the trapped dressed state into different Zeeman substates. Atoms in the high-field seeking state $|m_F = 1\rangle$ are quickly ejected from the quadrupole field, vanishing only after a short time-of-flight. The low-field seeking state $|m_F = -1\rangle$ remains trapped, but is not useful here. The $|m_F = 0\rangle$ states from each well fall freely together, and overlap as each cloud expands. A downside of this method is that only a fraction of the atoms are projected into the $|m_F = 0\rangle$ state we observe, which reduces the signal to noise ratio. For our current work this limitation is insignificant compared to those of imaging resolution and condensate fraction (see Sec 4.5.1).

In light of the misleading artefacts arising in the horizontal imaging, we sought an independent measurement to verify when the population has been split between the two wells, and to identify which distributions in the absorption images correspond to the populations of each well. The rf spectroscopy technique is once more well suited for this task. As already noted, balancing the potential energy of each well requires that the amplitudes B_1 and B_3 are different to compensate for gravitational potential energy. Consequently, atoms in each well have different rf transitions, and each population is independently addressable.

We perform rf spectroscopy on a cloud of thermal atoms at a temperature of

0.3 μK after loading the double-well potential with a balanced atom distribution (see Fig 4.6). Before applying the rf probe the barrier is raised to separate the two potential wells, which prevents the redistribution of atoms between the wells when a resonant rf probe induces loss in one of them. The weak rf probe is applied for a duration of 40 ms, after which the quadrupole field is switched off to remove the confinement. Atoms are imaged after 5 ms time-of-flight, allowing the population from each well to separate into two resolvable distributions as before. We count the measured atom number in these two regions of the image, and take this as a measure of the number of atoms remaining in each well. An example absorption image is shown in Fig 4.6c, along with the regions of interest for each well. A clear signal is visible, with distinct resonances for each cloud identified in the absorption image. The observed resonance features show excellent agreement with the first-order calculated candidate transition frequencies, as shown in Fig 4.6, verifying that the different clouds correspond to atoms from each well. A small amount of ‘cross-talk’ is apparent between the measured atom numbers of each well, which is likely to be an artefact of the image analysis.

There may also be evidence of a higher-order transition for the lower well, labelled ‘v’ on the figure. This resonance occurs at the frequency predicted for a three-photon transition, $3\omega_p = 0.102$ MHz. This transition is expected to have a narrower lineshape, here reduced by a factor of three, however the current data is not of sufficient quality to assert with confidence that we have observed this higher-order process. As before, we stress that our current numerical model, based on a semi-classical Floquet theory, cannot be used to identify which transitions are allowed. It can only provide candidate frequencies, based on the energy separation between dressed eigenstates, with no regard to selection rules. Clearly, not all candidate transitions are observed in the spectra, and some may correspond to forbidden processes. Nonetheless, we are able to identify a number of transitions unambiguously. Their occurrence at such low rf

probe frequencies emphasises the importance of our earlier work to clear the spectrum of noise; a dense forest of transitions exists, with many opportunities for extraneous noise to have a deleterious effect on atom number in either well. For our particular case, it shows that the spectrum must be clear over an almost continuous range from 80 kHz to 120 kHz to avoid loss in either well - and this only corresponds to the region we actively probed, with many other transitions likely elsewhere.

4.3.3 Balancing the potential

We use the following procedure to find suitable rf amplitudes that produce a balanced double-well potential, working with thermal atoms at a temperature of $0.5 \mu\text{K}$ and resolving the wells in time-of-flight. First, a value of B_2 that flattens the barrier is found; we begin by deliberately unbalancing the potential energy of the two wells, choosing a small value of B_3 so that the 4.0 MHz well is energetically lower. We then sweep the final barrier depth of each sequence by changing the maximum of B_2 . When B_2 is sufficiently high that the barrier becomes flat, atoms are violently decanted from the 3.6 MHz well into the 4.0 MHz well, which is clear to see from the velocity distribution of the cloud after 10 ms time-of-flight. Taking this value of B_2 as our maximum, we rebalance the potential energy minima of both wells, setting B_3 to a value that compensates for the difference in gravitational potential energy. To achieve an even load, we compare sequences with different amplitudes B_3 , which adjusts the potential energy difference of each minimum and affects how the population distributes between them during the split (see Fig 4.7). As a further aide, we record the pickup coil trace each experiment, extract the amplitudes and phases of the multiple rf field, and use the semi-classical Floquet theory to calculate the dressed potential. This approach allows us to quickly converge on our target potential after only a few iterations.

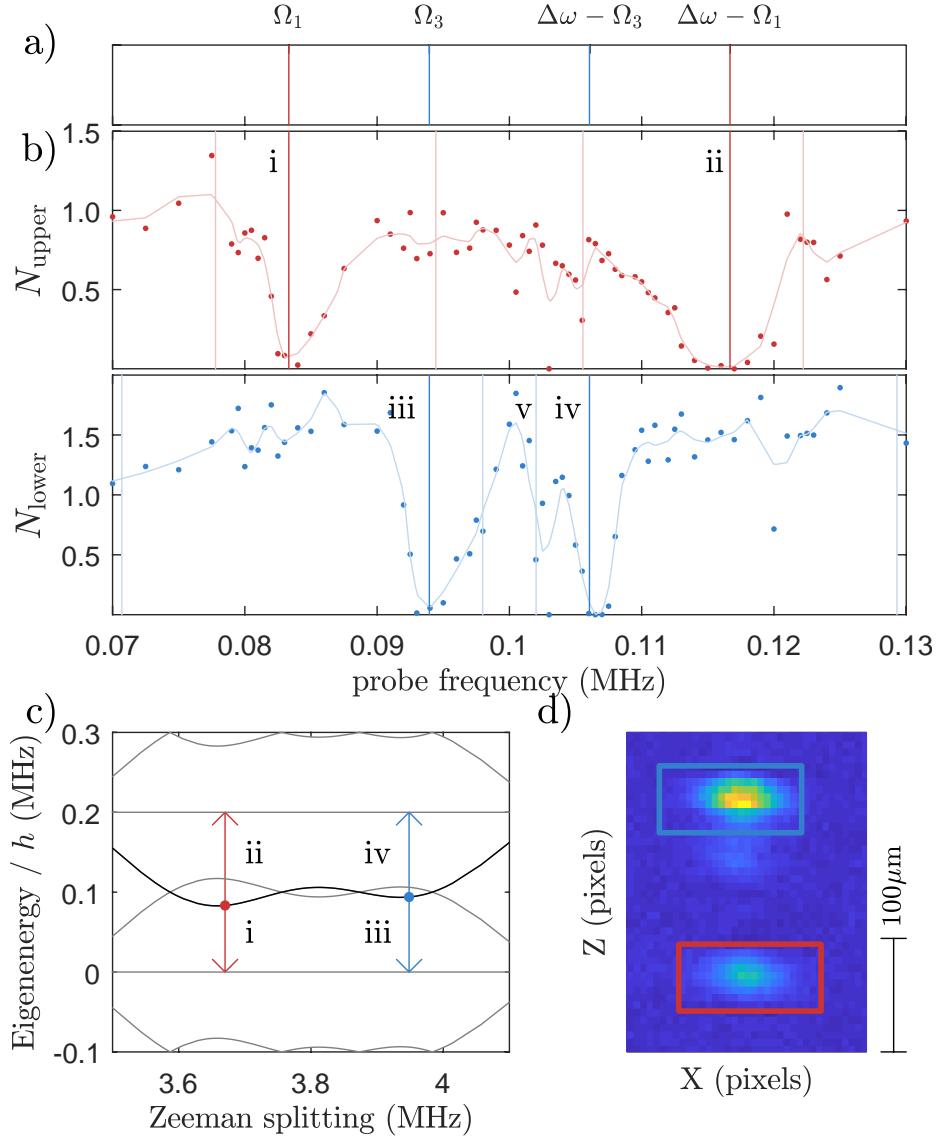


Figure 4.6: **rf spectroscopy in the double-well potential:** **a)** Spectrum of predicted first-order transitions in each well, labelled by analytic quantities (factors of 2π omitted for clarity). **b)** Points correspond to measured atom number remaining in each well after applying an rf probe to a thermal cloud for a duration of 40 ms. A trendline has been added to each set as a guide to the eye; it represents a moving average over points. Heavy vertical lines correspond to expected transition frequencies inferred from the separation between dressed eigenstates. Light lines show $3 \times \omega_p/2\pi$ for candidate higher order transitions. Selected transitions have been labelled. **c)** Calculated dressed eigenenergies used in (a). Dots indicate the position of atoms, including gravitational sag. Arrows identify transitions responsible for the resonance features i-iv in (a). **d)** Example absorption image showing regions of interest used for analysis.

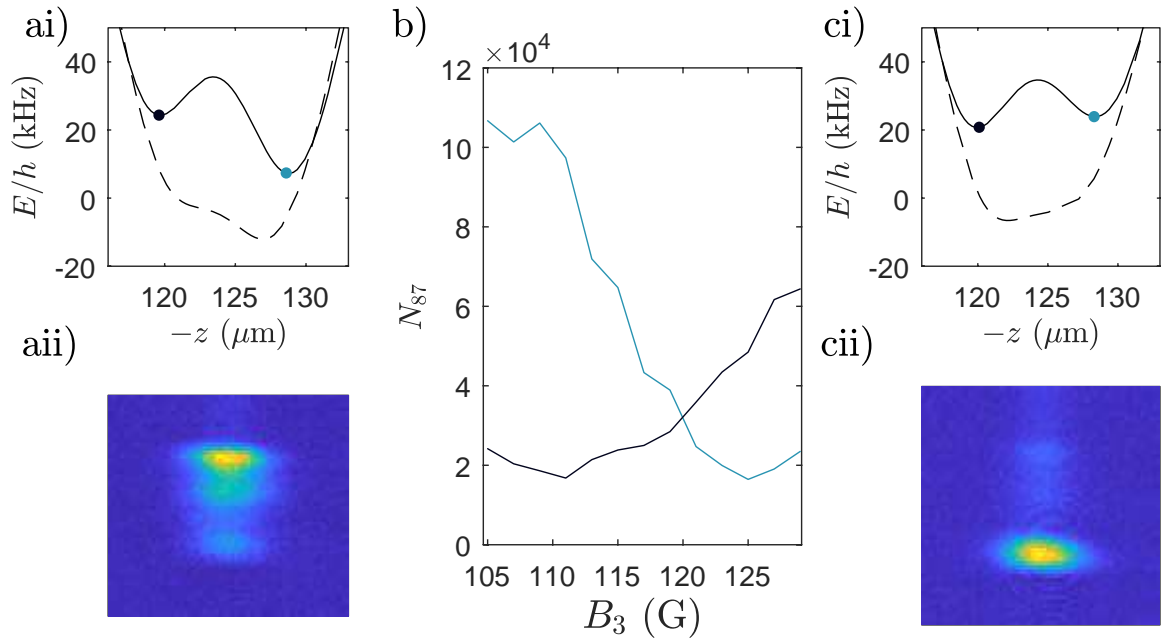


Figure 4.7: **Manipulating the double-well potential:** The rf amplitude B_3 adjusts the potential energy of the lower well, which alters the equilibrium distribution of atoms between the wells when the barrier is lowered. **ai,ci)** The potential energy at the end of the sequence (solid) and when the barrier is lowest (dashed), for $B_3 = 105, 130$ mG respectively. **aii,cii)** Corresponding absorption images after 5 ms time-of-flight. **b)** Atom number in each well measured from absorption images as a function of B_3 . The color indicates which of the two wells in ai and ci each line corresponds to.

4.4 Matter-wave interference

Once balanced loading is achieved with thermal atoms, we use the same sequence to load a BEC into the double-well potential. Fine adjustment to B_3 is usually required at this stage to split the condensate evenly, since it has a lower energy scale than the thermal cloud and is thus more sensitive to an imbalance in the potential minima. The ramps are further optimised to minimise the rate of change of the potential, and so reduce heating. We lower the maximum amplitude of B_2 to the minimum required to split the wells, and increase the final value of B_2 to the maximum that still separates the wells. This guarantees the full duration of the final ramp is used in the critical splitting process.

The final rf evaporation cut is made in the TAAP stage of the experimental sequence; the BEC is loaded from the TAAP to the circular polarised shell, then to the linearly-polarised shell, then to the double-well potential without further evaporation. Heating during this loading reduces the condensate fraction, and typically a large thermal component is also visible at the end of the sequence. In spite of this, a clear bimodal distribution¹² is visible after time-of-flight expansion for the populations of each well (*eg* see Fig 4.8a), as is the inversion of aspect ratio that is characteristic for expansion of the BEC component [84].

To observe interference, we release the clouds by turning off the dressing rf field while leaving the quadrupole field on, so that the atoms projected into the $|m_F = 0\rangle$ state from each well overlap as they fall under gravity, as previously described. A fringe pattern is observed, resulting from matter-wave interference between the separate condensates in each well as they expand and overlap in time of flight, as shown in Fig 4.8. The fringes align perpendicular to the separation of the wells, as expected. For comparison, Fig 4.8b shows an image from a sequence in which splitting does not occur - a condensate is released from only one of the wells and no fringes are visible.

¹²Thomas-Fermi for the BEC component, Gaussian wings for the thermal cloud

To process the images, we examine columns of pixels from each image that incorporate the condensate. Each column is a measurement of optical density $OD(z)$ perpendicular to the fringes, from which we can extract the periodicity by taking the Fourier transform. In Fig 4.8c, we plot the average $OD(z)$ for all columns in an image, and in Fig 4.8d we show the overlaid Fourier transforms from 9 such columns (light grey). Averaging the spectral power over a number of images decreases the relative power of the random background noise, improving the signal to noise ratio (black line of Fig 4.8d). The peak at a wavelength of $(15.6 \pm 0.8) \mu\text{m}$ corresponds to the Fourier component of the interference fringes, with stated error corresponding to the half-width half-maximum of the peak. It is only visible for sequences in which a BEC is split by the double-well potential. The fringe periodicity for matter-wave interference is equal to $\lambda_z = ht/md$, for particles of mass m , time-of-flight duration t and well spacing d [85]. The observed period corresponds to a distance between the wells of $(6.8 \pm 0.4) \mu\text{m}$ for the 23 ms time of flight. Using the pickup coils to measure the amplitude and relative phase of the rf components, we calculate the dressed eigenstates at the instant before our condensates are released from the double-well potential. This gives a predicted double-well separation of $6.7 \mu\text{m}$ (see Fig 4.4), in good agreement with the value determined from the interference pattern.

While we have observed matter-wave interference, we admit that the contrast is extremely poor. A number of suggestions to improve the visibility are made in the outlook.

4.5 Conclusion and Outlook

Our results prove that multiple-rf dressing is a useful technique, able to create a double-well potential with sufficiently small separation to observe matter-wave interferometry. Combined with the anisotropic confinement of the shell trap, the poten-

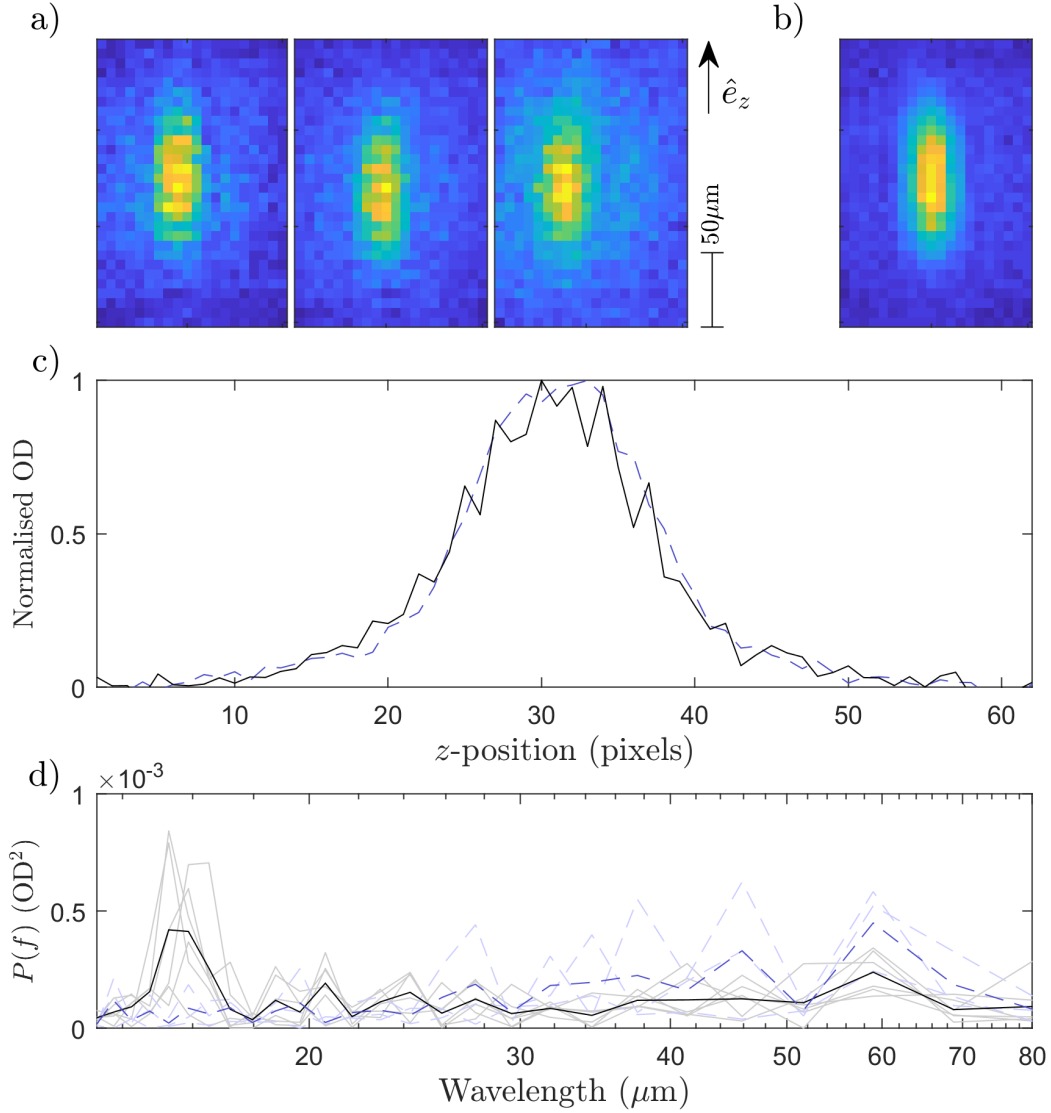


Figure 4.8: **Signature of matter-wave interferometry:** **a)** Three separate absorption images of split BECs released from the double-well potential and overlapped after time-of-flight expansion. Interference fringes are visible, aligned perpendicular to the vertical direction \vec{e}_z . **b)** Absorption image when only one of the wells is populated - no pattern is visible. **c)** Optical density (OD) integrated over horizontal slices as a function of vertical position. The solid line depicts the profile of a fringe pattern (first image of subfigure a) while the dashed line shows an image without interference for comparison (subfigure b). **d)** The power $P(f)$ of Fourier components along \vec{e}_z , in units of optical density squared, measured from a Fourier transform of the optical density profile for each pixel column containing the fringe pattern. Light grey lines depict the noisier measurements from each individual column. The solid black line shows the average power from the images in subfigure a, revealing a prominent peak at $15.6\mu\text{m}$. The dashed lines are analogous for the control image without fringes (subfigure b).

tial could be harnessed to make interferometric measurements of phase fluctuations in two-dimensional potentials, analogous to those that have been performed for one-dimensional systems using rf dressed potentials on an atom chip [86, 87, 88, 89, 90]. There is currently great theoretical interest in extending this to two-dimensional experiments [91, 92, 93, 94]. Further work is required before the apparatus is ready for such physics experiments, and to determine if the splitting is coherent, and we discuss the next steps here.

4.5.1 Improving the quality of the fringes

Future interferometric experiments will require a significantly improved resolution and contrast ratio compared to the interference fringes shown here. Fortunately, a great enhancement to our apparatus is possible through a simple upgrade of the optical system used to repump and image the atoms.

The horizontal imaging system was constructed to monitor and diagnose issues with transport from the MOT chamber and evaporation to BEC in the TOP trap. It was designed to image large clouds at both short and long time-of-flights, with a $\times 1$ magnification to give a wide field-of-view. The $6.5\ \mu\text{m}$ size of a pixel in image space is well above the diffraction limit of our 25 mm diameter, 10 cm focal-length objective. A straightforward improvement to the imaging resolution could be achieved by increasing the magnification by a factor of 2. Greater magnification is also possible, but requires more careful design as the diffraction limit is approached, or other limitations such as spherical aberration by the walls of the glass cell.

A second, complementary approach is to expand the fringes with a longer time-of-flight t , exploiting that the fringe wavelength $\lambda \propto t$. The maximum t used in this work was limited by the field of view, but a new purpose built system could observe longer fall times, with t limited only by the fall time for atoms to reach the bottom of the glass cell. In principle, up to around 50 ms is possible in our apparatus, more

than doubling the fringe spacing. Use of a levitation scheme would permit even longer times.

A third improvement is to selectively repump only atoms in a thin plane, normal to the imaging direction. This method prevents fluctuations in the phase of the fringes along the direction of the imaging system from reducing the observed fringe contrast. Andrews *et. al.* attributed the high visibility of their interference fringes to this technique [85].

Finally, further development of the sequences we use to load condensates into the double-well potential will increase the fringe visibility by reducing the large thermal population. For the sequences used here, evaporation to BEC in the TAAP trap finished half a second before the atoms were released, and even for our low heating rate this reduces the condensate fraction. In future, a second stage of rf evaporation will be performed when atoms are in the double-well potential but before the splitting, thus regenerating a high condensate fraction to improve contrast. The results of rf spectroscopy in the multiple-rf dressed potential shows this technique is feasible.

These upgrades will allow us to determine whether the splitting process is coherent or not. Improving the fringe visibility is a vital step towards increasing the information that can be extracted from the fringes as required for more detailed interferometry experiments.

4.5.2 Stability of the double-well potential

The stability of the dressing rf fields required to produce the double-well potential pose a limitation to the current apparatus, which relies on passive stability of the rf amplifiers and impedance matching network to ensure the dressing rf amplitudes do not drift with time. Long-term variations in the radiated rf power change the dressing rf Rabi frequencies by kHz, imbalancing the double-well potential. Fig 4.9a shows the drifts in the amplitudes of the three-frequency field as measured using the pickup coil.

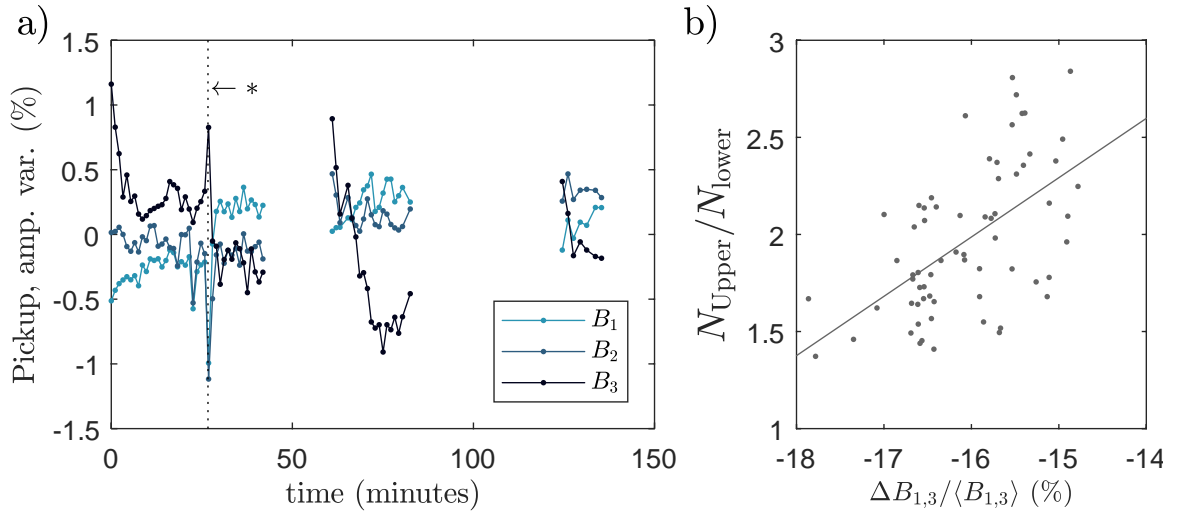


Figure 4.9: **Stability of the MRF double-well potential:** see text for discussion. **a)** Drift in the dressing rf amplitudes over a long period of operation. The asterisk shows a ‘mode-hop’ in the amplifier output. **b)** The ratio of atoms in the top and bottom well, as a function of the difference in the drifting amplitudes $\Delta B_{1,3}/\langle B_{1,3} \rangle$ (see text for definition). The straight line is a least squares fit, and the correlation coefficient is 0.57.

Discrete ‘mode hops’ are observed to occur in the rf amplifier, with one such event indicated with an asterisk. The effect of these drifts on the distribution of atoms between the wells is shown in Fig 4.9b where we plot the ratio of atoms in each well, as a function of $\Delta B_{1,3}/\langle B_{1,3} \rangle = 2(B_3 - B_1)/\langle B_3 + B_1 \rangle$, with the average $\langle B_1 + B_3 \rangle$ taken over the entire series; the drift in the amplitude difference of a few percent is enough to imbalance the double-well potential, and a correlation is observed in the ratio of atoms split between the wells.

To achieve a more stable operation active feedback should be implemented. Each rf amplitude could be measured from the pickup waveform using lock-in amplification or equivalent digital techniques. A simple PID loop could then servo the amplitude of each frequency component using a voltage controlled attenuator.

4.5.3 Towards quantum tunnelling

A key feature of quantum double-well potentials is tunnelling and it will be possible to achieve this with a further reduction in the distance between the wells. Theoretically tunnelling always occurs, since an atom localised in one side of a double-well potential must be in a superposition of the lowest energy odd and even eigenstates [95]. The tunnelling rate $J = \Delta E/\hbar$, where ΔE is the difference between the odd and even eigenenergies. When the barrier in the double-well potential is high these energies are nearly degenerate, and the tunnelling rate is extremely low.

To estimate achievable tunnelling rates we numerically solve the time-independent Schrödinger equation for a single ^{87}Rb atom moving in the double-well potential, using the Shooting method [96]. The numerics are verified by comparing numerically calculated wave functions and eigenenergies for a harmonic oscillator potential to their analytic solutions. We neglect gravity, noting that tunnelling favours smaller well separations and so requires higher quadrupole gradients in which the gravitational sag is negligible. Fig 4.10a presents the results of these calculations. Parameters used correspond to a quadrupole gradient along the vertical axis of $2B' = 2 \times 200 \text{ G cm}^{-1}$. The dressing frequencies are 3.5, 3.6, 3.7 MHz with $B_{1,3} = 57 \text{ mG}$, and B_2 in the range 107 to 118 mG. By adjusting B_2 , the tunnelling rate J is adjusted from a negligible value to $\sim 100 \text{ Hz}$. The dotted line in Fig 4.10a marks realistic parameters for an experiment; a rate of $J = 30 \text{ Hz}$ for a barrier height of 30 nK requires temperatures that can be obtained.

Although our apparatus is capable of producing higher quadrupole gradients, we chose a conservative value of $B' = 200 \text{ G cm}^{-1}$ in combination with these rf amplitudes to ensure that the constraint for adiabatic following is satisfied, providing a sufficiently long lifetime for the trapped atoms; this constraint is stressed at greater B' and lower rf amplitudes. For comparison, lifetimes of many seconds have been reported for a single rf trap at a steeper gradient of $B' = 216 \text{ G cm}^{-1}$ and smaller

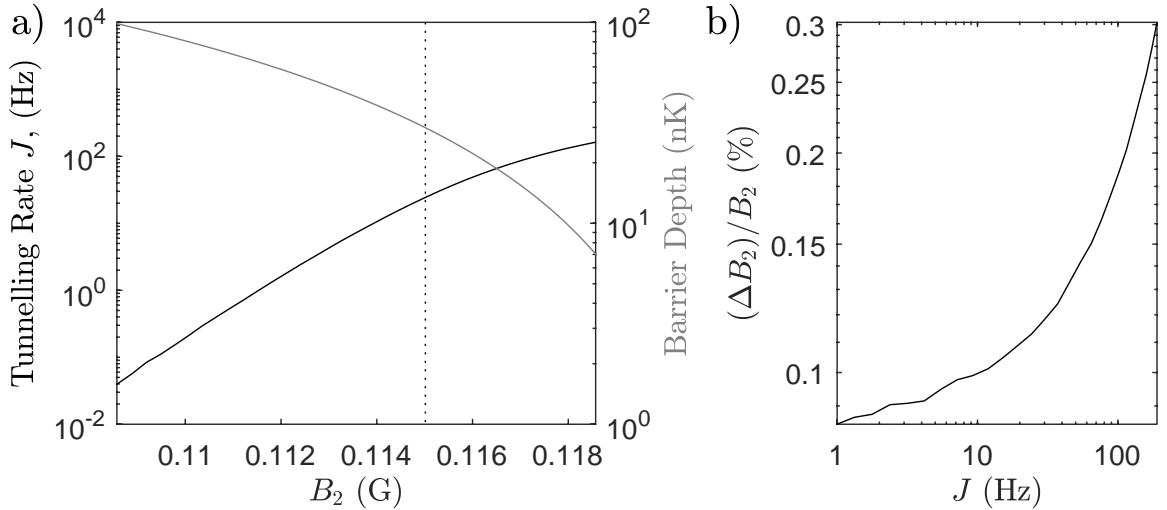


Figure 4.10: **Predicted tunneling rates in the multiple rf double-well potential:** see text for parameters. **a)** Calculated tunneling rates J and barrier height as a function of the amplitude B_2 of the rf field. **b)** The relative stability of B_2 required to keep fluctuations in the tunnelling rate ΔJ below 10% of the rate J .

ressing rf amplitude of Rabi frequency 27 kHz (39 mG) [19]. These estimates show that tunnelling at an observable rate is possible within this adiabaticity constraint. It is likely that pushing these limits further will lead to even faster tunnelling rates.

It is also important to consider the experimental feasibility of the tunnelling scheme. For example, drifts or instability in the rf amplitudes cause the dressed eigenenergies to fluctuate, varying the barrier height and consequently the tunnelling rate. With sufficiently large variations the rate changes to such an extent that the oscillatory behaviour is ‘washed out’ and tunnelling cannot be observed between consecutive single-shot experiments. As a measure of the resilience of this scheme we determine a threshold amount of rate fluctuation ΔJ that is tolerable, taking $\Delta J/J \approx 0.1$ to allow a number of oscillations to be observed. The derivative $\partial B_2/\partial J$ is numerically computed and used to determine the rf amplitude fluctuation $\Delta B_2 = \Delta J(\partial B_2/\partial J)$ that would cause this fractional variation of tunnelling rate, plotted in Fig 4.10b. This suggests that amplitude stability on the order of 10^{-3} is required; this is beyond the present capabilities of the apparatus, but achievable with active feedback.

Chapter 5

Species-Selective rf-dressed potentials

There are many applications for species-selective potentials, and this chapter describes the strengths of using rf-dressed potentials for this purpose. It has been shown previously that the polarisation of an rf field can be used to manipulate different hyperfine states. We show that a single-frequency rf field combined with a time-averaging field can also be used to independently manipulate species with different $|g_F|$, and demonstrate elementary species-selective manipulations of ^{85}Rb and ^{87}Rb . We extend the discussion to include multiple radiofrequency dressed potentials, proposing double-well potentials in which two species can be independently manipulated. One approach is suitable for different hyperfine states and the other for species where $|g_F|$ differs, such as isotopes [97]. We also examine practical aspects, and demonstrate schemes to load these potentials from the TAAP.

5.1 Introduction

Advances in the experimental techniques used to manipulate ultracold atomic gas mixtures have opened new pathways for the exploration of many-body quantum

physics [98, 99, 8], thermodynamics [100, 101], and the formation of ultracold molecules [102, 59, 103]. Quantum simulation experiments that use mixtures of atomic species promise new insight into the behaviour of impurities coupled to larger quantum systems. Experiments in this field have observed non-equilibrium dynamics [8, 9], polaronic phenomena [10, 11] and the disruption and localisation of phases by scattered impurities [12], while control over individual impurities has led to the successful doping of cold gases with single atoms [13, 14]. Using the impurities as a probe of the larger system presents many prospects for future experimental work, including the observation of impurity decoherence [104], Markovianity [105, 106, 107], and the non-destructive probing of reservoir excitations [16] and correlations [108, 109].

Many of these experiments rely on the use of species-selective potentials to give individual control over the constituent species. This is often implemented using optical fields at specific wavelengths chosen to have a stronger interaction with one species than the other [110, 111]. The optical dipole force experienced by an atom depends on the electronic structure, which determines the optical transition frequencies. For some mixtures, the wavelengths required cannot be reconciled with the constraint of a low heating rate, which requires a large frequency detuning of the dipole trap beam to suppress photon scattering. For example, the trapping force is similar for isotopes of the same element at large detunings because the \sim GHz hyperfine structure is not resolved.

An alternative method of species-selective confinement is to use rf dressed potentials, which arise from the interaction between an external magnetic field and the atom's magnetic dipole moment (see Chapter 2). They are species-selective whenever the Landé g_F -factor differs between species. The method is applicable to combinations of species that would otherwise experience similar confinement in optical dipole force traps.

In examining this feature of rf-dressed potentials we consider two scenarios. The

first confines each species in an independent harmonic well, and the wells can be brought together or separated. This elementary species-selective operation moves the species in and out of contact, and provides an alternative way to control the inter-species interactions when a suitable Feshbach resonance is not accessible. Our second scenario incorporates multiple-radiofrequency dressing to produce independently tunable double-well potentials for both species, and the ideas here are readily extensible to more general potentials. The discussed techniques can be broadly categorised into two classes, suitable when either the sign or magnitude of each species' g_F -factor differs. Either method, or a hybrid approach, can be taken for combinations of species where both are different.

5.2 The sign of the Landé g_F -Factor

The first manipulations we discuss apply to mixtures of two species with the same $|g_F|$ but different sign (g_F). Such combinations include alkali atoms in different hyperfine states of their electronic ground state, *eg* $|F = 1\rangle$ and $|F = 2\rangle$ for ^{87}Rb . As single rf manipulations of these mixtures are established in the literature [20, 112, 113] the discussion here will be limited to the bare principles required to understand the later multiple rf manipulations.

In a static quadrupole field, a change in position \vec{r} rotates the direction of the local static magnetic field. Viewed from a frame aligned to the field, this causes a spatial dependency of the magnitude of clockwise and counter-clockwise components of the uniform rf field. In Sec 2.5.1.1, we showed how this gives rise to the concept of a 'coupling strength' that quantifies the strength of atom-photon interactions around the resonant spheroid. Nodes are located at points where the circular polarisation that couples the dressed states in the rotating wave approximation has zero amplitude, and antinodes where it is maximum.

The sign of g_F determines the handedness of the circular polarised rf field that couples the Zeeman states, which arises through conservation of angular momentum¹. It follows that two species of different sign (g_F) interchange nodes and antinodes of coupling strength in a circularly-polarised laboratory rf field, and the derivative of coupling strength thus pushes them in opposite directions. For example, consider an rf field that is circularly polarised about \vec{e}_y ; a force $F = -\tilde{m}_F \hbar (\partial\Omega/\partial y)$ pushes $F = 1$ atoms at the bottom of the resonant spheroid to positive y and $F = 2$ atoms to negative y .

We typically use rf that is circularly-polarised about \vec{e}_z for both the shell and TAAP. Tilting the polarisation axis into the (y, z) plane can be viewed as adding an amplitude of circular polarisation about \vec{e}_y , which thus separates the minima for each species in the \vec{e}_y direction. This technique was used to create state-dependent traps for $F = 1$ and $F = 2$ atoms of ^{87}Rb in ref [113]. By using an elliptical polarisation to independently tune the Rabi frequency for each species at the bottom of the shell, it is also possible to adjust their vertical trap frequencies $\omega_z \propto 1/\sqrt{\Omega}$.

5.3 The magnitude of the Landé g_F -factor

The magnitude of g_F determines the energy difference $\Delta E = g_F \mu_B B$ between Zeeman sublevels in an applied static magnetic field \vec{B} . When two species with different $|g_F|$ are confined at the same location, resonances occur for different rf-dressing frequencies ($g_F \mu_B B(\vec{r}) = \hbar\omega$), thus different dressing frequencies can be used to manipulate each species. The first use of rf-dressed potentials to manipulate two species with different $|g_F|$ was undertaken by Extavour *et. al.* [114]. This atom-chip apparatus simultaneously confined ^{87}Rb and ^{40}K using an Ioffe-Pritchard static magnetic field geometry, in which the static field has a non-zero magnitude at the potential minimum of the trap. The distinct values of $|g_F|$ for ^{87}Rb and ^{40}K result in different Zeeman

¹for more detail, see Sec 2.2

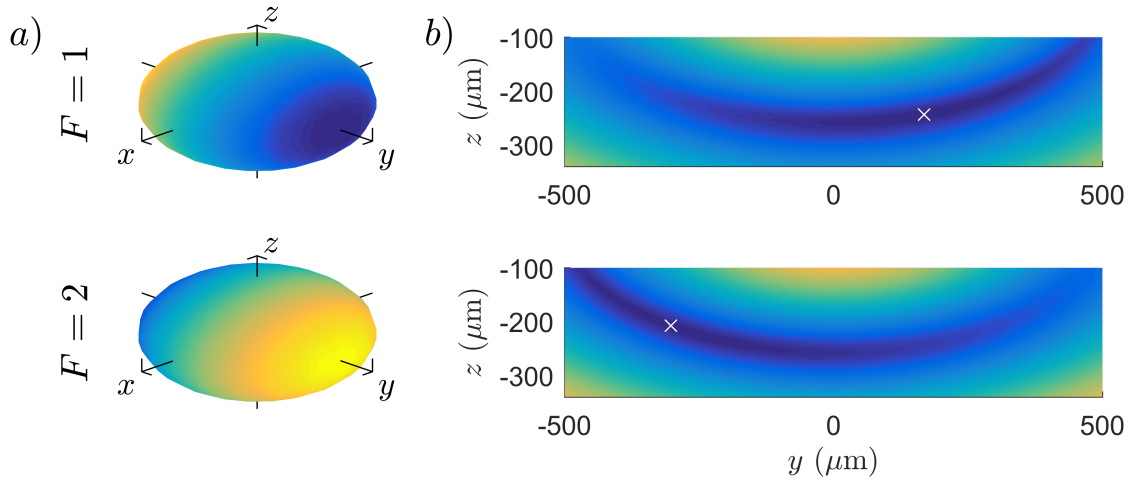


Figure 5.1: **Manipulating species of different sign (g_F) with a single rf:** Two hyperfine ground states of ^{87}Rb are dressed with an rf field that is circularly polarised around \vec{e}_y in the lab frame. **a)** Coupling strength over resonant spheroids of $F = 1$ and $F = 2$. Larger Rabi frequencies are indicated by light, yellow colors and smaller Rabi frequencies by dark, blue colors. Nodes for $F = 1$ ($F = 2$) occur for points along the positive (negative) y -axis. **b)** Potential energies plotted in the plane $x = 0$ for the two states. The minima for each (marked by white crosses) are displaced in opposite directions along the y -axis. Only a portion of the lower hemisphere of the resonant spheroid is shown. Note that the displacement is not symmetric, but larger for $F = 2$ in $\tilde{m}_F = 2$ than for $F = 1$ in $\tilde{m}_F = 1$; the coupling force is larger by a factor of 2.

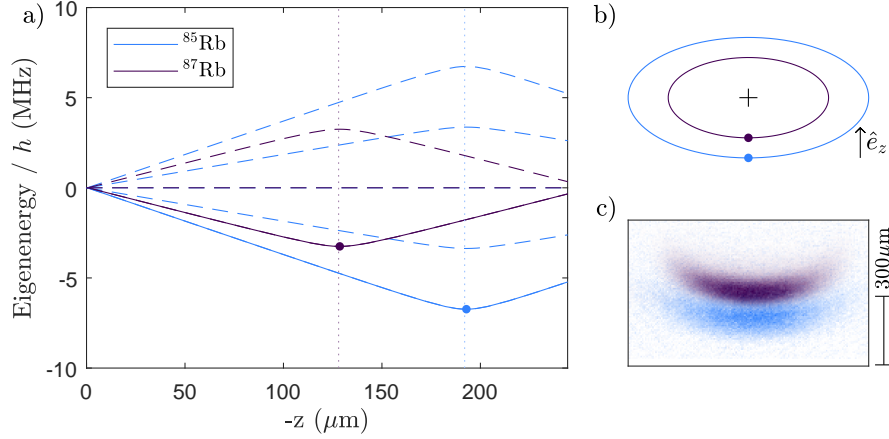


Figure 5.2: **Isotopes in a single-rf shell trap:** **a)** rf-dressed eigenstates of ^{85}Rb and ^{87}Rb in the single frequency shell trap, plotted versus vertical coordinate $z < 0$. A solid dot marks the potential energy minima for each species, trapped on the solid eigenstates, and the position of each resonance is shown by a dotted line. **b)** Illustration of the resonant spheroids for ^{85}Rb and ^{87}Rb , which are coincident but of different radii. **c)** Composite absorption image of ^{85}Rb and ^{87}Rb atoms confined in a single rf shell trap. The image is composed from two absorption images, each with probe light resonant with one of the species.

splittings for each species at the trap bottom. By applying an rf-dressing field resonant with the ^{87}Rb splitting, Extavour *et. al.* were able to create a double-well potential² for ^{87}Rb while only mildly perturbing the ^{40}K , to which the rf was far detuned.

In our experiment, we seek to use rf-dressed potentials to independently manipulate the isotopes ^{85}Rb and ^{87}Rb in their lower hyperfine states, with $g_{\text{F}}^{85} = -1/3$ and $g_{\text{F}}^{87} = -1/2$. To achieve an interaction between these two species requires a spatial overlap between them. Unlike in Extavour's experiment, with our apparatus it is not possible to achieve this overlap using static fields and a single dressing frequency. Atoms are trapped in rf-dressed eigenstates which have energy minima where the rf resonance condition is fulfilled, which for our spherical quadrupole static field occurs on the surface of a resonant spheroid. The issue is immediately apparent on inspection of Fig 5.2a, which shows the dressed eigenenergies as a function of the coordinate

²The double well for ^{87}Rb is formed using the same principles used by Schumm *et. al.* [37]

z . The different values of $|g_F|$ cause the resonance condition for each species to be fulfilled at different positions, thus atoms of each species reside at potential minima on resonant spheroids of different radii. Two species, A and B , trapped in this configuration have a large spatial separation of

$$\Delta z = \frac{\hbar\omega}{2\mu_B B'} \left(\frac{1}{g_F^A} - \frac{1}{g_F^B} \right) \quad (5.1)$$

to first order, where $2B'$ is the quadrupole gradient along the z -axis. The spatial overlap between them is extremely poor, with little interaction possible. Although increasing B' decreases Δz , it also increases the vertical trap frequencies and thus reduces the spatial extent of the cloud in the vertical direction. Furthermore, even if good overlap could be achieved it would not be possible to independently manipulate the two species. For these reasons the single frequency shell trap is not well suited to the manipulation of species with different $|g_F|$.

5.3.1 The Species-Selective TAAP (SSTAAP)

These problems are solved by the inclusion of a time-averaging field, of the same form as used in the TAAP trap (see Sec 3.1.7). The general approach is to load only one of the species into a TAAP, while the other remains in the TOP far detuned from the rf resonance³. Independent control over the TAAP species is possible through a combination of rf-field modifications and small adjustments to B_{TOP} , which only weakly affect the species confined in the TOP. The choice of species that is loaded into the TAAP is determined by the value of B_{TOP} when the rf-dressing field is turned on. We will discuss in detail the particular case where ^{85}Rb is loaded into the TAAP and ^{87}Rb remains in the TOP, taking g_F^{85} and g_F^{87} to be the Landé g_F -factor for each isotope in their lower hyperfine states. The roles of each species are interchangeable

³This is similar to the scheme of Extavour [114] with the rotating field B_{TOP} playing the role of an adjustable bias field.

depending on the loading procedure, as discussed presently in Sec 5.3.1.2.

5.3.1.1 Controlling the overlap

A notable advantage of this scheme is that it allows the overlap between two species to be precisely controlled, moving them from coincidence to completely out of contact. An experimental demonstration is shown in Fig 5.3 for the specific examples of ^{85}Rb and ^{87}Rb in their lower hyperfine states. The vertical positions are determined from a Gaussian fit to the absorption images. A small 1.4 ms time-of-flight is required to completely repump the ^{85}Rb , and some systematic error is expected; the collapsing quadrupole field exerts a small kick on the released atoms, the magnitude of which is unknown and likely varies with trap frequency, itself a function of B_{TOP} . Three distinct situations are apparent, separated by the resonances at $\hbar\omega = g_{\text{F}}^{85}\mu_{\text{B}}B_{\text{TOP}}$ and $\hbar\omega = g_{\text{F}}^{87}\mu_{\text{B}}B_{\text{TOP}}$.

When $B_{\text{TOP}} > \hbar\omega/g_{\text{F}}^{85}\mu_{\text{B}}$, both species are in the TOP trap (see Fig 5.3a). Decreasing B_{TOP} raises the positions of both ^{87}Rb and ^{85}Rb , as expected; the vertical trap frequency $f_z \propto 1/B_{\text{TOP}}$ increases for both species, reducing the gravitational sag of $\Delta z = g/(2\pi f_z)^2$ (see dotted line of Fig 5.3d). For $\hbar\omega/g_{\text{F}}^{87}\mu_{\text{B}} < B_{\text{TOP}} < \hbar\omega/g_{\text{F}}^{85}\mu_{\text{B}}$, ^{85}Rb is held in the TAAP trap and ^{87}Rb in the TOP trap (see Fig 5.3b). The potential minima for both species remain constrained along \vec{e}_z , but the vertical position of ^{85}Rb is here more sensitive to B_{TOP} than that of ^{87}Rb . It is within this range that manipulations are most species-selective. The potential energy minimum for the TAAP-trapped ^{85}Rb occurs approximately at the intersection of the resonant spheroid with the rotation axis \vec{e}_z , located at

$$z_{85} = -\frac{1}{2} \left[\left(\frac{\hbar\omega}{\mu_{\text{B}}g_{\text{F}}^{85}B'} \right)^2 - \left(\frac{B_{\text{TOP}}}{B'} \right)^2 \right]^{\frac{1}{2}} \quad (5.2)$$

Thus ^{85}Rb is lowered with decreasing B_{TOP} while ^{87}Rb continues to rise in the TOP.

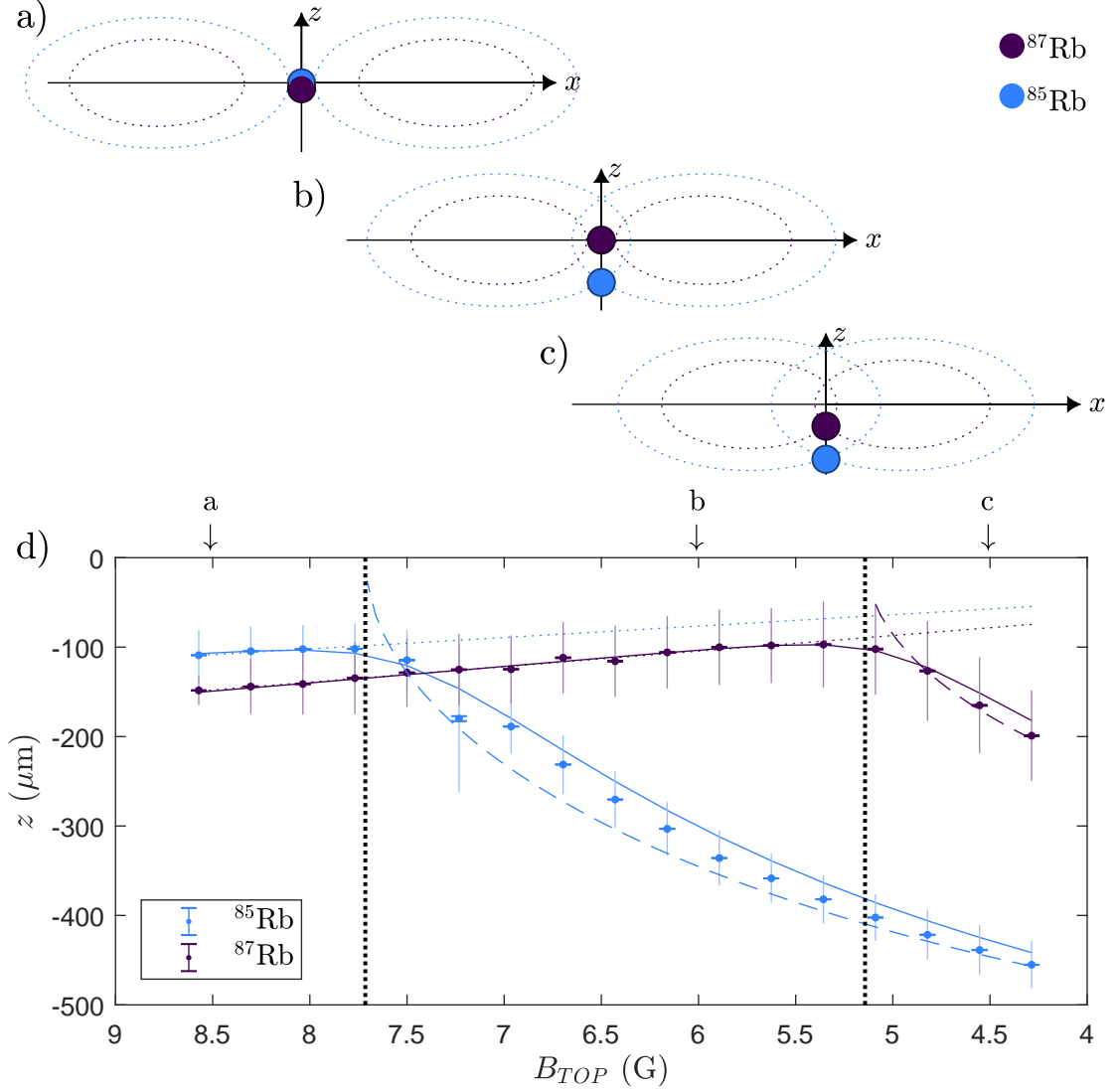


Figure 5.3: **Isotope-selective manipulations using a single rf in the SSTAAP:** (a-c) Illustrations of the SSTAAP at three different values of B_{TOP} (indicated by arrows above d). Resonant spheroids (colour-coded by species, dotted) are shown for TOP field rotation angles of $\theta = 0, \pi$ and the position of each species is depicted by colored circles. d) Measured vertical positions of ^{85}Rb and ^{87}Rb , as a function of B_{TOP} . The 3.6 MHz rf-dressing field has amplitude 0.86 G, and is circularly-polarised in the lab frame. Both species load from the TOP to the TAAP at their respective resonances, which occur at 7.7 G for ^{85}Rb and 5.1 G for ^{87}Rb (dotted, vertical). Measurements are of the fitted centre of the Gaussian cloud. Narrow error bars correspond to the 1σ uncertainty in the fitted position, and the wider bars to the measured FWHM of the thermal cloud. The lines correspond to positions in the TOP trap (dotted), the value of eqn. (5.2) (dashed), and full numerical calculations that include gravitational sag and the variation of coupling strength (solid). The slight disagreement is attributed to anisotropy of the TOP fields, here $B_y = 1.25B_x$.

As depicted in Fig 5.3, this allows us to separate or overlap these two species. The maximum separation Δz_{\max} occurs at the rf resonance for ^{87}Rb , when $g_{\text{F}}^{87}\mu_{\text{B}}B_{\text{TOP}} = \hbar\omega$,

$$\Delta z_{\max} = \frac{\hbar\omega}{2\mu_{\text{B}}B'} \left[\left(\frac{1}{g_{\text{F}}^{85}} \right)^2 - \left(\frac{1}{g_{\text{F}}^{87}} \right)^2 \right]^{\frac{1}{2}} \quad (5.3)$$

This separation can be hundreds of microns in size. Below this value of B_{TOP} , ^{87}Rb also loads into a TAAP trap, and the separation between both species subsequently decreases if B_{TOP} is reduced further (see Fig 5.3c).

This single rf approach works particularly well for this combination of states, where the species loaded into the TAAP (^{85}Rb , $F = 2$) is initially located above that which remains in the TOP (^{87}Rb , $F = 1$) - an improved overlap is then achievable when the TAAP species is lowered. More generally, the requirement for two species A (TOP) and B (TAAP) in their lower hyperfine states is that $F^A g_{\text{F}}^A < F^B g_{\text{F}}^B$, so that the maximally stretched states $|F, m_F\rangle = |F, -F\rangle$ have a smaller gravitational sag in the TOP trap for B than A . Although varying the overlap is still possible when this condition is not fulfilled, the two species cannot be brought to perfect vertical overlap.

5.3.1.2 Loading the trap

Loading the SSTAAP is a straightforward extension of the loading scheme used previously to load ^{87}Rb into the TAAP [61], and the procedure is illustrated in Fig 5.4. Initially both species are held in the TOP trap in the maximally stretched states, $|F, m_F\rangle = |F, -F\rangle$. The rf-dressing field is turned on, projecting atoms into dressed states $|\tilde{m}_F\rangle$ according to their overlap $\langle m_F | \tilde{m}_F \rangle$ with the initial undressed Zeeman state. This overlap depends on the detuning from the rf resonance. As such, the value of B_{TOP} at the instant the rf field is turned on determines the subsequent amplitude of each dressed eigenstate (see Fig 5.5), and so selects which species to load into the

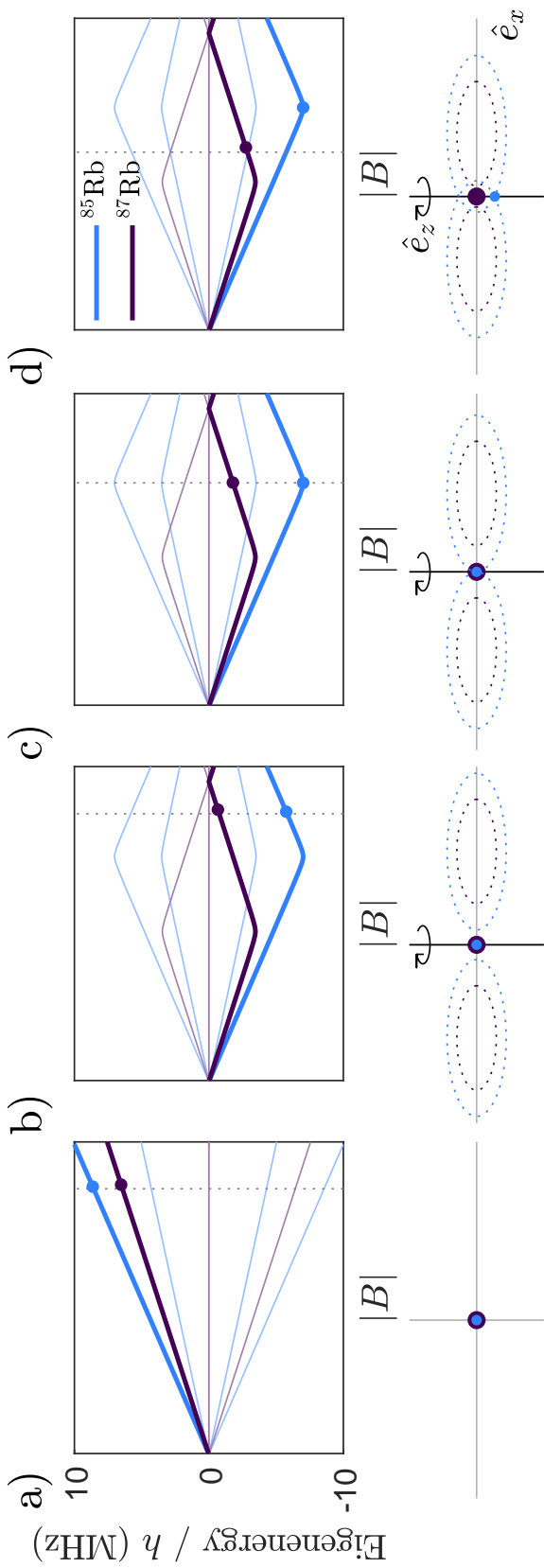


Figure 5.4: **Loading the SSTAAP trap:** An illustration of the experimental sequence required to load ^{85}Rb into the TAAP and retain ^{87}Rb in the TOP. The upper panels show the (a) Zeeman states or (b-d) rf-dressed eigenstates as a function of static magnetic field magnitude $|B|$. The dotted vertical line indicates $B = B_{\text{TOP}}$ and filled circles show the field at which atoms are trapped. The lower panels illustrate the position of atoms (filled circles) in space. The rotation axis of the TOP is shown (black, vertical). Resonant spheroids (colored, dotted) are shown for TOP field rotation angles 0 and π . **a)** The TOP trap before the rf field is turned on. **b)** Immediately after the rf field is turned on, showing ^{85}Rb and ^{87}Rb projected into a dressed state. Neither resonant spheroid intersects the rotation axis **c)** B_{TOP} is reduced. The resonant spheroid for ^{85}Rb touches the rotation axis, loading ^{85}Rb into the TAAP **d)** B_{TOP} further reduced. ^{87}Rb remains in TOP, while ^{85}Rb in the TAAP moves vertically downward.

TAAP and which to remain in the TOP.

To place ^{85}Rb in the TAAP, we turn on the rf field with $g_{\text{F}}^{85}\mu_{\text{B}}B_{\text{TOP}} > \hbar\omega$. It is important to avoid loss of ^{87}Rb near to the weak resonance with the harmonic at $g_{\text{F}}^{87}\mu_{\text{B}}B_{\text{TOP}} = 2\hbar\omega$, which occurs through adiabatic following to an untrapped state, analogous to the ‘rf-knife’ of rf evaporation. This ‘cut’ limits the potential depth of the ^{87}Rb TOP trap, with ^{87}Rb atom loss occurring unless the mixture is sufficiently cold that atoms of ^{87}Rb lack the energy required to reach the cut. The potential energy of the cut corresponds to:

$$E_{\text{cut}} = \frac{|\tilde{m}_{\text{F}}g_{\text{F}}|\mu_{\text{B}}}{B_{\text{TOP}}} \left(\frac{\hbar\omega}{g_{\text{F}}\mu_{\text{B}}} - \frac{B_{\text{TOP}}}{2} \right)^2 \quad (5.4)$$

as determined from an analytical form of the TOP trap frequency and the known position of the ^{87}Rb harmonic resonance. The potential depth decreases as B_{TOP} approaches $g_{\text{F}}^{87}\mu_{\text{B}}B_{\text{TOP}} = 2\hbar\omega$. The value of B_{TOP} at turn on is taken to be about half-way between the ^{87}Rb harmonic and ^{85}Rb fundamental resonances, at $B_{\text{TOP}} = \frac{7}{2}\hbar\omega/\mu_{\text{B}}$, so as to project both species into the correct dressed states and minimise losses. The potential depth $E_{\text{cut}} \approx 0.009\hbar\omega$, corresponding to about $1.5\mu\text{K}$ for a 3.6MHz rf-dressing field. To minimise atom loss we typically load mixtures at temperatures of $0.5\mu\text{K}$.

Cold temperatures are also advantageous to maximise the total atom number projected into the desired state; the finite width of the cloud in the TOP trap means that atoms span a range of static field magnitudes at rf turn on, over which $\langle m_{\text{F}}|\tilde{m}_{\text{F}}\rangle$ changes. For scale, this width is demonstrated for typical experimental parameters in Fig 5.5. With rf-dressing field amplitudes that correspond to Rabi frequencies of 100s of kHz, such as used in this work, each dressed state is a superposition of different $|m_{\text{F}}\rangle$ states even when detuned 100s of kHz from the rf resonance. This reduces our ability to cleanly project each species from an initial Zeeman state into a single

$|\tilde{m}_F\rangle$ unless cold clouds are used. In principle the rf could be turned on with a low amplitude, and subsequently ramped adiabatically to the higher amplitudes required for trapping. In doing so, the initial projection into dressed states occurs for weak rf fields where the avoided crossing is small and $\langle \tilde{m}_F | m_F \rangle \sim 1$ over a larger region of the trap. Unfortunately, a slower loading process leads to an unacceptable reduction in atom number due to the inelastic loss we observe between the constituents of our mixture. This is discussed further in Chapter 6.

A slight adjustment to the loading scheme allows ^{87}Rb to be loaded into the TAAP and ^{85}Rb to remain in the TOP. In this instance, the rf is turned on with B_{TOP} above the ^{87}Rb rf resonance ($g_{\text{F}}^{87}\mu_{\text{B}}B_{\text{TOP}} > \hbar\omega$) and below the ^{85}Rb rf resonance ($g_{\text{F}}^{85}\mu_{\text{B}}B_{\text{TOP}} < \hbar\omega$). The resonant spheroid for ^{85}Rb already surrounds the atoms at the centre of the TOP trap when the rf-dressing field is turned on. Subsequently decreasing the value of B_{TOP} loads ^{87}Rb into the TAAP, but ^{85}Rb remains in the TOP.

5.3.1.3 Further control using the rf field

Control over the rf field provides an additional handle with which to manipulate atoms confined in the TAAP, with minimal effect on those in the TOP. For example, trap frequencies in the TAAP are strongly influenced by the dressing rf amplitude, which enables the implementation of very dissimilar trap frequencies for the two species. One scenario in which this is useful is to pin a handful of atoms of an ‘impurity’ species within a larger ‘reservoir’ of a second, degenerate species. For repulsive inter-species interactions, such as those that occur between ^{85}Rb and ^{87}Rb , the use of similar trap frequencies for both species leads to expulsion of impurities by the mean field of the condensate, which introduces an energy cost to overlapping the impurities with the BEC⁴. To overcome this it is preferable to use tight trap frequencies for the impurity

⁴Whether a mixture of two condensed species is miscible or immiscible depends on the relative strengths of the inter- and intra-species interactions [53, 115, 116]. Miscibility requires a repulsive

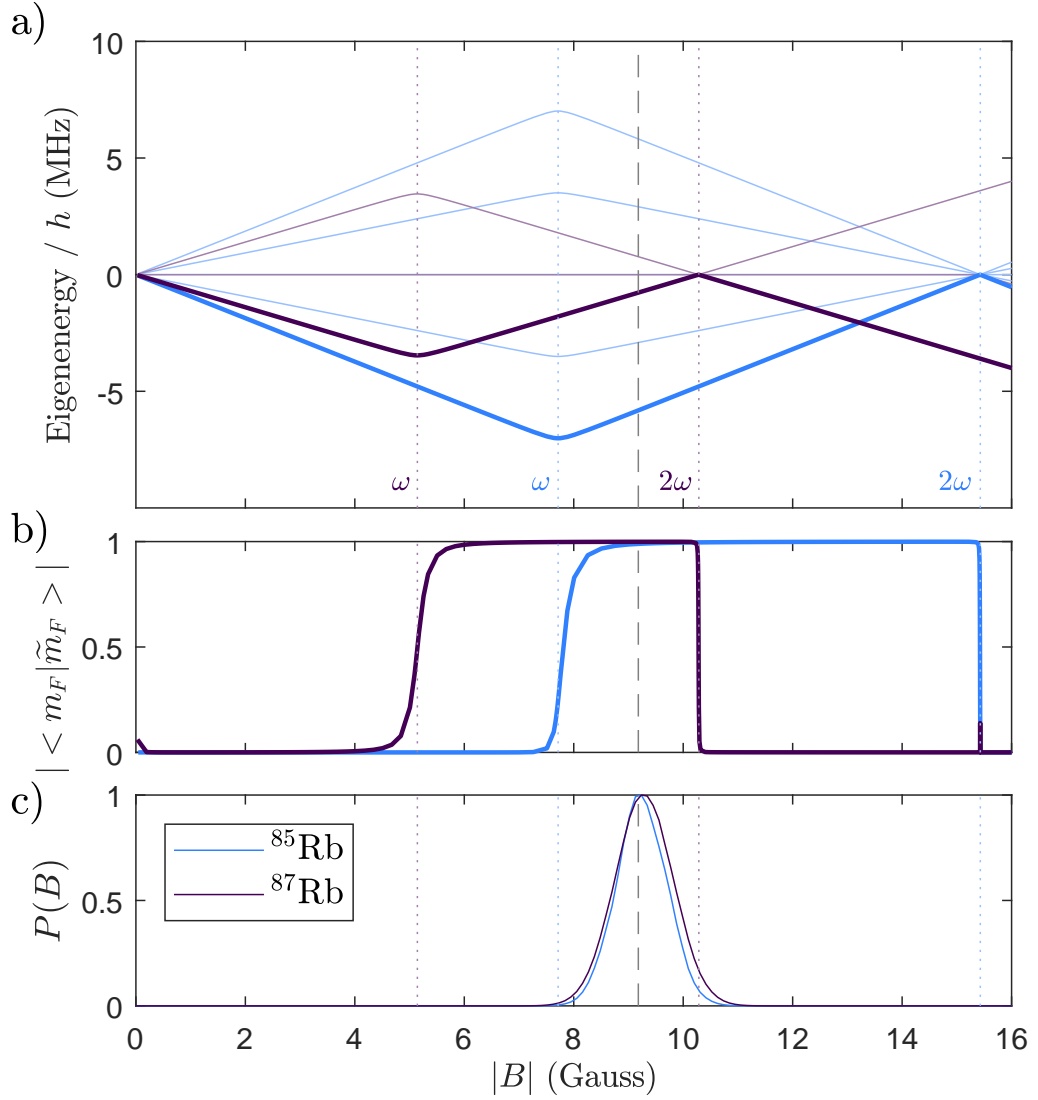


Figure 5.5: **Projection into dressed states:** Several relevant quantities are shown for ^{85}Rb and ^{87}Rb in their lower hyperfine states as a function of field magnitude $|B|$. At the centre of the TOP trap, $|B| \approx B_{\text{TOP}}$. **a)** Dressed eigenenergies. The dressed states for operation with ^{87}Rb in TOP and ^{85}Rb in TAAP are shown in bold. Vertical dotted lines depict resonances with the fundamental ($g_F\mu_B|B| = \hbar\omega$) and harmonic ($g_F\mu_B|B| = 2\hbar\omega$) for both species. **b)** Overlap between the highlighted dressed states and the initial maximally stretched, bare Zeeman states ($|F, m_F\rangle = |1, -1\rangle, |2, -2\rangle$ for ^{87}Rb , ^{85}Rb respectively). **c)** The relative thermal distribution of atoms over different field magnitudes in the TOP, at a temperature of $0.5\ \mu\text{K}$ and $B_{\text{TOP}} = 8.8\ \text{G}$ (indicated by the dashed vertical line). This is the value of B_{TOP} used when the rf-dressing field is turned on.

that ‘pin’ it to the desired location, and weak trap frequencies for the reservoir. These expand the condensate size, reducing the gradient of the chemical potential in spatial coordinates, and thus the force exerted by the mean field on the impurities.

For illustrative purposes, we consider experimental parameters for this scenario. The dressing field is circular-polarised, of frequency 8 MHz and amplitude 0.54 G. The potential minima for ^{85}Rb and ^{87}Rb are coincident when $B_{\text{TOP}} = 16.9\text{ G}$, with quadrupole gradient $B' = 60\text{ G cm}^{-1}$. Large values of B_{TOP} are used to disproportionately decrease the ^{87}Rb trap frequencies, and as a result a large dressing rf frequency is required so that this large B_{TOP} corresponds to the loading of ^{85}Rb into the TAAP where both species overlap and the radial confinement is greatest. We calculate that the ^{85}Rb trap frequencies correspond to $f_x = 46\text{ Hz}$, $f_z = 39\text{ Hz}$, which exceed the predicted ^{87}Rb trap frequencies of $f_x = 9\text{ Hz}$, $f_z = 24\text{ Hz}$. In particular, the radial trap frequencies for ^{85}Rb are approximately 5 times greater than those of ^{87}Rb . By varying B_{TOP} to move the TAAP minimum, one could drag atoms of ^{85}Rb through the condensate of ^{87}Rb , without allowing them to pass around the sides, providing a testing ground for microscopic theories of superfluid drag [117, 118].

By controlling the polarisation of the dressing rf field, it is also possible to horizontally displace the TAAP-trapped species with respect to the TOP-trapped species, by exploiting the coupling force (described in Sec 2.5.1.1). However, the tight radial trap frequencies in the TAAP limit the extent of the displacement. Furthermore, the choice of usable rf-dressing field polarisations is constrained by the need to keep the lifetime in the trap long; the coupling strength must remain sufficiently high to maintain adiabatic following over any part of the resonant spheroid that intersects with the atoms during time-averaging. Additionally, the variation of coupling strength at the atoms’ location during time-averaging causes the frequencies of rf transitions to

mean-field interaction for the second species to make the scenario of overlapped species energetically favorable [115]. For very low numbers of impurities, such a term is negligible and the constituents will separate.

untrapped states to vary. This increases the width of the rf spectrum over which atoms are susceptible to extraneous noise. These concerns add considerable obstacles to implementing a relative horizontal displacement, and we have not explored this possibility further.

5.4 Multiple radiofrequencies

The preceding sections have examined the principles of species-selective manipulations using rf-dressed potentials. The methods so far have been limited to scenarios in which each species experiences an approximately harmonic confinement in a single well. In Chapter 4 we showed how additional frequency components enable the implementation of a wider variety of confining potentials. Combining these advantages with the inherent species-selectivity of rf dressing provides a flexible way to individually extend and sculpt the potentials of each species.

5.4.1 Mixtures of hyperfine states

As noted previously, when $\text{sign}(g_F)$ differs the Zeeman states of each species are coupled by rf fields of different handedness; the dressed potentials for each hyperfine state are individually tuned by controlling the polarisation of each rf component. It is convenient to express the multiple rf field as

$$\begin{aligned}\vec{B}_{\text{rf}} &= \sum_{i=1}^N B_i \left(\cos(\omega_i t) \vec{e}_x - \sin(\omega_i t) \vec{e}_y \right) + A_i \left(\cos(\omega_i t) \vec{e}_x + \sin(\omega_i t) \vec{e}_y \right) \\ &= \sum_{i=1}^N \left(B_i + A_i \right) \cos(\omega_i t) \vec{e}_x - \left(B_i - A_i \right) \sin(\omega_i t) \vec{e}_y\end{aligned}\quad (5.5)$$

where $\sqrt{2}B_i$ and $\sqrt{2}A_i$ correspond to the circular rf field amplitudes that couple the $F = 1$ and $F = 2$ states along $-\vec{e}_z$ respectively. The sum and difference of A_i , B_i correspond to the magnitudes of the linear \vec{e}_x and \vec{e}_y dressing fields required of the x

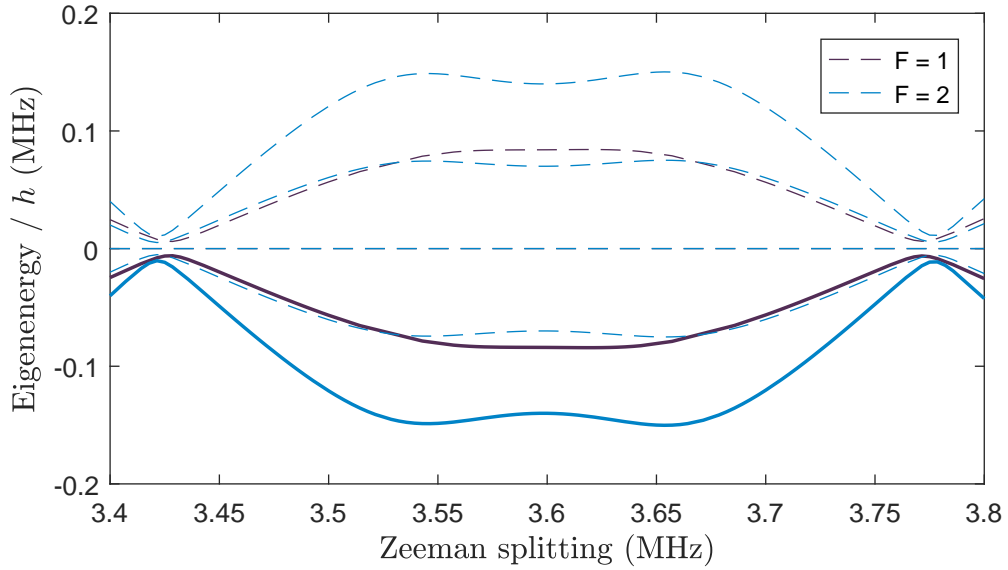


Figure 5.6: **Multiple rf for two hyperfine states:** A single well for $F = 1$ is superimposed over a double well for $F = 2$. The plot shows eigenenergies along \vec{e}_z , $z < 0$, and the eigenstates of interest are highlighted as solid lines. Gravitational potential energy is not included.

and y coil pairs. When $A_i = B_i$, the rf component i has a linear polarisation along \vec{e}_x .

In Chapter 4 we demonstrated a double well formed by dressing with three rf components, where control over B_2 provided a means to adjust the barrier height. A species-selective variant is plotted in Fig 5.6. The first and third frequency components of 3.5 MHz and 3.7 MHz are linear polarised along \vec{e}_x with amplitude $(B_i + A_i) = 57$ mG. The second (barrier) 3.6 MHz rf component is elliptically polarised, with $A_2 = 0.1$ G and $B_2 = 0.12$ G. This is sufficient to create a broad single well for the $F = 1$ state superimposed with a double well for the $F = 2$ state.

Compared to the work of Chapter 4, the only additional requirement to lift the degeneracy between $F = 1$ and $F = 2$ is to add a dressing component along \vec{e}_y ; this capability already exists on our apparatus in order to create circularly-polarised dressing fields that are used when loading the TAAP and shell trap. The sequence would follow exactly that used for splitting the BEC, plus an additional final stage

where the \vec{e}_y -coil is slowly ramped back on at frequency ω_2 , lowering the barrier for one species and raising it for the other. During the course of this work we did not, however, possess a high-power source of microwave radiation for the controlled production of atoms in the $F = 2$ state.

The parameters here have been chosen to exaggerate the differences between the $F = 1$ and $F = 2$ eigenstates. We note that the Rabi frequencies for both species are sufficient to maintain adiabatic following. A logical application of this technique is to achieve tunnelling for one species, with the other acting as a reservoir, as per the scheme of Hangleitner *et. al.* [16].

5.4.2 Mixtures of isotopes or atomic species

Use of multiple dressing frequencies also provides new ways to manipulate mixtures where $|g_F|$ differs between constituents, such as for the isotopes ^{85}Rb and ^{87}Rb in their electronic ground states. The simplest example consists of a magnetic quadrupole field dressed with two radiofrequencies, which implements a single potential well for each species with a controllable overlap and separation between them. We consider an rf field of the form

$$\vec{B}_{\text{rf}} = \sum_{i=1}^N B_i \left(\cos(\omega_i t) \vec{e}_x - \sin(\omega_i t) \vec{e}_y \right) \quad (5.6)$$

with the frequency components $i = 1, 2$ circularly polarised in the laboratory frame. Each of these components produces an avoided crossing near the location \vec{r} where the species-dependent resonance condition $\hbar\omega_i = g_F \mu_B B(\vec{r})$ is satisfied (see Fig 5.7). The frequencies ω_1 and ω_2 are chosen to overlap the resonant spheroids corresponding to these frequencies for ^{85}Rb and ^{87}Rb , respectively, as depicted in Fig 5.7c. This is satisfied by a choice of frequencies in the ratio of the g_F -factors, $\omega_1/\omega_2 = g_F^{85}/g_F^{87}$. For the associated experimental work, we take $\omega_1/2\pi = 3$ MHz and $\omega_2/2\pi = 4.5$ MHz.

Atoms of each species can be trapped at the location where these resonances

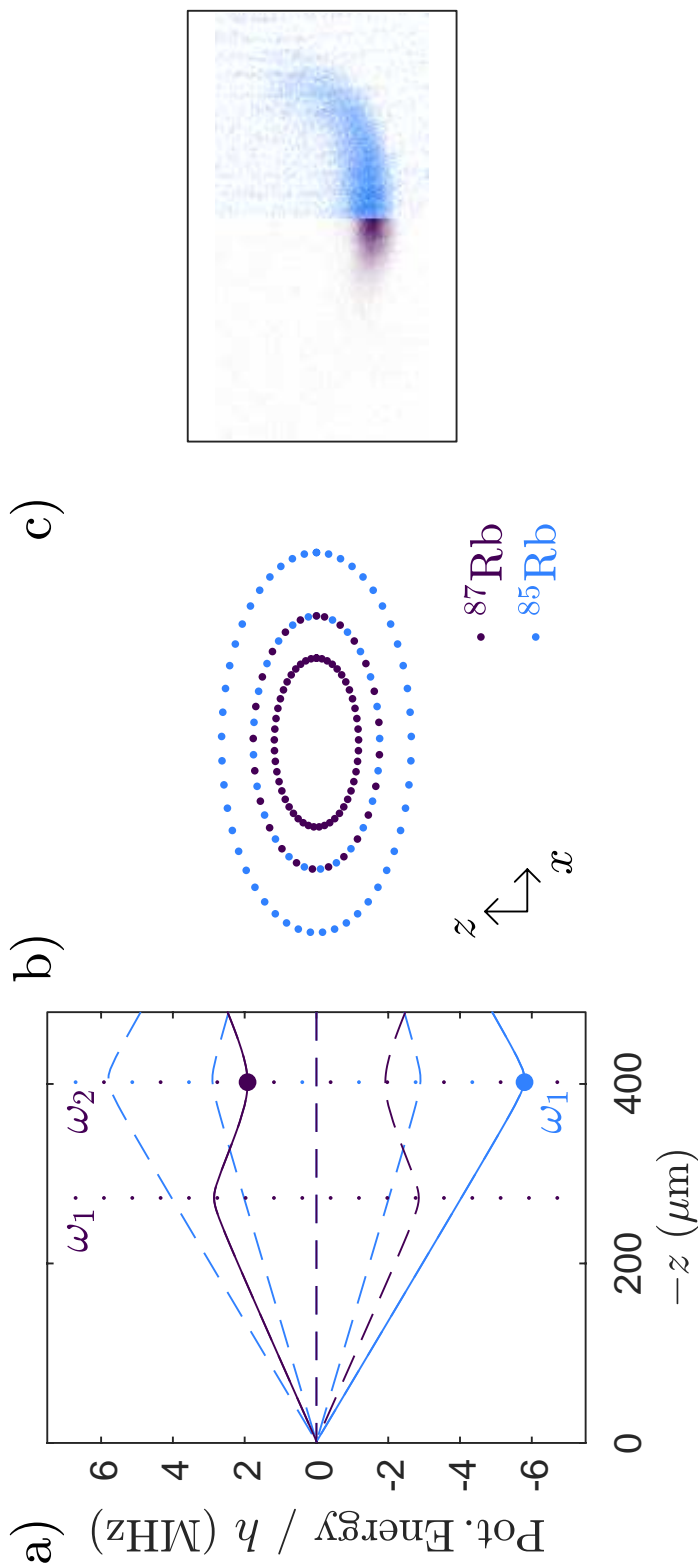


Figure 5.7: **A scheme for confining two species with different $|g_F|$ in overlapped shell traps:** A rf-dressing field of two frequencies is used, with one species trapped at resonance with each frequency component. **a)** Dressed state eigenenergies as a function of position along the z -axis (dashed). The position of rf resonances for each species are depicted by dotted lines. Atoms are trapped on the eigenstates plotted as solid lines at the potential minima indicated by filled circles. **b)** An illustration of the resonant spheroids for each species, showing the ω_1 spheroid for ^{87}Rb overlapped with the ω_2 spheroid for ^{85}Rb . **d)** Absorption images of ^{85}Rb and ^{87}Rb trapped in this configuration. Both species are trapped on resonant spheroids of the same radius, but ^{85}Rb has a weaker radial trap frequency. One half of the region of interest is shown for each species to clearly distinguish between them.

overlap by preparing them in eigenstates that have energy minima there. In this configuration, ^{85}Rb is trapped in the vicinity of the resonance with the field component at frequency ω_1 , and ^{87}Rb with that of ω_2 . Species-selective control is attained by modifying parameters of the corresponding rf field, enabling a range of species-selective manipulations.

5.4.2.1 Manipulations

A simple example demonstrates how the polarisation of each field component can be used to selectively manipulate each species. In Fig 5.8 we show the potential energies of the dressed states ^{85}Rb $|\tilde{m}_F=2\rangle$ and ^{87}Rb $|\tilde{m}_F=1\rangle$ when both frequency components are circularly polarised around \vec{e}_y in the laboratory frame, but of different handedness. The coupling force displaces each species along the \vec{e}_y axis, but in different directions. It is analogous to the scheme of Fig 5.1, which was applicable to two different hyperfine states. This technique could be used to drag one species horizontally through a bulk of another, or to selectively produce a stirring motion to prepare mixtures with only one rotating species, or where the species counter-rotate.

In principle, each species can be vertically raised or lowered by changing the frequency of the associated rf field component, giving precise control over their relative displacements. However, our experimental implementation is constrained by the technical issues of noise discussed in Chapter 4, and in particular the intermodulation products discussed in Sec 4.2.2. These constrain the multiple frequencies to be integer multiples of a common fundamental, which must itself be suitably high so as not to limit the trap depth. This technical issue prevents us from independently sweeping the frequencies ω_1 and ω_2 to move each species.

Instead, two fixed frequencies can be chosen to ensure that the intermodulation products do not cause atom loss, and the relative position of the two species adjusted over a smaller range through the amplitudes of the field components. Such amplitude

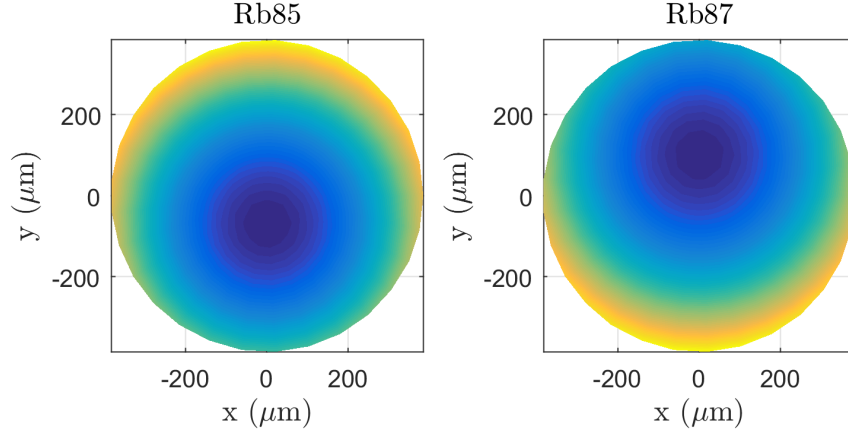


Figure 5.8: **Manipulating ^{85}Rb and ^{87}Rb using the rf polarisation:** Potential energies of the dressed states are plotted for ^{85}Rb and ^{87}Rb over the lower hemisphere of the resonant spheroid that confines each. Dark, blue colors correspond to lower potential energy. Each rf is circular polarised about \vec{e}_y but with a different handedness. The ^{85}Rb minimum is displaced along the negative of the y -axis, while ^{87}Rb is displaced in the positive direction.

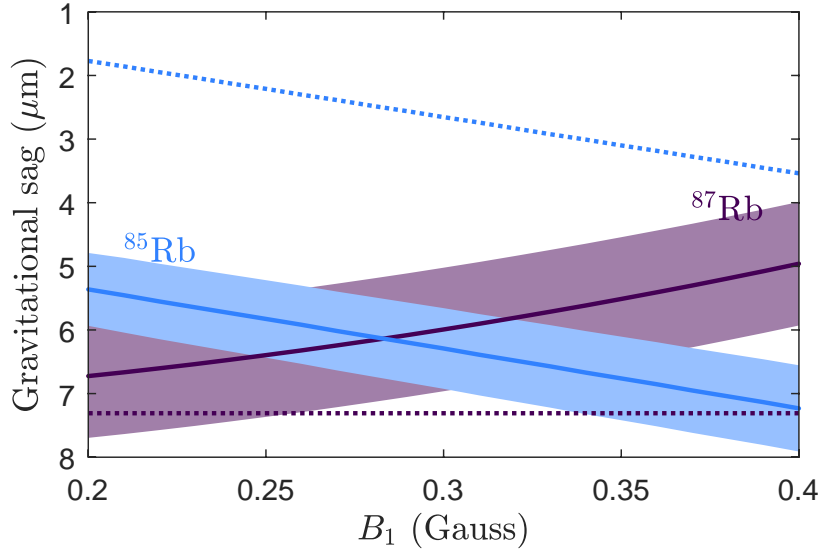


Figure 5.9: **Raising and lowering ^{85}Rb and ^{87}Rb :** The vertical axis is the displacement below the unshifted resonance at $z = \hbar\omega_1/2g_F^{85}\mu_B B'$. Solid lines are results from a full multiple-rf Floquet calculation while dotted lines show positions from a single-rf calculation to demonstrate the magnitude of the shifts in eqn. (5.7). To provide scale, the filled regions either side of the lines correspond to the harmonic oscillator length of ^{85}Rb atoms, and the Thomas-Fermi radius of a Bose-Einstein condensate of 10^4 ^{87}Rb atoms with a radial trap frequency of 9.3 Hz.

control permits the independent adjustment of the vertical trap frequency f_z for each species, which in turn varies the gravitational sag of each cloud, $\Delta z = -g/(2\pi f_z)^2$. For our fixed frequencies ω_1, ω_2 of 3.0, 4.5 MHz the intermodulation products only occur at integer multiples of 1.5 MHz, which are well separated from transitions to untrapped states for low energy atoms in the trap and atom loss is avoided. In Fig 5.9 the amplitude B_1 is varied between 0.2 and 0.4 G while B_2 is held at 0.6 G, corresponding to trap frequencies $f_z^{85} = 362$ to 259 Hz and $f_z^{87} = 180$ Hz. The vertical separation changes sufficiently to sweep the clouds between separation and overlap, but a notable drawback of this scheme is that the vertical trap frequencies are not free parameters, as they are constrained by the desired degree of overlap between the two species.

Additionally, each rf resonance is shifted by the presence of the other rf field component. This displaces the locations of the potential minima, and must be accounted for to achieve good overlap in cold, degenerate samples. The leading term is a quadratic shift, which shifts the i th resonance by $\delta\omega = \Omega_j^2/2\Delta\omega$, where $\Omega_j (j \neq i)$ is the Rabi frequency of the other dressing rf component and $\Delta\omega = \omega_2 - \omega_1$ is the frequency separation [45]. These shifts pull the two rf resonances closer together, raising the position of the resonance associated with ω_2 and lowering that of ω_1 by

$$\delta z_i = \frac{\hbar\Omega_j^2}{4\Delta\omega g_F \mu_B B'} \quad (5.7)$$

For our parameters, the displacement caused by this effect is comparable to the gravitational sag, as shown by the difference between the solid and dotted lines in Fig 5.9. This ‘cross-talk’ means that the position of the second species is also affected by the first rf component, and vice versa, causing ^{87}Rb to rise as ^{85}Rb moves downward and so increasing the maximum achievable separation. If undesired, this effect could be mitigated by changing the amplitude of the other rf component in a complementary

fashion.

5.4.2.2 Loading

The loading scheme follows the same approach as used to load ^{85}Rb and ^{87}Rb in the SSTAAP (see Sec 5.3.1.2). The rf dressing field must be turned on with B_{TOP} at a value that projects both species into the correct eigenstates, but also avoids loss of ^{87}Rb due to the weak harmonic at 6 MHz. We have successfully simultaneously loaded both species by turning on both frequency components of the rf dressing field with $B_{\text{TOP}} \approx 7.1$ G, which keeps the ^{87}Rb Zeeman splitting between the resonances at ω_2 and $2\omega_1$. After this the B_{TOP} field is adiabatically decreased to load both species into their respective shells.

5.4.2.3 Extension to additional frequencies

More complex species-selective potentials can be engineered by increasing the number of dressing rf frequencies, as for the single rf case [45]. The calculated eigenenergies using an rf field with four frequency components are shown in Fig 5.10; the lower three frequencies (2.9 MHz, 3.0 MHz and 3.1 MHz) form a double well potential for ^{85}Rb and the highest (4.5 MHz) a single well to confine ^{87}Rb at the same location. These energies are plotted against position along the vertical axis of the static quadrupole field with gradient $B' = 200$ G cm $^{-1}$, and so depict the dressed eigenenergies perpendicular to the surface at the bottom of the resonant spheroids.

All Rabi frequencies are kept in excess of 30 kHz to maintain adiabatic following. Similar parameters for an rf-dressed potential with a single frequency have been demonstrated experimentally, with lifetimes of many seconds [19]. The tight vertical trap frequencies present in this scheme render the gravitational sag negligible (for clarity we omit it from the plot). Higher-order interactions between each atom and the rf field generate additional avoided crossings that limit the potential depths, as

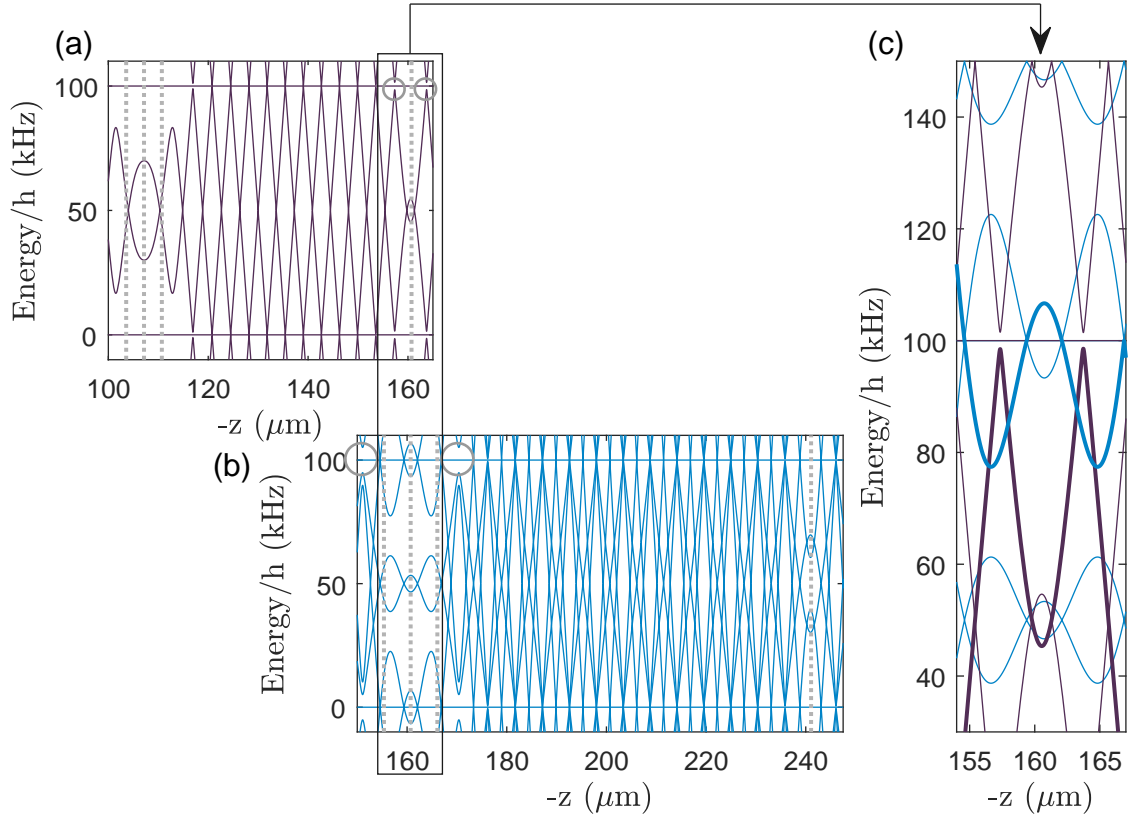


Figure 5.10: **Multiple-rf ^{87}Rb single well and ^{85}Rb double well:** The dressed eigenstates, including the untrapped states, are shown for (a) ^{87}Rb and (b) ^{85}Rb , as a function of position along the vertical axis below the quadrupole centre. The three frequencies 2.9 MHz, 3.0 MHz and 3.1 MHz create a double well for ^{85}Rb centred around 160 μm (blue lines). The fourth frequency, 4.5 MHz, creates a single well for ^{87}Rb at the same position (purple lines). The eigenstates are similar but with a scaling factor of $g_F^{85}/g_F^{87} = 2/3$ for position, represented by the shifted and scaled axes. Light grey dotted lines depict the unshifted resonances of the dressing frequencies. Additionally, there are more levels for ^{85}Rb in $F = 2$ compared to ^{87}Rb in $F = 1$. Both confinements have a finite depth caused by small avoided crossings that arise from higher order interactions between the atom and rf field (grey circles). In (c) we overlay the eigenstates of interest to emphasise the single well/double well structure. The higher trap frequencies of this scheme renders the gravitational sag insignificant here.

for a single species.

The ^{87}Rb atoms, confined in the single well potential, experience a vertical oscillation frequency of $f_z^{87} = 1.37$ kHz. While some adjustment to f_z^{87} is possible through the amplitude B_4 , significantly larger amplitudes cause shifts in the resonances that will separate the two species. The height of the barrier is determined by the amplitude of the second rf field, which can be varied dynamically. At a field amplitude $B_2 = 0.1$ G the barrier is $h \times 29$ kHz above the double well minima, each well having a harmonic trap frequency of 1.12 kHz. Increasing the amplitude of B_2 to 0.18 G lowers the barrier to form a flat potential.

5.5 Conclusions

In this chapter we have explored a number of schemes for performing species-selective manipulations in rf-dressed potentials. These techniques are applicable to combinations of species that are not well suited to individual manipulations using optical dipole traps, such as isotopes of a single element or different hyperfine states. The crucial requirement is that the magnetic dipole moments of each species are dissimilar, and thus that the Landé g_{F} -factors differ between them. Separate approaches are valid according to whether sign (g_{F}) or $|g_{\text{F}}|$ differs. The complexity of these potentials can be easily extended using additional frequency components of the rf-dressing field, and we described examples to combine a single well of one species with a double well of the other.

Elementary species-selective manipulations were demonstrated for ^{85}Rb and ^{87}Rb in a single-radiofrequency dressed TAAP, and we also loaded these isotopes into overlapping shell traps, produced by dressing with a two-frequency field. Unfortunately, inelastic loss in the mixture prevented us from exploring the proposed manipulations further. Instead, we chose to investigate the loss mechanism in more detail, which is

the subject of the next chapter.

Chapter 6

Inelastic Collisions in rf-dressed potentials

The collisional properties of atoms are effected by external fields, such as when collisions are dressed by optical [119], microwave [120], or rf fields [121]. Understanding these collisions is vital to cold atom experiments, as poor collision properties prevent the high phase-space densities required for degenerate quantum gases [122] or lead to instability once Bose-Einstein condensation is reached [123]. Feshbach resonances are widely used to adjust the interaction strengths between different species [124], and often controlled using static fields. The use of rf-fields to control Feshbach resonances has been examined in detail [125, 126, 127, 128].

An inelastic collision is one which changes the internal state of one or more colliding atoms [54]. This results in atom loss when the final states are no longer confined by the external fields, with a loss rate characterised by a rate constant k and proportional to the number densities of the atoms involved. For example, for a two-body collision between species A and B , atoms of species A are lost at a rate given by $\partial N_A / \partial t = \int -n_A n_B k_2^{A,B} dV$, where n_i are the number densities of each species. These changes occur through various processes, but the two most relevant to the current

work are fast *spin-exchange* collisions, with rate constants k on the order of 10^{-13} to 10^{-11} cm³/s, and *spin-relaxation* collisions, with rates that are between 10^{-2} and 10^{-4} times slower [54].

The spin-exchange process is mediated by an interaction between the total electronic spins of the individual colliding atoms, and is typically the dominant inelastic mechanism unless forbidden by selection rules or energy conservation. For instance, spin-exchange is prohibited when two ⁸⁷Rb atoms in the doubly-polarised¹ states $|F = 2, m_F = 2\rangle$ collide in the presence of a static field; it must conserve the total spin angular momentum, and no other channels² exist with the same total spin angular momentum projection onto the quantisation axis. Spin-exchange is allowed for colliding atoms in the maximally-stretched lower hyperfine states $|F = 1, m_F = -1\rangle$, but angular momentum conservation requires a change in F . For large hyperfine splittings the rate is strongly suppressed at low collision energies.

The spin-relaxation process arises from the magnetic dipole-dipole interaction. These collisions can change not just the individual spin angular momenta of each atom but also the orbital angular momentum of their relative motion. This allows spin-relaxation to proceed between states for which spin-exchange is forbidden, but the required increase in the angular kinetic energy of the relative motion suppresses this process at low temperatures where the collision energies are insufficient to overcome this ‘centrifugal barrier’. Although these arguments identify when each process can occur, calculating their rates requires a full quantum-mechanical treatment of the scattering problem.

Although the rf dressed eigenstates are superpositions of Zeeman states, spin-exchange collisions do not occur for collisions between atoms of the same species [121, 129]. Instead, loss is predicted to be dominated by a combination of spin-relaxation

¹Here, we use the terms ‘doubly-polarised’ and ‘maximally-stretched’ as defined in Pethick & Smith [54]

²The different eigenstates of the two-atom system are referred to as channels. When the atoms are well separated, each channel is a tensor product of the individual atomic states.

and an rf-induced equivalent that has no centrifugal barrier to suppress it³ [130]. However, most experiments⁴ to date have trapped ⁸⁷Rb, for which the inelastic loss rate is small in the absence of Feshbach resonances [125] due to the similarity between singlet and triplet scattering lengths [132]. No previous experimental work has characterised mixed-species collisions in rf dressed potentials.

Following the procedure outlined in the previous chapter, we load mixtures of ⁸⁵Rb and ⁸⁷Rb into multiple rf, species-selective potentials. Despite long lifetimes of the individual constituent species in rf-dressed potentials, we observe short lifetimes of the mixture due to interspecies inelastic loss. To understand the loss mechanism, we return to a simpler scheme that uses only a single dressing radiofrequency. The background loss rate is characterised for each species, and is slow compared to the inter-species loss rate. For our mixture of ⁸⁵Rb and ⁸⁷Rb, fast spin-exchange collisions occur freely in the rf-dressed trap, even though they are forbidden in an undressed trap comprised only of static fields; the inter-species rate constant k_2^{85-87} increases by at least five orders of magnitude when ⁸⁵Rb becomes near to resonance with the dressing rf. The occurrence of spin-exchange collisions is consistent with a simple model [129], and we observe that the inelastic rate constant k_2^{85-87} varies with detuning from the rf resonance. Our experimental results are compared to rates calculated by Owens *et. al.* using a coupled-channel approach based on known molecular potentials for ⁸⁵Rb and ⁸⁷Rb [130], finding agreement within an order of magnitude.

6.1 ⁸⁵Rb and ⁸⁷Rb in the TOP: a benchmark

Throughout this chapter we are concerned with understanding inelastic loss processes. In general the ⁸⁵Rb atom number N_{85} decreases over time through spontaneous loss

³Angular momentum conservation can also be satisfied by absorption or emission of an rf photon, rather than a change in the angular momentum of the relative motion

⁴With the exceptions of potassium [114] and ongoing work on sodium [131]

and collisions between trapped atoms and the background gas, at a rate given by

$$\begin{aligned}
\frac{\partial N_{85}}{\partial t} &= -\alpha N_{85} && \text{(one-body)} \\
&- \int k_2^{85,85} n_{85}^2 dV - \int k_3^{85,85,85} n_{85}^3 dV && \text{(intraspecies)} \\
&- \int k_2^{85,87} n_{85} n_{87} dV - \int k_3^{85,87,87} n_{85} n_{87}^2 dV - \int k_3^{85,85,87} n_{85}^2 n_{87} dV && \text{(interspecies)}
\end{aligned} \tag{6.1}$$

where two-body and three-body inelastic processes are grouped according to whether they are inter-species or intra-species collisions. The loss rates are quantified by the rate coefficients k_2 , k_3 , where superscripts identify the participating atoms and subscripts the total number of atoms involved. Collision rates are proportional to the product of the participating atomic densities. The integrals are taken over the volume of the trap to account for the varying atom number density. The ‘one-body’ loss rate includes all processes that limit the lifetime of atoms in the trap, such as loss due to rf noise or that due to vacuum pressure. The ^{87}Rb loss rate is similar, but intra-species inelastic loss rates are generally negligible due to the extremely favorable collision properties of ^{87}Rb . When $N_{87} \gg N_{85}$, inter-species inelastic loss barely affects N_{87} , which decays exponentially according to the $1/e$ lifetime of ^{87}Rb atoms in the trap.

The TOP is used to prepare and load cold samples of ^{85}Rb and ^{87}Rb into rf-dressed potentials. Efficient sympathetic cooling has been demonstrated for this mixture of isotopes in either their maximally-stretched lower hyperfine [57, 56] or doubly-polarised upper hyperfine states [55] - we use a mixture of the maximally stretched states $^{85}\text{Rb} |F = 2, m_F = -2\rangle$ and $^{87}\text{Rb} |F = 1, m_F = -1\rangle$. Sympathetic cooling works well in the TOP trap because spin-exchange is forbidden for this mixture, giving low inelastic rate constants for both inter- and intra-species collisions [58].

To emphasise the stability of this mixture in a static magnetic trap, we search for evidence of interspecies inelastic loss in our TOP trap. This gives a benchmark

against which we can compare the (significantly faster) loss rates when this mixture is dressed with radiofrequency fields. Overlapped thermal clouds of each species are prepared at a temperature of 2 μK with $N_{87} \gg N_{85}$ in the TOP, and after holding for a specified duration the remaining atom number for each species are measured. The rf evaporation follows our usual sequence, with a final rf evaporation frequency of 7.6 MHz. The anisotropic TOP field has $B_x = 7.5 \text{ G}$ and $B_y = 9.4 \text{ G}$, and the quadrupole gradient $B' = 174 \text{ G cm}^{-1}$ gives harmonic trap frequencies f_x, f_y, f_z of 45.8, 43.4, 126.0 Hz for ^{85}Rb and 39.2, 37.0, 107.8 Hz for ^{87}Rb , which are calculated numerically [133]. The sample slowly heats from 2 μK to 3 μK over 80 s of hold in the trap. At these temperatures, the *in situ* Gaussian widths of each cloud are larger than the difference in their gravitational sag, $\Delta z = g((2\pi f_z^{87})^{-2} - (2\pi f_z^{85})^{-2})$, so the species remain well overlapped and in good thermal contact throughout the duration of the hold. The temperatures of both clouds are equal, as verified from their expansion after 3 ms and 18 ms time-of-flight for ^{85}Rb and ^{87}Rb respectively.

The atom number decay of each species in the TOP is illustrated in Fig 6.1a. Both N_{85} and N_{87} decay exponentially with long time constants that correspond to the vacuum-limited lifetime in the glass cell; fitted $1/e$ -lifetimes for these datasets are about three minutes. There is no signature of interspecies inelastic loss, which would otherwise lead to a faster relative loss rate of $N_{85}(t)/N_{85}(0)$ than of $N_{87}(t)/N_{87}(0)$. The fact that the inelastic loss rate constants are unmeasurably small in these data implies maximum bounds for these coefficients. For example, the overlap-weighted⁵ average of the two-body interspecies rate constant, $\langle k_2^{85,87} \rangle = \int k_2^{85,87} n_{85} n_{87} d^3r / \int n_{85} n_{87} d^3r$, must obey $\langle k_2^{85,87} \rangle \int n_{85} n_{87} d^3r \ll N_{85}(0)\alpha$. At a temperature of 2 μK the initial value of this overlap integral is $\int n_{85} n_{87} d^3r = 2.7 \times 10^{16} \text{ cm}^{-3}$, thus $\langle k_2^{85,87} \rangle \ll 7.4 \times 10^{-15} \text{ cm}^3/\text{s}$. In a similar way, using overlap integrands of $n_{85}^2 n_{87}$ or $n_{85} n_{87}^2$ constrains the values of

⁵This weighting is required because the magnetic field magnitude is not homogenous in the TOP, and so k_2 may vary as a function of position in the trap.

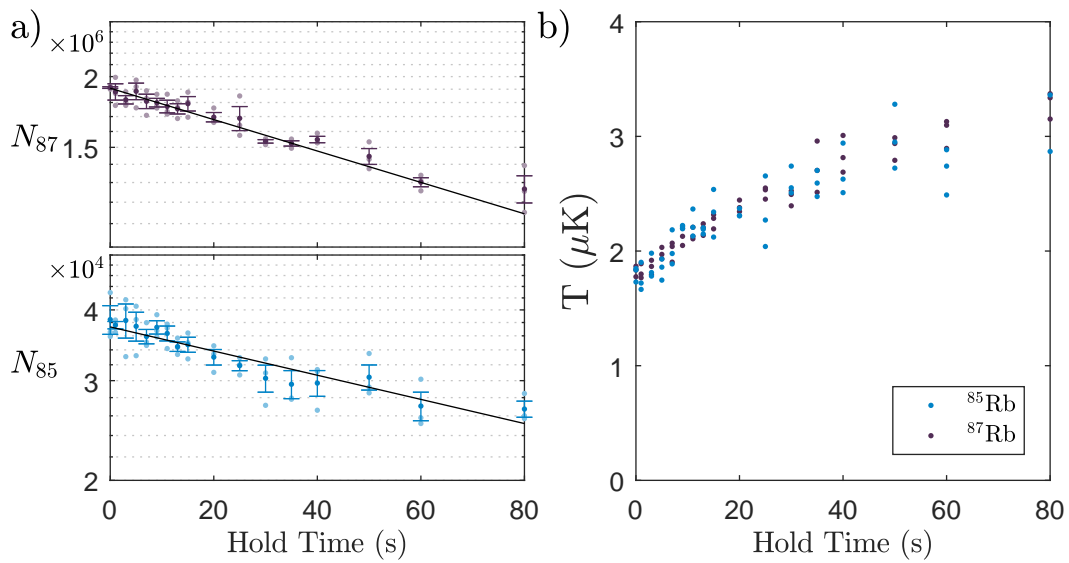


Figure 6.1: **Searching for inelastic loss in the TOP:** A number imbalanced mixture of ^{85}Rb $|F = 2, m_F = -2\rangle$ and ^{87}Rb $|F = 1, m_F = -1\rangle$ is held in the TOP over 80s. **a)** Atom number at different hold times for each species, three repeats per hold time. Both decay exponentially (solid lines are best fit). No inelastic loss is visible, and the $1/e$ lifetime of both species is limited by the vacuum. **b)** Temperature of both clouds, measured after time of flight.

$\langle k_3^{85,85,87} \rangle \ll 2.7 \times 10^{-25} \text{ cm}^6/\text{s}$ and $\langle k_3^{85,87,87} \rangle \ll 7.1 \times 10^{-27} \text{ cm}^6/\text{s}$ for this mixture⁶.

Despite the use of this mixture for sympathetic cooling in a number of experiments, the literature is surprisingly sparse when it comes to inelastic rate constants at low fields. Most experiments using this combination are interested in operating near the inter-species Feshbach resonance around 260 G, and measured rates are primarily near this region [134, 135, 56, 59]. For sympathetic cooling at low fields, it appears that inelastic ^{85}Rb loss typically becomes the limiting factor before the ^{85}Rb - ^{87}Rb inelastic rate does [56], which may explain the dearth of published data on low-field interspecies loss rates. Theoretical calculations predict that low-field dipole inelastic collisions have a strong magnetic field dependence [136], but they still remain below the bounds determined here [58]. Nevertheless, it is clear that collision properties are extremely favorable for this mixture in a static magnetic trap, and a marked difference to when the mixture is rf-dressed.

6.2 Interspecies inelastic loss in the 2RF trap

Our first observation of fast inelastic loss in rf-dressed mixtures occurred when overlapping ^{85}Rb and ^{87}Rb in the 2RF trap (see Fig 6.2). Using methods discussed in the previous chapter, we load a mixture of ^{85}Rb and ^{87}Rb into a 2RF TAAP, created using a dressing field of amplitudes 0.28 G, 0.28 G at frequencies 3 MHz, 4.5 MHz to overlap the two species. The time-averaging field B_{TOP} was slightly anisotropic, with $B_x = 2.9 \text{ G}$, $B_y = 3.6 \text{ G}$, and the quadrupole gradient $B' = 116 \text{ G cm}^{-1}$.

We observe lifetimes of many seconds when only one species is loaded into the trap. When both species are present, however, the lifetimes are significantly reduced, suggesting that inter-species inelastic collisions cause loss (see Fig 6.2a). To load only ^{85}Rb , we increase the initial ^{85}Rb atom number loaded from the dual-species

⁶We define $\langle k_3^{85,85,87} \rangle = \frac{\int k_3^{85,85,87} n_{85}^2 n_{87} d^3 r}{\int n_{85}^2 n_{87} d^3 r}$ and $\langle k_3^{85,87,87} \rangle = \frac{\int k_3^{85,87,87} n_{85} n_{87}^2 d^3 r}{\int n_{85} n_{87}^2 d^3 r}$

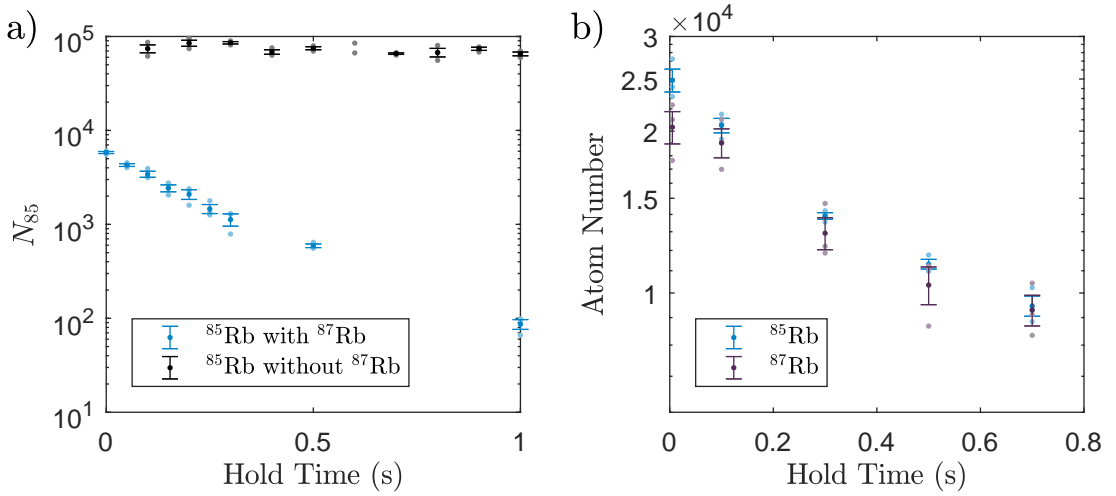


Figure 6.2: **Inelastic loss in the 2RF TAAP:** **a)** Comparison of decay in ^{85}Rb atom number with and without ^{87}Rb present. For the series with ^{87}Rb , $N_{87} \gg N_{85}$ and N_{87} is constant over the 1 s hold period. **b)** Decay of ^{85}Rb and ^{87}Rb due to inelastic collisions, with initial $N_{85} \approx N_{87}$ so that inelastic loss is visible on both species.

MOT and rely on the sympathetic cooling stage in the TOP becoming inefficient so that the ^{87}Rb population is depleted. A side effect is the difference in initial N_{85} seen in Fig 6.2a for the two series. Throughout this chapter, we typically use mixtures which have a large difference in atom number between each species, most often $N_{85} \ll N_{87}$; in this case the inelastic collisions cause a measurable decrease in N_{85} , but with an associated change in N_{87} that is too small to observe above the shot-to-shot fluctuations in atom number. Conversely when $N_{87} \ll N_{85}$ we see short lifetimes of ^{87}Rb . Fig 6.2b shows a sequence with approximately equal atom numbers, in which the inelastic loss is detectable for both populations; the loss rates for ^{85}Rb and ^{87}Rb are similar, which suggests that an equal number of atoms of each species are lost during collisions in the 2RF trap. This detail is proven more rigorously in Sec 6.4.1, where the loss mechanism is identified as two-body ^{85}Rb - ^{87}Rb collisions.

6.3 Inelastic loss in rf-dressed ^{85}Rb - ^{85}Rb

To our knowledge, ^{85}Rb has not been trapped in an rf-dressed potential before, and therefore we investigated the collisional stability of this isotope in detail before examining that of the ^{85}Rb and ^{87}Rb mixture. We observe inelastic loss in pure rf-dressed samples of ^{85}Rb , but these occur at similar inelastic loss rates to those seen in static magnetic field traps. As for the TOP trap, the method to load only ^{85}Rb is to increase the ^{85}Rb atom number in the MOT and so deplete all of the ^{87}Rb during the sympathetic cooling stage. The TAAP for ^{85}Rb is loaded using the same routine we use for the TAAP for ^{87}Rb , turning on the rf field at $B_{\text{TOP}} = 10.3\text{ G}$ before ramping down to $B_{\text{TOP}} = 5.7\text{ G}$ during 100 ms to load the trap. The dressing rf is 3.6 MHz with $B = 860\text{ mG}$.

To achieve sufficient densities to observe inelastic loss in ^{85}Rb we adiabatically compressed the TAAP immediately after loading by ramping the quadrupole gradient from 116 G cm^{-1} to 232 G cm^{-1} over 100 ms. The fast increase in n_{85} is followed by a rapid loss rate which slows as atoms are lost from the trap, a signature of inelastic loss. We caution that the thermal energy of the cloud is only slightly below the calculated depth of the TAAP potential, and loss from atoms escaping the potential depth of the trap is indistinguishable from that due to inelastic collisions; measured rate coefficients should be taken as upper bounds.

6.3.1 Determining rate coefficients

The loss rate of a pure sample of ^{85}Rb atoms can be written:

$$\frac{\partial N_{85}(t)}{\partial t} = -\alpha N_{85}(t) - \int k_2^{85,85} n_{85}(t)^2 dV - \int k_3^{85,85,85} n_{85}(t)^3 dV \quad (6.2)$$

which corresponds to eqn. (6.1) without terms involving ^{87}Rb . For convenience we introduce the normalised density $\tilde{n}_{85}(\vec{r})$, writing $n_{85} = N_{85}\tilde{n}_{85}$, with $\int \tilde{n}_{85} dV = 1$

where \tilde{n}_{85} depends on the trap parameters and temperature of the ensemble. Thus we can rewrite (6.2) as

$$\frac{\partial N_{85}(t)}{\partial t} = -\alpha N_{85}(t) - N_{85}(t)^2 \int k_2^{85,85} \tilde{n}_{85}^2 dV - N_{85}(t)^3 \int k_3^{85,85,85} \tilde{n}_{85}^3 dV \quad (6.3)$$

$$= -\alpha N_{85}(t) - \beta(T) N_{85}(t)^2 - \gamma(T) N_{85}(t)^3 \quad (6.4)$$

The temperature-dependent integrals over \tilde{n}_{85} for fixed trap parameters are absorbed into the coefficients β , γ .

Figure 6.3 shows the ^{85}Rb atom number in this tight trap as a function of time. Immediately after the compression, when n_{85} is highest, rapid decay occurs which we attribute to inelastic collisions. This quickly reduces the density, and the atom number decreases faster than the best fit for exponential decay at these short hold times. At longer times with reduced n_{85} the inelastic loss is negligible, and the behaviour follows an exponential decay limited by the lifetime of atoms in the trap.

We measure the Gaussian width and height of clouds after 5 ms time-of-flight expansion, and from these determine the temperature of the cloud before release. For typical temperatures of 10 μK , the collisions are only s -wave in character. The temperature slightly decreases over time (see Fig 6.3c), but to a reasonable approximation it can be taken as constant, so that β and γ are constant in the analysis⁷. The standard deviation of T_{85} is only 7% of the mean value across all hold times. Fitted lines are shown on Fig 6.3 for four different models, which are defined in Table 6.1. It is clear that pure exponential decay fails to capture the behaviour at short hold time when it is dominated by inelastic loss, but the other three models are closer to the data points.

⁷We ultimately seek to obtain bounds of the rate constants $k_2^{85,85}$ and $k_3^{85,85,85}$ so as to decide whether the intra-species loss is negligible compared to inter-species loss in Sec 6.4.1; given that the temperature slightly changes over time we expect a systematic error. However, the values of these intra-species rate constants imply that the intra-species inelastic loss rate is so small compared to the inter-species loss rate that this systematic error will not change our conclusions.

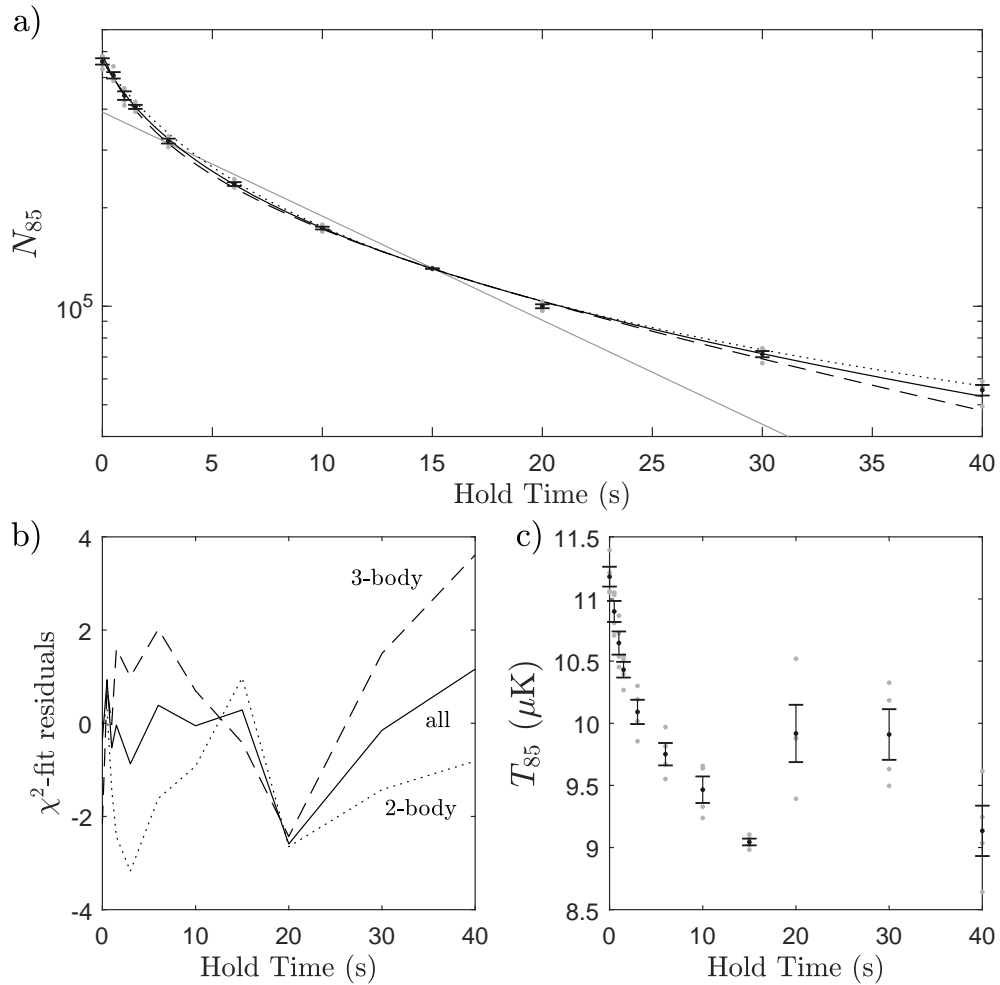


Figure 6.3: **Inelastic loss of ^{85}Rb in the TAAP:** **a)** Measured N_{85} at different hold times (grey dots). The best fit lines correspond to exponential decay (grey, solid), 2-body (dotted, black), 3-body (dashed, black) and the full model (solid, black), as defined in Table 6.1. **b)** A plot of the best-fit residuals for each model. The initial rate is well described by the full model, but underestimated for the 2-body model and overestimated for the 3-body model. **c)** Measured temperatures T_{85} at each hold time. At longer hold times the lower atom number reduces the signal, and the fit becomes less stable.

Model	Constraints
exponential	$\alpha \neq 0, \beta = 0, \gamma = 0$
two-body	$\alpha \neq 0, \beta \neq 0, \gamma = 0$
three-body	$\alpha \neq 0, \beta = 0, \gamma \neq 0$
two- & three-body	all free

Table 6.1: Constraints of eqn. (6.4) used for the four different fit models.

Distinguishing between pure two-body and pure three-body loss (or combinations thereof) is a notoriously difficult task [134, 135, 56]. As noted by Roberts, the rapid increase in loss rate at higher densities prevents the preparation of significantly denser samples that would otherwise make the distinction between two- and three-body processes trivial [135]. Although more dilute samples can be used, this often results in loss dominated by one-body processes, concealing that due to inelastic collisions. We fit eqn. (6.4) to the observed decay of N_{85} for each model with constraints as defined in Table 6.1. All models incorporate a one-body loss term (α) to account for the finite lifetime of atoms in the trap.

Our data, with four repeats per hold time, is not of sufficient quality to confidently select one inelastic model as superior. A $\tilde{\chi}^2$ -test of the best-fit residuals at the 5 % level of significance would marginally reject pure two-body and pure-three body models but accept the fit model with both rates. This goodness-of-fit test considers the significance of the test statistic $\tilde{\chi}^2 = \sum_i r_i^2$, where the residual $r_i = (y_i - y(x_i))/\alpha_i$ for dependent variable x_i , and measurements y_i of the independent variable with best-fit value $y(x_i)$ and uncertainty α_i [137]. However, it is of questionable validity to apply a $\tilde{\chi}^2$ -test with only four repeats per hold time; the unknown variance α_i^2 of the parent distribution must be estimated from the variance of the observed values, and is underestimated for small numbers of repeats, in turn overestimating the residuals, inflating $\sum_i r_i^2$ and with it the statistical significance of rejecting the two-body or three-body models.

B (G)	Fit Parameters			Overlap integrals		Rate Coefficients	
	α (mHz)	β (μ Hz)	γ (pHz)	\tilde{n}_{85}^2 (10^6 cm^{-3})	\tilde{n}_{85}^3 (10^{12} cm^{-6})	$\langle k_2^{85,85} \rangle$ ($10^{-13} \text{ cm}^3 \text{ s}^{-1}$)	$\langle k_3^{85,85,85} \rangle$ ($10^{-25} \text{ cm}^6 \text{ s}^{-1}$)
0.54	35(4)	0.26(5)	0.36(12)	1.00(12)	1.6(3)	2.6(3)	2.3(6)
0.64	36(4)	0.24(5)	0.43(13)	0.94(10)	1.3(3)	2.6(3)	3.2(7)
0.86	15(5)	0.21(6)	0.45(19)	0.87(10)	1.2(2)	2.4(3)	3.8(9)
1.07	18(4)	0.23(5)	0.55(17)	0.93(12)	1.3(4)	2.6(3)	4(1)
1.21	23(6)	0.34(8)	0.42(35)	0.98(28)	2(1)	3(1)	3(2)

Table 6.2: Measured inelastic rate constants for ^{85}Rb in the TAAP, assuming **both** two-body and three-body loss, for different dressing rf amplitudes B .

B (G)	Two-body		Three-body		Overlap integrals		Rate Coefficients	
	α (mHz)	β (μ Hz)	α (mHz)	γ (pHz)	\tilde{n}_{85}^2 (10^6 cm^{-3})	\tilde{n}_{85}^3 (10^{12} cm^{-6})	$\langle k_2^{85,85} \rangle$ ($10^{-13} \text{ cm}^3 \text{ s}^{-1}$)	$\langle k_3^{85,85,85} \rangle$ ($10^{-25} \text{ cm}^6 \text{ s}^{-1}$)
0.54	24(3)	0.40(2)	54(2)	1.02(5)	1.00(12)	1.6(3)	4.0(5)	6(2)
0.64	19(4)	0.43(3)	54(2)	1.02(6)	0.94(10)	1.3(3)	4.6(6)	8(2)
0.86	0(5)	0.39(3)	33(1)	1.0(1)	0.87(10)	1.2(2)	4.5(6)	8(3)
1.07	5(2)	0.43(2)	34(1)	1.20(8)	0.93(12)	1.3(4)	4.6(6)	9(3)
1.21	16(3)	0.46(2)	42(1)	1.50(7)	0.98(28)	2(1)	5(1)	9(7)

Table 6.3: Measured inelastic rate constants for ^{85}Rb in the TAAP, assuming **either** two-body **or** three-body loss, for different dressing rf amplitudes B .

The fitted parameters β and γ from each model are used to calculate the overlap-weighted averages of the rate constants $\langle k_2^{85,85} \rangle$, $\langle k_3^{85,85,85} \rangle$, where $\langle k_2^{85,85} \rangle = \beta / \int \tilde{n}_{85}^2 dV$ and $\langle k_3^{85,85,85} \rangle = \gamma / \int \tilde{n}_{85}^3 dV$. As before, we define $\langle k_2^{85,85} \rangle = \int k_2^{85,85} \tilde{n}_{85}^2 dV / \int \tilde{n}_{85}^2 dV$ and $\langle k_3^{85,85,85} \rangle = \int k_3^{85,85,85} \tilde{n}_{85}^3 dV / \int \tilde{n}_{85}^3 dV$, which accounts for spatial dependence in either rate constant within the trap, *eg* due to the inhomogeneous field. These values and associated errors are listed in Table 6.2 and Table 6.3 for five different dressing rf amplitudes. The pure two-body and three-body decay models provide upper bounds for the rate constants, which are used to discount ^{85}Rb - ^{85}Rb loss from the analysis of inter-species loss in Sec 6.4.

The best-fit parameters minimise the square sum of the normalised residuals, $\sum r^2$. The stated uncertainties of Table 6.2 correspond to the change in each parameter that is required to increase the minimum value of $\sum r^2$ by 1, while freely adjusting the other parameters to minimise $\sum r^2$ [137]. The uncertainties in the overlap integrals are dominated by variation in the temperature T_{85} , and a fluctuation in the B_{TOP} field that influences the harmonic trap frequencies. We quantify these using the following Monte-Carlo method. The integrals are calculated for many randomly drawn values of T_{85} and B_{TOP} , from which the distributions of the overlap integrals are found. T_{85} is randomly drawn from a normal distribution with the same standard deviation and mean as the measured values. The uncertainty in the TOP field is systematic⁸, with an anisotropy of $B_y/B_x = 1.25$ (with 1% standard deviation), and $B_x = 5.74$ G (2% standard deviation). The 234 G cm⁻¹ quadrupole gradient and properties of the dressing rf field contribute negligible uncertainty. We take the standard deviation of the calculated distribution as the uncertainty, not the standard error, due to the inclusion of systematic errors. These uncertainties are combined in quadrature, along with the uncertainty in the fit parameters, to give those of the $k_2^{85,85}$ and $k_3^{85,85,85}$ rate

⁸We later discovered that one of two Crown XLR5000 audio-amplifier channels used to produce the TOP field was faulty, producing an anisotropy of $B_y/B_x = 1.25$ and increasing the uncertainty in the TOP field. This has since been fixed.

constants.

Surprisingly little data is available for the undressed loss rate of ^{85}Rb at low field, and we reiterate that most experiments using ^{85}Rb work at higher fields to exploit the intra- or ^{87}Rb inter-species Feshbach resonances. Values of $k_2^{85,85} = 3 \times 10^{-14} \text{ cm}^3/\text{s}$ and $k_3^{85,85,85} = 5 \times 10^{-25} \text{ cm}^6/\text{s}$ at a static field of 2 G are given in Papp, PhD thesis [56]. Values of $k_2^{85,85} = 2 \times 10^{-13} \text{ cm}^3/\text{s}$ and $k_3^{85,85,85} = 2 \times 10^{-24} \text{ cm}^6/\text{s}$ at a field of 100 G, far from the ^{85}Rb - ^{85}Rb Feshbach resonance on the low-field side, are reported by Roberts [134]. The rates that we measure for rf-dressed atoms are of similar magnitude to these. Although the rf dressing may itself influence the inelastic loss rate, within our uncertainties we do not observe a dependence of rates on the amplitude of the dressing field.

It is unusual that the temperature of ^{85}Rb slightly decreases over time as inelastic loss typically leads to heating because density-dependent loss favours removal of atoms of below average energy at the centre of the trap, and energy released from a change in an atom's internal state can be imparted as kinetic energy. A likely cause is that there is also loss due to the finite potential depth of the TAAP, allowing the most energetic atoms to escape and providing a cooling effect (evaporation). Under extremely different TAAP parameters, this effect has previously been used to cool ^{87}Rb to degeneracy [44]. The trap depth here is 30 μK , calculated numerically, which is comparable to the 10 μK temperature of the clouds. This loss cannot be distinguished from that directly caused by inelastic collisions. It is hard to quantify the size of this systematic error, and as such our best-fit $k_2^{85,85}$ and $k_3^{85,85,85}$ rate constants should be interpreted as upper bounds that assume the finite trap depth causes no loss.

The characterisation of inelastic loss of ^{85}Rb in the rf-dressed trap forms part of our complete investigation into inelastic loss in our ^{85}Rb - ^{87}Rb mixture. From these results, we conclude that for the next interspecies rate experiments the density of ^{85}Rb is sufficiently low that it is safe to neglect loss from 3-body and 2-body inelastic

collisions of this isotope when measuring the interspecies ^{85}Rb - ^{87}Rb loss.

6.4 Inelastic loss in rf-dressed ^{85}Rb - ^{87}Rb mixtures

We now examine the inter-species inelastic loss of rf-dressed atoms. Overlapping the clouds of the two isotopes ^{85}Rb and ^{87}Rb in the shell trap requires the use of a dressing field with multiple frequency components as described in Sec 5.4.2. This provides a method for species-selective manipulations, but is not the best choice for an investigation into rf-induced inelastic loss where the additional frequencies make a theoretical treatment of the loss process more complicated. Therefore, having observed inelastic loss in the 2RF trap, we returned to a simpler, single-rf situation to investigate further. The SSTAAP, described in the previous chapter, allows the two species to be overlapped while dressing with only a single rf component, and also provides a way to tune the magnitude of the static field at which collisions occur. This trapping scheme was exploited for the results reported in the remainder of this chapter.

6.4.1 Identifying the inter-species loss mechanism

The first step towards understanding the mechanism behind the rapid inter-species loss between ^{85}Rb in $|F = 2, \tilde{m}_F = 2\rangle$ and ^{87}Rb in $|F = 1, \tilde{m}_F = 1\rangle$ is to identify the nature of the collisions. It is reasonable to assume that only two- and three-body collisions are significant; although collisions involving more atoms can occur [138, 139], they typically require higher densities than used here, or Feshbach resonances, to proceed at an appreciable rate.

The identification of the dominant loss mechanism is easier when using a strongly number-imbalanced mixture, such as $N_{85} \ll N_{87}$. The decrease in N_{85} over time provides a clear signal from which to measure the inelastic collision rate, which follows

eqn. (6.1), and small ^{85}Rb atom numbers reduce the significance of ^{85}Rb intraspecies collisions. Collisions also lead to loss of ^{87}Rb , but for $N_{85} \ll N_{87}$ the change in total ^{87}Rb atom number is not observable within the shot-to-shot variations, and $N_{87}(t)$ stays approximately constant over the hold times of interest when the lifetime of ^{87}Rb is much larger than for ^{85}Rb .

Our experimental method is as follows. We load atoms in the states $^{85}\text{Rb} |F=2, m_F=-2\rangle$ and $^{87}\text{Rb} |F=1, m_F=-1\rangle$ into the TOP trap and perform rf evaporation on ^{87}Rb to produce cold mixtures at temperatures of $0.5\ \mu\text{K}$. The $3.6\ \text{MHz}$ rf-dressing field is turned on with an amplitude of $0.85\ \text{G}$, projecting both species into dressed states and loading the SSTAAP. The TOP magnetic field is ramped down over $400\ \text{ms}$ until the magnitude of B_{TOP} equals $7.3\ \text{G}$ ⁹, giving good overlap of the thermal clouds of each species. The trap frequencies for $^{85}\text{Rb} |F=2, \tilde{m}_F=2\rangle$ are $f_x = 45\ \text{Hz}$ and $f_z = 55\ \text{Hz}$, and for $^{87}\text{Rb} |F=1, \tilde{m}_F=1\rangle$ are $f_x = 16\ \text{Hz}$ and $f_z = 40\ \text{Hz}$, as measured directly by observing oscillations of atoms in the trap, and these agree with numerical calculations of the potential. The quadrupole gradient is $70\ \text{G cm}^{-1}$.

We vary the hold duration t between experimental runs, before releasing the atoms to measure either N_{87} or N_{85} using absorption imaging. Different hold durations, and repeats thereof, are combined to form a series in which $N_{85}(t)$ is measured. The density n_{87} is varied for each series by changing the relative atom numbers of ^{85}Rb and ^{87}Rb that are initially loaded into the MOT, which affects the number of ^{87}Rb atoms remaining after the sympathetic cooling stage. The ^{87}Rb time-of-flight is chosen as a compromise between signal-to-noise ratio (which favors denser clouds at shorter flight durations) and the desire to reduce systematic errors in the temperature measurement from time-of-flight expansion (which favors longer times). All series use a ^{87}Rb time-of-flight in excess of $20\ \text{ms}$, where the systematic error is negligible

⁹The problems with the TOP audio amplifier were not yet discovered at this stage. The TOP field for these measurements was anisotropic, such that $B_y = 1.25B_x$. The field amplitude quoted here is for B_x .

compared to the shot-to-shot variation of temperature T_{87} within each series (average standard deviation 6 % of mean). Measurements of the temperature of the ^{85}Rb atoms have larger systematic uncertainties because the small atom number, typically 3×10^4 atoms, requires short time-of-flight to achieve a good signal-to-noise ratio in the atom number measurement. The ^{85}Rb atoms must be illuminated with repumping light for 1.5 ms before imaging to allow sufficient time for the weak resonant laser sideband to completely drive atoms into the upper hyperfine level. The shortest possible duration, 1.5 ms, is used for all sets bar two with higher N_{85} where 5 ms is used.

6.4.1.1 Determining the dominant loss mechanism

To determine which is the dominant loss mechanism, we rewrite eqn. (6.1), gathering together terms with the same power of n_{85} .

$$\begin{aligned}
\frac{\partial N_{85}}{\partial t} = & -\alpha_i N_{85} \\
& - \int n_{85} (k_2^{85,87} n_{87} + k_3^{85,87,87} n_{87}^2) dV \\
& - \int n_{85}^2 (k_2^{85,85} + k_3^{85,85,87} n_{87}) dV \\
& - \int n_{85}^3 (k_3^{85,85,85}) dV
\end{aligned} \tag{6.5}$$

The terms that contribute significant loss are revealed by identifying an appropriate fit model for N_{85} , and the scaling of the fitted rate parameters with n_{87} .

The series with only ^{85}Rb present (see Fig 6.4) determines the background lifetime at these trap parameters in the absence of ^{87}Rb . The atom number undergoes an exponential decay with a $1/e$ -lifetime of 48 s that is significantly longer than when ^{87}Rb is present. The width of the imaged cloud in time-of-flight approximately doubles over the 45 s hold time, suggesting that heating occurs over this timescale. It is plausible that heating arises from ambient 50 Hz mains noise, as both vertical (45 Hz)

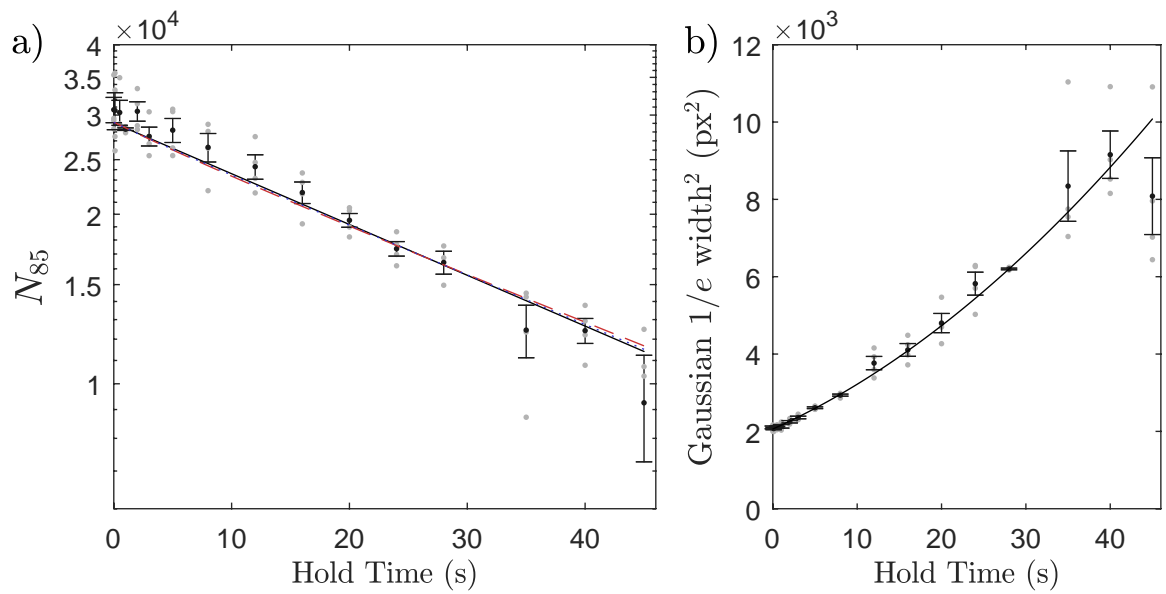


Figure 6.4: **Benchmark for the lifetime of ^{85}Rb alone in the SSTAAP:**
a) Measured N_{85} at different hold times, logarithmic vertical axis. The fit lines correspond to a pure exponential (solid, black), a two-body plus exponential model (dashed, red) and a three-body plus exponential model (dotted, blue). The best fit for each model has a loss rate dominated by the exponential term, and all fit lines are almost perfectly superimposed as a result. **b)** Measured Gaussian width at different hold times (a proxy for T_{85}). A quadratic fit is shown.

and horizontal (55 Hz) trap frequencies are near by. Assuming that $T \propto w^2$, where w is the width after time-of-flight expansion, the temperature over time is well described by a quadratic function. We see no sign of ^{85}Rb inelastic loss at these densities.

To obtain upper bounds for the inelastic loss rates, we fit models that include exponential decay and either a two-body or three-body loss term, and which account for the in-trap heating¹⁰. Although these constraints are not as tight as those of Sec 6.3.1, they are taken at a temperature that is similar to other series in the present investigation¹¹, whereas the results of Sec 6.3.1 are measured at 10 μK . The best-fit parameters are consistent with two-body and three-body inelastic loss rates of zero, but the associated uncertainties are large due to the heating that reduces $\int \tilde{n}^2 dV$ and $\int \tilde{n}^3 dV$ at longer times. For an initial temperature $T_{85}(0) = 1 \mu\text{K}$, these uncertainties impose upper bounds of $k_2 < 1 \times 10^{-12} \text{ cm}^3/\text{s}$ and $k_3 < 7 \times 10^{-23} \text{ cm}^6/\text{s}$, assuming that any inelastic loss is either purely two-body or three-body.

On the other hand, N_{85} decreases quickly in the presence of ^{87}Rb , depicted in Fig 6.6a. This loss greatly exceeds the rates due to two-body and three-body ^{85}Rb inelastic collisions alone. The small ^{85}Rb atom numbers (10^3 to 10^4 atoms) result in low signal-to-noise ratios, and multiple repeats at each hold time t are required to extract the general trend. Assuming $T_{85} = T_{87}$, which is constant over these timescales, and the above upper-bounds on $k_2^{85,85}$ and $k_3^{85,85,85}$, we find that on average a maximum of only 2% of the initial loss rate can be attributed to two-body ^{85}Rb collisions, and 6% to three-body ^{85}Rb collisions¹². If instead using the maximum values of $k_2^{85,85}$ and $k_3^{85,85,85}$ determined in Sec 6.3.1, the two-body and three-body

¹⁰corresponding to ‘two-body’ and ‘three-body’ models of Table 6.1, also including the fitted time-dependence of T_{85} .

¹¹The constant $k_3 \propto a^4$ [140], which is independent of temperature in the limit $T \rightarrow 0$ where collisions become purely s -wave in character. Likewise, k_2 is constant in the limit of $T \rightarrow 0$, provided there are no resonances [130]. To err on the side of caution in our analysis, we also use these looser constraints on $k_2^{85,85}$ and $k_3^{85,85,85}$ principally because they are measured at a lower temperature. Either values reach the same conclusion - that ^{85}Rb intra-species inelastic loss is negligible compared to the interspecies ^{85}Rb - ^{87}Rb loss.

¹²predicted two-body and three-body rates for each series compared to the best-fit exponential loss rate of N_{85} at $t = 0$.

^{85}Rb loss amounts to only 0.5 % and 0.08 % of the initial loss rate respectively. We conclude the overwhelming majority of ^{85}Rb loss arises from inelastic collisions with ^{87}Rb , hence eqn. (6.5) approximates to

$$\begin{aligned} \frac{\partial N_{85}}{\partial t} \approx & - \int n_{85} (k_2^{85,87} n_{87} + k_3^{85,87,87} n_{87}^2) dV \\ & - \int n_{85}^2 (k_3^{85,85,87} n_{87}) dV \end{aligned} \quad (6.6)$$

Both T_{87} and N_{87} are constant over the measurement period within each series. The measured widths of the ^{85}Rb clouds after short time-of-flight also suggest it is valid to take T_{85} as constant, although these fits become unreliable at long times where N_{85} has been greatly reduced. The quadratic heating rate observed for ^{85}Rb alone in Fig 6.4b supports this assumption over short timescales of seconds. Thus the overlap integrals $\int \tilde{n}_{85}^i \tilde{n}_{87}^j dV$ are also constant, and eqn. (6.6) is recast as a rate equation for N_{85} of the form $\partial N_{85}(t)/\partial t = -\alpha N_{85}(t) - \beta N_{85}(t)^2$.

The task of identifying the appropriate decay model is complicated by the existence of two trapped states for ^{85}Rb , $|\tilde{m}_F = 1\rangle$ and $|\tilde{m}_F = 2\rangle$, both of which are observed in the rf-dressed trap (see Fig 6.5). In-situ images reveal two Gaussian distributions, with centres separated in the vertical direction by about 60 μm , consistent with our expectations for the gravitational sag of each state. At short hold times a greater number of atoms are in the $|\tilde{m}_F = 2\rangle$ state; loading parameters are chosen to optimise the overlap with the initial state in the TOP, $\langle m_F = -2 | \tilde{m}_F = 2 \rangle$, and thus most atoms are put into $|\tilde{m}_F = 2\rangle$. However, a small number are loaded into $|\tilde{m}_F = 1\rangle$ due to the non-zero overlap of $\langle m_F = -2 | \tilde{m}_F = 1 \rangle$. The *in situ* width of this distribution is also wider than that of the $|\tilde{m}_F = 2\rangle$ state, indicating that the population in the $|\tilde{m}_F = 1\rangle$ state is characterised by a higher temperature. This is also expected; at TAAP load the potential energy for the initial $|m_F = -2\rangle$ state in the TOP closely resembles that of the $|\tilde{m}_F = 2\rangle$ state, but not that of the $|\tilde{m}_F = 1\rangle$

state. The sudden mismatch between the distribution of atoms and the confinement when the dressing field is applied increases the potential energy of atoms projected into the $|\tilde{m}_F = 1\rangle$ state, heating the cloud. Furthermore, additional atoms are likely supplied to the $|\tilde{m}_F = 1\rangle$ population via inelastic loss from the $|\tilde{m}_F = 2\rangle$ state. These atoms also receive excess potential energy, in addition to any energy released from the inelastic collisions themselves.

Ideally, the decay of only the $|\tilde{m}_F = 2\rangle$ state would be observed for comparison to eqn. (6.4). However, even *in situ* both ^{85}Rb distributions overlap due to the increased temperature of the $|\tilde{m}_F = 1\rangle$ cloud, and it is not possible to completely separate them and only count atoms in the $|\tilde{m}_F = 2\rangle$ state. Instead, the sum of atom numbers in the two states $N_{85} = N_1 + N_2$ is observed. Our trap parameters are chosen to maximise the overlap between the distributions of ^{85}Rb in $|\tilde{m}_F = 2\rangle$ and ^{87}Rb in $|\tilde{m}_F = 1\rangle$, but this gives worse overlap between ^{87}Rb and ^{85}Rb in $|\tilde{m}_F = 1\rangle$, which sags below the $|\tilde{m}_F = 2\rangle$ cloud. Although initially $N_2 \gg N_1$, inelastic ^{85}Rb - ^{87}Rb collisions proceed at a slower rate for the $|\tilde{m}_F = 1\rangle$ state due to this poor overlap, and it typically lingers long after the $|\tilde{m}_F = 2\rangle$ cloud has completely vanished.

To reveal the inelastic loss mechanism we compare the goodness of fit for two models of N_{85} decay, both of which account for the individual populations of the two trapped states. The first ‘two-exponential’ model is one in which both $N_1(t)$ and $N_2(t)$ decay by exponential loss,

$$N(t) = N_1(0)e^{-\alpha_1 t} + N_2(0)e^{-\alpha_2 t} \quad (6.7)$$

which is applicable when either the terms $k_2^{85,87}$ or $k_3^{85,87,87}$ dominate the inelastic loss. The time constants α_1 and α_2 differ for both ^{85}Rb states due to their different overlaps. The time-independence of α_1 and α_2 implicitly assumes that the distributions (and hence temperatures) are also constant, so that the overlap between ^{85}Rb and ^{87}Rb

does not change. We have not included a term to account for scattering from $|\tilde{m}_F = 2\rangle$ into $|\tilde{m}_F = 1\rangle$. This may seem odd given that initially $N_2 \gg N_1$, but we emphasise that the impact of N_1 on the total atom number only becomes visible when N_1 is comparable to N_2 , by which time the largest change in N_2 has already occurred. Thus, it is likely that this scattering just changes the fitted value $N_1(0)$.

In the second model loss is proportional to N_i^2 ,

$$N_{85} = N_1 + N_2, \quad \text{and } N_i(t) \text{ obeys } \frac{\partial N_i}{\partial t} = -\beta_i N_i^2 - \alpha N_i \quad (6.8)$$

which is appropriate when the $k_3^{85,85,87}$ term dominates, and termed the two- N^2 model. The constant α is not a fit parameter, and corresponds to the measured 48 s natural lifetime of ^{85}Rb atoms in the trap. As before, the two coefficients β_i account for the different overlap and rate coefficients of the two ^{85}Rb states, and we continue to neglect the population exchange between $|\tilde{m}_F = 1\rangle$ and $|\tilde{m}_F = 2\rangle$.

The presence of two clouds increases the difficulty of differentiating between these models. For example, the two-exponential model resembles a curve with rate proportional to N^2 if the coefficients N_1 and N_2 are similar, and for many of our data sets it is impossible to distinguish between the two models. A clear distinction is only apparent when $N_1(0) \ll N_2(0)$. For those data sets where the difference in population is sufficiently large, we find a clear preference for the two-exponential model (see *eg* Fig 6.5c). This suggests that the dominant mechanism of inelastic loss involves a single atom of ^{85}Rb , as the loss rate is proportional to n_{85} .

To determine the number of ^{87}Rb atoms involved, we observe the change in loss rate as a function of n_{87}^{\max} , the peak density of ^{87}Rb . These measurements are taken over a shorter range of hold times for which $N_2 > N_1$ that is sufficient to clearly observe the fast exponential decay behaviour, corresponding to the loss rate of $|\tilde{m}_F = 2\rangle$. A function of the form $Ae^{-\alpha t} + c$ is fitted to $N_{85}(t)$ to extract the exponential rates

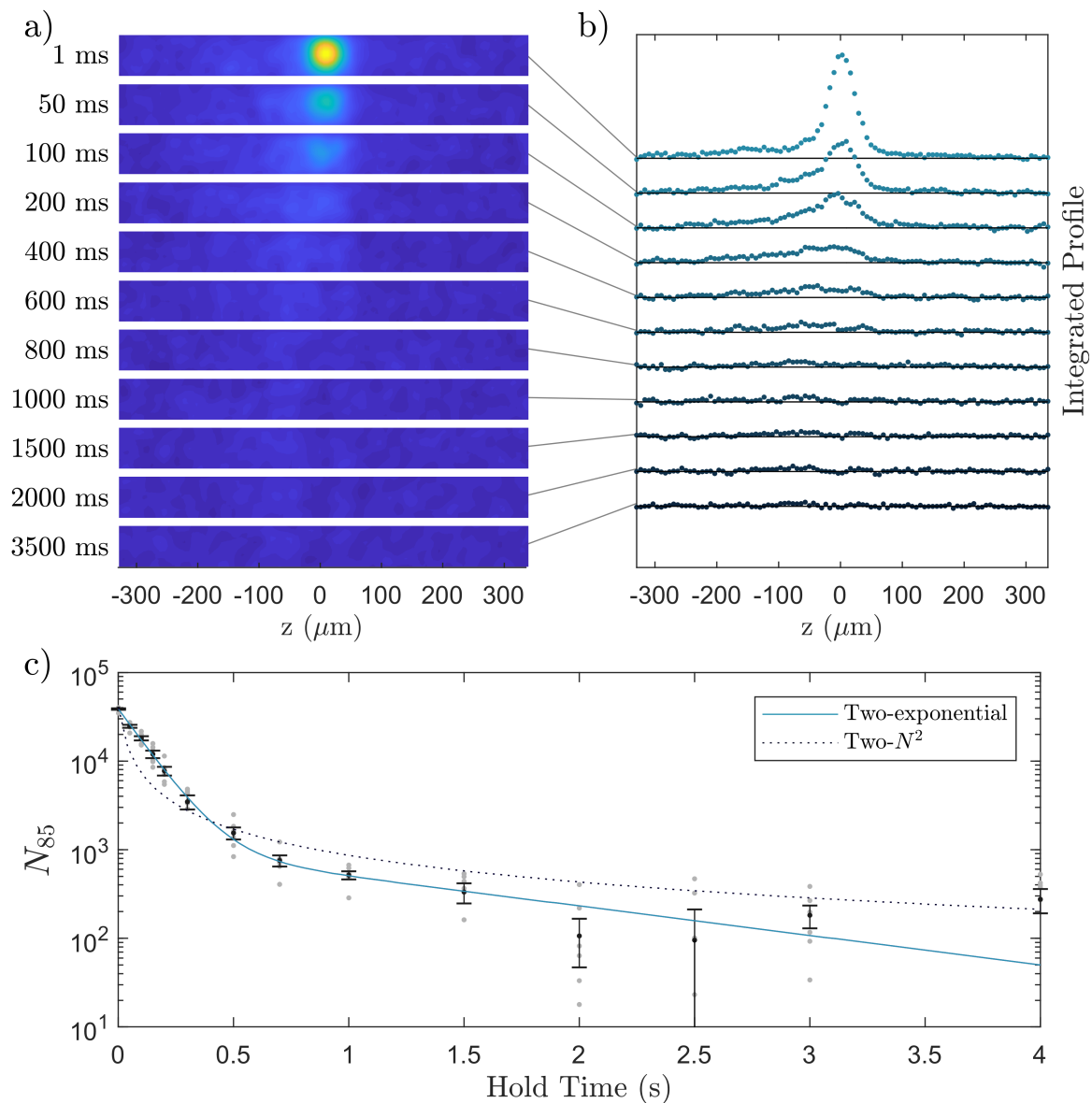


Figure 6.5: **Identifying the loss mechanism:** **a)** Absorption images showing the density of ^{85}Rb after a short 1.5 ms time-of-flight, after different hold times (labelled). ^{85}Rb atoms in $|F = 2, \tilde{m}_F = 2\rangle$ are visible as a bright spot that quickly decays away. A broader cloud, composed of ^{85}Rb $|F = 2, \tilde{m}_F = 1\rangle$ atoms, lingers beneath (to the left in the images). For ease of comparison, the reference $z = 0$ is taken to coincide with the $|F = 2, \tilde{m}_F = 2\rangle$ cloud, and a Gaussian blur has been applied to more clearly see the diffuse $|F = 2, \tilde{m}_F = 1\rangle$ cloud above noise. **b)** The presence of both clouds is easier to see when each image is integrated along the shorter dimension. The black lines show the zero for each profile, and the horizontal axis limits are the same as for (a). **c)** The total atom number within a circle of radius 20 pixels, centered on the $|\tilde{m}_F = 2\rangle$ cloud. The measured decay is consistent with the two exponential model and does not agree with the two- N^2 model. This dataset is not the same as that plotted in (a) and (b) - it used a longer 4 ms time-of-flight to reduce the effect of the $|\tilde{m}_F = 1\rangle$ cloud on the measured atom number in $|\tilde{m}_F = 2\rangle$.

α , with the constant c representing the small number of ^{85}Rb atoms remaining in the $|\tilde{m}_F = 1\rangle$ state that decays slower than these time scales¹³. The best-fit exponential decay constants for ^{85}Rb lifetime, as a function of peak ^{87}Rb density n_{87}^{max} , are shown in Fig 6.6. The loss rate increases linearly with n_{87} , from which we conclude that a single ^{87}Rb atom participates in the inelastic process. In conclusion, a model assuming only collisions involving one ^{85}Rb atom and one ^{87}Rb atom is sufficient to explain the observed fast N_{85} decay in the presence of ^{87}Rb .

6.4.2 An intuitive model for the two-body loss

An intuitive picture explains the collisional stability of pure ^{85}Rb or ^{87}Rb in an rf-dressed trap, and the instability of their mixture. The idea was first suggested by Agosta *et. al.* [120] in the context of a microwave dressed trap and explored in greater detail by Moerdijk *et. al.* [121] and Suominen *et. al.* [129], and has so far only been applied to collisions of a single species. In the rotating wave approximation the dressed eigenstates $|\tilde{m}_F\rangle$ of a single atom are equivalent to Zeeman states in an ‘effective field’ B_{eff} , which is coplanar to the quantisation axis \vec{B}_0 and the rotating rf field \vec{B}_{rf} . The effective field is rotated from \vec{B}_0 toward \vec{B}_{rf} by a tilt angle θ , and precesses around the axis \vec{B}_0 at the dressing rf frequency. The tilt angle θ depends on the resonant angular Rabi frequency Ω and angular detuning from the rf resonance δ , where $\tan \theta = \Omega/\delta$. At large positive (negative) detunings, B_{eff} is (anti)parallel to the static field direction, and the dressed states are approximately Zeeman states, $|\tilde{m}_F\rangle \approx |m_F\rangle$.

The toy model requires two assumptions. The first is that the length-scale of the collision interaction is small compared to any inhomogeneity in B_0 , so that the magnitude of B_0 is the same for colliding atoms at different positions [86]. The second

¹³Consistent with our earlier deductions, a fitmodel with constant offset and loss rate $\propto N_{85}$ provides a better fit to these datasets than a fitmodel with constant offset and loss rate $\propto N_{85}^2$. However, the statistical significance was not sufficiently large to confidently select one fitmodel over the other for these sets where n_{87} is varied.

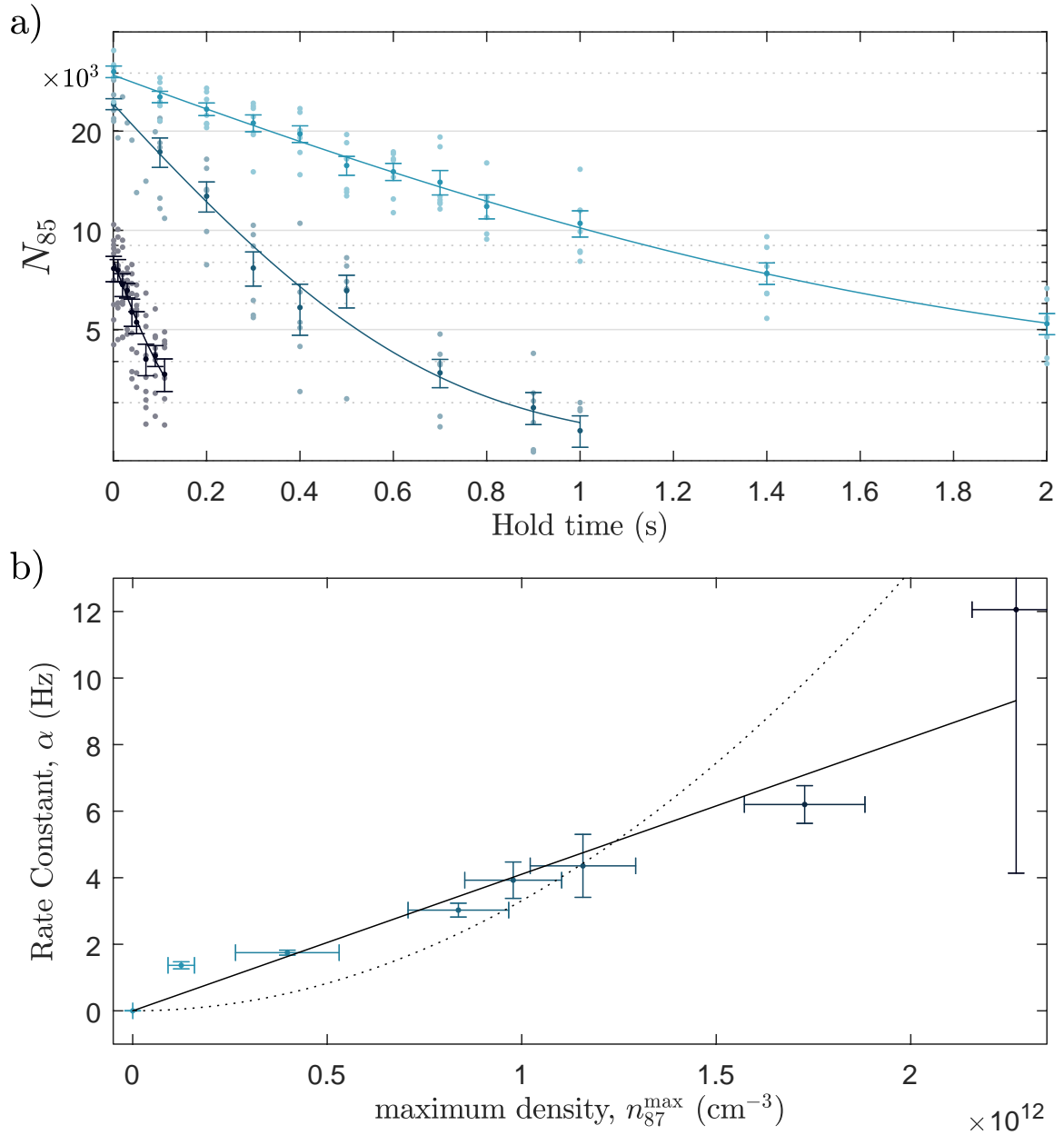


Figure 6.6: **Loss of ^{85}Rb at different densities n_{87}^{max} :** **a)** Decay of N_{85} in the SSTAAP when overlapped with a ^{87}Rb cloud. Three different densities are shown to demonstrate the significant change in rate. The fit lines correspond to the best fit for $Ae^{-\alpha t} + c$, see text. **b)** The change in measured exponential rate constant α as a function of the peak density of ^{87}Rb in the trap, n_{87}^{max} . The solid black line shows a best-fit linear model, the dashed line a quadratic model, both intercept the point (0,0).

is that the time-scale of the inelastic collision is fast compared to the static field's Larmor frequency, the dressing frequency and the Rabi frequency $\Omega/2\pi$ [121], such that the dynamics resulting from these fields may be neglected during the collision itself (the 'degenerate internal states' approximation). When two atoms of the same species collide, the tilt angles of both are matched (see Fig 6.7). Each atom, being in a dressed state, has a well defined angular momentum projection onto the direction of the effective field, with $\hat{F}_{\text{eff}} |\tilde{m}_F\rangle = \tilde{m}_F |\tilde{m}_F\rangle$. The total angular momentum of both atoms therefore also has a well defined projection $\hat{F}_{\text{eff}}^{\text{tot}} = \hat{F}_{\text{eff}}^{\beta} + \hat{F}_{\text{eff}}^{\alpha}$ along this axis with good quantum number $M_F^{\text{eff}} = \tilde{m}_F^{\alpha} + \tilde{m}_F^{\beta}$. When both atoms are in states of maximum \tilde{m}_F the expectation value of $\hat{F}_{\text{eff}}^{\text{tot}}$ is an extremum. Inelastic collisions must conserve the projection of angular momentum M_F^{eff} , but there exist no exit channels for the collision which have the same value as the entrance channel. Rapid inelastic loss mediated by the spin-exchange mechanism cannot happen.

This is not the case when collisions occur between two species with different g_F . For example, consider when $|g_F|$ is different and thus both Ω and δ differ. The tilt angles of each species' 'effective field' are not equal, and they rotate around B_0 with a constant difference in tilt angles $\Delta\theta = \theta_{\alpha} - \theta_{\beta} = \arctan \Omega_{\alpha}/\delta_{\alpha} - \arctan \Omega_{\beta}/\delta_{\beta}$. In general no frame exists in which the angular momentum projection of both atoms are good quantum numbers, let alone that both are extrema. Other exit channels are now accessible by spin-exchange, and loss proceeds quickly. When $|g_F|$ is the same but $\text{sign}(g_F)$ differs the tilt angles are matched - but the effective fields precess in opposite directions about B_0 , and the problem persists. Likewise, when dressing with two rfs each species' effective field precesses at a different frequency around B_0 , so that rapid loss remains even if the tilt angles are matched through an appropriate choice of rf amplitudes. In short, the effective fields are only co-linear at all times if the g_F -factor is the same for both species, which exactly contradicts the requirements for species selectivity in rf-dressed potentials.

Situation	Effective Fields			
	t_1	t_2	t_3	t_4
g_F equal				
$ g_F $ different				
sign(g_F) different				
2 rfs				

Figure 6.7: **Precession of the rotating frames:** Precession of the effective fields about the (grey) quantisation axis of the static field are shown for two atoms (dark and light blue). Subsequent images show the two rotating frames at a later time, t .

Even though this model is crude, it predicts some general features of the two-body loss rate between rf-dressed mixtures of ^{85}Rb and ^{87}Rb in a static field B_0 (see Fig 6.8). When above the ^{85}Rb resonance, *ie* $g_F^{85}\mu_B B_0 > \hbar\omega$, both species have a large positive detuning from resonance and both tilt angles are small. Although not perfectly colinear, the effective fields point in similar directions and spin-exchange is suppressed. If B_0 is decreased towards the ^{85}Rb resonance the difference in tilt angles $\Delta\theta$ increases, and the inelastic loss rate should increase. This continues past $g_F^{85}\mu_B B_0 < \hbar\omega$ as the ^{85}Rb effective field aligns antiparallel to the static field. The difference in angles $\Delta\theta$ reaches a maximum in the region between the rf resonances for each species, giving a maximum to the inelastic loss rate. Further decreasing B_0 now decreases $\Delta\theta$, as the tilt angle of the ^{87}Rb effective field increases faster than that of ^{85}Rb . Finally, when B_0 is significantly below the ^{87}Rb resonance, both effective fields align antiparallel to B_0 and the spin-exchange mechanism is again suppressed. The rf amplitude dictates the rate at which both tilt angles change with respect to B_0 ; we thus expect a larger rf amplitude to smooth these changes in $k_2^{85,87}$ over a greater

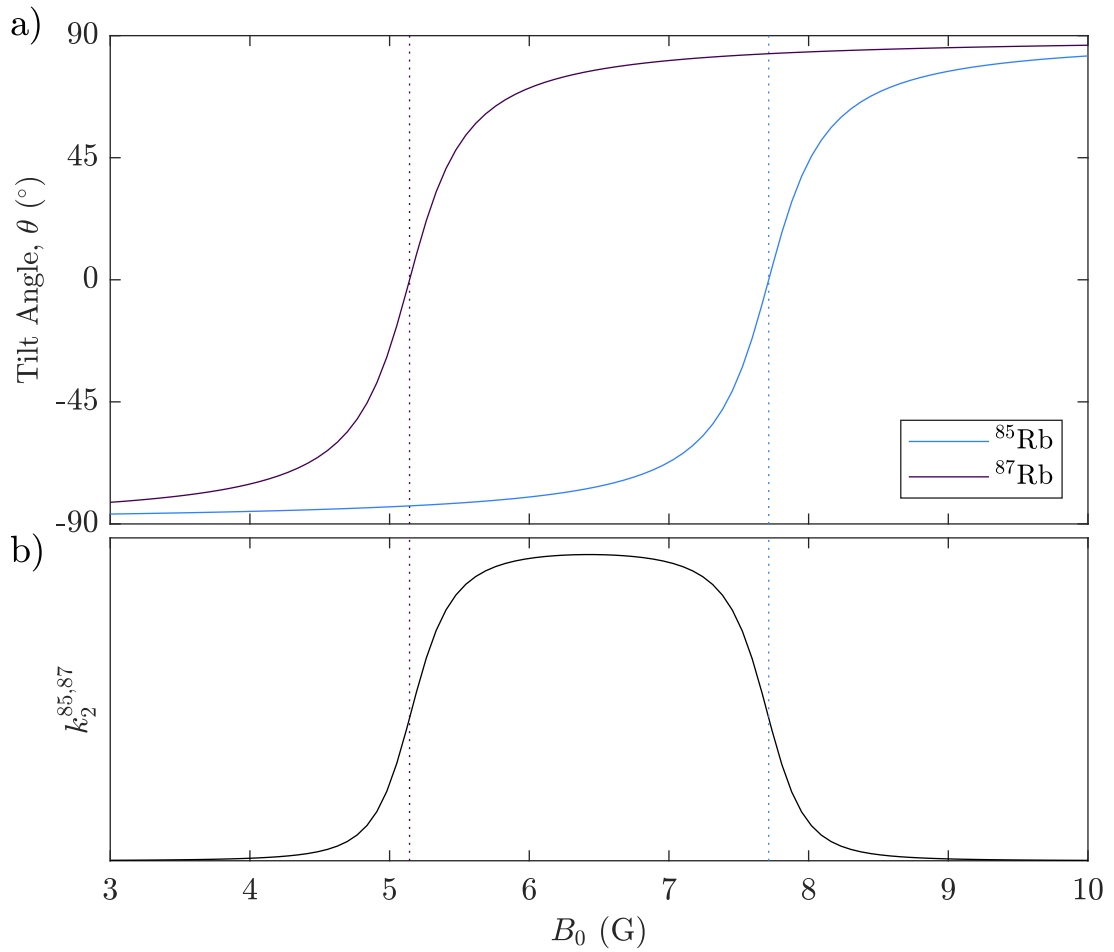


Figure 6.8: **Expected behaviour of $k_2^{85,87}$ versus B_0 :** **a)** The effective field's tilt angle θ for both ^{85}Rb and ^{87}Rb is plotted as a function of static magnetic field magnitude B_0 . The dressing frequency $\omega = 3.6$ MHz. **b)** Qualitative sketch of the expected dependency of $k_2^{85,87}$. See text for discussion.

range of static fields.

In the SSTAAP, the role of the static field B_0 is taken by the time-averaging field B_{TOP} . Above the ^{85}Rb rf resonance, changing B_{TOP} allows the dependence of $k_2^{85,87}$ on the frequency detuning to be measured, as described in the next section. It is not possible to measure loss rates for $g_{\text{F}}^{85}\mu_{\text{B}}B_{\text{TOP}} < \hbar\omega$ as the two species separate.

6.4.3 Measuring the two-body inelastic rate constant $k_2^{85,87}$

With ^{85}Rb - ^{87}Rb collisions as the dominant loss mechanism, eqn. (6.1) approximates to

$$\frac{\partial N_{85}}{\partial t} \approx - \int k_2^{85,87}(\vec{r}) n_{87}(\vec{r}) n_{85}(\vec{r}) dV \quad (6.9)$$

Measuring the inelastic loss rate reveals the rate constant $k_2^{85,87}$. As before, only the ensemble average $\langle k_2^{85,87} \rangle$ can be inferred; inelastic collisions take place over a range of different static field magnitudes due to the finite temperature of the cloud and the quadrupole gradient. $k_2^{85,87}$ is a function of many parameters, but since many of these carry a spatial dependence $k_2^{85,87}$ is written as an explicit function of position in eqn. (6.9).

To measure $k_2^{85,87}$ for different parameters, the SSTAAP is operated with $g_{\text{F}}^{85}\mu_{\text{B}}B_{\text{TOP}} > \hbar\omega$ and close to the ^{85}Rb resonance $g_{\text{F}}^{85}\mu_{\text{B}}B_{\text{TOP}} = \hbar\omega$. In this configuration both ^{85}Rb and ^{87}Rb remain well-overlapped in the TOP, with B_{TOP} determining the static magnetic field magnitude B_0 at which collisions occur. The adjustment of each species' position with B_{TOP} (such as described in Sec 5.3.1, and illustrated in Fig 5.3) is here an unwanted side-effect that varies the overlap between the species and thus modifies the rate of inelastic collisions. Nonetheless, normalising measured rates with respect to this change enables the dependence of k_2 on B_0 to be explored.

The experimental method follows closely that of Sec 6.4.1. A mixture of ^{85}Rb and ^{87}Rb is loaded into the TOP, and cooled through rf-evaporation of ^{87}Rb to about

0.4 μK . The 3.6 MHz rf-dressing field is turned on, and ^{85}Rb and ^{87}Rb atoms projected into dressed states $|\tilde{m}_F = 2\rangle$ and $|\tilde{m}_F = 1\rangle$ respectively as before. B_{TOP} is ramped down linearly over 100 ms to a final value, typically between 7.8 G to 8.5 G, where the number imbalanced mixture ($N_{87} \gg N_{85}$) is held and loss observed. A ‘series’ in this context refers to a selection of sequences with same final value of the control parameter B_{TOP} . The quadrupole gradient used is 116 G cm^{-1} .

We measure the ^{85}Rb - ^{87}Rb inelastic loss rate by fitting $Ae^{-\beta t} + c$ to $N_{85}(t)$. The loss rates of ^{85}Rb range from 1 Hz to 30 Hz depending on the value of B_{TOP} . As it is feasible that changing B_{TOP} could also vary the lifetime of ^{85}Rb , for instance due to the presence of rf noise or an increased loss rate through non-adiabatic following as the TAAP regime is approached, we also take rough measurements of the ^{85}Rb lifetime in the absence of ^{87}Rb , which confirm that interspecies inelastic collisions remain the dominant cause of loss.

To accurately calculate the overlap integral $\int n_{85}n_{87}dV$ requires knowledge of each species’ distribution. In Sec 6.4.1 it was assumed that $T_{85} = T_{87}$. Here, the distribution of ^{85}Rb for each series is determined by measuring the expanded cloud’s width after various time-of-flight durations, and fitting to the cloud’s expansion rate. The low signal-to-noise ratio at small N_{85} restricts the maximum time-of-flight to 7 ms, above which Gaussian fits become unstable. It also prevents measuring T_{85} at hold times where the population of ^{85}Rb has been diminished, and all measurements of T_{85} are therefore taken immediately after the B_{TOP} ramp when N_{85} is greatest. On the other hand, T_{87} is accurately determined from individual images after a single, long time-of-flight; the large atom number N_{87} gives a sufficient signal-to-noise ratio for fitting after a long 24 ms time-of-flight expansion, where the in-trap size of the cloud is negligible with respect to the expanded cloud width.

Determining the density distribution of each species also requires knowledge of the confining potentials. It would have been too time intensive to directly measure

the trap frequencies of both species at each value of B_{TOP} and rf amplitude. Instead, numerical methods are used to calculate the confining potentials of both species, and the spatial offset between them. These agree with trap frequencies for both ^{85}Rb and ^{87}Rb reported in Sec 6.4.1 and with previously measured trap frequencies in the TAAP [28, 61].

6.4.3.1 Discussion of results

The measured $\langle k_2^{85,87} \rangle$ versus static field magnitude $\langle B_0 \rangle$ is presented in Fig 6.9 for three rf amplitudes. Both quantities shown are overlap-weighted averages, $\langle x \rangle = \int x n_{85} n_{87} dV / \int n_{85} n_{87} dV$. There is evidence that the inelastic rate constant increases at smaller detunings from the ^{85}Rb rf resonance (at 7.7 G), as predicted from the intuitive model. We did not find a noticeable dependence on rf amplitude (as discussed further at the end of this section).

The methodology used to determine the error bars of Fig 6.9 considered that errors in both overlap-weighted average quantities depend on the uncertainties in the distributions n_{85} and n_{87} , which themselves depend on the temperatures of the atomic distributions and properties of the trap. As before, a Monte-Carlo approach is used; integrals are calculated for randomly drawn temperatures and trap parameters, and repeated many times to determine the distributions of $\langle B_0 \rangle$ and $\langle k_2^{85,87} \rangle$. This method also accounts for any correlations between errors in these two variables, although the distribution of individual simulations in Fig 6.9 suggests there is little correlation. The error in $\langle B_0 \rangle$ is taken as the standard deviation of 500 Monte-Carlo calculated values¹⁴. For the error in $\langle k_2^{85,87} \rangle$, the standard deviation of the Monte-Carlo values as a percentage of the mean is combined in quadrature with the percentage uncertainty in the fitted exponential rate parameter. The distribution of points increases at smaller values of B_{TOP} because the position of the ^{85}Rb potential minimum (and

¹⁴The variances used for the Monte-Carlo parameters are a mixture of systematic uncertainties and shot-to-shot variation, which is why we take standard deviations as our final uncertainties here.

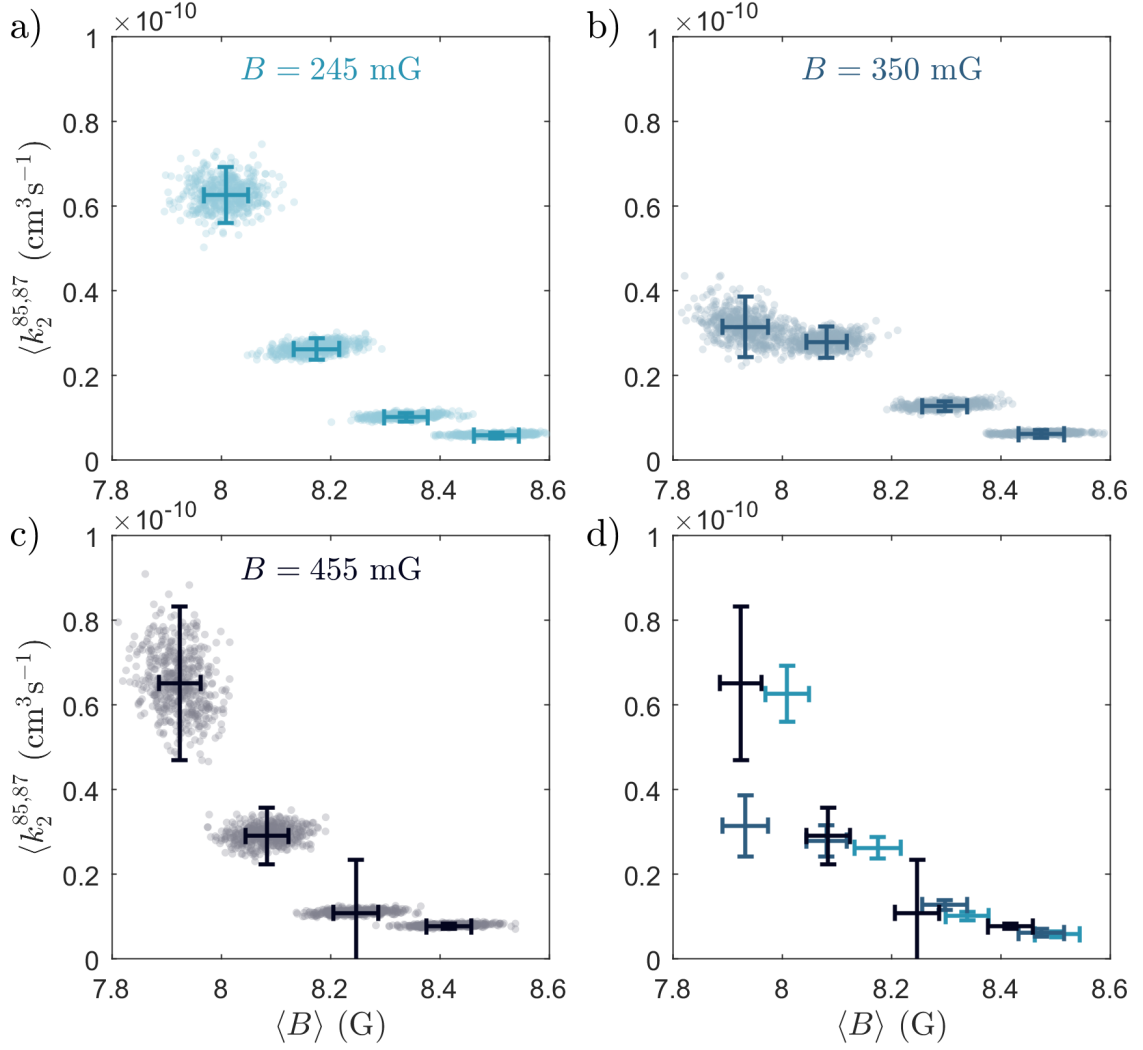


Figure 6.9: **Change in two-body rate constant with static field:** The overlap-weighted average of the inelastic rate constant $\langle k_2^{85,87} \rangle$ is plotted against the overlap-weighted average of the static magnetic field $\langle B \rangle$ for three values of rf amplitude B_{rf} . Each light dot on (a-c) is the result of an individual Monte-Carlo calculation, which are used to determine the uncertainties in $\langle B \rangle$ and $\langle k_2^{85,87} \rangle$ (see text). **d)** The data shown in (a-c) is combined onto a single plot. No clear dependence on rf amplitude is noticeable.

thus the inter-species overlap) becomes more sensitive to fluctuations in B_{TOP} . A 0.5% systematic error in the magnitude of B_{TOP} is included.

The distribution of T_{87} is determined from the set of ^{87}Rb absorption images at long time-of-flight, with mean typically around $0.4\ \mu\text{K}$. The fitted temperatures of ^{85}Rb are between $0.7\ \mu\text{K}$ to $1\ \mu\text{K}$, and typically show some anisotropy in the horizontal and vertical directions. These features are likely the result of heating during the short loading ramp, which causes large changes in the ^{85}Rb trap frequencies. This heating is reduced for longer ramp durations, but this leads to increased inelastic losses during loading and results in unacceptably low signal-to-noise ratios for the measurements of $N_{85}(t)$. The anisotropy is neglected in the analysis, with T_{85} taken as the mean of the fitted horizontal and vertical temperatures. It is hard to quantify the variation in T_{85} to use for the Monte-Carlo method, as the uncertainties in the fit parameter do not necessarily represent the shot-to-shot variation in T_{85} . We combine in quadrature the relative uncertainty of the fit parameter with that of the standard deviation of T_{87} , reasoning that the shot-to-shot fluctuations in T_{85} cannot be smaller than the T_{87} reservoir even when the uncertainty of the fit is small.

Given the sensitivity of the overlap with B_{TOP} , extra care is taken to characterise any variation of this field. The field magnitude in both \vec{e}_x and \vec{e}_y directions is measured on a calibrated pickup coil each sequence, from which the mean and variance is determined and used in the Monte-Carlo calculations. Variation of the rf frequency and amplitude is neglected; both are defined with an accuracy far beyond that which is required for the current experiment, and have negligible shot-to-shot variation. So too is the quadrupole gradient B' .

No rf amplitude dependence is visible in Fig 6.9, although we predicted a larger rf amplitude would smooth out the dependence of $k_2^{85,87}$ on the static field magnitude at which collisions occur. It seems likely that a broadening of $\langle k_2^{85,87} \rangle$ from the thermal distribution of the cloud dominates that arising from the rf amplitude. In Fig 6.10

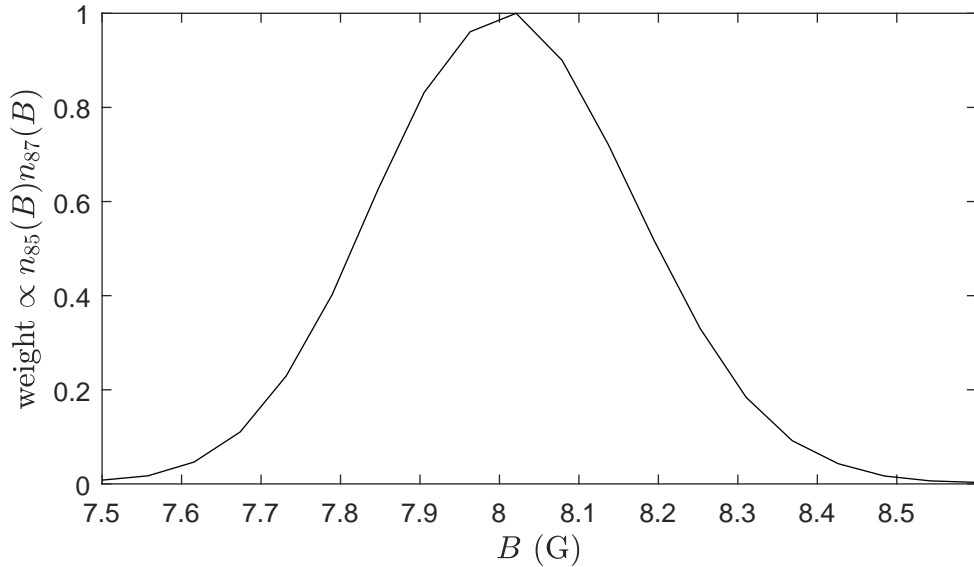


Figure 6.10: **Distribution of overlap by magnetic field magnitude:** A histogram showing the relative weights $n_{85}n_{87}$ given to each magnetic field magnitude during the overlap-weighted average of $\langle B_0 \rangle$ and $\langle k_2^{85,87} \rangle$ due to the thermal distributions of both species in the trap.

a histogram of the static field magnitude B_0 is shown, weighted by $n_{85}n_{87}$, showing that for these thermal distributions the region of overlap is spread over a range of static fields B_0 that is comparable to the rf amplitude.

6.4.4 Comparison to a coupled channel model

The toy model of Sec 6.4.2 gives an intuitive picture of why the interspecies loss is rapid, but it is not able to make quantitative predictions for the rate constant. When this is required a full quantum mechanical scattering calculation must be performed. Owens *et. al.* have recently extended such calculations to examine inelastic loss in rf dressed traps of a single species [130], using a dressed-state formalism to incorporate the energies of the rf photons and atom-photon interaction. A large number of possible exit channels exist, varying in both dressed-state photon number and the state of each atom. The total calculated loss rate is the sum of that from each separate exit channel,

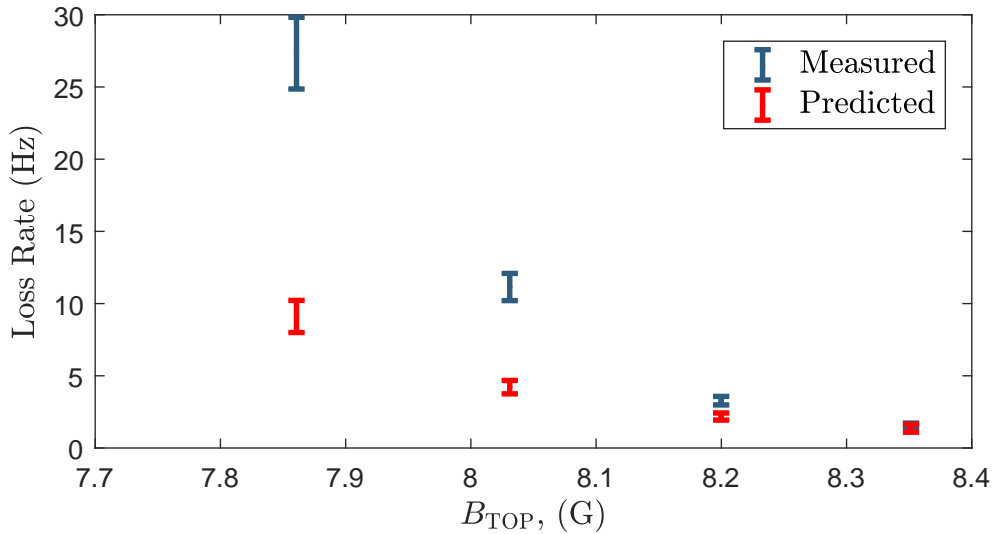


Figure 6.11: **Comparison to coupled channels for 350 mG series:** Predicted loss rates are compared to those measured on the apparatus.

which individually have different rate constants. This model includes the evolution of the internal states due to the rf field during the collision.

We compare our measured rates to analytical predictions from the theoretical model developed at Durham University [130], which have kindly been provided by Owens himself [141]. The predicted rates (and error bars) are determined using a Monte-Carlo method that incorporates the systematic errors and shot-to-shot noise variations identified in the previous section, taking the exponential loss rate to be $\int k_2^{85,87}(B_0)\tilde{n}_{85}\tilde{n}_{87}N_{87}dV$, with $k_2^{85,87}(B_0)$ specified by the calculations. The measured rates are well within an order of magnitude of the predicted inelastic loss rate, which is impressive considering that the theoretical model determines rates from *ab initio* calculations using only the molecular potentials with no free parameters. There does appear to be a systematic factor between the measured and predicted rates, the source of which we have not yet been able to identify though work is ongoing. Predicting k_2 to within an order of magnitude is sufficient for planning an experiment, and the model is able to do this.

6.5 Conclusions and Outlook

In this chapter the inelastic loss of mixtures in rf-dressed potentials has been investigated. Mixtures of ^{85}Rb and ^{87}Rb atoms in the maximally-stretched, lower hyperfine states are collisionally stable when confined by static fields, and no measurable interspecies inelastic loss occurs the TOP trap. By contrast, the lower hyperfine states of these isotopes undergo rapid loss in an rf-dressed potential, which we identified as arising from ^{85}Rb - ^{87}Rb inelastic collisions. A simple model gives an intuitive explanation for these losses, and suggests fast inelastic loss by spin-exchange collisions can proceed when the Landé g_{F} -factors of the species differ. Thus, the requirement for species-selective manipulations using rf-dressed potentials is incompatible with that of collisional stability of the mixture. Consistent with this model, the measured inelastic loss coefficients increase near the rf resonance for ^{85}Rb , but we cannot observe any dependence on the rf amplitude which may be obscured by the thermal distribution of the atoms. Finally, comparisons were made to the predicted rates of a coupled-channel model.

In future, we may capitalize on our well characterised rf-dressing apparatus to improve these measurements, providing a rigorous test of the coupled-channel model. Rather than using the rf-dressing fields for confinement, a crossed-beam dipole trap would keep the ^{85}Rb - ^{87}Rb overlap constant as the static field is changed, reducing systematic errors and permitting the investigation of $k_2^{85,87}(B)$ over a wider range of fields for which ^{85}Rb and ^{87}Rb would separate in the SSTAAP. Some of the required optics was installed during previous alignment of an imaging lattice. The large predicted values of $k_2^{85,87}$ would produce measurable loss rates even with low densities, thus sub-optimal loading is acceptable. Producing the magnetic field by using an existing Helmholtz coil pair, with minimal quadrupole gradient, would reduce the spread of static field magnitudes experienced by the atomic distributions.

Although problematic for ^{85}Rb - ^{87}Rb , inelastic loss is not necessarily the definitive

end of species-selective rf-dressed potentials. Preliminary lifetime measurements of rf dressed $^{87}\text{Rb}|F = 2\rangle$ impurities in contact with a $^{87}\text{Rb}|F = 1\rangle$ BEC have shown $1/e$ -lifetimes of about a second. While some reduction in inter-species overlap may result from the expulsion of the impurities by the mean field of the condensate, this is a promising result that suggests using mixtures of the ^{87}Rb hyperfine levels in rf-dressed potentials may be workable. One possible explanation is that although spin-exchange collisions can occur between constituents of this mixture when rf-dressed, they naturally proceed at a slow rate. Low spin-exchange rates in ^{87}Rb hyperfine mixtures have previously been reported [53, 142], and attributed to the similarity of singlet and triplet scattering lengths in ^{87}Rb - ^{87}Rb collisions [132]. Alternatively, the simple model that suggested fast loss when $\text{sign}(g_{\text{F}})$ differs may not be valid. Further work is required to characterise this mixture, which was not possible within the time available. It would also be interesting to see if spin-exchange occurs between rf dressed mixtures of ^{87}Rb and ^{41}K ; the g_{F} -factors of these species can be matched¹⁵, which may suppress spin-exchange according to the simple model.

There is also great interest in Feshbach resonances induced by the applied rf field [125, 126, 127, 128], and our measurements provide a benchmark against which to test theories of rf-dressed collisions. Trapping atomic mixtures in an rf dressed potential that induces a Feshbach resonance (such as that between $^{87}\text{Rb}|F = 1\rangle$ and $|F = 2\rangle$ states occurring at 9 G) could provide an additional means to control the interactions between the constituent species.

¹⁵up to a small correction because of the slightly different nuclear g_I -factors

Chapter 7

Conclusions

This thesis describes experimental work to extend the technique of rf dressed potentials to multiple frequencies, allowing the low heating rates, stability and smoothness of these potentials to be harnessed in a greater range of experiments. A double-well potential was produced by dressing atoms with a polychromatic field of three frequency components, with the energy of both the wells and barrier tunable by modifying the rf-dressing field. After a preliminary demonstration of the technique [21], the separation between the wells was reduced to $6.7\ \mu\text{m}$ which is sufficiently small to observe matter-wave interference between the two components of a split condensate after time-of-flight expansion. In principle this separation can be reduced further to achieve quantum tunnelling between the wells in future experiments.

We investigated the species-selectivity of rf-dressed potentials, especially when using multiple frequency components [97], and proposed a number of schemes in which species with different magnetic moments can be individually manipulated using combinations of time-averaging and rf-dressing fields. In implementing these techniques for ^{85}Rb and ^{87}Rb , we observed fast inelastic loss between components of the mixture. We show the loss is caused by two-body ^{85}Rb - ^{87}Rb collisions, and interpret the results as evidence that rapid spin-exchange collisions occur for co-trapped species

with different g_F -factors. The rate constants we measure provide a benchmark for theoretical models of dressed collisions being developed by collaborators at Durham University. Although loss is unwanted, a better understanding of these processes will offer new insight into manipulating Feshbach resonances with rf fields. We predict that loss will limit the applicability of the proposed species-selective methods, but they remain viable for hyperfine mixtures of ^{87}Rb in which the inelastic loss proceeds slowly.

Our work to upgrade several components of the BEC machine has resulted in a stable apparatus that is capable of automated operation, providing a strong foundation for the next experiments. The increased scope of magnetic potentials when using the novel techniques described herein provides a number of exciting opportunities for future research.

7.1 Future experiments

7.1.1 2D gases

The anisotropic confinement of the shell trap is well suited to the production of quasi two-dimensional (2D) gases [19]. With further work, our double-well potential will provide a system in which a quantum-degenerate 2D gas is split and subsequently recombined. This naturally lends itself to interferometric measurements of phase correlations in a 2D system, similar to ground-breaking experiments performed for a one-dimensional system [86, 87, 88, 89, 90].

7.1.2 Quantum-tunnelling

After improving the stability of the multiple-rf dressing field, experiments involving quantum tunnelling will become accessible by a further reduction of the double-well separation. The difficulties encountered so far have been technical rather than funda-

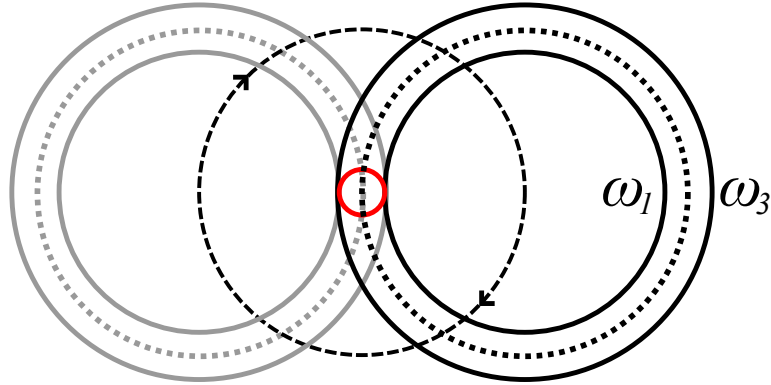


Figure 7.1: **A time-averaged ring with multiple dressing frequencies.:** The time-averaged ring potential is illustrated in red. Resonant spheroids for ω_1, ω_3 are shown in solid black, with the barrier resonant spheroid ω_2 shown as a dotted line. Their positions after half a rotation period of the time-averaging field is shown in grey. The dashed line shows the locus of the quadrupole node during time averaging.

mental, and it would be interesting to determine the minimum achievable separation before non-adiabatic losses become unsurmountable. This technique may compare favorably to optical potentials that require a stable alignment and are adversely affected by interference arising from defects along the optical path. Tunnelling of vortices has been examined theoretically [143], and the multiple-rf double-well is well-suited to this proposal; controlling the rf-dressing field to rotate only one half of a split BEC would permit the seeding of vortices in one well, and angular momentum exchange between the two populations may allow the vortex to tunnel through the barrier.

7.1.3 Combining time-averaging techniques with multiple-rf dressing

Although used in this work primarily to load atoms into shell traps, TAAP traps are capable of producing double-well potentials [61] and large diameter rings [60] with proven applications in interferometry [113]. Combining these techniques with a multiple-rf field would create a greater number of potential minima, a fact noted in the original TAAP proposal [40]. Multiple concentric ring traps would be useful

for interferometric measurements of rotation; simultaneously observing interference fringes using rings of very different radii (and thus enclosed areas) provides a high dynamic-range of sensitivity, similar to recent work in an accelerometer using two species diffracted with different momentum kicks [144].

The ring radii characteristic of single rf TAAP traps are not well suited to trapping annular BECs; the large circumference gives a low chemical potential, and it is technically challenging to keep the trap sufficiently level to keep the BEC connected around the ring [60]. Dressing with multiple frequencies may provide a solution (see Fig 7.1). The principle is to trap atoms on the overlapping paths traced by two resonant spheroids as a horizontal bias field rotates. The radius of this time-averaged ring trap is determined by the difference in the dressing frequencies. For example, the dressing field used to create our $6.7\ \mu\text{m}$ double-well potential would here produce a ring of diameter $6.7\ \mu\text{m}$. It may be possible to observe spontaneous emergence of angular momentum Josephson oscillations between two coupled superfluid rings [145].

Other possibilities exist for this configuration. Unlike when time-averaging a single-rf shell, the instantaneous potential does not possess a cylindrical symmetry about the \vec{e}_z axis. Displacing the instantaneous minima up and down as the horizontal field rotates, *eg* by using a vertical time-averaging field, could produce one-dimensional lattices with periodic boundary conditions around the circumference of the ring. Further work is required to determine if this scheme will have acceptable non-adiabatic loss rates.

7.1.4 Experiments with mixtures

Inelastic loss in the rf dressed potential has limited the range of experiments that can be undertaken with ^{85}Rb and ^{87}Rb in this thesis, but mixtures of ^{85}Rb and ^{87}Rb atoms in the maximally stretched states of the lower hyperfine level are collisionally stable in static magnetic fields. Experiments in which species-selectivity is not required,

such as trapping impurity atoms in a vortex lattice of a second species [146], can still be undertaken in the TOP trap.

Preliminary observations show that inelastic collisions between the different hyperfine states of ^{87}Rb do not suffer from rapid losses when the mixture is rf-dressed. Future experiments should characterise this loss in detail, but this system appears extremely promising for species-selective manipulations on our apparatus, capable of examining quantum quenches [147], the self-trapping of impurities in the condensate [148], or the superfluid drag force exerted on impurities [149]. $F = 2$ impurities can be controllably created using a microwave transition, with an ability to selectively drive the transition in either well of our double-well potential to control the location at which the impurities are produced.

The ability to tune the double-well potential experienced by each species provides a capable platform for future experiments involving impurity atoms coupled to a large Bose-Einstein condensate reservoir. In the absence of tunnelling, insights can be made into Markovianity [104, 105, 106, 107] or the chaotic behaviour of a reservoir coupled to two separate quantum systems (here, the two wells) [150]. Conversely, with tunnelling between the wells, demonstrations of non-destructive thermometry and probing of excitations [16], of many-particle correlations [108], and collective decoherence [104] are possible.

References

- [1] M. H. Anderson, J. R. Ensher, M. R. Matthews, C. E. Wieman, and E. A. Cornell. Observation of Bose-Einstein condensation in a dilute atomic vapor. *Science*, 269(5221):198–201, Jul 1995.
- [2] K. B. Davis, M. O. Mewes, M. R. Andrews, N. J. van Druten, D. S. Durfee, D. M. Kurn, and W. Ketterle. Bose-Einstein condensation in a gas of sodium atoms. *Phys. Rev. Lett.*, 75:3969–3973, Nov 1995.
- [3] B. DeMarco and D. S. Jin. Onset of Fermi degeneracy in a trapped atomic gas. *Science*, 285(5434):1703–1706, 1999.
- [4] M. Lu, N. Q. Burdick, and B. L. Lev. Quantum degenerate dipolar Fermi gas. *Phys. Rev. Lett.*, 108:215301, May 2012.
- [5] K. Aikawa, A. Frisch, M. Mark, S. Baier, A. Rietzler, R. Grimm, and F. Ferlaino. Bose-Einstein condensation of erbium. *Phys. Rev. Lett.*, 108:210401, May 2012.
- [6] K.-K. Ni, S. Ospelkaus, M. H. G. de Miranda, A. Pe’er, B. Neyenhuis, J. J. Zirbel, S. Kotochigova, P. S. Julienne, D. S. Jin, and J. Ye. A high phase-space-density gas of polar molecules. *Science*, 322(5899):231–235, 2008.
- [7] S. A. Moses, J. P. Covey, M. T. Miecnikowski, B. Yan, B. Gadway, J. Ye, and D. S. Jin. Creation of a low-entropy quantum gas of polar molecules in an optical lattice. *Science*, 350(6261):659–662, 2015.

- [8] M. Cetina, M. Jag, R. S. Lous, I. Fritsche, J. T. M. Walraven, R. Grimm, J. Levinsen, M. M. Parish, R. Schmidt, M. Knap, and E. Demler. Ultrafast many-body interferometry of impurities coupled to a Fermi sea. *Science*, 354(6308):96–99, Oct 2016.
- [9] R. Scelle, T. Rentrop, A. Trautmann, T. Schuster, and M. K. Oberthaler. Motional coherence of Fermions immersed in a Bose gas. *Phys. Rev. Lett.*, 111:070401, Aug 2013.
- [10] C. Kohstall, M. Zaccanti, M. Jag, A. Trenkwalder, P. Massignan, G. M. Bruun, F. Schreck, and R. Grimm. Metastability and coherence of repulsive polarons in a strongly interacting Fermi mixture. *Nature*, 485:615–618, May 2012.
- [11] J. Catani, G. Lamporesi, D. Naik, M. Gring, M. Inguscio, F. Minardi, A. Kantian, and T. Giamarchi. Quantum dynamics of impurities in a one-dimensional Bose gas. *Phys. Rev. A*, 85:023623, Feb 2012.
- [12] S. Ospelkaus, C. Ospelkaus, O. Wille, M. Succo, P. Ernst, K. Sengstock, and K. Bongs. Localization of Bosonic atoms by Fermionic impurities in a three-dimensional optical lattice. *Phys. Rev. Lett.*, 96:180403, May 2006.
- [13] N. Spethmann, F. Kindermann, S. John, C. Weber, D. Meschede, and A. Widera. Dynamics of single neutral impurity atoms immersed in an ultracold gas. *Phys. Rev. Lett.*, 109:235301, Dec 2012.
- [14] M. Hohmann, F. Kindermann, T. Lausch, D. Mayer, F. Schmidt, and A. Widera. Single-atom thermometer for ultracold gases. *Phys. Rev. A*, 93:043607, Apr 2016.
- [15] T. Fukuhara, A. Kantian, M. Endres, M. Cheneau, P. Schauß, S. Hild, D. Bellem, U. Schollwöck, T. Giamarchi, C. Gross, I. Bloch, and S. Kuhr.

- Quantum dynamics of a mobile spin impurity. *Nature Physics*, 9:235–241, Apr 2013.
- [16] D. Hangleiter, M. T. Mitchison, T. H. Johnson, M. Bruderer, M. B. Plenio, and D. Jaksch. Nondestructive selective probing of phononic excitations in a cold Bose gas using impurities. *Phys. Rev. A*, 91:013611, Jan 2015.
- [17] O. Zobay and B. M. Garraway. Atom trapping and two-dimensional Bose-Einstein condensates in field-induced adiabatic potentials. *Phys. Rev. A*, 69:023605, Feb 2004.
- [18] B. M. Garraway and H. Perrin. Recent developments in trapping and manipulation of atoms with adiabatic potentials. *Journal of Physics B: Atomic, Molecular and Optical Physics*, 49(17):172001, Aug 2016.
- [19] K. Merloti, R. Dubessy, L. Longchambon, A. Perrin, P.-E. Pottie, V. Lorent, and H. Perrin. A two-dimensional quantum gas in a magnetic trap. *New Journal of Physics*, 15(3), Mar.
- [20] I. Lesanovsky, T. Schumm, S. Hofferberth, L. M. Andersson, P. Krüger, and J. Schmiedmayer. Adiabatic radio-frequency potentials for the coherent manipulation of matter waves. *Phys. Rev. A*, 73:033619, Mar 2006.
- [21] T. L. Harte, E. Bentine, K. Luksch, A. J. Barker, D. Trypogeorgos, B. Yuen, and C. J. Foot. Ultracold atoms in multiple radio-frequency dressed adiabatic potentials. *Phys. Rev. A*, 97:013616, Jan 2018.
- [22] T. Harte. *Ultracold atoms in dressed potentials*. PhD thesis, University of Oxford, 2017.
- [23] C. J. Foot. *Atomic Physics*. Oxford University Press, Great Clarendon Street, Oxford OX2 6DP, UK, 1 edition, 2005.

- [24] C. Cohen-Tannoudji and D. Guéry-Odelin. *Advances in Atomic Physics: An Overview*. World Scientific, 57 Shelton Street, Covent Garden, London WC2H 9HE, 2011.
- [25] C. Cohen-Tannoudji and S. Reynaud. Dressed-atom description of resonance fluorescence and absorption spectra of a multi-level atom in an intense laser beam. *Journal of Physics B: Atomic and Molecular Physics*, 10(3):345, 1977.
- [26] I. Lesanovsky, S. Hofferberth, J. Schmiedmayer, and P. Schmelcher. Manipulation of ultracold atoms in dressed adiabatic radio-frequency potentials. *Phys. Rev. A*, 74:033619, Sep 2006.
- [27] T. Yabuzaki, S. Nakayama, Y. Murakami, and T. Ogawa. Interaction between a spin-1/2 atom and a strong rf field. *Phys. Rev. A*, 10:1955–1963, Dec 1974.
- [28] M. Gildemeister. *Trapping ultracold atoms in time-averaged adiabatic potentials*. PhD thesis, University of Oxford, 2010.
- [29] G.W. Series. A semi-classical approach to radiation problems. *Physics Reports*, 43(1):1 – 41, 1978.
- [30] F. Bloch and A. Siegert. Magnetic resonance for nonrotating fields. *Phys. Rev.*, 57:522–527, Mar 1940.
- [31] D. T. Pegg. Semi-classical model of magnetic resonance in intense rf fields. *Journal of Physics B: Atomic and Molecular Physics*, 6(2):246, 1973.
- [32] C. Cohen-Tannoudji, J. Dupont-Roc, and C. Fabre. A quantum calculation of the higher order terms in the Bloch-Siegert shift. *Journal of Physics B: Atomic and Molecular Physics*, 6(8):L214, 1973.

- [33] S. Hofferberth, B. Fischer, T. Schumm, J. Schmiedmayer, and I. Lesanovsky. Ultracold atoms in radio-frequency dressed potentials beyond the rotating-wave approximation. *Phys. Rev. A*, 76:013401, Jul 2007.
- [34] J. H. Shirley. Solution of the Schrödinger equation with a Hamiltonian periodic in time. *Phys. Rev.*, 138:B979–B987, May 1965.
- [35] F. Bloch. Über die quantenmechanik der elektronen in kristallgittern. *Zeitschrift für Physik*, 52(7):555–600, Jul 1929.
- [36] D. Trypogeorgos. *Periodically Driven Atomic Systems*. PhD thesis, University of Oxford, 2014.
- [37] T. Schumm, S. Hofferberth, L. M. Andersson, S. Wildermuth, S. Groth, I. Bar-Joseph, J. Schmiedmayer, and P. Krüger. Matter-wave interferometry in a double well on an atom chip. *Nature Physics*, 1:57, Sep 2005.
- [38] L. Landau. Zur Theorie der Energieübertragung. II. *Phys. Z. Sowjetunion*, 2:4651, 1932.
- [39] C. Zener. Non-adiabatic crossing of energy levels. *Proc. Roy. Soc. London A: Math. Phys. & Eng. Sci.*, 137(833):696–702, 1932.
- [40] I. Lesanovsky and W. von Klitzing. Time-averaged adiabatic potentials: Versatile matter-wave guides and atom traps. *Phys. Rev. Lett.*, 99:083001, Aug 2007.
- [41] C. V. Sukumar and D. M. Brink. Spin-flip transitions in a magnetic trap. *Phys. Rev. A*, 56:2451–2454, Sep 1997.
- [42] K. A. Burrows, H. Perrin, and B. M. Garraway. Nonadiabatic losses from radio-frequency-dressed cold-atom traps: Beyond the Landau-Zener model. *Phys. Rev. A*, 96:023429, Aug 2017.

- [43] W. Heathcote. *A Toroidal Trap for Ultracold Atoms in a RF-Dressed State*. PhD thesis, University of Oxford, 2007.
- [44] M. Gildemeister, B. E. Sherlock, and C. J. Foot. Techniques to cool and rotate Bose-Einstein condensates in time-averaged adiabatic potentials. *Phys. Rev. A*, 85:053401, May 2012.
- [45] P. W. Courteille, B. Deh, J. Fortgh, A. Gnther, S. Kraft, C. Marzok, S. Slama, and C. Zimmermann. Highly versatile atomic micro traps generated by multi-frequency magnetic field modulation. *Journal of Physics B: Atomic, Molecular and Optical Physics*, 39(5):1055, Feb 2006.
- [46] B. Yuen. A basis for polychromatic dressed atoms. *in preparation*.
- [47] R. Kollengode Easwaran, L. Longchambon, P.-E. Pottie, V. Lorent, H. Perrin, and B. M. Garraway. RF spectroscopy in a resonant rf-dressed trap. *Journal of Physics B: Atomic, Molecular and Optical Physics*, 43(6):065302, 2010.
- [48] T. Fernholz, R. Gerritsma, S. Whitlock, I. Barb, and R. J. C. Spreeuw. Fully permanent magnet atom chip for Bose-Einstein condensation. *Phys. Rev. A*, 77:033409, Mar 2008.
- [49] B. Sheard. *Magnetic Transport and Bose-Einstein Condensation of Rubidium Atoms*. PhD thesis, University of Oxford, 2010.
- [50] B. Sherlock. *Ultracold quantum gases in time-averaged adiabatic potentials*. PhD thesis, University of Oxford, 2011.
- [51] K. I. Lee, J. A. Kim, H. R. Noh, and W. Jhe. Single-beam atom trap in a pyramidal and conical hollow mirror. *Opt. Lett.*, 21(15):1177–1179, Aug 1996.
- [52] D. A. Steck. Rubidium 87 D line data, Jan 2015. revision 2.1.5, available online at <http://steck.us/alkalidata>.

- [53] C. J. Myatt, E. A. Burt, R. W. Ghrist, E. A. Cornell, and C. E. Wieman. Production of two overlapping Bose-Einstein condensates by sympathetic cooling. *Phys. Rev. Lett.*, 78:586–589, Jan 1997.
- [54] C. J. Pethick and H. Smith. *Bose-Einstein Condensation in Dilute Gases*. Cambridge University Press, The Edinburgh Building, Cambridge CB2 2RU, UK, 1 edition, 2002.
- [55] I. Bloch, M. Greiner, O. Mandel, T. W. Hänsch, and T. Esslinger. Sympathetic cooling of ^{85}Rb and ^{87}Rb . *Phys. Rev. A*, 64:021402, Jul 2001.
- [56] S. B. Papp. *Experiments with a two-species Bose-Einstein condensate utilizing widely tunable interparticle interactions*. PhD thesis, University of Colorado, 2007.
- [57] P. A. Altin, N. P. Robins, D. Dring, J. E. Debs, R. Poldy, C. Figl, and J. D. Close. ^{85}Rb tunable-interaction Bose-Einstein condensate machine. *Review of Scientific Instruments*, 81(6):063103, Jun 2010.
- [58] J. P. Burke, J. L. Bohn, B. D. Esry, and C. H. Greene. Prospects for mixed-isotope Bose-Einstein condensates in rubidium. *Phys. Rev. Lett.*, 80:2097–2100, Mar 1998.
- [59] S. B. Papp and C. E. Wieman. Observation of heteronuclear Feshbach molecules from a ^{85}Rb - ^{87}Rb gas. *Phys. Rev. Lett.*, 97:180404, Oct 2006.
- [60] B. E. Sherlock, M. Gildemeister, E. Owen, E. Nugent, and C. J. Foot. Time-averaged adiabatic ring potential for ultracold atoms. *Phys. Rev. A*, 83:043408, Apr 2011.

- [61] M. Gildemeister, E. Nugent, B. E. Sherlock, M. Kubasik, B. T. Sheard, and C. J. Foot. Trapping ultracold atoms in a time-averaged adiabatic potential. *Phys. Rev. A*, 81:031402, Mar 2010.
- [62] D. J. McCarron, S. A. King, and S. L. Cornish. Modulation transfer spectroscopy in atomic rubidium. *Measurement Science and Technology*, 19(10):105601, Aug 2008.
- [63] J. H. Shirley. Modulation transfer processes in optical heterodyne saturation spectroscopy. *Opt. Lett.*, 7(11):537–539, Nov 1982.
- [64] M. Gajdacz, P. L. Pedersen, T. M., A. J. Hilliard, J. Arlt, and J. F. Sherson. Non-destructive Faraday imaging of dynamically controlled ultracold atoms. *Review of Scientific Instruments*, 84(8):083105, Aug 2013.
- [65] Sindhu J., Tadas P., Mark G. B., Hans Marin F., and Thomas F. Dispersive detection of radio-frequency-dressed states. *Phys. Rev. A*, 97:043416, Apr 2018.
- [66] Analog Devices. *PLL Frequency Synthesizer: ADF4107 Datasheet*, 2013. Rev. D.
- [67] J. Appel, A. MacRae, and A. I. Lvovsky. A versatile digital ghz phase lock for external cavity diode lasers. *Measurement Science and Technology*, 20(5):055302, Apr 2009.
- [68] M. Jasperse. *Faraday magnetic resonance imaging of Bose-Einstein condensates*. PhD thesis, Monash University, 2017.
- [69] P. Horowitz and W. Hill. *The Art of Electronics*. Cambridge University Press, 32 Avenue of the Americas, New York, NY 10013-2473, USA, 3 edition, 2015.

- [70] V. M. Valenzuela, S. H. Hamzeloui, M. Gutiérrez, and E. Gomez. Multiple isotope magneto-optical trap from a single diode laser. *J. Opt. Soc. Am. B*, 30(5):1205–1210, May 2013.
- [71] A. Bonnin, N. Zahzam, Y. Bidel, and A. Bresson. Simultaneous dual-species matter-wave accelerometer. *Phys. Rev. A*, 88:043615, Oct 2013.
- [72] C. J. Myatt, N. R. Newbury, and C. E. Wieman. Simplified atom trap by using direct microwave modulation of a diode laser. *Opt. Lett.*, 18(8):649–651, Apr 1993.
- [73] R. Kowalski, S. Root, S. D. Gensemer, and P. L. Gould. A frequency-modulated injection-locked diode laser for two-frequency generation. *Review of Scientific Instruments*, 72(6):2532–2534, May 2001.
- [74] D. Sahagun, V. Bolpasi, and W. Von Klitzing. A simple and highly reliable laser system with microwave generated repumping light for cold atom experiments. *Optics Communications*, 290:110–114, Mar 2013.
- [75] M. J. Snadden, R. B. M. Clarke, and E. Riis. Injection-locking technique for heterodyne optical phase locking of a diode laser. *Opt. Lett.*, 22(12):892–894, Jun 1997.
- [76] G. Ferrari, M.-O. Mewes, F. Schreck, and C. Salomon. High-power multiple-frequency narrow-linewidth laser source based on a semiconductor tapered amplifier. *Opt. Lett.*, 24(3):151–153, Feb 1999.
- [77] G. Zuern. High current control for magnetic transport of cold atoms, 2008. Project report.
- [78] O. Morizot, L. Longchambon, R. Kollengode Easwaran, R. Dubessy, E. Knyazchyan, P.-E. Pottie, V. Lorent, and H. Perrin. Influence of the radio-

- frequency source properties on rf-based atom traps. *The European Physical Journal D*, 47(2):209–214, Apr 2008.
- [79] P. Baranowski. Towards number correlated states of a Bose-Einstein condensed gas. Master’s thesis, Freie Universität Berlin, 2005.
- [80] G. Reinaudi, T. Lahaye, Z. Wang, and D. Guéry-Odelin. Strong saturation absorption imaging of dense clouds of ultracold atoms. *Optics Letters*, 32:3143, 2007.
- [81] X. Li, M. Ke, B. Yan, and Y. Wang. Reduction of interference fringes in absorption imaging of cold atom cloud using eigenface method. *Chin. Opt. Lett.*, 5(3):128–130, Mar 2007.
- [82] C. F. Ockeloen, A. F. Tauschinsky, R. J. C. Spreeuw, and S. Whitlock. Detection of small atom numbers through image processing. *Phys. Rev. A*, 82:061606, Dec 2010.
- [83] J. Williams. AN25: Switching regulators for poets: A gentle guide for the trepidatious, 1987. (Linear Technology application note).
- [84] Y. Castin and R. Dum. Bose-Einstein condensates in time dependent traps. *Phys. Rev. Lett.*, 77:5315–5319, Dec 1996.
- [85] M. R. Andrews, C. G. Townsend, H.-J. Miesner, D. S. Durfee, D. M. Kurn, and W. Ketterle. Observation of interference between two Bose condensates. *Science*, 275(5300):637–641, Jan 1997.
- [86] S. Hofferberth, I. Lesanovsky, B. Fischer, J. Verdu, and J. Schmiedmayer. Radiofrequency-dressed-state potentials for neutral atoms. *Nature Physics*, 2(10):710–716, Sep 2006.

- [87] T. Langen, R. Geiger, M. Kuhnert, B. Rauer, and J. Schmiedmayer. Local emergence of thermal correlations in an isolated quantum many-body system. *Nature Physics*, 9:640–643, Oct 2013.
- [88] T. Schweigler, V. Kasper, S. Erne, I. Mazets, B. Rauer, F. Cataldini, T. Langen, T. Gasenzer, J. Berges, and J. Schmiedmayer. Experimental characterization of a quantum many-body system via higher-order correlations. *Nature*, 545:323, May 2017.
- [89] M. Gring, M. Kuhnert, T. Langen, T. Kitagawa, B. Rauer, M. Schreitl, I. Mazets, D. A. Smith, E. Demler, and J. Schmiedmayer. Relaxation and Prethermalization in an Isolated Quantum System. *Science*, 337:1318, Sep 2012.
- [90] B. Rauer, S. Erne, T. Schweigler, F. Cataldini, M. Tajik, and J. Schmiedmayer. Recurrences in an isolated quantum many-body system. *Science*, 7938, Feb 2018.
- [91] A. Polkovnikov, E. Altman, and E. Demler. Interference between independent fluctuating condensates. *Proceedings of the National Academy of Sciences*, 103(16):6125–6129, Apr 2006.
- [92] A. Imambekov, V. Gritsev, and E. Demler. Fundamental noise in matter interferometers. *Proc. 2006 Enrico-Fermi Summer School on Ultracold Fermi Gases*, 02138, Mar 2007.
- [93] L. Mathey and A. Polkovnikov. Light cone dynamics and reverse Kibble-Zurek mechanism in two-dimensional superfluids following a quantum quench. *Phys. Rev. A*, 81(3):033605, Mar 2010.
- [94] L. Mathey, K. J. Günter, J. Dalibard, and A. Polkovnikov. Dynamic Kosterlitz-Thouless transition in two-dimensional Bose mixtures of ultracold atoms. *Physical Review A*, 95(5):053630, May 2017.

- [95] C. J. Foot and M. D. Shotter. Double well potentials and quantum gates. *American Journal of Physics*, 79(7):762–768, Feb 2011.
- [96] A. W. Sandvik. Numerical solutions of the Schrödinger equation, Sept 2017. Lecture notes, Boston University.
- [97] E. Bentine, T. L. Harte, K. Luksch, A. J. Barker, J. Mur-Petit, B. Yuen, and C. J. Foot. Species-selective confinement of atoms dressed with multiple radiofrequencies. *J. Phys. B: Atom., Mol. & Opt. Phys.*, 50(9):094002, Apr 2017.
- [98] G. Modugno, G. Roati, F. Riboli, F. Ferlaino, R. J. Brecha, and M. Inguscio. Collapse of a degenerate Fermi gas. *Science*, 297(5590):2240–2243, Sep 2002.
- [99] Kenneth G., Thilo S., H. Moritz, M. Köhl, and T. Esslinger. Bose-Fermi mixtures in a three-dimensional optical lattice. *Phys. Rev. Lett.*, 96:180402, May 2006.
- [100] J. Catani, G. Barontini, G. Lamporesi, F. Rabatti, G. Thalhammer, F. Minardi, S. Stringari, and M. Inguscio. Entropy exchange in a mixture of ultracold atoms. *Phys. Rev. Lett.*, 103:140401, Sep 2009.
- [101] D. C. McKay, C. Meldgin, D. Chen, and B. DeMarco. Slow thermalization between a lattice and free Bose gas. *Phys. Rev. Lett.*, 111:063002, Aug 2013.
- [102] A. J. Kerman, J. M. Sage, S. Sainis, T. Bergeman, and D. DeMille. Production of ultracold, polar Rb-Cs molecules via photoassociation. *Phys. Rev. Lett.*, 92:033004, Jan 2004.
- [103] C. Ospelkaus, S. Ospelkaus, L. Humbert, P. Ernst, K. Sengstock, and K. Bongs. Ultracold heteronuclear molecules in a 3d optical lattice. *Phys. Rev. Lett.*, 97:120402, Sep 2006.

- [104] M. A. Cirone, G. De Chiara, G. M. Palma, and A. Recati. Collective decoherence of cold atoms coupled to a BoseEinstein condensate. *New Journal of Physics*, 11(10):103055, Oct 2009.
- [105] F. Galve, G. L. Giorgi, and R. Zambrini. Entanglement dynamics of nonidentical oscillators under decohering environments. *Phys. Rev. A*, 81:062117, Jun 2010.
- [106] P. Haikka, S. McEndoo, G. De Chiara, G. M. Palma, and S. Maniscalco. Quantifying, characterizing, and controlling information flow in ultracold atomic gases. *Phys. Rev. A*, 84:031602, Sep 2011.
- [107] C. Addis, P. Haikka, S. McEndoo, C. Macchiavello, and S. Maniscalco. Two-qubit non-markovianity induced by a common environment. *Phys. Rev. A*, 87:052109, May 2013.
- [108] M. Streif, A. Buchleitner, D. Jaksch, and J. Mur-Petit. Measuring correlations of cold-atom systems using multiple quantum probes. *Phys. Rev. A*, 94:053634, Nov 2016.
- [109] T. J. Elliott and T. H. Johnson. Nondestructive probing of means, variances, and correlations of ultracold-atomic-system densities via qubit impurities. *Phys. Rev. A*, 93:043612, Apr 2016.
- [110] R. Onofrio and C. Presilla. Reaching Fermi degeneracy in two-species optical dipole traps. *Phys. Rev. Lett.*, 89:100401, Aug 2002.
- [111] L. J. LeBlanc and J. H. Thywissen. Species-specific optical lattices. *Phys. Rev. A*, 75:053612, May 2007.

- [112] T. Fernholz, R. Gerritsma, P. Krüger, and R. J. C. Spreeuw. Dynamically controlled toroidal and ring-shaped magnetic traps. *Phys. Rev. A*, 75:063406, Jun 2007.
- [113] P. Navez, S. Pandey, H. Mas, K. Poullos, T. Fernholz, and W. von Klitzing. Matter-wave interferometers using taap rings. *New Journal of Physics*, 18(7):075014, Jul 2016.
- [114] M. H. T. Extavour, L. J. LeBlanc, T. Schumm, B. Cieslak, S. Myrskog, A. Stummer, S. Aubin, and J. H. Thywissen. Dual species quantum degeneracy of ^{40}K and ^{87}Rb on an atom chip. *AIP Conference Proceedings*, 869(1):241–249, Nov 2006.
- [115] B. D. Esry, C. H. Greene, J. P. Burke, Jr., and J. L. Bohn. Hartree-fock theory for double condensates. *Phys. Rev. Lett.*, 78:3594–3597, May 1997.
- [116] S. B. Papp, J. M. Pino, and C. E. Wieman. Tunable miscibility in a dual-species Bose-Einstein condensate. *Phys. Rev. Lett.*, 101:040402, Jul 2008.
- [117] F. Pinsker. Gaussian impurity moving through a Bose-Einstein superfluid. *Physica B: Condensed Matter*, 521:36 – 42, Sep 2017.
- [118] G. C. Katsimiga, S. I. Mistakidis, G. M. Koutentakis, P. G. Kevrekidis, and P. Schmelcher. Many-Body dissipative flow of a confined scalar Bose-Einstein condensate driven by a Gaussian impurity. *ArXiv e-prints*, May 2018.
- [119] P. S. Julienne. Laser modification of ultracold atomic collisions in optical traps. *Phys. Rev. Lett.*, 61:698–701, Aug 1988.
- [120] C. C. Agosta, I. F. Silvera, H. T. C. Stoof, and B. J. Verhaar. Trapping of neutral atoms with resonant microwave radiation. *Phys. Rev. Lett.*, 62:2361–2364, May 1989.

- [121] A. J. Moerdijk, B. J. Verhaar, and T. M. Nagtegaal. Collisions of dressed ground-state atoms. *Phys. Rev. A*, 53:4343–4351, Jun 1996.
- [122] T. Weber, J. Herbig, M. Mark, H.-C. Nägerl, and R. Grimm. Bose-Einstein condensation of cesium. *Science*, 299(5604):232–235, Jan 2003.
- [123] S. L. Cornish, N. R. Claussen, J. L. Roberts, E. A. Cornell, and C. E. Wieman. Stable ^{85}Rb Bose-Einstein condensates with widely tunable interactions. *Phys. Rev. Lett.*, 85:1795–1798, Aug 2000.
- [124] C. Chin, R. Grimm, P. Julienne, and E. Tiesinga. Feshbach resonances in ultracold gases. *Rev. Mod. Phys.*, 82:1225–1286, Apr 2010.
- [125] A. M. Kaufman, R. P. Anderson, Thomas M. Hanna, E. Tiesinga, P. S. Julienne, and D. S. Hall. Radio-frequency dressing of multiple Feshbach resonances. *Phys. Rev. A*, 80:050701, Nov 2009.
- [126] T. M. Hanna, E. Tiesinga, and P. S. Julienne. Creation and manipulation of Feshbach resonances with radiofrequency radiation. *New Journal of Physics*, 12(8):083031, Aug 2010.
- [127] T. V. Tscherbul, T. Calarco, I. Lesanovsky, R. V. Krems, A. Dalgarno, and J. Schmiedmayer. rf-field-induced Feshbach resonances. *Phys. Rev. A*, 81:050701, May 2010.
- [128] D. J. Owens, T. Xie, and J. M. Hutson. Creating Feshbach resonances for ultracold molecule formation with radio-frequency fields. *Phys. Rev. A*, 94:023619, Aug 2016.
- [129] K.-A. Suominen, E. Tiesinga, and P. S. Julienne. Nonadiabatic dynamics in evaporative cooling of trapped atoms by a radio-frequency field. *Phys. Rev. A*, 58:3983–3992, Nov 1998.

- [130] D. J. Owens and J. M. Hutson. Inelastic losses in radio-frequency-dressed traps for ultracold atoms. *Phys. Rev. A*, 96:042707, Oct 2017.
- [131] D. B. Ali. *Design and construction of a cold atoms experiment: towards sodium condensates on a chip*. PhD thesis, Université Paris 13, 2016.
- [132] P. S. Julienne, F. H. Mies, E. Tiesinga, and C. J. Williams. Collisional stability of double Bose condensates. *Phys. Rev. Lett.*, 78:1880–1883, Mar 1997.
- [133] J. Arlt, O. Marag, E. Hodby, S. A. Hopkins, G. Hechenblaikner, S. Webster, and C. J. Foot. Bose-Einstein condensation in a rotating anisotropic TOP trap. *Journal of Physics B: Atomic, Molecular and Optical Physics*, 32(24):5861, Oct 1999.
- [134] J. L. Roberts, N. R. Claussen, S. L. Cornish, and C. E. Wieman. Magnetic field dependence of ultracold inelastic collisions near a Feshbach resonance. *Phys. Rev. Lett.*, 85:728–731, Jul 2000.
- [135] J. L. Roberts. *Bose-Einstein Condensates with Tunable Atom-atom Interactions: The First Experiments with ^{85}Rb BECs*. PhD thesis, University of Colorado, 2001.
- [136] H. M. J. M. Boesten, A. J. Moerdijk, and B. J. Verhaar. Dipolar decay in two recent Bose-Einstein condensation experiments. *Phys. Rev. A*, 54:R29–R32, Jul 1996.
- [137] I. Hughes and T. Hase. *Measurements and their Uncertainties*. Oxford University Press, Great Clarendon Street, Oxford OX2 6DP, UK, 1 edition, 2010.
- [138] M. Zaccanti, B. Deissler, C. D. Errico, M. Fattori, S. Müller, G. Roati, M. Inguscio, and G. Modugno. Observation of an Efimov spectrum in an atomic system. *Nature Physics*, 5(8):586–591, Jul 2009.

- [139] A. Zenesini, B. Huang, M. Berninger, S. Besler, H.-C. Nägerl, F. Ferlaino, R. Grimm, C. H. Greene, and J. von Stecher. Resonant five-body recombination in an ultracold gas of bosonic atoms. *New Journal of Physics*, 15(4):043040, Apr 2013.
- [140] B. D. Esry, Chris H. Greene, and James P. Burke. Recombination of three atoms in the ultracold limit. *Phys. Rev. Lett.*, 83:1751–1754, Aug 1999.
- [141] D. J. Owens. personal communication.
- [142] P. Böhi, M. F. Riedel, J. Hoffrogge, J. Reichel, T. W. Hänsch, and P. Treutlein. Coherent manipulation of Bose-Einstein condensates with state-dependent microwave potentials on an atom chip. *Nature Physics*, 5:592–597, August 2009.
- [143] O. Fialko, A. S. Bradley, and J. Brand. Quantum tunneling of a vortex between two pinning potentials. *Phys. Rev. Lett.*, 108:015301, Jan 2012.
- [144] A. Bonnin, C. Diboone, N. Zahzam, Y. Bidel, M. Cadoret, and A. Bresson. New concepts of inertial measurements with multi-species atom interferometry. *ArXiv e-prints*, October 2017.
- [145] I. Lesanovsky and W. von Klitzing. Spontaneous emergence of angular momentum Josephson oscillations in coupled annular Bose-Einstein condensates. *Phys. Rev. Lett.*, 98:050401, Jan 2007.
- [146] T. H. Johnson, Y. Yuan, W. Bao, S. R. Clark, C. Foot, and D. Jaksch. Hubbard model for atomic impurities bound by the vortex lattice of a rotating Bose-Einstein condensate. *Phys. Rev. Lett.*, 116:240402, Jun 2016.
- [147] P. Calabrese and J. Cardy. Time dependence of correlation functions following a quantum quench. *Phys. Rev. Lett.*, 96:136801, Apr 2006.

- [148] F. M. Cucchietti and E. Timmermans. Strong-coupling polarons in dilute gas Bose-Einstein condensates. *Phys. Rev. Lett.*, 96:210401, Jun 2006.
- [149] A. G. Sykes, M. J. Davis, and D. C. Roberts. Drag force on an impurity below the superfluid critical velocity in a quasi-one-dimensional Bose-Einstein condensate. *Phys. Rev. Lett.*, 103:085302, Aug 2009.
- [150] A. Relaño, J. Dukelsky, and R. A. Molina. Decoherence induced by an interacting spin environment in the transition from integrability to chaos. *Phys. Rev. E*, 76:046223, Oct 2007.